555363
216P

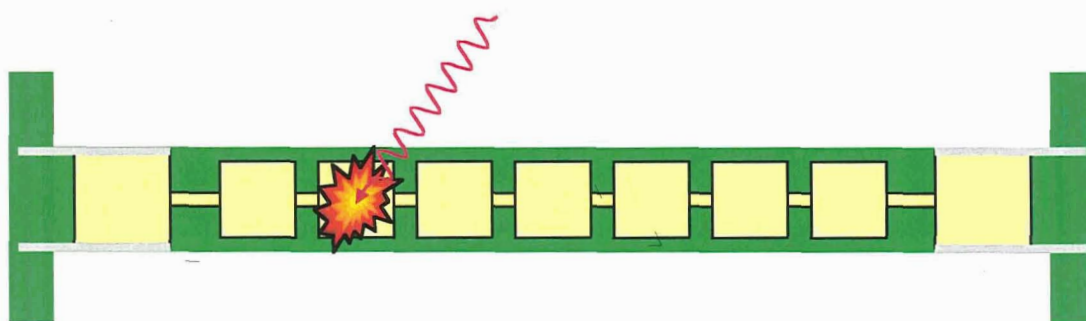# Theory and Development of Position-Sensitive Quantum Calorimeters

E. Figueroa-Feliciano

TR/IN/76
2002 001 670

October 2001

The NASA STI Program Office ... in Profile

Since its founding, NASA has been dedicated to the advancement of aeronautics and space science. The NASA Scientific and Technical Information (STI) Program Office plays a key part in helping NASA maintain this important role.

The NASA STI Program Office is operated by Langley Research Center, the lead center for NASA's scientific and technical information. The NASA STI Program Office provides access to the NASA STI Database, the largest collection of aeronautical and space science STI in the world. The Program Office is also NASA's institutional mechanism for disseminating the results of its research and development activities. These results are published by NASA in the NASA STI Report Series, which includes the following report types:

- TECHNICAL PUBLICATION. Reports of completed research or a major significant phase of research that present the results of NASA programs and include extensive data or theoretical analysis. Includes compilations of significant scientific and technical data and information deemed to be of continuing reference value. NASA's counterpart of peer-reviewed formal professional papers but has less stringent limitations on manuscript length and extent of graphic presentations.

- TECHNICAL MEMORANDUM. Scientific and technical findings that are preliminary or of specialized interest, e.g., quick release reports, working papers, and bibliographies that contain minimal annotation. Does not contain extensive analysis.

- CONTRACTOR REPORT. Scientific and technical findings by NASA-sponsored contractors and grantees.

- CONFERENCE PUBLICATION. Collected papers from scientific and technical conferences, symposia, seminars, or other meetings sponsored or cosponsored by NASA.

- SPECIAL PUBLICATION. Scientific, technical, or historical information from NASA programs, projects, and mission, often concerned with subjects having substantial public interest.

- TECHNICAL TRANSLATION. English-language translations of foreign scientific and technical material pertinent to NASA's mission.

Specialized services that complement the STI Program Office's diverse offerings include creating custom thesauri, building customized databases, organizing and publishing research results . . . even providing videos.

For more information about the NASA STI Program Office, see the following:

- Access the NASA STI Program Home Page at http://www.sti.nasa.gov/STI-homepage.html

- E-mail your question via the Internet to help@sti.nasa.gov

- Fax your question to the NASA Access Help Desk at (301) 621-0134

- Telephone the NASA Access Help Desk at (301) 621-0390

- Write to:
  NASA Access Help Desk
  NASA Center for AeroSpace Information
  7121 Standard Drive
  Hanover, MD 21076-1320

Theory and Development of Position-Sensitive Quantum Calorimeters

Enectalí Figueroa-Feliciano
NASA Goddard Space Flight Center, Greenbelt, Maryland

Available from:

THEORY AND DEVELOPMENT OF
POSITION-SENSITIVE QUANTUM CALORIMETERS

A DISSERTATION
SUBMITTED TO THE DEPARTMENT OF PHYSICS
AND THE COMMITTEE ON GRADUATE STUDIES
OF STANFORD UNIVERSITY
IN PARTIAL FULFILLMENT OF THE REQUIREMENTS
FOR THE DEGREE OF
DOCTOR OF PHILOSOPHY

Enectalí Figueroa Feliciano
October 2001

ii

I certify that I have read this dissertation and that in my opinion it is fully adequate, in scope and quality, as a dissertation for the degree of Doctor of Philosophy.

_____
Blas Cabrera
(Principal Adviser)

I certify that I have read this dissertation and that in my opinion it is fully adequate, in scope and quality, as a dissertation for the degree of Doctor of Philosophy.

_____
Caroline K. Stahle
(NASA Goddard Space Flight Center)

I certify that I have read this dissertation and that in my opinion it is fully adequate, in scope and quality, as a dissertation for the degree of Doctor of Philosophy.

_____
Sarah Church

Approved for the University Committee on Graduate Studies:

_____

iv

Abstract

Quantum calorimeters are being developed as imaging spectrometers for future X-ray astrophysics observatories. Much of the science to be done by these instruments could benefit greatly from larger focal-plane coverage of the detector (without increasing pixel size). An order of magnitude more area will greatly increase the science throughput of these future instruments. One of the main deterrents to achieving this goal is the complexity of the readout schemes involved. We have devised a way to increase the number of pixels from the current baseline designs by an order of magnitude without increasing the number of channels required for readout.

The instrument is a high energy resolution, distributed-readout imaging spectrometer called a Position-Sensitive Transition-Edge Sensor (PoST). A PoST is a quantum calorimeter consisting of two Transition-Edge Sensors (TESs) on the ends of a long absorber capable of one-dimensional imaging spectroscopy. Comparing rise time and energy information from the two TESs, the position of the event in the PoST is determined. The energy of the event is inferred from the sum of the two pulses.

We have developed a generalized theoretical formalism for distributed-readout calorimeters and apply it to our devices. We derive the noise theory and calculate the theoretical energy resolution of a PoST. Our calculations show that a 7-pixel PoST with 6 keV saturation energy can achieve 2.3 eV resolution, making this a competitive design for future quantum calorimeter instruments.

For this thesis we fabricated 7- and 15-pixel PoSTs using Mo/Au TESs and gold absorbers, and moved from concept drawings on scraps of napkins to a 32 eV energy resolution at 1.5 keV, 7-pixel PoST calorimeter.

vi.

Preface

For you, the reader:

With your permission, I'd like to offer my suggestions on how to get the best (or suffer the least) from this thesis. After the introduction, the thesis is divided into two parts: Theory and Experiment.

Part I:

Chapter 2 gives an introduction to quantum calorimeters and the position-sensitive quantum calorimeter concept, and will give you a good sense of what this thesis is about. Chapters 3 and 4 provide very detailed derivations of the noise theory and the energy resolution of single-pixel and position-sensitive calorimeters.

Part II:

Chapter 5 briefly describes our refrigerator, detector mount and data acquisition system. Chapter 6 is a continuation of Chapter 2 and describes our design in more detail. The last two chapters show our results and discuss the future of this development.

I expect that you will fall somewhere in between these three categories:

1. just skimming over to get an idea of what I did

2. interested in learning about calorimeter theory

3. rolling up your sleeves, ready to get really into PoSTs

If you resonate with (1) above, then I'd suggest glancing over Chapters 1 and 2 and then skipping to Part II, which has lots of pretty pictures.

If you feel like a (2), then add Chapter 3.

Between (2) and (3)? Serve up Sections 4.1 and 4.5.1 to the end of the chapter.

A hardy soul? Then add the rest!

By the way, I stuck in a great recipe for cheese flan on page ### ...

To Prof. Arthur B. C. Walker II (1936–2001)

It was the summer of 1993. I was a young student trying to decide what I wanted to be when I grew up. An engineering major, I nevertheless felt the desire to explore physics. I came to Stanford to visit the physics department, and there I met Art. I had no idea this man was going to change my life.

Art talked to me with candor and enthusiasm, and brushed away my doubts about an engineering student from Puerto Rico wanting to do physics at Stanford. "Why don't you come next summer and work for me?" he said. Amazed and delighted at the offer, I instantly accepted.

The summer of 1994 was a turning point in my life. Under Art's tutelage, I worked on his MSSTA sounding rocket payload, my first experience with space experimentation hardware. Art's office was a very interesting place. Entrenched in now legendary mountains of paper, we would sit with Art and discuss the state of the Universe. We would start with work, then move to more general physics questions, and inevitably end up talking about things not in the least related with physics. Art was a great listener. He would sit back and let you talk; only when you were through would he answer with one (from his seemingly never-ending supply) of his stories. His stories, bits and threads from his life, always carried that special knowledge that comes from deep understanding of human nature coupled with years of experience.

Art became my advisor when I came to Stanford, and many a time did I go into his office for another of our discussions on work, studies, politics (he sure had a strong view on *that* subject), and personal affairs.

The last time I saw Art was the day I presented my pre-defense talk at Stanford. He was already very ill, but he came to the physics department that day to see my talk. Afterwards we went to his office and talked one last time about my work, my career, and my future. As I was listening to him, I could not help but think of how lucky I was to share that time with such a sage and warmhearted human being.

With the deepest gratitude for his role in shaping my life, as he shaped so many others before me, I want to dedicate this thesis to my professor, my mentor, my friend, Arthur B. C. Walker.

Thanks for everything, Art.

x   x

Acknowledgements

This thesis is the culmination of 6 very intense years of my life. Although I started this work at Stanford, most of the content in this thesis was developed at the NASA Goddard Space Flight Center, where I have been a Co-op student for the last three years. There is no way I will be able to give thanks to all the people that in one way or another made this work possible. To all of you who are not named, thank you.

I again thank Art Walker for opening the door for me into physics. I would not be here without him. I thank his wife Victoria for representing Art at my graduation, and for the warm friendship she has extended toward me in the little time we've spent together.

I must thank my advisor, Blas Cabrera. His is the repository of all knowledge in the universe. Through my four years working with him, I've grown a great deal intellectually by just being near him. Blas not only has a incredible amount of knowledge at his fingertips, but has that great intuition that really sets the standard for what an experimental physicist ought to be.

My thesis work would have gone nowhere without Caroline Stahle. In the development of my thesis, Caroline has been my closest mentor and advisor. She has gone through my derivations so many times I'm sure she feels this is as much her thesis as it is mine. She has been the person that has kept me on the right track, the person who has explained all those things I was supposed to know and didn't. We have also spent many hours in front of chalkboard figuring things out as a team. I thank her for always treating me as an equal, since my first day at the job. That really meant a lot to me.

I thank Sarah Church for taking the time to be on my reading committee, I hope we get to work together soon. Also thanks to Doug Osheroff and Bruce Clemens for being in my dissertation committee.

The first year at Stanford was very hard for me. If it weren't for Hakeem Olusyei, my spirit brother, I would have not made it. Hakeem always kept it real, kept me on my toes, and was always there for loosening up and having a laugh. Thanks for all the fun, man. If Hakeem was my spirit brother, David Santiago was my spirit guide. Without David I would *not* have passed E&M, and with his help I was able to start up that hard learning curve that first year.

My second year was very different. This is when I met my physics support group. You all know who you are. Special thanks to Tim, Danna, and Nicci. To all of you, thanks for the movies, the problem sets, the volleyball games, the food, the journal talks about volleyball strategy and other more esoteric stuff. Thanks for being there for me and supporting me

through the good times and the bad ones too.

In the lab, I want to thank Sae Woo for being so dang smart, and so willing to share it with us. I want to thank Tarek for being so weird, annoying and strange, somehow in an incredibly likeable way. I still have nightmares about your face smiling at me on my computer screen ...

Aaron, what can I say. Thanks for teaching me the fridge, for being my problem set buddy, for being such a geek in your own Jockish sort of way. Thanks for all those uncountable little things that we shared together.

A very special thanks to Marcia Keating. Marcia, I love you. I know you know it, but I just wanted to say it here. You were much more than the graduate student coordinator, you became my surrogate mother, and a good friend. Thanks for being there for me, for your support, for your help, for just being the great person you are.

I want to thank Kathleen Guan for being such a great help in these past few months. Thanks for your diligence, thanks for your friendship. I truly hope you find your way. Thanks to Linda, Jeniffer, Cindy, Rosenna, Rick, Karlheinz, Joel and all the other staff that made Varian more than a set of brick walls.

OK, now to Goddard. I want to thank Jerry Soffen, who passed away before he could see this work. He introduced me to Goddard, and the summer I spent here as a NASA Academy research associate was one of the most exciting of my life. That summer prepared me for coming back. A special thanks to Jonathan Ormes, who offered me my coop position, I would not be here without him. Thanks to Andy for showing me the FEA and getting me interested in calorimetry, and for all the seemingly random information you have in your head at all times. Thanks to Don Horner for keeping me awake while I wrote this thing. Thanks to Rich, Caroline, Scott, Kevin, Keith, Greg, John, Fred, Regis, Mark, Mary and Carl for your great discussions, for making my devices, for the beverages, the cookouts, the hikes, the concerts, the dog walks, the guitar tunes, the lame jokes, the good jokes, the "free" food collected at 2:00 am, all the stuff I've learned from you guys, all the stuff I *will* learn from you guys, and all the fun we will have. Thanks to Pam, Joan, Nancy and Rhonda for the paperwork and the hugs.

Gracias al Dr. José Roberto López, mi inspiración. Mire a donde a llegado la semilla que usted plantó. Gracias al Dr. Juan González Lagoa, por creer en mí, por apoyarme y ser el luchador que es, a María y Mabel por su cariño y ayuda, las quiero mucho a las dos. Gracias a Mayra por tu amistad, y ¡por tu receta de flan!

Bueno, gracias a la multitud CROEMita que me recibieron hace tantos años atrás, todavía los recuerdo a todos con cariño. A Chopper y Salgado, ustedes saben que siempre están cerca de mí, los llevo guardados en mi corazón. Gracias por ser mis hermanos además de mis amigos.

Teresa, nunca te veo, pero tú sabes lo que hay. Un beso bien grande y gracias por la terapia telefónica ...

A mami, gracias por traerme a este mundo, por enseñarme el valor de la vida y del esfuerzo, por tu apoyo y amor. Papi, gracias por enseñarme el camino, por darme tu fuerza y tu paz. Gracias a ambos por sus oraciones y fé. A abuelita, te quiero, gracias por los

flanes y natillas que hacíamos juntos. A Kianna y Mary, las amo, cuídense mucho, ¡de aquí pa' Hollywood!

Finalmente, a Bárbara, gracias por soportarme todo este tiempo, por esperar en casa cuando nos veíamos cinco horas a la semana, tú sabes que sin tí me hubiera comido un caballo mellao. Gracias por ser mi amiga y mi esposa. Te amo.

Quiso volar igual que las gaviotas,
libre en el aire, por el aire libre.
Y los demás dijeron: pobre idiota,
¿no sabe que volar es imposible?
Mas extendió sus alas hacia el cielo,
y poco a poco fue ganando altura,
y los demás quedaron en el suelo,
guardando la cordura.

-Alberto Cortez

Contents

xx

List of Tables

List of Figures

Chapter 1

Introduction

1.1 X-ray Astrophysics: Exploring the Hot Universe

In the last 35 years, X-ray astronomy has matured into one of the most exciting branches of astrophysics. The field has evolved from a small sub-branch of astrophysics into a vital window to the mysteries of our Universe. X-rays are emitted by some of the most energetic phenomena in the Universe. The study of these high-energy photons is crucial for understanding the fundamental questions in astrophysics involving high temperatures or explosions. In essentially all cases in which gravitational forces are important to the dynamics and energetics of a system, the presence of X-ray emitting gas is a natural consequence. As such, X-ray observations play a crucial role in addressing the origin, structure, and evolution of the Universe and of its principal material constituents: dark matter, clusters of galaxies, galaxies, stars, and planets.

Because soft X-rays do not penetrate the Earth's atmosphere, X-ray astrophysics instruments are by necessity space-borne. Above 20 keV, hard-X-rays are accessible from balloons, but most of the astrophysics done with X-rays needs all the atomic line emission that occurs below 9 keV.

The first X-ray observation of an astronomical source was obtained by a sounding rocket payload in 1962. Within the last decade, the ROSAT, ASCA and RXTE X-ray satellites have made great progress in the field. ROSAT resolved 80% of the X-ray background at 1 keV into discrete sources. RXTE discovered millisecond oscillations and pulsations from the environs of neutron stars and black holes in X-ray binaries. ASCA measured for the first time the relativistically broadened iron K_α emission line from active galactic nuclei, opening the door for tests of general relativity in the strong gravity limit. Today, with the successful launch of the Chandra and XMM-Newton X-ray observatories, and the launch of Astro-E2 in 2005, we have entered a new era for this exciting field.

1.2   The Constellation-X quantum calorimeter

The Constellation X-ray Observatory (or Constellation-X) is a next-generation X-ray tele-scope that will illuminate the mysteries of black holes, dark matter, clusters of galaxies and life cycles in the universe. If Chandra is the Hubble of X-ray astronomy, Constellation-X will become the Keck of X-ray astrophysics, providing high energy resolution spectra of objects only barely visible with Chandra. Constellation-X will have a throughput 20 to 100 times higher than the spectrometers in Chandra, XMM-Newton or Astro-E2.

The prime objective of Constellation-X is to obtain high-quality X-ray spectra. To that end, three different spectrometers are under development: a grating coupled to a CCD for energies between 0.2 and 1.5 keV, a non-dispersive imaging quantum calorimeter for energies between 0.25 and 10 keV, and a CZT solid state detector for the 6 to 40 keV range.

A major advancement in X-ray detectors will be the Constellation-X Quantum Calorime-ter. This revolutionary instrument is capable of imaging extended sources while taking high-resolution spectra at each pixel with almost 100% quantum efficiency and high count rate. The spectral resolution of this instrument will be 2 eV FWHM in the 0.25 to 6 keV band. Coupled to the large effective area of the Constellation-X optics, the quantum calorimeter will be capable, among other things, of imaging spectroscopy of faint extended objects at cosmological distances.

A quantum calorimeter (also commonly called a microcalorimeter) measures the temper-ature increase in a pixel when an X-ray is absorbed by it. The first technology developed for X-ray quantum calorimeters was silicon implanted thermistors. These devices have been de-veloped for flight missions by our group at the NASA Goddard Space Flight Center. Such calorimeters have been flown in the X-ray Quantum Calorimeter rocket payload (Porter et al., 2000a), and will fly in the X-ray Spectrometer (XRS) on the reflight of Astro-E (Kelley et al., 1999). The Constellation-X calorimeter differs from the previous calorimeter both in the type of detector and the type of readout that it uses to determine the energy of incoming X-rays (we will discuss all the details in Chapter 2).

To obtain high energy resolution spectra, diffraction gratings are often used. Gratings spread out the incoming X-rays into a spectrum on the focal plane much like a prism spreads out a beam of light into a rainbow on a piece of paper. This is called dispersive spectroscopy, because a point source appears stretched out on the focal plane. Because of this dispersion, gratings cannot image extended objects, so spectra of objects such as nearby galaxies, supernova remnants, or galaxy clusters are vastly more difficult, if not impossible, to unravel with gratings. Gratings also tend to have low quantum efficiency, so obtaining spectra of faint sources requires large amounts of valuable observing time. X-ray CCD cameras have excellent imaging capabilities (much better than calorimeters are able to do), but have only modest energy resolution ($E/\Delta E \sim 50$), and for the science objectives of Constellation-X one needs imaging ability, high efficiency, and especially energy resolution. The quantum calorimeter provides all of these things. The technologies that make this possible are discussed in Chapters 2 and 6.

Due to mission design constraints, Constellation-X optics have to be very light. To obtain the huge collecting area, the optics have given up some spatial resolution and will

have a half power diameter of ∼ 15 arcsec or better. The Constellation-X soft X-ray telescope has a 10 m focal length. Both of these design parameters establish the current Constellation-X plate scale and required pixel size: greater than a 2.5 arcmin field-of-view (FOV) with 5 arcsec pixels. This can be achieved by a 32 × 32 imaging array, each pixel being a 250 μm square. The resolution specifications are 2 eV FWHM below 6 keV ($E/\Delta E = 3000$ @ 6 keV), with a very high quantum efficiency and a high throughput (∼ 1000 counts/sec/pixel). The optic's point-spread-function (PSF) drives the pixel size, but the array size is a compromise between desire and current technological reality.

1.3 The need for large field-of-view spectrometers

The collecting area and the spectroscopic prowess of Constellation-X will revolutionize X-ray astrophysics. The current baseline design of 2.5 arcmin for the quantum calorimeter leaves many objects bulging out of the field-of-view (FOV) of the device. The FOV was determined by balancing technological constraints and scientific needs. We will discuss some of the cases where a larger FOV would make a big difference in the science output of the observatory.

Clusters of galaxies, the largest objects in the Universe, serve as an ideal laboratory for studying the structure and evolution of the Universe. Most of the matter in galaxy clusters (and the entire Universe) is dark matter. The bulk of baryonic matter (i.e., not dark matter) is in the form of hot gas, not galaxies. The X-ray emission from the hot gas of the intra-cluster medium will allow us to map out dark matter in clusters. Constellation-X will also provide an accurate measurement of the elemental abundances in clusters to large distances, providing information about the metals produced by member galaxies over cosmic time scales. Detection of the non-thermal emission in clusters of galaxies has significant impacts on the underlying cosmological models through the estimation of the cosmological parameter Ω. Constellation-X will measure for the first time the mass motion of gas in clusters, and map out the velocity field of the gas. Without these observations the determination of the total mass from X-ray temperature profiles is uncertain. Mapping the emission as a function of radius will benefit greatly from a larger FOV.

Groups and clusters of galaxies have a virial radius (the radius within which the intra-cluster medium (ICM) gas is bound) of $R = 2.48\sqrt{T_x/10\text{keV}}$Mpc where T_x is the "emission-weighted temperature" and Mpc is "Mega parsec" (Evrard et al., 1996). For a cluster with temperature $T_x = 5$ keV, $R = 1.76$ Mpc. At a redshift $z = .1$ (570 Mpc), the size of the cluster would be 21.2 arcmin. This is the angular size of the virial diameter, but an observation of the cluster might not be able to image out to that distance because the surface brightness drops rapidly toward the edges of the cluster. The calculation of the image size on a particular instrument depends on the spectrum, intensity profile of the cluster, and instrument collection area. We will call "*equivalent* angular size" the angular size of the virial radius. Taking the ASCA Cluster Catalog data from Horner (2001) and plotting the equivalent angular size vs. redshift, we arrive at Figure 1.1. The data have been divided into temperature bands, which are a good measure of their size. Thus, hotter
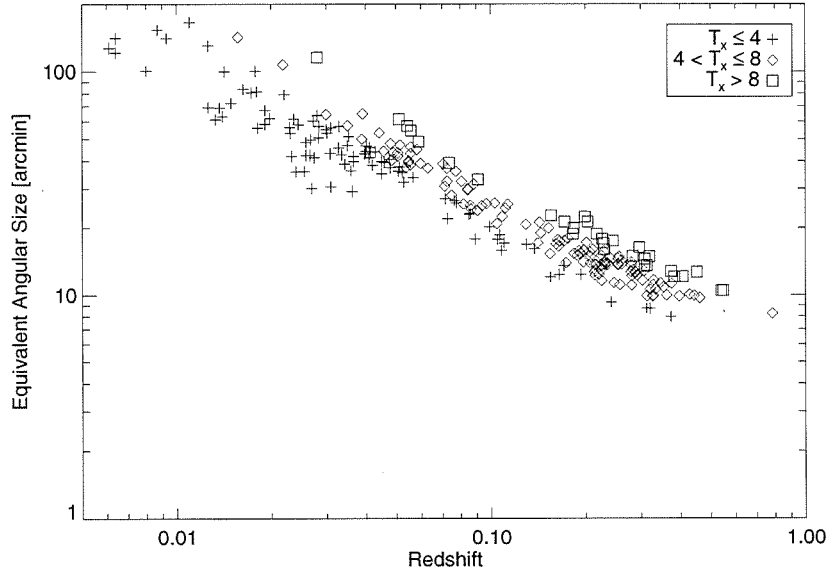
Figure 1.1: Galaxy cluster equivalent angular size as a function of redshift. The data is divided into three temperature bands: $T_x \leq 4$ keV, T_x between 4 and 8 keV, and $T_x > 8$ keV. For this figure $H_o = 50$ km/s/Mpc and $\Omega = 0.5$. Figure courtesy of Dr. Don Horner.

clusters at a particular redshift will be larger than cool ones. We see that all the clusters in this sample are much larger than 2.5 arcmin.

Because the angular size of an object does not decrease monotonically with redshift (due to cosmological effects) (Hogg 2000; Peebles 1993, pp. 325-327), there is a minimum size a cluster will appear (which occurs at a redshift z of 1.2 to 3.5, depending on the cosmological model used). The minimum angular size for a cluster of intrinsic diameter D is from $1.95D$ to $2.87D$ arcmin Mpc^{-1}, depending on the cosmological model used. For our example cluster diameter of 3.52 Mpc, the minimum equivalent angular size will be from 6.86 arcmin to 10.1 arcmin. For cluster observations, the benefits of a larger FOV are evident.

Of X-ray interesting objects, next down in size are galaxies. Giant elliptical galaxies are on average 50 kpc in diameter. The Virgo cluster of galaxies is about 16 Mpc away, so a giant elliptical in the Virgo cluster would have an angular size of 10.7 arcmin in diameter. Spiral galaxies, on average, are about 20 kpc in diameter. A spiral in the Virgo cluster would have an angular size of 4.3 arcmin in diameter.

Figure 1.2 shows NGC1399, a giant elliptical galaxy, as seen by ROSAT. This galaxy is in the center of the Fornax galaxy cluster. The bright object to the lower left is another galaxy. The PSF of this image is similar to the PSF expected from Constellation-X, so it is a good comparison for what a future Constellation-X observation would look like. The black square is 2.5 arcmin to a side. To measure a spectral profile of this object, multiple observations would have to be patched together with the current Constellation-X FOV.
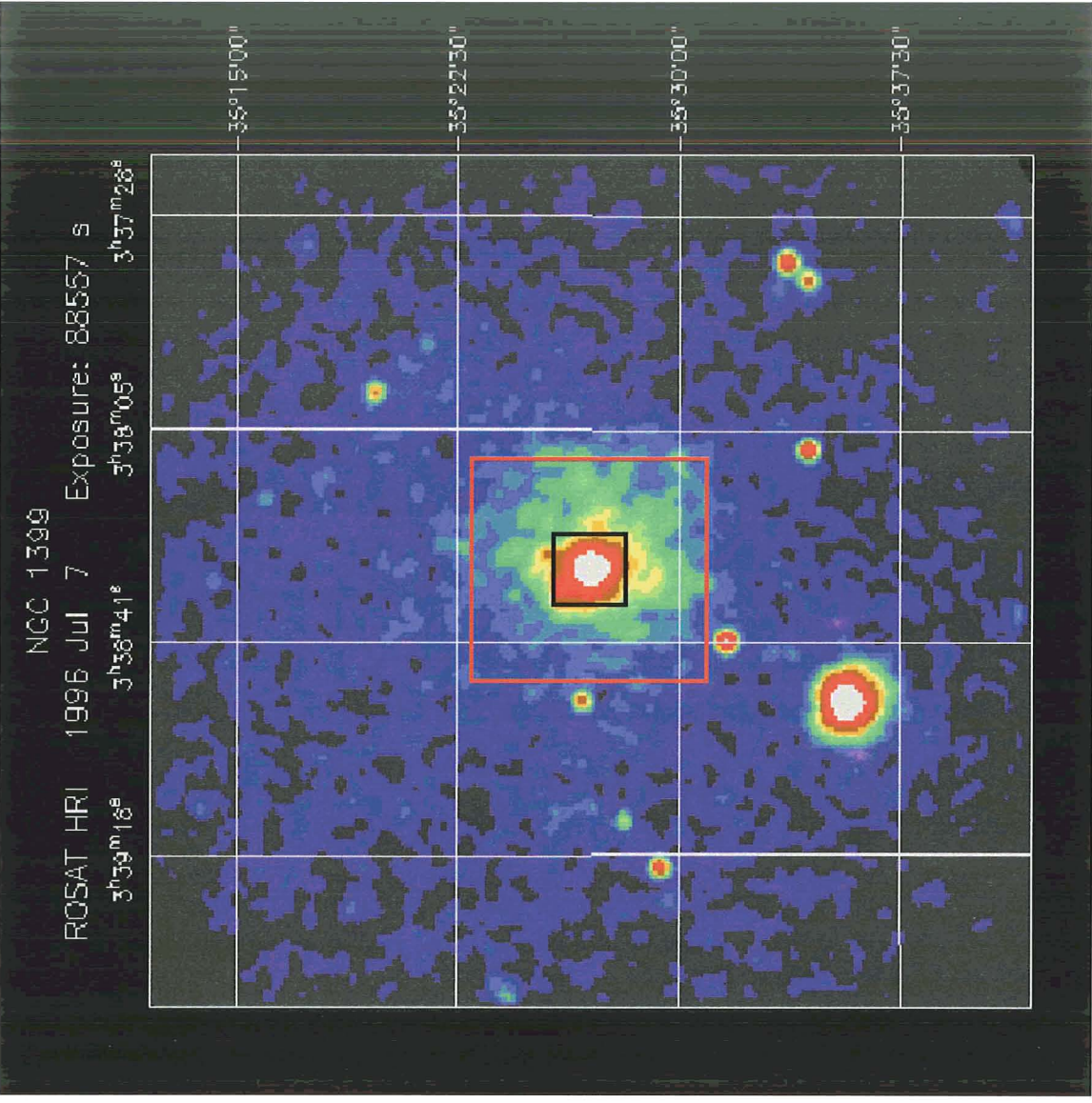
Figure 1.2: NGC1399 is a giant elliptical galaxy in the center of the Fornax galaxy cluster. The black square is the baseline 2.5 arcmin Constellation-X FOV. The red square is the 10-fold improvement in area using our position-sensitive quantum calorimeters.

The large observing time required to do these type of observations will make it difficult to do detailed profiles for a large number of these objects. If the area of the detector was increased by an order of magnitude, we would obtain the ~ 8 arcmin square shown in red. The difference is striking.

Even further down the size scale of X-ray interesting objects are supernova remnants. The study of supernova remnants illuminates the processes for elemental enrichment of the inter-stellar medium, the mechanism from which all planets and known life are formed. Almost all galactic supernova remnants have diameters larger than 3 arcmin. Here the same arguments hold. A very important part of supernova remnant research involves spatially-resolved spectroscopy to understand the composition and structure of the remnant. This means spectra at all radii of the remnant are needed. With a small FOV, multiple observations of each remnant will be required.

In all these calculations, we have ignored the need for background subtraction. One would always like to have a section of the FOV looking at the background, which means the FOV should ideally be larger than the source size. If this is not possible, multiple exposures will again be required.

There are many X-ray objects that are point sources. Most deep (far z) objects that will be studied will obviously be point sources. But these studies tend to be statistical. The larger the FOV, the more sources one will be able to study at a time. An order of magnitude increase in area equals an order of magnitude more sources, or an order of magnitude fewer observations.

With the effective area of Constellation-X, 100 ks observations of any object are almost guaranteed to detect objects in the foreground and/or background that emit X-rays. These "serendipitous" sources will provide valuable extra science for each observation, especially considering the quality of the serendipitous spectra due to the Constellation-X effective area. The larger the FOV, the more serendipitous sources will be detected.

The current Constellation-X baseline optics will have an unvignetted FOV of ~ 12 arcmin. Only 2.5 arcmin will be used by the quantum calorimeter in the current design.

The above arguments make a solid case for an increase in the FOV for Constellation-X. This is the challenge undertaken by this thesis.

1.4   A viable solution

Our group at the NASA Goddard Space Flight Center is developing transition-edge-sensor (TES) calorimeters for the Constellation-X mission (Section 6.1). These calorimeters use superconducting quantum interference devices (SQUIDs) to read out the signal (Section 5.2). Our collaborators as NIST are developing SQUID multiplexing technology that will allow a 1000 channel system to be implemented (Chervenak et al., 1999). Although potential exists for this design to move beyond 1000 channels, with the current technology it will be exceedingly difficult to implement a 10,000 channel flight-qualified system. Thus the number of available readout channels is the main obstacle toward moving to larger number of pixels for Constellation-X.

The need for many pixels coupled to the limitation on the number of readout channels motivated our design. We have developed a position-sensitive quantum calorimeter that can read out many pixels per SQUID channel, therefore increasing the total number of pixels without increasing the number of SQUID readout channels needed. If we have the Constellation-X readout system of 1000 channels, then using this technology an array of 3,500 to 15,500 pixels could be read out by this 1000 channel system. By having this greater number of pixels, we would obtain from 3.5 to 15.5 times more area for the Constellation-X focal plane instrument, without changing the detector pixel size.

The question to be answered by this thesis is whether position-sensitive calorimeters can obtain the same energy resolution and count rates as single-pixel arrays.

Part I

Theory

Chapter 2

Foundations

2.1 Quantum calorimeter basics

The idea behind a quantum calorimeter is deceptively simple. A "calorimeter" is an instrument that measures energy,[1] and the word "quantum" refers to the fact that we are measuring the energy of quanta of light. Figure 2.1 is a schematic of the simplest calorimeter. An absorber with heat capacity C is connected via a weak link with thermal conductance G to a heat sink (also called a cold bath) at temperature T_b. If no power is applied, the absorber temperature $T(t)$ will be equal to the bath temperature. If a photon with energy E_γ is absorbed, then the temperature of the absorber will rise and then cool back to the bath temperature. The rise in temperature will be proportional to the energy of the photon ($\Delta T_\gamma = E_\gamma/C$). Thus by measuring the rise in temperature ΔT_γ as each photon comes in, the energy of the photons can be determined. That is quantum calorimetry in a nutshell.

If constant power is applied, then the absorber will rise to a temperature above the bath temperature until the power flowing into the absorber equals the power flowing out through the weak link into the cold bath. The thermal equation for this system is

$$C\frac{dT(t)}{dt} = P - P_{\text{link}}\big(T(t), T_b\big) + E_\gamma \delta(t - t_\gamma) \tag{2.1}$$

where P is the heat flow into the absorber[2], (which for now we are assuming constant or zero), and $P_{\text{link}}\big(T(t), T_b\big)$ is the power that flows from the absorber to the cold bath through the weak link. $E_\gamma \delta(t - t_\gamma)$ is an absorption event; the delta function deposition of the energy of photon γ into the absorber at time t_γ. The functional form of $P_{\text{link}}\big(T(t), T_b\big)$ depends on the physics of the particular device, and for now we will assume

$$P_{\text{link}}\big(T(t), T_b\big) = G\big(T(t) - T_b\big) \tag{2.2}$$

---

[1] According to Webster, a calorimeter is "any of several apparatuses for measuring quantities of absorbed or evolved heat or for determining specific heats. From Latin *calor*."

[2] This power usually refers to the power dissipated by a thermometer with bias applied, but it could be radiation from the environment or any other parasitic load.
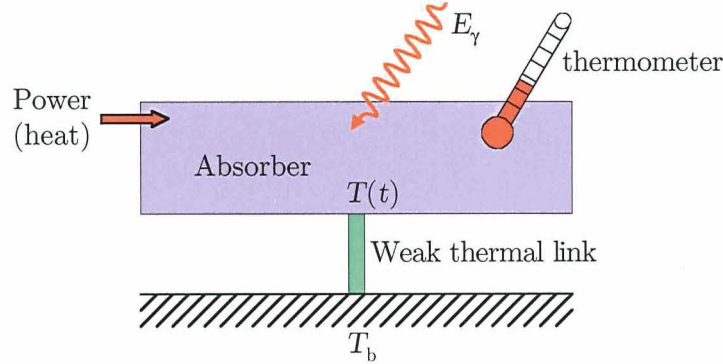
Figure 2.1: A simple calorimeter. An X-ray is absorbed in a pixel which has a weak thermal link to a cold bath. The pixel heats up when the X-ray deposits its energy in it, and then cools back down as heat flows from the pixel to the cold bath. This temperature pulse is measured by a thermometer. The height of the pulse is proportional to the energy of the X-ray.

which makes Eq. (2.1) linear, and taking $t_\gamma = 0$ we can immediately solve to obtain

$$T(t) = \frac{E_\gamma}{C}e^{-t/\tau_o} + \left(\frac{P}{G} + T_{\rm b}\right) \tag{2.3}$$

with a time constant $\tau_o \equiv C/G$ and a quiescent absorber temperature $P/G + T_{\rm b}$. So the simplest calorimeter has an exponential decay response with a time constant of C/G and an initial temperature rise $\Delta T_\gamma = E_\gamma/C$. By measuring $T(t)$ the energy and timing of incoming photons can be determined.

A bolometer is essentially the same device, but looking at many photons instead of one. The difference between a bolometer and a calorimeter is that the bolometer measures the power, usually from a flux of photons hitting the absorber in rapid succession, while a calorimeter usually measures the energy deposited by a single photon or particle.

For a basic overview of quantum calorimetry, see Stahle et al. (1999) or a more in depth treatment in Stahle (2000). For a general review of low temperature detectors and their applications, see Booth et al. (1996).

2.1.1   X-ray absorption and thermalization

In the calculation above we made the simplifying assumption that the photon thermalizes immediately into the absorber. Next, we briefly look at the process of absorption and thermalization.

In the 0.1 to 10 keV energy band (our band of interest for this thesis), the primary interactions of X-rays with matter are the photoelectric effect, Rayleigh scattering, and Compton scattering (Knoll, 1979). Rayleigh scattering is a coherent process where the X-ray is deflected off one of the atoms in the absorber. No energy is deposited in the absorber. Rayleigh scattering therefore does not produce any signal in our thermometer. In Compton

scattering, the X-ray scatters off an electron and imparts some of its energy to it. For X-rays in our energy band and the materials we use as absorbers, the cross section (probability to for the interaction to occur, see Knoll (1979), chap. 2) of Compton scattering is orders of magnitude less than for the photoelectric effect (Evans, 1955).

In the photoelectric effect, the X-ray is absorbed by an atom in the absorber, which ejects a previously bound electron with an energy $E_e = E_\gamma - E_b$, where E_γ is the X-ray energy and E_b is the binding energy of the electron to the atom. The binding energy of the electron must be lower than the energy of the X-ray. The most probable origin of the electron is the highest-energy bound state that satisfies the $E_b < E_\gamma$ condition. For absorbers like bismuth, rhenium and tin, X-rays in the 0.1 to 10 keV band will not have enough energy to kick off a K shell electron (see Center for X-ray optics; NIST physical reference data). L shell and higher bound electrons will be accessible depending on the material and the X-ray energy.

This ejected electron is called a "photoelectron." This photoelectron now has a much higher energy (E_e) than the average electron energy, and has a huge cross section with other electrons. The photoelectron's mean free path[3] is extremely short, and it collides with other electrons, shedding its energy. Also, the interaction of the X-ray with the atom leaves the atom with a vacancy in one of its bound shells. This vacancy is quickly filled by the capture of a free electron and/or the rearrangement of electrons from the other shells of the atom. In these processes one or more characteristic X-rays may be generated. In most cases these secondary X-rays are quickly reabsorbed close to the original site through photoelectric absorption with less tightly bound shells, and the process starts again. Another possibility is that the atom relaxes by the emission of an Auger electron. In this process, the excitation energy of the atom is transferred directly to one of its outer shell electrons, causing the electron to be ejected from the atom. This electron (called an Auger electron) appears with an energy given by the difference between the original atomic excitation energy and the binding energy of shell from which the electron was ejected. This process dominates for lower energy photoelectric absorption events and higher bound-shell vacancies.

Soon a ball of energetic electrons is created around the absorption point. As the number of electrons in this process increases, the average energy of any one electron goes down. As the mean electron energy goes down, electrons have a higher probability of releasing energy by the emission of phonons.[4] When the electron energy drops below a few eV, phonon emission becomes the dominant energy-loss mechanism. The mean free path increases as the energy of the particles decreases, so the size of the ball grows rapidly. Finally, the mean energy of all the particles in the detector rises and a Maxwell-Boltzman distribution

---

[3] The mean free path is the average distance a particle travels before hitting another particle, a quantity related to the cross section and the speed of the particle.

[4] In a perfect, infinite crystal made of atomic nuclei with their corresponding electrons that has been cooled to absolute zero, conduction band electrons propagating through the crystal would never collide with the nuclei. But no crystal is perfect or infinite or at absolute zero, and electrons do collide with the nuclei and excite the crystal vibrational modes. One can equivalently describe these vibrational modes by fundamental excitations called phonons. When we talk about phonons we are talking about the excited vibrational modes of the crystal. Ashcroft and Mermin (1976, chap. 23) gives a good description of phonons in the low-temperature limit.

around a higher mean energy is reached. This is what we call "thermalization," because the increase in mean energy is detected as an increase in the temperature of the detector.[5]

Cabrera et al. (1993) has done Monte-Carlo simulations and taken measurements on Si detectors to study these thermalization processes. Fann et al. (1993); Maris (1993); Tamura (1993) are other excellent papers on the subject.

2.2 Transition-edge sensors

Many methods of measuring the absorber temperature exist. Our group uses thermistors, i.e. resistive elements whose resistance is a function of temperature. This work is based on superconducting-Transition-Edge Sensors (TESs), sometimes called Superconducting Phase Thermometers (SPTs). A TES is a superconducting film operated in its superconducting transition (Figure 2.2). Since the R vs. T curve is very steep at the TES operation point, a small change in temperature causes a large change in resistance. Hoevers (2002) gives a review of current TES efforts.

2.2.1 Electrothermal feedback and pulse decay time

Several different ways of maintaining the TES in its transition have been developed (Galeazzi, 1998; Irwin, 1995b; Meier et al., 2000). We use the method developed by Irwin (1995b) called the electrothermal feedback TES (ETF-TES), and reproduce some of his theoretical results below. In this scheme the TES is voltage biased, and Joule heating of the TES maintains its temperature in the transition. The power input is a function of resistance $P(T) = V^2/R(T)$ and thus of temperature. Figure 2.2(b) shows the two power terms in Eq. (2.1) vs. temperature for the curve in Figure 2.2(a) and using typical values for the constants. When the TES is normal, the resistance is large, and the input power $P(T)$ is lower than the output power, so the TES cools. As it cools, it enters its transition, and the resistance rapidly decreases. As the resistance decreases, the input power $P(T)$ increases, slowing the cooling rate. The TES enters a stable equilibrium between the power leaving the device through the weak link and the power input through the Joule heating of the TES (the crossing point in the figure). If the temperature drops, the input power rapidly increases and heats the device back to the bias point. This is called negative ETF. The negative ETF makes the TES a self-biasing device which is very stable and easy to operate. As we shall see, the large negative slope of the output power curve that results from ETF also causes the pulses to decay more quickly, an added benefit which allows for devices with very high count rates. We will now derive the pulse decay time (τ_{eff}) and demonstrate its dependence on the device parameters.

---

[5]Electron-phonon decoupling at low energies produces an out of equilibrium electron temperature which is higher than the phonon temperature for 100's of μsec (Roukes et al., 1985). In our transition-edge sensors we measure the electron temperature.
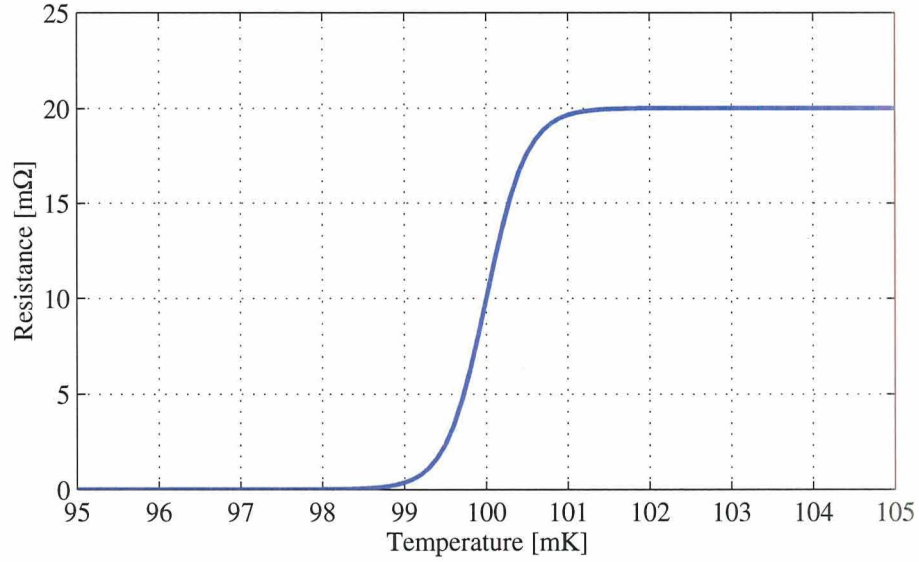
(a) Schematic of R vs. T curve for a transition-edge sensor. A TES is a superconducting film biased within its transition. Within the transition, a small temperature change creates a large change in the resistance, making a very sensitive thermometer within a small operating range.
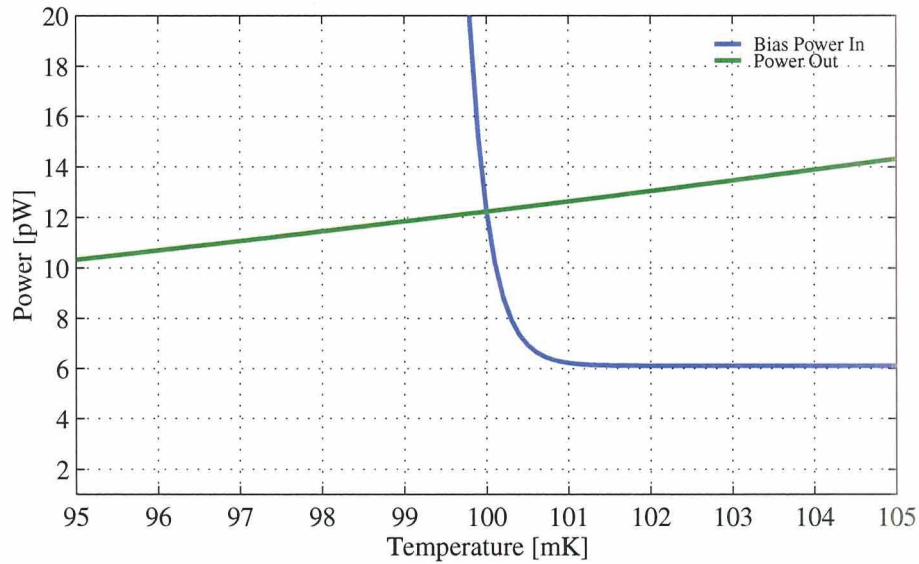
(b) Power into calorimeter at constant voltage V from bias $V^2/R(T)$ (at constant V) and power out of calorimeter through weak link as a function of temperature. The crossing point is the stable quiescent operating point of the TES. Notice the very sharp slope of the input power.

Figure 2.2: R and P vs. T for a TES

To gauge the sharpness of the transition, we define the dimensionless parameter α:

$$\alpha \equiv \frac{T}{R(T)}\frac{\partial R(T)}{\partial T} \tag{2.4}$$

where, for now, we have assumed that the resistance is only a function of temperature (it is also a function of current, but we will take that up in Chapter 3).

As we mentioned before, the functional form of the power output to the cold bath through the weak link depends on the physics of the weak link. In our devices the power output is of the form

$$P_{\text{link}}\big(T(t), T_{\text{b}}\big) = K\big(T(t)^n - T_{\text{b}}^n\big) \tag{2.5}$$

where K is a constant and n is a number between 2 and 5 depending on the dominant mechanism of heat transfer and the dimensionality of the link (Anghel et al. 1998; Ashcroft and Mermin 1976, chap. 25).

Rewriting the thermal equation (Eq. (2.1)) we obtain

$$C\frac{dT(t)}{dt} = \frac{V^2}{R(T)} - K\big(T(t)^n - T_{\text{b}}^n\big) + E_\gamma \delta(t - t_\gamma) \tag{2.6}$$

where again $E_\gamma \delta(t - t_\gamma)$ is a delta function input of energy E_γ at time t_γ, i.e. a photon. In quiescence

$$P = \frac{V^2}{R} = K(T^n - T_{\text{b}}^n) \tag{2.7}$$

where P is the input power at a particular bias V.[6] To solve this non-linear differential equation analytically we must linearize the system. Using Taylor expansion (the procedure is explained in Section 3.1.1), we expand to first order in ΔT:

$$C\Delta\dot{T}(t) = \frac{V^2}{R} - K(T^n - T_{\text{b}}^n) - \frac{V^2}{R^2}\frac{\partial R}{\partial T}\Delta T - nKT^{n-1}\Delta T + E_\gamma \delta(t - t_\gamma) \tag{2.8}$$

where R and T are the quiescent values and ΔT is the dynamic variable. Then from Eq. (2.7) the first two terms cancel. We define

$$G \equiv \frac{dP}{dT} = nKT^{n-1} \tag{2.9}$$

---

[6]Since we are operating in the transition of the TES, the change in temperature as R goes from zero to R_{n} can be very small. If we assume that $T = T_{\text{c}}$ (where T_{c} is the critical superconducting transition temperature) for all points in the transition, then the quiescent power will be the same for any bias. Note that we are referring to the quiescent value of the power. This is reflected in the almost horizontal slope of the output power in Figure 2.2(b). The bias point is the intersection of the two lines.

set $P = V^2/R$, and use Eq. (2.4) to arrive at

$$\Delta \dot{T}(t) = -\left(\frac{\alpha P}{TC} + \frac{G}{C} \right) \Delta T + \frac{E_\gamma}{C} \delta(t - t_\gamma) \tag{2.10}$$

The solution to this equation as before is a simple exponential, but the effective time constant is now

$$\tau_{\text{eff}} = \frac{\tau_o}{1 + \frac{\alpha P}{TG}} \tag{2.11}$$

Substituting the definitions above for P and G and using Eq. (2.7) we get the equivalent

$$\tau_{\text{eff}} = \frac{\tau_o}{1 + \frac{\alpha}{n}\left(1 - \frac{T_{\text{b}}^n}{T^n}\right)} = \frac{\tau_o}{1 + \frac{\alpha\phi}{n}} \tag{2.12}$$

where

$$\phi \equiv \left(1 - \frac{T_{\text{b}}^n}{T^n}\right) \tag{2.13}$$

so ϕ goes from 1 to 0 as the bath temperature increases from absolute zero to the detector temperature. With this nomenclature the variables are the operating temperature and the base temperature; α and n can be determined from theory or more commonly from fitting data for each device. To keep the derivations general we will resort to the $\alpha\phi/n$ notation sparingly.

Defining "extreme electrothermal feedback regime" as a state where $T^n \gg T_{\text{b}}^n$ and $\alpha/n \gg 1$ we can express the decay time as

$$\tau_{\text{eff}} = \frac{n\tau_o}{\alpha} \tag{2.14}$$

For large α, ETF can thus make TES calorimeters have much faster decay times than their intrinsic time constants. We will see in the next section why it is desirable to have fast decay times. Looking at Eq. (2.11), one could argue that if one had a device with $\alpha \sim 5$ (as in semiconductors), one could just increase G to decrease τ_o to get the desired decay time. This is true, but in practice non-linear effects make it hard to achieve the same decay times in semiconductor calorimeters that are found in TES calorimeters. The main problem is power. As one increases G, one needs to increase the power into the thermistor (per Eq. (2.7)) to keep the thermistor at its same operating point. In both semiconductor and TES detectors, non-linear effects prevent the arbitrary increase of the input power. So once this limit has been reached, increasing α is the only way to make the decay time faster.

A note to the reader: this discussion is valid only for ETF calorimeters and assuming each X-ray is recorded for several decay-time constants after the peak (as explained in the next sections). Other bias techniques or other filtering methods that record only to slightly after the peak have different constraints and trade-offs. One must take great care when

comparing across these methods, since one must look at count rate, dead time, and energy resolution simultaneously.

2.2.2   Decay time and pile-up

To understand the importance of pulse decay time, we must talk about count rate, pile-up, dead time, and energy resolution. Count rate is the number of X-rays per unit time that hit the detector. Pile-up is the condition where an X-ray hits the detector, and while the detector is still recovering from the increase in temperature imparted by this first X-ray, a second X-ray hits. In a temperature vs. time plot, one sees the second X-ray on the "tail" of the first. Dead time is the percentage of time the detector is unusable while operating.

As we will discuss in more detail in Sections 2.3 and 3.1.5, the best energy resolution attainable by a calorimeter depends on various factors. One of these factors is bandwidth. Bandwidth is the width in frequency space over which the signal-to-noise ratio (See Section 3.1.3) is greater than some fiducial number, which we will take as 1. To get the high energy resolution desired, we must record the time evolution of an X-ray event to several times the decay time constant of the device. The longer we record the data, the larger our bandwidth becomes. Of course, there is an obvious reason for not making these records arbitrarily long: other X-rays will hit the detector. We want to make detectors that can handle a large count rate of X-rays. This is where decay time comes in. The faster the decay time, the less total time we need to record a particular pulse before we are ready for the next one. Pile-up occurs when an X-ray hits the detector while we are still recording the previous one. More complex algorithms must be used to untangle both photons and determine their respective energies. These algorithms generally degrade the achievable resolution. Every time this happens those two X-rays get a medium- or low-energy-resolution energy estimate, and cannot be counted in the high-energy resolution histogram. The percentage of time this happens accrues as dead time. We will discuss the other side of our bandwidth window (the high frequency side) and its effect on energy resolution in Section 2.3.1.

Photon emission is a stochastic process. We can determine what the *average* count rate in the detector is, but it is not possible to know *a priori* the time between any two consecutive events. The time could be long, or two photons could arrive almost simultaneously. So for any decay time and X-ray count rate there is pile-up. As the count rate or decay time goes down, pile-up becomes a rare event. The relation between pile-up and dead time, for a given count rate and decay time, obeys Poisson statistics and one must take these into account when designing a detector.

2.2.3   Stability condition

The temperature evolution after a photon is absorbed at $t_\gamma = 0$ is

$$\Delta T(t) = \frac{E_\gamma}{C} e^{-t/\tau_{\text{eff}}} \tag{2.15}$$

Using the definition of α and $\Delta I = -\frac{V}{R^2}\frac{\partial R}{\partial T}\Delta T$ we obtain the relation between current and temperature[7]

$$\Delta I = -\frac{\alpha I}{T}\Delta T \tag{2.16}$$

Thus the current will follow the equation

$$\begin{aligned}
\Delta I(t) &= -\frac{\alpha I}{T}\frac{E_\gamma}{C}e^{-t/\tau_{\text{eff}}} \\
&= -\left(\frac{1}{\tau_{\text{eff}}} - \frac{1}{\tau_o}\right)\frac{E_\gamma}{V}e^{-t/\tau_{\text{eff}}} \\
&= \Delta I_{\text{meas}}e^{-t/\tau_{\text{eff}}}
\end{aligned} \tag{2.17}$$

where $\Delta I_{\text{meas}} = -\frac{E_\gamma}{C}\frac{\alpha I}{T}$ is the initial drop in current measured from the resulting increase in resistance after the photon was absorbed.

Looking at Eq. (2.17) we see that for the current signal to be a decaying exponential, τ_{eff} has to be a positive number. From Eq. (2.11) we see that τ_{eff} will be as long as

$$\frac{\alpha P}{TG} > -1 \tag{2.18}$$

This equation defines the stability condition for this simple TES. Since P, G, and T are always positive, the only way that expression can be negative is to have a negative α. The sign of α depends on the slope of the R vs. T curve. For TESs, the slope is positive and so is α. For silicon thermistors, the resistance increases as the temperature decreases, so α is *negative* for these devices (a typical value is $\alpha = -5$). This is why TESs are voltage biased and silicon thermistors are current biased. *Negative* ETF will occur for voltage-biased positive-α and current-biased negative-α thermistors.

It is interesting to note that the crossover between stable and unstable (positive and negative τ_{eff}) does *not* occur when $\alpha = 0$, rather when $\alpha P/T = -G$. This effect can be explained by looking at the energy flow in the calorimeter. To set up this explanation let us take a short detour for another look at electrothermal feedback.

2.2.4 ETF revisited

Consider the calorimeter in Figure 2.1. In the steady state, with no noise sources (which we will talk about in Section 2.3), and no incident radiation, there are only two ways for energy to come in or go out of the calorimeter: through Joule heating of the thermistor, or through the weak link to the cold bath. The weak link to the cold bath is always there, and is a "pipe" through which any excess heat in the calorimeter will be siphoned away with a time constant $\tau_o = C/G$.

---

[7]Eq. (2.16) is valid only for perfect voltage bias and a resistance curve that is only a function of temperature. See Section 3.1.1, Eq. (3.16).

If one turns the current through the thermistor off, the Joule power will be zero, and the quiescent temperature of the calorimeter will be the same as the cold bath temperature; $T = T_b$. A photon incident on the calorimeter will heat it up to a temperature $T_b + E_\gamma/C$, and consequently this heat will be released into the cold bath with a decaying exponential form with a time constant of τ_o.

Now we turn the voltage across the thermistor on. The Joule power heats the calorimeter, and it comes to a stable equilibrium at some temperature $T > T_b$. As can be seen on Figure 2.2(b), the Joule power dissipated in the TES is much larger than the power leaking to the weak link into the cold bath for $T < 100$ mK, and the reverse for $T > 100$ mK. The TES is stable only at $T = 100$ mK ($T_b = 50$ mK in the model used for the figure). Now a photon is absorbed and heats the calorimeter to a temperature $T + E_\gamma/C$. Since the temperature is higher than T, we see in Figure 2.2(b) that the Joule power drops. From Eq. (2.10) we see that the term $\alpha P/T$ has the same units as thermal conductance, and comes into the equation in the same place as G. In fact, these two terms act as two thermal conductances in parallel, one real (the cold bath siphoning heat out of the calorimeter through the weak link), and one *virtual* (the electrical circuit *siphoning heat* out of the calorimeter by reducing the amount it put in). We can then make the definitions

$$G_{\mathrm{ETF}} \equiv \frac{\alpha P}{T} \qquad\qquad \tau_{\mathrm{ETF}} \equiv \frac{C}{G_{\mathrm{ETF}}} = \frac{C}{\frac{\alpha P}{T}} = \frac{\alpha P}{TG}\tau_o \qquad (2.19)$$

G and G_{ETF} added in parallel give an effective ETF thermal conductance out of the calorimeter of $G_{\mathrm{eff}} = G + \alpha P/T$, for an effective time constant of

$$\tau_{\mathrm{eff}} = \frac{C}{G_{\mathrm{eff}}} = \frac{C}{G + G_{\mathrm{ETF}}} = \frac{C/G}{1 + \frac{\alpha P}{TG}} = \frac{1}{\frac{1}{\tau_o} + \frac{1}{\tau_{\mathrm{ETF}}}} \qquad (2.20)$$

Now it is clear why ETF speeds up pulses. In extreme ETF, the "conductance" $G_{\mathrm{ETF}} = \alpha P/T \gg G$ and so dominates the effective time constant; in extreme ETF, $\tau_{\mathrm{eff}} \to \tau_{\mathrm{ETF}}$.

In fact, any power source applied to the calorimeter that is fed back (turned down in response to a pulse) will act as a virtual conductance and exhibit this speed-up behavior. Various techniques have been proposed and implemented to substitute or augment ETF (Galeazzi, 1998; Meier et al., 2000; Nam et al., 1999). The advantages and disadvantages of these other techniques need to be properly assessed.

It is now easy to see why the calorimeter stability point is not when $\alpha = 0$. Under voltage bias, when α is negative, the system is in positive feedback. For $\alpha < 0$, $\alpha P/T$ is not a conductance siphoning out heat, but a pipe pumping it in, in proportion to an excitation ΔT. But as long as $|\alpha|P/T < G$, the heat can go out through G faster than it can get in through $\alpha T/P$, and the calorimeter is stable (although for this regime where $\alpha < 0$ and the calorimeter is still stable the time constant $\tau_{\mathrm{eff}} > \tau_o$). In other words, as long as Eq. (2.18) holds, a device in positive feedback (negative G_{ETF}) will still be stable. If $\alpha P/T < G$, then the positive feedback puts more power in the calorimeter than what goes out to the cold bath through the conductance G, and the TES will heat up and "latch" at the normal resistance R_n.

Actually, when the TES is unstable, positive feedback will make the TES run away in whatever direction a small perturbation takes it from the quiescent temperature. So if a little dip in temperature occurs, the positive ETF will shut the power down and the TES will "latch" at $R = 0$. Whether it goes to $R = 0$ or $R = R_n$ just depends on the initial perturbation, the important thing is that if the stability condition is not met, the TES is unusable as a thermometer.

2.2.5 Energy integral

Since $\Delta P(t) = V \Delta I(t)$ for constant voltage bias, we can integrate the current to obtain the total energy removed from the system from the reduction in Joule power,[8] which will be

$$E_{\text{Joule}} = -\tau_{\text{eff}} V \Delta I_{\text{meas}} = -\frac{1}{1 + \frac{TG}{\alpha P}} E_\gamma \qquad (2.21)$$

$$= -\frac{1}{1 + \frac{n}{\alpha \phi}} E_\gamma \qquad (2.22)$$

$$= -\left(1 - \frac{\tau_{\text{eff}}}{\tau_o}\right) E_\gamma \qquad (2.23)$$

As we can see, the decrease in Joule power does not integrate to the energy of the photon for low values of α, but approaches that value as one moves into the extreme ETF regime, where $\tau_{\text{eff}} \rightarrow 0$. For a detector with an α of 100 (representative or our current TESs), with $n = 4$ and $\phi \sim 1$, $E_{\text{Joule}} = 0.96 E_\gamma$. For a detector with $\alpha = 5$ (representative of our current silicon thermistors), $E_{\text{Joule}} = 0.56 E_\gamma$. Note that this derivation assumes perfect voltage bias and a resistance function that does not depend on current. Both these factors change the measured energy, and we show that derivation in Section 3.1.1.

Finally, we point out that we are assuming that all the energy of the photon is deposited and thermalizes in the TES, i.e., the thermalization efficiency is 1. If a fraction of the energy of each photon is not thermalized, then this energy will not be measured, and one must multiply the above E_γ by the thermalization efficiency to get the correct E_{Joule}. The loss mechanism is usually due to hot electron or hot phonon effects which make the thermalization of the absorber non-ideal. For example, Miller (2001) finds the Stanford optical tungsten TESs have a thermalization efficiency of 42% due to phonon losses to the substrate.

2.2.6 Saturation in a TES

A TES is a very sensitive thermometer, but it only operates within a finite range of temperatures. This range is dictated by the width of the transition of the TES. In Figure 2.2(a) the total transition width is about 1.5 mK. The linear portion is roughly 0.5 mK. If the transition were wider, we would have a larger operating range, but at the same time the gain of our thermistor would decrease, as the slope of the R vs. T curve decreases.

---

[8]This is basically the amount of energy siphoned by G_{ETF}.
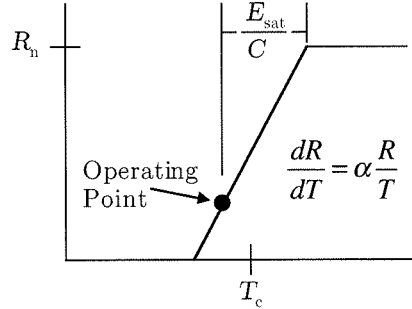
Figure 2.3: Assumed R vs. T curve for this thesis. $\Delta T_{\text{sat}} = E_{\text{sat}}/C$ only for the single-pixel TES.

In a linear model, the resistance vs. temperature function is a straight line, with the slope determined by $\alpha \frac{R}{T}$ evaluated at the steady state point of the real curve (Figure 2.2(a)). For the purposes of this thesis, we will model the R-T curve as in Figure 2.3. The curve is a straight line from zero to R_{n} and then abruptly becomes horizontal.

We define *saturation energy* as the photon energy that causes any TES in a calorimeter to have a temperature swing large enough that its resistance reaches R_{n}. For a single pixel calorimeter without a decoupled absorber, this energy is

$$E_{\text{sat}} = C\Delta T_{\text{sat}} \tag{2.24}$$

where ΔT_{sat} is the maximum temperature excursion from the operating point that is still in the linear range. From the definition of α, we can rewrite this as

$$E_{\text{sat}} = \frac{C}{\alpha} \frac{\Delta R_{\text{sat}}}{R} T \tag{2.25}$$

If we assume we bias the device in the middle of its transition, then $R = \Delta R_{\text{sat}} = R_{\text{n}}/2$, and $T = T_{\text{c}}$. We then have

$$E_{\text{sat}} \approx \frac{C}{\alpha} T_{\text{c}} \tag{2.26}$$

For any application, there is always a desired energy range one wants the detector to operate in. The maximum energy one needs to be able to resolve determines E_{sat}. This in turn places constraints on the value of C, α and T_{c}. This saturation energy has direct implications on the ultimate resolution of a TES, since (as we will see in the next section) the theoretical resolution is a function of all these variables:

$$\Delta E_{\text{rms}} \propto \sqrt{\frac{C}{\alpha} T^2} \propto \sqrt{E_{\text{sat}}} \tag{2.27}$$

For Part I of this thesis, we will assume $\Delta T_{\text{sat}} = 0.5$ mK, and since we are interested in X-ray detectors, we will use an $E_{\text{sat}} = 6$ keV, which means $C = 1.92$ pJ/K (using Eq. (2.24)).

We will use 0.5 mK as the fiducial value of ΔT_{sat} for our single-pixel TES benchmarks, and keep the overall temperature excursion of the position-sensitive TESs to this number. There is nothing magical about 0.5 mK, we just need a yard stick to define saturation and that value is consistent with our current data. Note that if this value for the heat capacity is used in Eq. (2.26), with a 6 keV saturation energy and a critical temperature of 75 mK, we obtain an α of 150. For this thesis we will use a more conservative α of 90, which is more consistent with our data. Eq. (2.26) does not take into account the curvature of the real R vs. T curves, which are not as steep near saturation as in the middle of the transition. We will use Eq. (2.24) as our saturation condition.

There is a very important point that must be made here. The limiting factor for the amount of energy the calorimeter can absorb and stay linear is the maximum change in temperature that the *thermistor* incurs. In designs where the absorber is decoupled by a thermal link from the thermistor, the initial rise in temperature of the absorber will be E/C_{abs}, but the temperature rise of the thermistor will depend on the strength of the thermal link (in the limit of a very weak thermal link, the thermistor's temperature change tends toward zero, and it acts as a bolometer). The problem is that the moment one decouples the absorber from the thermistor, a phonon noise term due to this link enters the equations, and worsens the energy resolution. But since a calorimeter cannot be fully described by an energy resolution at a single energy, there are trade-offs to be made between dynamic range, energy resolution at a particular energy of interest, and the energy resolution as a function of energy. The non-linearities and range of operating and analysis modes encountered when pushing the dynamic-range/energy-resolution envelope do not allow for a succinct final answer. We will be looking at detectors with low heat capacities in which we are able to see high energy X-rays because of the weak coupling between the absorbers and the TESs. We will discuss this in Chapter 7. The noise from a decoupled absorber is discussed in Appendix A.

2.3 Single-pixel energy resolution

To understand the energy resolution of a calorimeter, we will look at simple model of a single-pixel thermistor calorimeter where all amplifier and other external noise sources are assumed to be small enough to be negligible. In this case, we only have two sources of noise: the Johnson noise from the resistor, and phonon noise from the connection to the cold bath.

Phonon noise is the thermodynamic power fluctuations through the thermal conductance G connecting the calorimeter to the cold bath. These power fluctuations create temperature fluctuations in the calorimeter. The heat capacity of the calorimeter and how well it is coupled to the cold bath through the conductance G give the system its characteristic time constant $\tau_o = C/G$. This time constant is the decay time of a simple calorimeter with no feedback. It is also the time constant that determines how fast the calorimeter can change its temperature. Although the power fluctuations are fairly flat at all frequencies of interest, the response of the calorimeter is not. Temperature fluctuations faster than the frequency $\sim 1/2\pi\tau_o$ are damped, so the spectrum of the temperature fluctuations has a -3 dB point

(a 1 pole roll-off) at $1/2\pi\tau_o$.

Johnson noise is the voltage fluctuations across any resistor due to the Brownian motion of the electrons in the resistor. The frequency distribution of these fluctuations is white for all frequencies of interest. These voltage fluctuations cause a change in the measured resistance of the TES, and so become a source of noise.

The full calorimeter theory will be presented in Chapter 3, so we will just show some of the general trends here. With these two sources of noise, the energy resolution of a calorimeter in the limit where $\alpha P/TG \gg 1$ can be expressed as (Irwin, 1995b):

$$\Delta E_{\mathrm{FWHM}} = 2.355 \times \sqrt{4k_{\mathrm{B}}T^2 C\frac{1}{\alpha}\sqrt{\frac{n}{2}}} \tag{2.28}$$

where k_{B} is Boltzman's constant, T is the quiescent calorimeter temperature, C is the heat capacity, α is defined in Eq. (2.4), and n is the exponent in Eq. (2.7). See Eq. (3.75) for a more general expression of the energy the resolution.

Looking at the current signal for a pulse in Eq. (2.17) we see in the first line of that equation that the signal is proportional to α. Figure 2.4(a) shows a frequency power spectrum of a photon hit (the signal) and the noise terms on a set of calorimeters with progressively larger α. No electrothermal feedback has been applied to allow the intrinsic behavior to be seen. For $\alpha = 1$, both the signal and the phonon noise are below the horizontal Johnson noise level. As α increases, the signal gets bigger and rises above the Johnson noise. The "knee" of the curve occurs at the same frequency; without ETF, increasing α increases the size of the signal but does not speed up the pulses. A measure of the energy resolution can be made by looking at the signal-to-noise ratio (SNR). An quick estimate of the SNR can be made by looking at how much area there is between the signal and the noise. As α increases, even though the phonon noise increases along with the signal the SNR increases. Eq. (2.28) shows that the energy resolution indeed gets better (smaller ΔE) for higher α.

Figure 2.4(b) shows the same set of calorimeters, but with ETF turned on. There are two effects. First, pulse speed-up. Extreme ETF causes $\tau_{\mathrm{eff}} \rightarrow \tau_{\mathrm{ETF}} = C/G_{\mathrm{ETF}} \simeq nC/\alpha G$. So as α increases, the "knee" (at $1/2\pi\tau_{\mathrm{eff}}$) occurs at higher and higher frequencies. The second effect of ETF is to suppress all curves below $1/2\pi\tau_{\mathrm{eff}}$. Note that for each α, the amount suppressed in the signal, the Johnson noise and the phonon noise is the same, so the SNR for the ETF curves is identical to that for the respective no-ETF curves. We will see in Section 3.1.3 that this means the amount of ETF does *not* affect the resolution of a calorimeter. It *does* change the decay time τ_{eff}.

If one had a device with an α of 10, one could try to obtain the same fast decay times of the higher α devices by increasing G. Figure 2.5(a) shows a no-ETF plot of an $\alpha = 10$ device at different values of G. The "knee" goes out in frequency, but note that per Eq. (2.7) the power into the calorimeter must also increase as G increases to maintain the device in the same place in its transition. The effect of this necessary increase in power is that the energy resolution does not change. Thus, for all the curves in Figure 2.5 the resolution is 5 eV, just like the $\alpha = 10$ device in Figure 2.4.

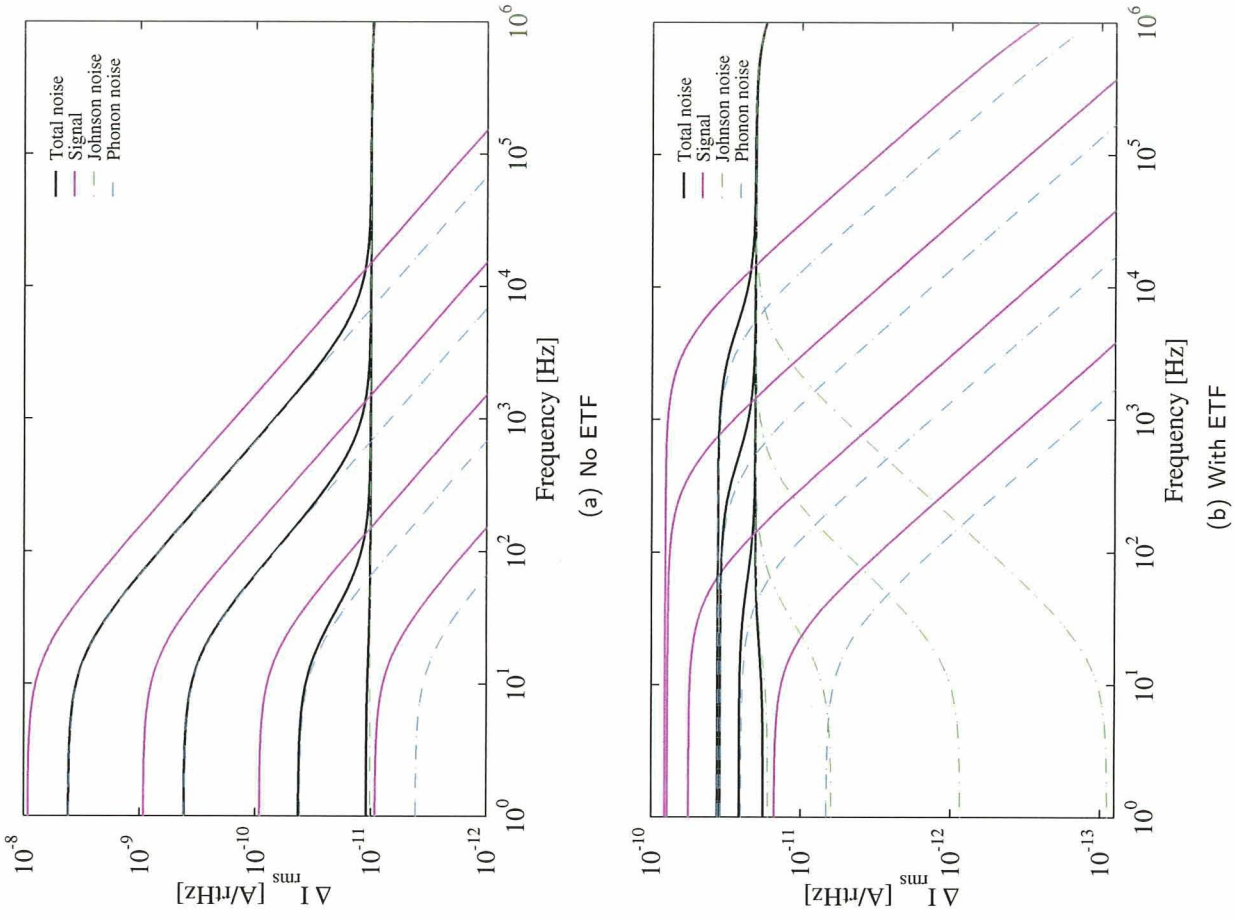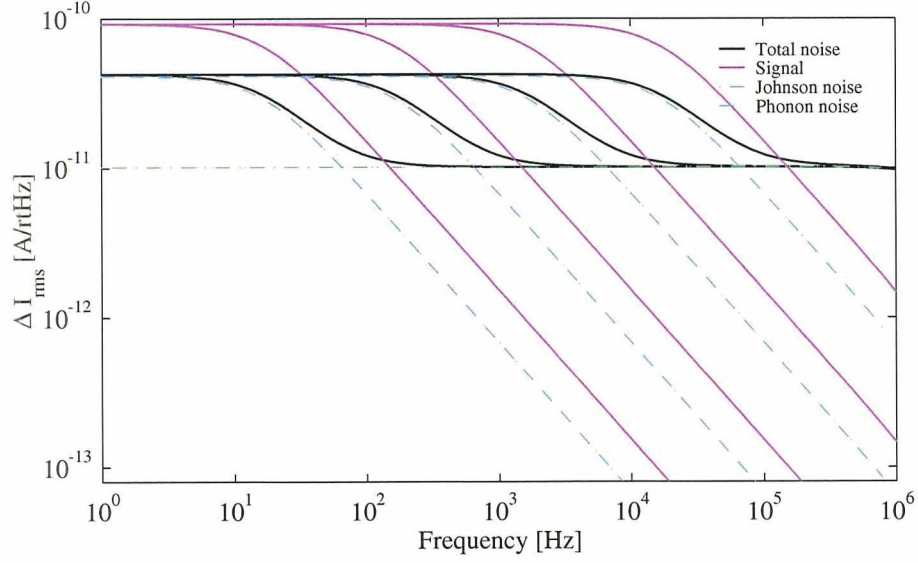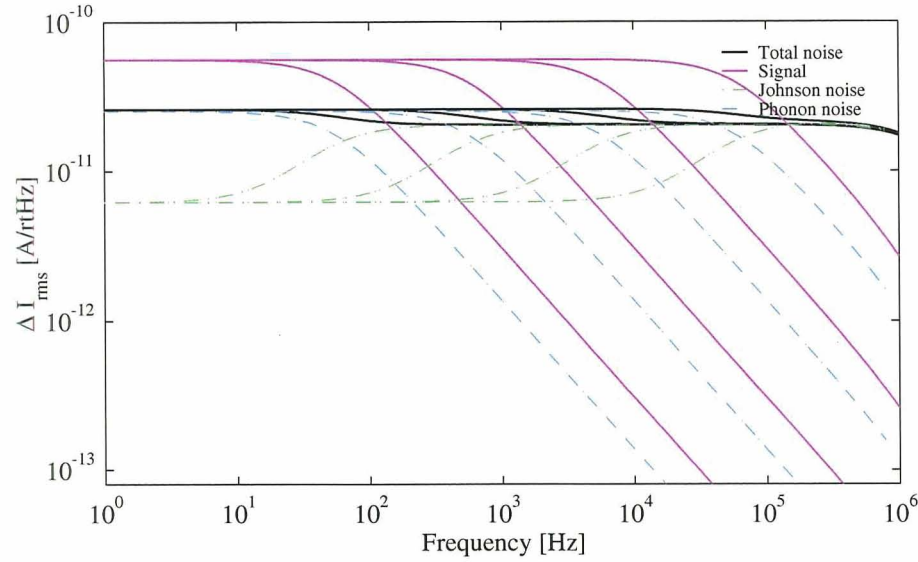**Figure 2.4:** Current noise for α of 1, 10, 100, and 1000. The lowest magnitude curves correspond to $\alpha = 1$, and the largest to $\alpha = 1000$. The energy resolution in each case is 25, 5, 1.5, and 0.5 eV, respectively.

(a) No ETF

(b) With ETF

Figure 2.5: Current noise for $\alpha = 10$, conductance of G, $10G$, $100G$, $1000G$. The energy resolution for each case is 5 eV.

One might be tempted to think that the bigger the α the better, since one obtains better resolution. The problem in this argument has to do with saturation. Since α is a measure of the steepness of the transition, the bigger the α, the steeper the transition. In Section 2.2.6 we imposed a fiducial temperature excursion of $1/2$ mK for a device with an α of 90. For each value of α, the temperature excursion to reach saturation and the heat capacity needed must be calculated. The result is that, for a maximum photon energy E_{sat} with which the detector reaches saturation, the ratio C/α remains the same. Using Eq. (2.26) we can rewrite the resolution as

$$\Delta E_{\text{FWHM}} = 2.355 \times \sqrt{4k_{\text{B}}TE_{\text{sat}}\sqrt{\frac{n}{2}}} \tag{2.29}$$

So in the strong ETF limit, where Eq. (2.28) is valid, energy resolution is independent of α (for the same saturation energy). For the low α case, where one might not be in the strong ETF limit, Eq. (3.75) must be used. This is the case of silicon thermistors, whose value of α is ~ -5.

2.3.1 Energy resolution and thermalization

In Section 2.2.2 we discussed the need to have long integration times to get more bandwidth at the lower frequencies. Looking at Figure 2.4(b) for the case $\alpha = 100$, we see the signal rolls off at about 300 Hz. To get good energy resolution we would want to get to as low an energy as possible given the rate and pile-up constraints. Up to now we have been assuming that the thermalization takes place instantly, which makes the rise of the pulse instantaneous also. The Fourier transform of this perfect exponential is the signal curve shown in Figure 2.4(b). But in the real world, there is some thermalization time, due to the processes discussed in Section 2.1.1. This means the rise of the pulse is not instantaneous, but has a rise that can be modeled as a rising exponential. This will create a second roll off at a frequency $1/2\pi\tau_{\text{r}}$ where τ_{r} is the rise time constant. This roll off will make the signal cross over the noise at a lower frequency, lowering the bandwidth and thus reducing the energy resolution. If the thermalization time is fast enough that this roll off occurs at frequencies above the bandwidth imposed by the ideal signal and Johnson noise crossover, then the thermalization time does not affect the resolution since it is outside the defined bandwidth. Thus fast thermalization is important in single-pixel TESs.

As we will see in Section 2.4.1 and Section 4.5.1, for a PoST there is always some degradation in energy resolution from roll offs at high frequencies. The trick is to loose as little resolution as possible while still determining the position of the X-ray absorption in the PoST. We will discuss these issues in more detail next.
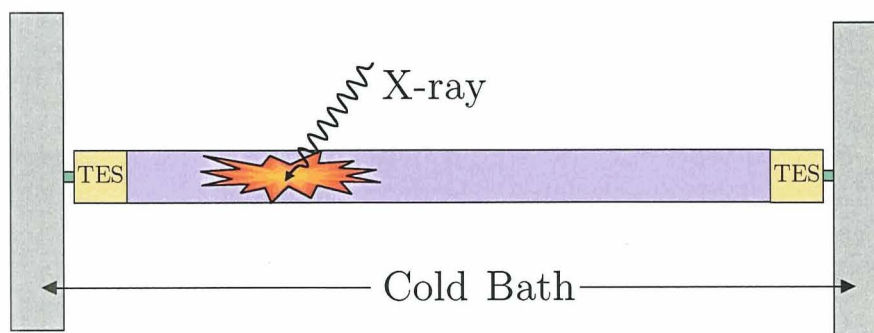
Figure 2.6: Concept for a one-dimensional imaging calorimeter. Two thermometers sense the same event, and the difference in signals provides the position information, while the pulse heights provide a measurement of the energy.

2.4   Position-sensitive calorimeters

As mentioned in Section 1.4 the current limiting factor to fabricating kilo-pixel calorimeter arrays is the available number of readout channels. Although great progress in SQUID multiplexing is being made (Chervenak et al., 1999), in the near future the total number of SQUID channels including multiplexing will be in the order of a few thousand. To increase the number of pixels another order of magnitude, we have developed the Position-Sensitive-TES (PoST) calorimeter.

In general, an imaging calorimeter uses one or more thermometers to analyze the signal produced by a photon absorption event in an absorber. For the same energy photons, the signal received by the thermometers varies in some detectable way depending on the position in the absorber where the event occurred. In other words, the absorber exhibits position dependence. If one can use the information in the signal shape to determine the location of photon absorption and the photon energy, one has an imaging calorimeter. This definition does not impose restrictions on the type of thermometer or absorber used, nor on the method of position or energy determination from the produced signal.

The imaging calorimeter can be a one-dimensional "strip" absorber with one or more thermometers, or a two-dimensional "plane" absorber with two or more thermometers. In this work we have concentrated on the simpler one-dimensional case, although the arguments put forth are equally valid for the two dimensional case, which we consider in Section 8.2.

Figure 2.6 shows a schematic of a one-dimensional position-sensitive calorimeter. The width of the PoST defines the pixel size in that direction, while the length-wise pixel size depends on how one bins the information from the detector and depends on the application. For example, Constellation-X detectors have a specified pixel size of 250 μm, so this would be the width of the PoST, while the number of pixels would be equal to the length of the absorber divided by 250 μm. When an X-ray event occurs, heat propagates down the absorber and reaches the thermometers. Since the PoST is connected to a cold heat sink,
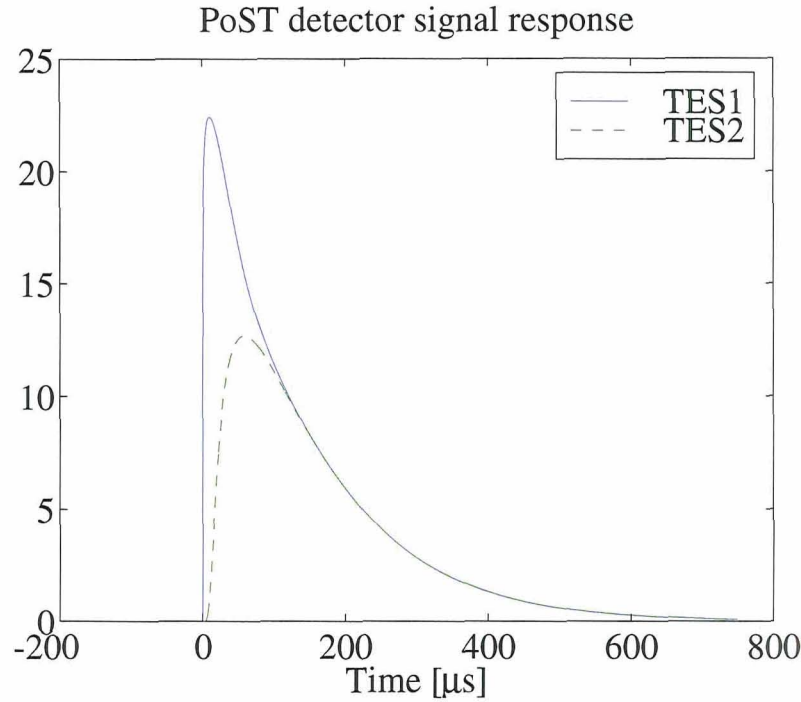
Figure 2.7: Response of a PoST to a photon absorption event. From the difference in pulse heights, the position of the event can be determined. The energy can be inferred from the pulse heights.

after the initial heating from the X-ray event it returns to its quiescent state. The timing, pulse height, and rise time differences of the pulse on each TES allow the determination of the absorption location (Figure 2.7).

On studying the idea of using imaging calorimeters, there are two issues to consider when comparing them to single pixel calorimeters: energy resolution and count rate. What follows is a hand-waving analysis of these issues. In Chapter 4 we develop the theory to quantify theses effects.

2.4.1   Energy resolution

Energy resolution is the most important parameter when designing a imaging calorimeter. No matter what the increase in field of view, the instrument is still first and foremost a spectrometer. If we achieve very large fields of view, but our resolution falls substantially, we will fall into the kingdom of CCDs, which are excellent for medium-energy-resolution, high-spatial-resolution, large-area imaging. Designing a worthy calorimetric opponent in this realm would be a challenge indeed. Thus, calculating the theoretical energy resolution of an imaging calorimeter design is our prime concern.

Let us look at how using two thermometers affects resolution. Consider a single pixel device that is 400 μm to a side, such as the one shown in Figure 2.8(a). It has an absorber and is suspended on silicon nitride to provide the thermal decoupling from the substrate.

(a) A simple TES

(b) Two TESs together on one absorber

(c) Two TESs on one absorber
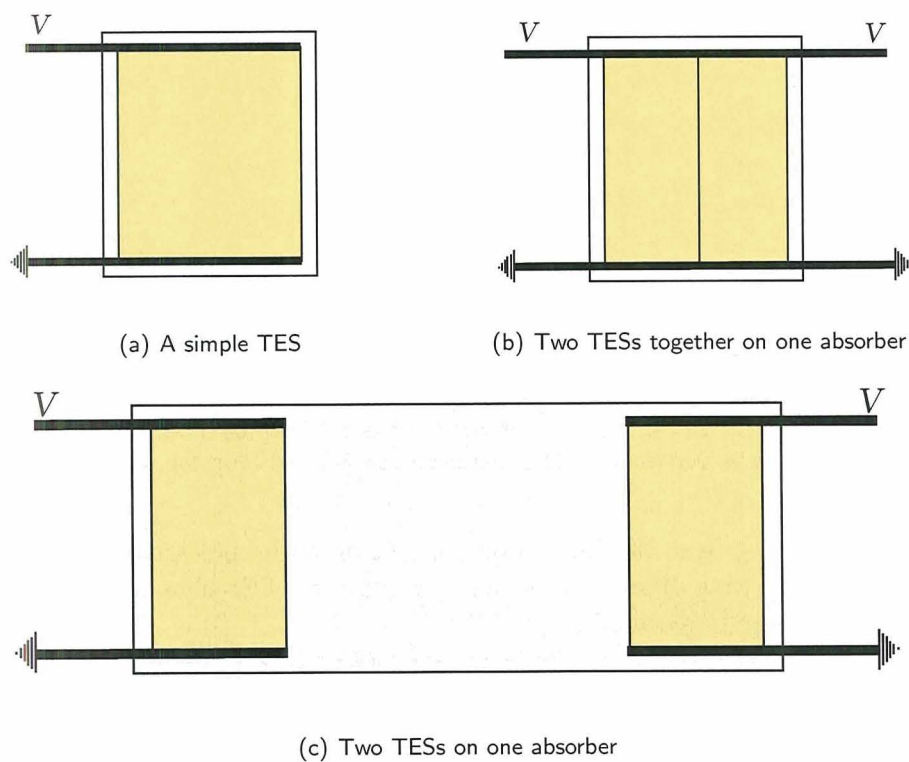
Figure 2.8: Logical extension of a TES to a PoST. The absorber (light gray) is assumed to have the same heat capacity on all three cases. The first two cases will give the same energy resolution. As the TESs are farther and farther apart, the thermalization time of the absorber begins to create position dependence and degrades the energy resolution. To quantify the theoretical energy resolution we need the methods developed in Chapter 4.

Now suppose we split this TES in two, creating two thermometers that are 200 μm wide and 400 μm long, shown in Figure 2.8(b). The power required to keep the TESs in their biased position is still the same, so each half must contribute $P/2$, where P was the original quiescent power dissipated in the TES. The total heat capacity is the same, and the thermal conductance to the reservoir is the same (since all we have done is slice the TES). This all implies that the pulse shape will be unaffected by our use of two thermometers. The signal obtained from each detector will be identical to that from the other. If the contacts on the split detector are placed so that each TES has twice the resistance of the original square, keeping the voltage the same means the quiescent current will be $I_{\text{new}} = V/(2R_{\text{old}})$, half of the original current. A photon absorbed will create the same ΔT as before, which will cause a change in resistance $\Delta R_{\text{new}} = 2\Delta R_{\text{old}}$. The current drop on each TES is then $\Delta I_{\text{new}} = \Delta I_{\text{old}}/2$. Adding the signals together we regain the original pulse.

Now what happens to the noise? We must look at each source of noise individually. The Johnson current noise is $I_{\text{J}} = \sqrt{4k_{\text{B}}T/R}$, where k_{B} is Boltzman's constant. The Johnson noise seen on each TES will be uncorrelated and thus adds in quadrature. The total Johnson noise is $I_{\text{Jtot}} = \sqrt{I_{\text{J1}}^2 + I_{\text{J2}}^2}$, from which follows that the total Johnson noise will the be same as the single pixel Johnson noise.

Phonon noise describes the thermal fluctuations of the TES. Thermal fluctuations translate into resistance fluctuations, which become a source of noise in our signal. Phonon noise scales with the signal, so it will be half as big in the new TESs. When the two TES signals are added together, the noise will also add. Is this noise correlated or uncorrelated? The answer is frequency dependent. The original TES had a thermalization time τ_{th}. This thermalization time is roughly the time constant of heat moving from one side of the TES to the other. We assume the fact that the TES is split in two does not change the overall thermalization time (the time τ_{th} it takes for heat to go from one side of the pixel to the other is still the same). For frequencies below $1/\tau_{th}$, phonon noise (which is a local excess or loss of energy) can equilibrate from one side to the other, and thus at these frequencies the phonon noise seen by the two TESs will be correlated. At frequencies much higher than $1/\tau_{th}$, phonon noise on one side does not have time to travel from one TES to the other, and at these frequencies the TESs act as if they where thermally decoupled. Thus the phonon noise will be uncorrelated. If this happens at high frequencies which are out of the signal band, for resolution purposes the noise can be treated as correlated and thus simply adds.

The result, as one might have guessed, is that splitting one TES in two and reading the halves out separately does not degrade resolution. You get back exactly the same signal.

Now consider the case in Figure 2.8(c). The same TESs are now placed in the ends of a longer absorber with the same heat capacity as the absorber in Figure 2.8(b). The time constant of this device will depend on the thermal conductance of the absorber and how long it is. If we assume the thermalization time is fast, so that the thermalization frequency $1/\tau_{th}$ is higher than the signal band, then there will be no position dependence and the detector behaves just like the device in Figure 2.8(b). As the thermalization frequency approaches the signal band, position dependence develops. Obviously, it is the slow thermalization

that gives us the position dependence, so in order to resolve position information the thermalization frequency must be inside our signal band. As detailed in Section 3.2.3 one the effects of absorber thermalization time in a position-sensitive calorimeter is to reduce the signal-to-noise ratio (SNR) at high frequencies, thus reducing the energy resolution of the detector. The slower the thermalization of the absorber, the worse the energy resolution.

This result can be intuitively restated as follows. For a photon event into the device in Figure 2.8(c), the more the two pulses are alike, the better we can resolve the energy. The more the pulses are different from each other, the better we can resolve the position. There is a tradeoff between these two quantities that must be made based on the application. Let us assume the design goal is a one-dimensional 20-pixel PoST with 2 eV resolution at 6 keV. Since we are looking for a part in 3000 energy resolution and a part in 20 position resolution, it makes sense to design for very fast thermalization. To quantify the degradation in energy resolution for a particular amount of position resolution requires the derivation of an analytical model for PoST detectors from which theoretical noise can be calculated. This theory is developed in Chapter 4.

Note that we are referring to the degradation in energy resolution of a PoST as a function of τ_{th} compared to the single-pixel energy resolution of the TESs used to read out the PoST. We are assuming the single-pixel resolution is fixed and we cannot improve on it. The better the energy resolution of the single-pixel TES, the better the energy and position resolution of the PoST.

There are other factors which may degrade the PoST energy resolution. One such possibility is in analysis. The signal from photons will have a continuously varying pulse shape depending on where they hit the absorber. Calculating the energy resolution from continuously varying pulse shapes can be a challenge (Figueroa-Feliciano et al., 2000a). In Section 2.4.3 we describe the problem and our solution.

2.4.2 Count rate

In general, PoSTs use each channel in a calorimeter to read out several pixels. To compare to a single channel calorimeter, we must define maximum count rate. By maximum count rate we mean the counts per second the calorimeter can absorb and still obtain high energy resolution with an acceptable dead time due to pile-up (Section 2.2.2). This rate will depend on the decay time constant of the pulse (τ_{eff}).

If the τ_{eff} for the PoST is the same as for a singe pixel TES, then the maximum count rate will go down as the number of pixels in the PoST increases. If the τ_{eff} is longer than the single pixel calorimeter, then the rate will go down further by a factor proportional to the ratios of the time constants. The important question is whether the maximum count rate goes down linearly with the number of pixels in the PoST. At first glance the answer is yes. If a single pixel TES can handle 1000 counts per second, then a PoST, with two TESs and 20 pixels will be able to see 1000 counts per second. Each pixel would only handle 50 counts per second, as long as the counts are distributed evenly among the pixels. That sounds very discouraging. But herein lies the catch. When looking at astrophysical sources, most objects that produce 1000 counts per second per pixel are point sources. If
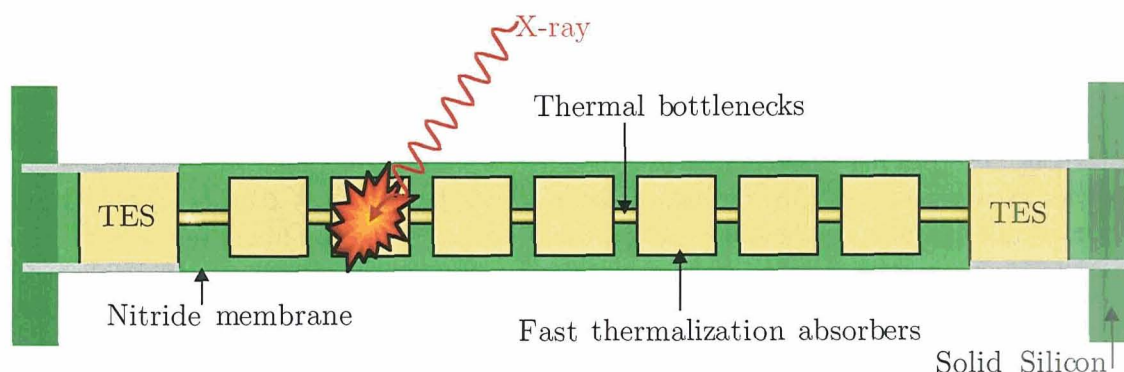
Figure 2.9: Pixellation of absorber to divide it into fast-thermalization absorption areas and thermal "bottlenecks" that slow down the signal to create distinct pulse shapes for each pixel in the absorber.

we over-sample the PSF of the telescope by a factor of three, the high count rate is seen by only three of the pixels in one PoST. The other 17 pixels see much reduced count rates. In other words, although the maximum rate is still 1000 counts per second, we would be able to look at sources that are around 300 counts per second whether the PoST has 5 pixels or 30. Then the question becomes whether an increase in field of view of 10 is worth a cut in throughput by a factor of 3.5.

As a final note on this point, our design is completely compatible with the single pixel TES processing. There is no reason why a viable flight instrument could not have a 6×6 single pixel array surrounded by PoSTs. The single pixel array would then handle the 1000 count per second objects, and extended objects would be imaged by the complete instrument. If 1000 readout channels are available, using 36 for single pixels still provides with 964 for PoSTs. For 20 pixel PoSTs, at 10 pixels per channel, that would add up to a 9,676 pixel instrument, compared to a 1000 pixel instrument without PoST technology. For 30 pixel PoSTs we would have a 14,500 pixel instrument.

2.4.3 Absorber pixellation

As mentioned in the end of Section 2.4.1, the analysis of the data from an absorber that generates pulse shapes that vary continuously with absorption position can be challenging. The high energy resolution required from these devices means that every effort must be made to get the best signal from the data. We use an optimal filter (Section 3.1.4) to get the best estimate of the energy of a photon. One of the assumptions in an optimal filter is that there is no variation in the pulse shape in your signal apart from a scaling factor that is proportional to the photon energy. The continuously varying pulse shape[9] of a long

---

[9]The time constant of the rise time of the pulses in the PoST depends on the thermal conductance of the absorber. A solid monolithic absorber has a constant thermal conductance from one end to the other. Pulses hitting at different points along the length of the absorber will take varying amounts of time to arrive at the TES, hence the continuously varying pulse shape.

monolithic absorber does not conform to this requirement.

To get around this problem one bins (pixellates in software) at small scales minimizing the pulse shape change over your defined pixel. If one desires very fine position resolution this makes sense, but if one is only looking for modest position resolution, then having a continuous absorber has disadvantages.

Since we were not designing for high position sensitivity, we chose another route. Instead of a constant thermal conductance across the absorber, we alternate areas of very high conductivity with "bottleneck" sections with lower thermal conductivity. In essence, we pixellate[10] the absorber. Figure 2.9 shows a schematic of the design. If the absorber sections have high enough conductance, and the "bottlenecks" have low enough conductance, a photon hitting anywhere in the pixel will thermalize rapidly in the pixel, then the heat will propagate through the bottleneck to the next pixel, and so on. The idea is to achieve no position dependence within each pixel, but adjust the bottlenecks so the pulse shape from each pixel is discernibly different. For a n pixel PoST, one gets n discrete pulse shapes; we have built the pixellation into the detector.

We are not claiming that pixellating the absorber improves energy resolution; it only makes the data analysis easier, since the pixellation is built into the device.

The discrete nature of the absorber signal is an advantage, but one must determine if indeed it is possible to have the same pulse shape for any event location within an absorber. Additional thermalization layers in the absorber might be necessary to stimulate rapid intra-pixel equilibration of temperature, which will translate into no position dependence within each pixel. Also, for applications were one needs fast response, pixellating the absorber might prove difficult without increasing the heat capacity of the absorbers (to make very fast thermalization pixels) which will degrade resolution. All these issues have to be weighted in the design phase of the development.

---

[10] "Pixellate" is not really a word. For this thesis, though, we will define "pixellate" as "to divide into pixels" and "pixellation" as "the act of pixellating"

Chapter 3

Single Pixel Calorimeter Theory

In this chapter we develop the machinery needed to tackle the linear noise theory of a PoST. In the first section we derive the theory and analytic solution for the spectral shape of various sources of calorimeter noise, including detector noise, noise from other circuit elements and pickup, and thermal noise sources such as phonon noise and stray radiation from the surroundings. We then derive the noise-equivalent power (NEP) and the energy resolution for a basic calorimeter and show that these are the same for voltage and current readout of a thermistor.

In Section 3.2 we present the matrix formulation needed to solve the theoretical noise of a PoST by determining the noise and energy resolution of a complex calorimeter (defined below). We demonstrate the power of this method by fitting the noise spectrum taken from the X-ray Quantum Calorimeter (XQC) rocket payload.

For the purposes of this thesis, a basic calorimeter is depicted in Figure 3.1. It consists of a single heat capacity connected to the cold bath by one thermal weak link. The heat capacity in the basic calorimeter may include an absorber, the electron system of the thermistor, the phonon system of the thermistor, and any other heat capacity on the calorimeter (absorber-thermistor epoxy, for example). The implicit assumption is that the thermal coupling time constants of the calorimeter constituents are much faster than the calorimeter-refrigerator time constant, and they can thus be treated as a single entity.

This assumption, however, is often incorrect and we need a more complex thermal model to compute the theoretical resolution of a calorimeter. A complex calorimeter therefore has more than one heat capacity in the thermal equation and thus more than one thermal time constant, and allows for more realistic models. Complex calorimeter models can include absorber-thermistor decoupling, electron-phonon decoupling, stray heat capacities, several thermal connections between the calorimeter components (an absorber that couples to both the electron and phonon systems of the thermistor, for example), etc. Figure 3.3 in page 57 shows one possible model of a complex calorimeter.
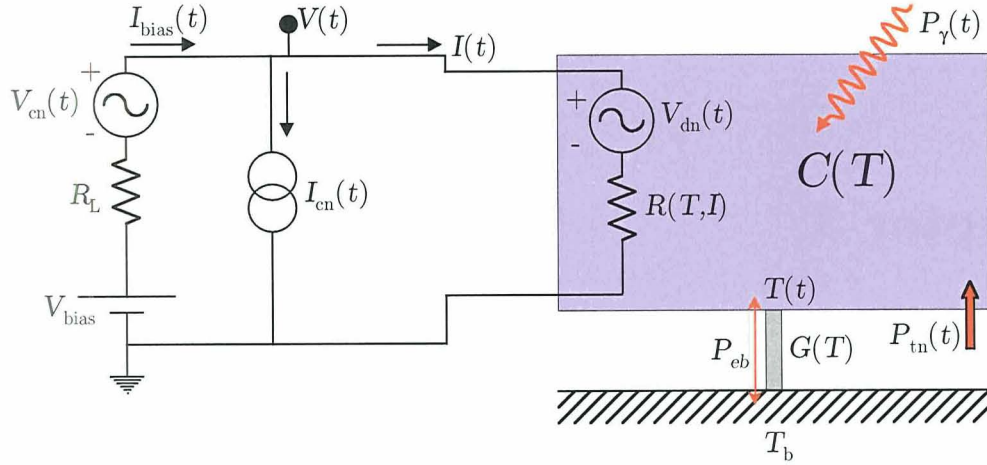
Figure 3.1: Simple calorimeter bias and thermal circuit. V_{bias}, R_{L}, and I_{bias} are the equivalent bias voltage, load resistance, and bias current. V_{cn} and I_{cn} are circuit noise sources. The shaded rectangle represents the detector with heat capacity C at temperature T. V_{dn} is the detector noise into the circuit. $R(T, I)$ is the resistance of the detector. $G(T)$ is the thermal weak link conductance to the heat sink, which is at temperature T_{b}. P_{eb} is the phonon noise through the link. P_{tn} is any general power noise input to the calorimeter such as infra-red radiation from the surroundings. When convenient we will group P_{eb} into P_{tn}. The circuit elements outside the detector can be at other temperatures depending on implementation.

3.1   Basic calorimeter theory

This section expands upon the work done by Irwin (1995a,b); Mather (1982, 1984) and Moseley, Mather, and McCammon (1984) by doing a general treatment of noise terms in the thermal and current equations, allowing for non-stiff biasing of the thermistor, and deriving the equations for all feedback conditions (i.e., accounting for a non-zero load resistor). We also treat the resistance as a function of both the temperature and the current, as done by Lindeman (2000).

3.1.1   Time domain analysis

We begin with the general calorimeter electrical and thermal circuit shown in Figure 3.1. We have assumed no inductance or capacitance in the electric circuit to simplify the derivation. With this simplification most calorimeter bias schemes[1] can be replaced with a Thévenin equivalent circuit resembling Figure 3.1, with a voltage source V_{bias} and a load (or shunt) resistor R_{L}. $V(t)$ and $I(t)$ are the voltage and current outputs of the detector. $R(T, I)$ is the resistance of the detector, which is taken to be a function of both temperature and current. $C(T)$ is the detector's heat capacity, which is a function of temperature. The temperature

---

[1]Our own bias scheme is shown in Figure 5.4. If the inductance of the input coil is assumed to be zero, the Thévenin equivalent circuit becomes Figure 3.1. We will add the inductance later in the thesis.

of the detector is $T(t)$, and it is connected to a cold bath (or heat sink) at temperature T_b through a weak link of conductance $G(T)$. The other components on the circuit will be at different temperatures depending on the particular implementation.

We have included three sources of noise in the electrical circuit. $V_{cn}(t)$ and $I_{cn}(t)$ are circuit noise sources outside the detector, such as bias resistor Johnson noise, JFET leakage current noise, or pickup. $V_{dn}(t)$ is noise produced *inside* the detector, such as detector Johnson noise, $1/f$ detector noise, or vortex flows (in superconducting calorimeters). Note that these are general noise terms, and can have any spectral shape from white noise to just being a sine wave. The main difference between detector noise and circuit noise is that the voltage through the detector $V(t) = V_{dn}(t) + I(t)R(T, I)$ includes the detector noise sources. As we shall see, this adds the detector noise sources to the thermal equation as well as the current equation and results in the suppression of these noise sources at low frequencies (via electrothermal feedback).

The thermal side in Figure 3.1 shows several thermal power inputs. P_{eb} is the phonon noise from the bath to the calorimeter. $P_{tn}(t)$ is a general thermal noise term that can be due to radiation, or any other way of coupling heat to the calorimeter. This term can also have any spectral shape, and since it is more general than the phonon term, we will absorb the phonon noise term into $P_{tn}(t)$ to reduce the complexity of the derivation. $P_\gamma(t)$ is the signal; it is the power deposited over a very short period of time by a photon absorption event. We can think of $P_\gamma(t) = E_\gamma \delta(t - t_\gamma)$ in the simplest case, but we can use more complex functional forms to model the thermalization time in the absorber. The important thing to note is that the signal and the thermal noise come into the calorimeter in the same way.

Using Kirkoff's laws we write

$$\sum_i I_i = 0 = I(t) + I_{cn}(t) - I_{bias}(t) \tag{3.1}$$

$$\sum_i V_i = 0 = V_{bias} - I_{bias}(t)R_L + V_{cn}(t) - V_{dn}(t) - I(t)R(T, I) \tag{3.2}$$

and as before

$$V(t) = I(t)R(T, I) + V_{dn}(t) \tag{3.3}$$

Now we can solve for either $V(t)$ or $I(t)$, depending on the method of readout. Note that we are not making any assumptions as to the method of biasing or readout of the calorimeter, and our results will be independent of these parameters. We choose to solve for $I(t)$, in which case we have the current equation

$$0 = V_{bias} - I(t)\Big(R_L + R(T, I)\Big) + V_{cn}(t) - R_L I_{cn}(t) - V_{dn}(t) \tag{3.4}$$

The thermal equation is

$$C(T)\frac{dT(t)}{dt} = I(t)V(t) - P_{\text{link}}(T(t), T_{\text{b}}) + P_{\text{tn}}(t) + P_{\gamma}(t) \qquad (3.5)$$

where $P_{\text{link}}(T(t), T_{\text{b}})$ is the power flow from the detector to the cold bath. We have absorbed the phonon noise term into the general thermal noise variable $P_{\text{tn}}(t)$. We assume $P_{\text{link}}(T(t), T_{\text{b}}) = K\left(T(t)^n - T_{\text{b}}{}^n\right)$. Substituting for $V(t)$ we obtain[2]

$$C(T)\frac{dT(t)}{dt} = I(t)^2 R(T, I) - K\left(T(t)^n - T_{\text{b}}{}^n\right) + I(t)V_{\text{dn}}(t)P_{\text{tn}}(t) + P_{\gamma}(t) \qquad (3.6)$$

Now with Eq. (3.4) and Eq. (3.6) we have fully characterized the system. If we had not neglected the inductance, we would have an $L\frac{dI(t)}{dt}$ term instead of the zero in Eq. (3.4). We can numerically solve these equations to obtain pulses, and if appropriate noise algorithms are implemented, fake data can be generated with the appropriate theoretical noise, which can be compared to real data or used to study analysis methods with a data set that has a controllable and known amount of noise. We have used this method to study the saturation effects of TESs, where the TES is operating in the very non-linear regime and the following linear analysis is no longer valid. Also, by incorporating the noise into the numerical solver, we can generate non-stationary noise, which is more realistic. Figueroa-Feliciano et al. (2000a) and Fixsen and Moseley (2002) propose ways to analyze non-stationary noise.

The obvious limitation of taking the numerical route is the lack of analytical equations to help shed light into what is going on. Also solving the numerical equations is much more computationally expensive than evaluating an analytical formula. To solve these equations analytically we will linearize the system. There are good reasons for doing this. One of the more important things we want to understand is the size and shape of the noise in the calorimeter. Noise is (hopefully!) a small signal on our detector, and as long as it is small the linear approximation should be very good at describing the noise. From the noise we will be able to get the theoretical energy resolution of the detector. Thus from the linear model we get two very important things to a very good approximation: the magnitude and spectral shape of the noise, and the ultimate theoretical resolution of the detector. Also, it makes the math tractable.

If we want to model pulses, the relevance of the linear model gets harder to quantify. The linear model is, by definition, linear. In the linear model no saturation exists; the pulse shape of the response to the absorption of a 1 eV photon will be the same as the pulse shape for a 1 GeV photon. In the real world, this is obviously not the case. But as discussed in Section 2.2.6, most TES designs choose the heat capacity of the calorimeter to keep the TES in the linear range for most if not all of the photon energies of interest. Thus the linear model should produce pulses that give good fits to the data. We have found that our single pixel X-ray TES calorimeters are very well described by a linear model for 1 keV

---

[2]There is a subtle point here. One *could* say that the detector heating term in Eq. (3.5) should be $V(t)^2/R(T, I)$, so substituting for V(t) we would get $I(t)^2 R(T, I) + 2I(t)V_{\text{dn}} + V_{\text{dn}}^2/R(T, I)$, but this is wrong.

X-rays (Lindeman et al., 2002). In summary, the linear approximation is an excellent tool for characterizing the resolution and response of a calorimeter design.

We will now linearize the system. We assume the noise sources $P_{tn}(t)$, $V_{cn}(t)$, and $V_{dn}(t)$ are small so that $\partial R/\partial T$, $\partial(I^2R)/\partial I$ and $\partial(T^n)/\partial T$ are locally constant through the range of values of $I(t)$ and $T(t)$. Another constraint on the size of the noise terms is that they have to be small enough so that noise terms multiplied by ΔT or ΔI can be considered second order. We also assume the signal term P_γ is small. With these restrictions we will show that the temperature dependence of the heat capacity is a second order effect. Now we are ready to linearize using the Taylor expansion formula:

$$f(\vec{x}(t)) = f(\vec{x}) + \sum_i \left.\frac{\partial f(\vec{x}(t))}{\partial x_i}\right|_{\vec{x}} \Delta\vec{x} + \mathcal{O}(\vec{x}^2(t)) \tag{3.7}$$

were we have introduced the convention where $\vec{x}(t)$ is the variable and $\vec{x}$ is the variable evaluated at its operating or quiescent point. $\Delta\vec{x}=(\vec{x}(t) - \vec{x})$ is our small signal variable, $\vec{x}(t) = [I(t), T(t)]$, and $|_{\vec{x}}$ means "evaluated at $\vec{x}(t)=\vec{x}$." From this definition of $\Delta\vec{x}$ one can see that $\frac{d}{dt}\vec{x}(t) = \frac{d}{dt}\Delta\vec{x}(t)$, since $\vec{x}$ is a constant. First the electrical equation:

$$0 = \overbrace{V_{bias} - I(R + R_L)}^{\emptyset} + V_{cn}(t) - R_L I_{cn}(t) - V_{dn}(t)$$
$$+ \frac{\partial}{\partial I}\left(V_{bias} - I(t)\Big(R(T,I) + R_L\Big) + V_{cn}(t) - R_L I_{cn}(t) - V_{dn}(t)\right)\Bigg|_{\substack{I\\T}} \Delta I$$
$$+ \frac{\partial}{\partial T}\left(V_{bias} - I(t)\Big(R(T,I) + R_L\Big) + V_{cn}(t) - R_L I_{cn}(t) - V_{dn}(t)\right)\Bigg|_{\substack{I\\T}} \Delta T$$
$$+ \mathcal{O}\big(I(t)^2, T(t)^2\big) \tag{3.8}$$

The first terms cancel from the steady state equation for the current. Remember the convention that I, R, etc. are the operating point values (constants); $I(t)$, $R(T,I)$, etc. are variables; and ΔI and ΔT are the small signal variables. Carrying out the derivatives and evaluating at the operating point we obtain

$$0 \simeq V_{cn}(t) - R_L I_{cn}(t) - V_{dn}(t) - \left(R + R_L + I\frac{\partial R(T,I)}{\partial I}\right)\Delta I - \left(I\frac{\partial R(I,T)}{\partial T}\right)\Delta T \tag{3.9}$$

We need to define the two derivatives of the resistance function. We define α_T and α_I:

$$\alpha_T = \alpha \equiv \frac{T}{R}\left.\frac{\partial R(T,I)}{\partial T}\right|_{\substack{I\\T}} \qquad\qquad \alpha_I \equiv \frac{I}{R}\left.\frac{\partial R(T,I)}{\partial I}\right|_{\substack{I\\T}} \tag{3.10}$$

These derivatives are evaluated at the quiescent point; in the linear model α_T and α_I are constants. Out of convention, we will refer to α_T as α to be consistent with previous authors.

The linear model assumes the curves are locally linear, and looking at Figure 2.2 we

can see that a large fraction of the transition has a fairly constant slope. The constants α and α_I are a measure of the slopes of the R vs. T curve and R vs. I curve at the operating point. We note that the important quantities in the linear model are the derivatives and *not* α and α_I. This means that it matters not that when a photon is absorbed and the resistance of the TES changes the function $\alpha(R, T)$ changes. In the linear model all that matters is the slope of the R vs. T curve, and the *constant* α defined in Eq. (3.10) is just a parametrization of this slope.

The reason we use α and not the slope of the R vs. T curve is that α is the pertinent parameter in the energy resolution equations, as we shall see later. Using these constants we can write

$$0 = -(R(1 + \alpha_I) + R_L)\,\Delta I - \frac{\alpha V}{T}\,\Delta T + V_{cn}(t) - R_L I_{cn}(t) - V_{dn}(t) \qquad (3.11)$$

We now turn our attention to the thermal equation, Eq. (3.6), and write

$$\frac{d}{dt}\Delta T = \frac{1}{C}\left(\overbrace{I^2 R - K(T^n - T_b^n) + IV_{dn}(t) + P_{tn}(t) + P_\gamma(t)}^{0} \right.$$

$$+ \frac{1}{C}\frac{\partial}{\partial I}\left(I(t)^2 R(T, I) - K(T(t)^n - T_b^n) + I(t)V_{dn}(t) + P_{tn}(t) + P_\gamma(t) \right)\Big|_{\frac{I}{T}} \Delta I$$

$$+ \frac{\partial}{\partial T}\left(\frac{1}{C(T)}\left(I(t)^2 R(T, I) - K(T(t)^n - T_b^n) + I(t)V_{dn}(t) + P_{tn}(t) + P_\gamma(t) \right) \right)\Big|_{\frac{I}{T}} \Delta T$$

$$\left. + \mathcal{O}(I(t)^2, T(t)^2) \right) \qquad (3.12)$$

Evaluating the derivatives and substituting for $\partial R(T, I)/\partial T$ and $\partial R(T, I)/\partial I$ as before we have

$$\frac{d}{dt}\Delta T \simeq \frac{1}{C}\left((2 + \alpha_I)IR\,\Delta I + \overbrace{V_{dn}(t)\Delta I}^{\mathcal{O}(\vec{x}^2)} + \frac{\alpha I^2 R}{T}\Delta T \right.$$

$$- K_n T^{n-1}\,\Delta T + IV_{dn}(t) + P_{tn}(t) + P_\gamma(t)$$

$$- \frac{1}{C^2}\frac{\partial C(T)}{\partial T}\Big|_n \overbrace{\left(IV_{dn}(t)P_{tn}(t) + P_\gamma(t) \right)\Delta T}^{\mathcal{O}(\vec{x}^2)} \qquad (3.13)$$

We can see from this equation that the terms with $\partial C(T)/\partial T$ are all second order which confirms our assertion that the temperature dependence of the heat capacity is a second

order effect. Now we define

$$G \equiv \frac{dP_{\text{link}}(T, T_{\text{b}})}{dT}\bigg|_T = KnT^{n-1} \tag{3.14}$$

and arrive at the following equation for the linearized thermal behavior of our system:

$$C\frac{d}{dt}\Delta T = (2 + \alpha_{\text{I}})V\,\Delta I + \left(\frac{\alpha P}{T} - G\right)\Delta T + IV_{\text{dn}}(t) + P_{\text{tn}}(t) + P_\gamma(t) \tag{3.15}$$

Now begins the fun part (go get more paper). Eq. (3.11) and Eq. (3.15) are redundant since there is a linear relationship between ΔT and ΔI. Since we want to know what the current noise for the detector is, we solve for ΔT in Eq. (3.11) and substitute into Eq. (3.15). We obtain the relation between current and temperature for this model:[3]

$$\Delta T = -\frac{T}{\alpha I}\left(1 + \alpha_{\text{I}} + \frac{R_{\text{L}}}{R}\right)\Delta I + \frac{T}{\alpha V}\left(V_{\text{cn}}(t) - R_{\text{L}}I_{\text{cn}}(t) - V_{\text{dn}}(t)\right) \tag{3.16}$$

After some heavy algebra we obtain

$$\frac{C}{G}\frac{d}{dt}\left(\Delta I + \frac{-V_{\text{cn}}(t) + R_{\text{L}}I_{\text{cn}}(t) + V_{\text{dn}}(t)}{R(1 + \alpha_{\text{I}}) + R_{\text{L}}}\right) =$$
$$-\left(1 + \frac{\alpha P}{TG}\frac{1 - \frac{R_{\text{L}}}{R}}{1 + \alpha_{\text{I}} + \frac{R_{\text{L}}}{R}}\right)\Delta I + \left(1 - \frac{\alpha P}{TG}\right)\frac{V_{\text{cn}}(t) - R_{\text{L}}I_{\text{cn}}(t)}{R(1 + \alpha_{\text{I}}) + R_{\text{L}}}$$
$$-\frac{V_{\text{dn}}(t)}{R(1 + \alpha_{\text{I}}) + R_{\text{L}}} - \frac{\alpha P}{TG}\frac{P_{\text{tn}}(t) + P_\gamma(t)}{I(R(1 + \alpha_{\text{I}}) + R_{\text{L}})} \tag{3.17}$$

The next step is to move to the frequency domain, where we will obtain the spectral shape of the noise for this calorimeter. But before we make that transition, we can solve this equation and compare it to the results of Section 2.2. To solve analytically in the time domain, we will ignore all noise terms in Eq. (3.17), since we are interested mainly in the current response to a photon. We then have

$$\frac{d}{dt}\Delta I = -\left(\frac{G}{C} + \frac{\alpha P}{TC}\frac{1 - \frac{R_{\text{L}}}{R}}{1 + \alpha_{\text{I}} + \frac{R_{\text{L}}}{R}}\right)\Delta I - \frac{1}{1 + \alpha_{\text{I}} + \frac{R_{\text{L}}}{R}}\frac{\alpha I}{T}\frac{E_\gamma}{C}\delta(t - t_\gamma) \tag{3.18}$$

where as before we have assumed a delta function for the photon absorption. We define the

---

[3]Compare to Eq. (2.16) for the simpler case with perfect voltage bias, no current dependence of the resistance, and no noise sources. Beware of the noise sources; one needs to take these into account where applicable when converting from current to temperature and vice-versa.

time constants

$$\tau_o \equiv \frac{C}{G} \qquad\qquad \tau_{\text{eff}} \equiv \frac{\tau_o}{1 + \frac{\alpha P}{TG} \frac{1 - \frac{R_\mathrm{L}}{R}}{1 + \alpha_\mathrm{I} + \frac{R_\mathrm{L}}{R}}} \qquad (3.19)$$

where now the electrothermal feedback time constant takes into account the "stiffness" of the voltage bias (non-zero R_L) and the effect of the current dependence of the resistance function $R(T, I)$ (compare with Eq. (2.11)). The current after a photon is absorbed at $t_\gamma = 0$ is now

$$\begin{aligned}
\Delta I(t) &= -\frac{1}{1 + \alpha_\mathrm{I} + \frac{R_\mathrm{L}}{R}} \frac{\alpha I}{T} \frac{E_\gamma}{C} e^{-t/\tau_{\text{eff}}} \\
&= -\left(\frac{1}{\tau_{\text{eff}}} - \frac{1}{\tau_o} \left(1 - \frac{R_\mathrm{L}/R}{1 + \alpha_\mathrm{I} + R_\mathrm{L}/R} \right) \right) \frac{E_\gamma}{V} \qquad (3.20) \\
&= \Delta I_{\text{meas}} e^{-t/\tau_{\text{eff}}}
\end{aligned}$$

Comparing with Eq. (2.17), we see that the stiffness of the voltage bias and the current dependence of the resistance affect both the time constant and the height of the pulse.

We can again calculate the stability condition (the point where the exponential changes sign) to be

$$G_{\text{ETF}} > -G \qquad (3.21)$$

where

$$G_{\text{ETF}} \equiv \frac{\alpha P}{T} \frac{1 - \frac{R_\mathrm{L}}{R}}{1 + \alpha_\mathrm{I} + \frac{R_\mathrm{L}}{R}} \qquad (3.22)$$

$$\tau_{\text{ETF}} = \frac{C}{G_{\text{ETF}}} \qquad (3.23)$$

where we have defined the ETF "conductance[4]" G_{ETF}. From this condition one can determine the range of values and combinations where the detector is stable. Here we have two things that can be negative. If $R_\mathrm{L} > R$, G_{ETF} will be negative, but as long as it is not smaller than $-G$ the α device will still be stable. Also α can be negative. Notably, here we see that for large negative α devices one wants a very large R_L to get a large G_{ETF}; this is just the proof that negative α devices need current bias for strong negative ETF. Note that when $G_{\text{ETF}} < 0$ the device is in positive feedback, but still stable as long as Eq. (3.21) holds.

Next we would like to integrate the pulse to obtain the measured energy E_{meas} for this device. To do this we must first calculate the drop in Joule heating of the TES. Since we are not assuming perfect voltage bias, $\Delta P \neq V \Delta I$ as in Section 2.2. Looking at Figure 3.1

---

[4]The ETF acts as a "virtual" conductance. See Section 2.2.4.

and taking all noise sources to be zero we can simply write

$$V(t) = V_{\text{bias}} - I(t)R_{\text{L}} \tag{3.24}$$

$$\Delta V = -R_{\text{L}}\Delta I \tag{3.25}$$

and now we can write the power dissipated in the detector and use our linearization procedure to arrive at the small signal power:

$$P(t) = V(t)I(t) = IV + I\left.\frac{\partial V(t)}{\partial I}\right|_I \Delta I + V\Delta I + \mathcal{O}\big(I(t)^2\big) \tag{3.26}$$

$$\Delta P = P(t) - IV \simeq V\Delta I + I(-R_{\text{L}})\Delta I = (V - IR_{\text{L}})\Delta I \tag{3.27}$$

We can see that for $R_{\text{L}} = 0$ we are back to the perfect voltage bias case. Using Eq (3.20) we can write the time evolution of the power as

$$\Delta P(t) = \frac{-(V - IR_{\text{L}})}{1 + \alpha_{\text{I}} + \frac{R_{\text{L}}}{R}} \frac{\alpha I}{T} \frac{E_\gamma}{C} e^{-t/\tau_{\text{eff}}} \tag{3.28}$$

We can now integrate to obtain the measured energy

$$E_{\text{meas}} = \int \Delta P(t)dt = \frac{-(V - IR_{\text{L}})}{1 + \alpha_{\text{I}} + \frac{R_{\text{L}}}{R}} \frac{\alpha I}{T} \frac{E_\gamma}{C} \tau_{\text{eff}} \tag{3.29}$$

Using Eq. (3.19) we substitute the first fraction and obtain

$$E_{\text{meas}} = -\left(1 - \frac{\tau_{\text{eff}}}{\tau_o}\right) E_\gamma \tag{3.30}$$

Compare with Eq. (2.23). It is the same equation, except for the more general definition of τ_{eff}. Now we arrive at a interesting point. In Eq. (2.23), the only way for $\tau_{\text{eff}} = \tau_o$ was for either $\alpha = 0$ or $T = T_{\text{b}}$. If $\alpha = 0$, there is no temperature dependence on the resistor, i.e., one no longer has a thermistor. If $T = T_{\text{b}}$ then $P = 0$, so there is no current through the device. In both of these cases it is easy to see there would be no signal and thus the integrated energy is zero. But now, looking at Eq. (3.19) we see that in our more complicated model there is one more way to get $\tau_{\text{eff}} = \tau_o$. If $R = R_{\text{L}}$ then we can have a dissipative thermometer, which deposits power into the calorimeter, with large α, and the integral of the power is still zero! This is because when $R_{\text{L}} = R$, $\partial P/\partial R = 0$. This means the power is a constant, so the integral of $\Delta P = 0$. But looking at Eq. (3.20) we see that the current is *not* zero at $R_{\text{L}} = R$. What happens is that the voltage and current change in exactly the correct way to keep $P(t) = I(t)V(t) =$ constant. But if we just integrate the current instead of the power, even at $R_{\text{L}} = R$ we can get a measure of the energy of the

absorbed photon:

$$\int \Delta I(t) dt = -\left(\left(1 - \frac{\tau_{\text{eff}}}{\tau_o} \right) + \frac{\frac{\tau_{\text{eff}}}{\tau_o} \frac{R_{\text{L}}}{R}}{1 + \alpha_{\text{I}} + \frac{R_{\text{L}}}{R}} \right) \frac{E_\gamma}{V} \qquad (3.31)$$

which is not zero at $R_{\text{L}} = R$.

3.1.2   Frequency domain analysis: current noise and responsivity

We will continue with our derivation of the noise spectrum for a calorimeter by looking at Eq. (3.17) and moving into the frequency domain. To do this we assume both the current ΔI and all noise sources and be Fourier transformed into the frequency domain.

We use the fact that

$$\frac{d}{dt} f(t) \xrightarrow{\mathcal{F}} i\omega f(\omega) \qquad (3.32)$$

with which the Fourier transform of Eq. (3.17) becomes

$$\left(i\omega \frac{C}{G} + 1 + \frac{\alpha P}{TG} \frac{1 - \frac{R_{\text{L}}}{R}}{1 + \alpha_{\text{I}} + \frac{R_{\text{L}}}{R}} \right) \Delta I =$$

$$\left(1 - \frac{\alpha P}{TG} + i\omega \frac{C}{G} \right) \frac{V_{\text{cn}}(\omega) - R_{\text{L}} I_{\text{cn}}(\omega)}{R(1 + \alpha_{\text{I}}) + R_{\text{L}}} - \left(1 + i\omega \frac{C}{G} \right) \frac{V_{\text{dn}}(\omega)}{R(1 + \alpha_{\text{I}}) + R_{\text{L}}}$$

$$- \frac{\alpha P}{TG} \frac{P_\gamma(\omega) + P_{\text{tn}}(\omega)}{I(R(1 + \alpha_{\text{I}}) + R_{\text{L}})} \quad (3.33)$$

The responsivity $S(\omega) \equiv d\Delta I / dP_\gamma$ is defined as the current signal measured for a given power input into the thermal system. From Eq. (3.33) we can determine the following derivatives:

$$S(\omega) \equiv \frac{d\Delta I}{dP_\gamma} = \frac{-1}{V(1 + \alpha_{\text{I}} + \frac{R_{\text{L}}}{R})} \frac{\frac{\alpha P}{TG}}{\left(1 + \frac{\alpha P}{TG} \frac{1 - \frac{R_{\text{L}}}{R}}{1 + \alpha_{\text{I}} + \frac{R_{\text{L}}}{R}} \right)} \frac{1}{(1 + i\omega\tau_{\text{eff}})} \qquad (3.34)$$

$$\frac{d\Delta I}{dV_{\text{dn}}} = \frac{-1}{1 + \alpha_{\text{I}} + \frac{R_{\text{L}}}{R}} \frac{1}{\left(1 + \frac{\alpha P}{TG} \frac{1 - \frac{R_{\text{L}}}{R}}{1 + \alpha_{\text{I}} + \frac{R_{\text{L}}}{R}} \right)} \frac{1 + i\omega\tau_o}{(1 + i\omega\tau_{\text{eff}})} \qquad (3.35)$$

$$\frac{d\Delta I}{dV_{\text{cn}}} = \frac{-1}{1 + \alpha_{\text{I}} + \frac{R_{\text{L}}}{R}} \frac{1}{\left(1 + \frac{\alpha P}{TG} \frac{1 - \frac{R_{\text{L}}}{R}}{1 + \alpha_{\text{I}} + \frac{R_{\text{L}}}{R}} \right)} \frac{\left(1 - \frac{\alpha P}{TG} + i\omega\tau_o \right)}{(1 + i\omega\tau_{\text{eff}})} \qquad (3.36)$$

Using the definition of τ_{eff} in Eq. (3.19) we can rewrite these derivatives as

$$S(\omega) \equiv \frac{d\Delta I}{dP_\gamma} = \frac{-\frac{\alpha P}{TG}}{1 + \alpha_{\text{I}} + \frac{R_{\text{L}}}{R}} \frac{\tau_{\text{eff}}}{\tau_o} \frac{1}{(1 + i\omega\tau_{\text{eff}})} \frac{1}{V} \tag{3.37}$$

$$\frac{d\Delta I}{dV_{\text{dn}}} = \frac{-1}{1 + \alpha_{\text{I}} + \frac{R_{\text{L}}}{R}} \frac{\tau_{\text{eff}}}{\tau_o} \frac{1 + i\omega\tau_o}{(1 + i\omega\tau_{\text{eff}})} \frac{1}{R} \tag{3.38}$$

$$\frac{d\Delta I}{dV_{\text{cn}}} = \frac{-1}{1 + \alpha_{\text{I}} + \frac{R_{\text{L}}}{R}} \frac{\tau_{\text{eff}}}{\tau_o} \frac{\left(1 - \frac{\alpha P}{TG} + i\omega\tau_o\right)}{(1 + i\omega\tau_{\text{eff}})} \frac{1}{R} \tag{3.39}$$

With the responsivity, we can determine the theoretical spectral response of the detector $\Delta I_{\text{signal}} = S(\omega)P_\gamma(\omega)$ to any input $P_\gamma(\omega)$. Since the input power and thermal noise come into the equations in the same way, the responsivity $S(\omega)$ of the detector will also give the spectral shape of the thermal noise. The output current noise for a given noise source $N(\omega)$ is the average of the magnitude of the noise, which in units of A^2/Hz is

$$\left\langle |\Delta I_N|^2 \right\rangle = \left\langle \left| \frac{d\Delta I}{dN} N(\omega) \right|^2 \right\rangle \tag{3.40}$$

We can then arrive at the theoretical current noise for each of our noise sources:

$$\left\langle |\Delta I_{\text{tn}}(\omega)|^2 \right\rangle = \frac{\left(\frac{\alpha P}{TG}\right)^2}{\left(1 + \alpha_{\text{I}} + \frac{R_{\text{L}}}{R}\right)^2} \left(\frac{\tau_{\text{eff}}}{\tau_o}\right)^2 \frac{1}{1 + \omega^2\tau_{\text{eff}}^2} \left(\frac{P_{\text{tn}}(\omega)}{V}\right)^2 \tag{3.41}$$

$$\left\langle |\Delta I_{\text{dn}}(\omega)|^2 \right\rangle = \frac{1}{\left(1 + \alpha_{\text{I}} + \frac{R_{\text{L}}}{R}\right)^2} \left(\frac{\tau_{\text{eff}}}{\tau_o}\right)^2 \frac{1 + \omega^2\tau_o^2}{1 + \omega^2\tau_{\text{eff}}^2} \left(\frac{V_{\text{dn}}(\omega)}{R}\right)^2 \tag{3.42}$$

$$\left\langle |\Delta I_{\text{cn}}(\omega)|^2 \right\rangle = \frac{1}{\left(1 + \alpha_{\text{I}} + \frac{R_{\text{L}}}{R}\right)^2} \left(\frac{\tau_{\text{eff}}}{\tau_o}\right)^2 \frac{\left(1 - \frac{\alpha P}{TG}\right)^2 + \omega^2\tau_o^2}{1 + \omega^2\tau_{\text{eff}}^2} \left(\frac{V_{\text{cn}}^2(\omega) + R_{\text{L}}^2 I_{\text{cn}}^2(\omega)}{R^2}\right)$$

$$\tag{3.43}$$

$$\left\langle |\Delta I_{\text{tot}}(\omega)|^2 \right\rangle = \left\langle |\Delta I_{\text{tn}}(\omega)|^2 \right\rangle + \left\langle |\Delta I_{\text{dn}}(\omega)|^2 \right\rangle + \left\langle |\Delta I_{\text{cn}}(\omega)|^2 \right\rangle \tag{3.44}$$

with τ_{eff} defined by Eq. (3.19). These results are valid over all ranges of α, T_{b}, and R_{L}

and are valid in or negative feedback. In the extreme negative ETF limit ($\alpha P/TG \gg 1$), with perfect voltage bias ($R_{\mathrm{L}} \to 0$) and no current dependence ($\alpha_{\mathrm{I}} \to 0$), at zero base temperature ($T_{\mathrm{b}} \to 0$), we have $\tau_{\mathrm{eff}}/\tau_o \to TG/\alpha P$ and we arrive at the extreme ETF equations for thermal and detector noise (Irwin, 1995b):

$$\left\langle |\Delta I_{\mathrm{tn}}(\omega)|^2 \right\rangle = \frac{P_{\mathrm{tn}}(\omega)^2}{V^2} \frac{1}{(1 + \omega^2 \tau_{\mathrm{eff}}^2)} \tag{3.45}$$

$$\left\langle |\Delta I_{\mathrm{dn}}(\omega)|^2 \right\rangle = \frac{V_{\mathrm{dn}}(\omega)^2}{R^2} \frac{\left(\frac{TG}{\alpha P}\right)^2 + \omega^2 \tau_{\mathrm{eff}}^2}{(1 + \omega^2 \tau_{\mathrm{eff}}^2)} \tag{3.46}$$

The circuit noise in this limit is:

$$\left\langle |\Delta I_{\mathrm{cn}}(\omega)|^2 \right\rangle = \frac{V_{\mathrm{cn}}(\omega)^2}{R^2} \tag{3.47}$$

This result shows that the inherent spectral shape of a circuit-noise source remains unchanged in this limit. Note that this derivation shows that the response to circuit noise sources in the electrical circuit is different than that due to detector (inside the TES) noise sources. Thus, the spectral distortion due to electrothermal feedback of the TES Johnson noise,[5] vortex flow noise, phase slip noise, and other detector noise will be different than for bias resistor Johnson noise, voltage source fluctuations, pickup, and other circuit noise.

To look at this effect, let's consider white noise sources, such as Johnson noise, on the detector and on the circuit. From the equations above we can calculate the effect of ETF and detector response on white noise. The ratio of low frequency detector noise to high frequency detector noise is

$$\frac{\left\langle |\Delta I_{\mathrm{dn}}(0)|^2 \right\rangle}{\left\langle |\Delta I_{\mathrm{dn}}(\infty)|^2 \right\rangle} = \left(\frac{\tau_{\mathrm{eff}}}{\tau_o}\right)^2 \tag{3.48}$$

From Eq. (3.19), we see that this ratio is less than 1 unless $R_{\mathrm{L}} > R$ (assuming positive α). Thus, for a TES in negative feedback, detector Johnson noise is always suppressed at low frequencies by $(\tau_{\mathrm{eff}}/\tau_o)^2$.

For the circuit noise, however, the factor is

$$\frac{\left\langle |\Delta I_{\mathrm{cn}}(0)|^2 \right\rangle}{\left\langle |\Delta I_{\mathrm{cn}}(\infty)|^2 \right\rangle} = \left(\frac{\tau_{\mathrm{eff}}}{\tau_o}\right)^2 \left(1 - \frac{\alpha P}{TG}\right)^2 \tag{3.49}$$

$$= \left(\frac{1 - \frac{\alpha P}{TG}}{1 + \frac{\alpha P}{TG}\frac{R - R_{\mathrm{L}}}{R(1+\alpha_{\mathrm{I}})+R_{\mathrm{L}}}}\right)^2 \tag{3.50}$$

A white circuit noise source of the same magnitude as a white detector noise source would be

---

[5]Examples of Johnson noise and phonon noise spectral distortion by ETF are shown in Figure 3.2(a).

larger at low frequencies by a factor $(1 - \alpha P/TG)^2$. When calculating energy resolution, one should take care of this fact and include the circuit noise terms in the calculation, as they can be much larger than the detector Johnson noise in the detector bandpass (frequencies below $1/2\pi\tau_{\text{eff}}$). For ideal TESs the dominant noise term in-band is the phonon noise. Under certain conditions (high load resistor temperature and/or $R_{\text{L}} \sim R$) the load resistor Johnson noise can become comparable to the phonon noise and thus become a non-negligible component in the noise.

In the next section we will see that the amount of negative electrothermal feedback does not change the energy resolution for a given TES. In the weak ETF regime, Eq. (3.50) gives ratios that can be much greater than one. This is because the lack of ETF shifts all noise sources up at low frequencies (see Figure 2.4 and 2.5). For the no-feedback case $(\tau_{\text{eff}} = \tau_o)$, the current noise spectrum for a white circuit noise source is larger at low frequency than at high frequency by the factor $(1 - \alpha P/TG)^2$, while the current noise spectrum for a white detector noise source is flat.

3.1.3 Implications on feedback and the signal-to-noise ratio

We can show that at constant α, changing the ETF does not change the signal-to-noise ratio at any frequency. Changing the ETF while keeping α constant is achieved by changing the value of the bias resistor R_{L}. If this statement is true, then we should be able to express the signal and the noise in the forms

$$I_{\text{signal}}(\omega) = g(\omega)f(\omega) \tag{3.51}$$

$$\Delta I_{\text{tot}}(\omega) = g(\omega)h(\omega) \tag{3.52}$$

where $I_{\text{signal}}(\omega)$ is the output current due to the signal, $\Delta I_{\text{tot}}(\omega)$ is the total noise, $g(\omega)$ is the feedback-dependent part of both the noise and the signal, and $f(\omega)$ and $h(\omega)$ are the rest of the functions. Then the signal-to-noise ratio is

$$SNR(\omega) = \left| \frac{I_{\text{signal}}(\omega)}{\Delta I_{\text{tot}}(\omega)} \right| = \left| \frac{f(\omega)}{h(\omega)} \right| \tag{3.53}$$

and is independent of feedback. From Eq. (3.37) we have $I_{\text{signal}}(\omega) = S(\omega)P_{\text{signal}}$ where P_{signal} is the input power. The total noise comes from Eq. (3.44). From these equations we see that

$$g(\omega) = \frac{\tau_{\text{eff}}/\tau_o}{\left(1 + \alpha_{\text{I}} + \frac{R_{\text{L}}}{R}\right)\sqrt{1 + \omega^2 \tau_{\text{eff}}^2}} \tag{3.54}$$

and the *SNR* is

$$SNR(\omega) = \frac{P_{\text{signal}}(\omega)\frac{\alpha P}{TG}}{I\sqrt{\left(P_{\text{tn}}(\omega)\frac{\alpha V}{TG}\right)^2 + V_{\text{dn}}(\omega)^2(1 + \omega^2\tau_o^2) + N_{\text{cn}}(\omega)^2\left((1 - \frac{\alpha P}{TG})^2 + \omega^2\tau_o^2\right)}} \qquad (3.55)$$

where $N_{\text{cn}}(\omega)^2 = V_{\text{cn}}(\omega)^2 + R_{\text{L}}^2 I_{\text{cn}}(\omega)^2$.

We see that the *SNR* is indeed independent of R_{L} and thus of feedback. We can also see what the dependence of the *SNR* is on α.

Importantly, the *SNR* is *not* dependent on α_{I} . Since the signal to noise is independent of this quantity, α_{I} should not (and does not) enter any of the resolution expressions; α_{I} only affects the τ_{eff} time constant and the overall magnitude of the noise. An important point to remember is that although the *SNR* and the resolution do not depend on α_{I}, they can still depend on the magnitude of the quiescent current I if the slope of the R vs. T curve $\partial R(T, I)/\partial T = \alpha$ is a function of I. Whether this is the case or not depends on the physics of the thermistor and the functional form of the $R(T, I)$ model used to represent it. If this is the case, then the value of the constant[6] α will be a function of the quiescent current I. Since the energy resolution is a function of α, in this case the energy resolution will by proxy be a function of the quiescent current I, but still not of α_{I}.

3.1.4   The "optimal" filter

Once we have calculated the theoretical $SNR(\omega)$, we are in a position to calculate the theoretical resolution for the detector. This will depend on the algorithm we use to analyze the data, and the structure and frequency spectrum of the noise. Following Szymkowiak et al. (1993) we will use the "optimal" filter method. The reason we places quotes on the word "optimal" is because this method is optimal only under certain conditions (which we will describe as applicable to our calorimeter signal):

1. The detector response is linear. This means that for photons being absorbed in the calorimeter of energy E_γ, the pulse shape of each photon will be identical in shape to that of every other photon irrespective of the energy of each photon to within an overall scale constant. In other words, $\Delta I \propto E_\gamma$.

2. The noise is stationary. The spectral shape and spectral amplitude of the noise is constant, i.e. not a function of time.

Of course in our detectors (1) is *not* valid for all energies, since as the photon energy increases the detector goes into saturation, and the pulse shape changes. Also if there is any position dependence in the detector, the pulse shape will be different depending on where the photon hits the absorber.[7]

---

[6] α is a constant in the model. We are talking about the value of the constant for each particular model being a function of the quiescent current (which is also a constant) in that model.

[7] This effect is obviously of particular interest when designing a PoST.

Item (2) is not realized in our detectors because the size of the Johnson noise from the detector is dependent of its resistance, which obviously changes with time, and so does the amplitude of the detector phonon noise. In a real detector we also have inductance or capacitance that create an L/R or RC time constant that rolls off the signal at some frequency. Since this frequency also depends on R, as R changes during a pulse the location of this "knee" or roll-off point changes. These effects make modeling realistic noise difficult since ones has to do it in the time domain to account for these time-evolving spectral noise shapes. Figueroa-Feliciano et al. (2000a); Fixsen and Moseley (2002) are working on the problem of finding the best way to analyze noise that does not conform to the conditions stated above.

Assuming these two conditions are met allows us to create the Weiner filter. Assume $D(t)$ is a segment of data containing a pulse and noise. We assume the actual pulse shape without noise is described by $H_\gamma S(t)$ where H_γ is number proportional to the photon energy E_γ and $S(t)$ is the invariant pulse shape.[8] The noise is described by $N(t)$. So $D(t) = H_\gamma S(t) + N(t)$, but we don't know $N(t)$ or H_γ. Here's where proper device calibration comes in. We can take many traces without pulses on them and average them in frequency space to get the *average* noise[9], $\langle |N(\omega)| \rangle$. We can also take many traces of pulses from a known energy source, and from this data we can obtain the average pulse shape. To get the responsivity $S(t)$ we simply divide the average pulse by its energy. Taking the Fourier transform of the data and responsivity[10] we can write the χ^2 condition to fit for the pulse height H_γ:

$$\chi^2 = \sum_\omega \frac{\left(D(\omega) - H_\gamma S(\omega)\right)^2}{\left\langle |N(\omega)|^2 \right\rangle} \tag{3.56}$$

Minimizing χ^2 with respect to H_γ, we obtain

$$H_\gamma = \frac{\sum \frac{D(\omega)S(\omega)^* + D(\omega)^* S(\omega)}{\langle |N(\omega)|^2 \rangle}}{2\sum \frac{S(\omega)S(\omega)^*}{\langle |N(\omega)|^2 \rangle}} \tag{3.57}$$

One can prove that the two terms in the sum in the numerator are equal. We can express H_γ as

---

[8]In the simplest case, the form of the time series of the response, $S(t)$, can be obtained by inverse Fourier transforming the responsivity, $S(\omega)$ (assuming that the complex phases of the responsivity are chosen correctly). This is only true if the energy is deposited in the calorimeter instantaneously, as only in that case is the pulse shape given by the impulse response of the system. If there is a finite thermalization time, we would use the real pulse shape, $T(t) = \int h(t - t')S(t)dt'$ (where $h(x)$ is the time redistribution function, expressing the thermalization profile) and the optimal filter derivation would use $T(\omega)$, instead of $S(\omega)$ (we leave $S(\omega)$ as always being the symbol for the responsivity).

[9]We see why item (2) is important, since to get the average noise we look at traces without pulses, and we are then implicitly assuming the noise is the same with or without pulses. This is only true in stationary noise. For our detectors, although not true, it is a good approximation.

[10]Since we get the average pulse shape from a single line, we must assume the detector is linear (condition (1)), and any other energy will produce the same pulse shape multiplied by an overall constant.

$$H_\gamma = \frac{\sum \frac{D(\omega)S(\omega)^*}{\left\langle |N(\omega)|^2 \right\rangle}}{\sum \frac{S^2(\omega)}{\left\langle |N(\omega)|^2 \right\rangle}} \tag{3.58}$$

If the energy of the photon where 1, then $H_\gamma = 1$ and $D(\omega) = S(\omega) + N(\omega)$. If there were no noise, we would get the right answer of $H_\gamma = 1$. We see that the sum in the denominator is just the normalization to make the estimate in units of energy. We can fold this term into a constant κ, and rewrite as

$$H_\gamma = \kappa \sum_\omega D(\omega) \frac{S(\omega)^*}{\left\langle |N(\omega)|^2 \right\rangle} = \kappa \sum_\omega \frac{D(\omega)}{S(\omega)} SNR^2(\omega) \tag{3.59}$$

The best estimate of H_γ is therefore the sum of the ratio of the data to the signal of a 1 eV photon at each frequency weighted by the square of the signal-to-noise ratio at that frequency. From this estimate, the energy resolution of the device can be derived.

Moving back to the time domain we have

$$H_\gamma = \kappa \sum_t D(t)s(t) \tag{3.60}$$

where $s(t)$ is the inverse Fourier transform of $S^*(\omega)/\left\langle |N(\omega)|^2 \right\rangle$. One of the nice features of this method is that once $S(\omega)$ and $N(\omega)$ are known, data can be analyzed in the time domain without the need for Fourier transforms.

3.1.5   NEP and ΔE

Now we want to determine the theoretical resolution of the detector. To do this we need to determine the noise equivalent power (NEP) of each noise term in our equations. The NEP, as its name implies, is the equivalent input referred power one would need to produce a given output noise. If the output signal for a given noise $N(\omega)$ is $\Delta I_N(\omega)$, then we have

$$\Delta I_N(\omega) = \frac{d\Delta I}{dN} N(\omega) \tag{3.61}$$

The input to our calorimeter (the photons) comes into the thermal circuit in the same way that the thermal noise does: the terms P_{tn} and P_γ appear side by side in the equations. So when we say "input referred" we mean referred to a thermal power input. The NEP of a noise term $N(\omega)$ is the input referred noise of $N(\omega)$; it is the amount of thermal noise that would give the same current noise $\Delta I_N(\omega)$:

$$\Delta I_N(\omega) = \frac{d\Delta I}{dP_{tn}} NEP_N(\omega) = S(\omega) NEP_N(\omega) \tag{3.62}$$

for a given noise source $N(\omega)$ the NEP is then

$$\text{NEP}_N(\omega) = \frac{\frac{d\Delta I}{dN}}{S(\omega)} N(\omega) \tag{3.63}$$

From the definition above it is obvious that

$$\text{NEP}_\text{tn}(\omega) = P_\text{tn}(\omega) \tag{3.64}$$

Looking at Eqs. (3.37)-(3.39) we can compute the NEP of detector and circuit noise terms to be

$$\text{NEP}_\text{dn}(\omega) = \frac{1 + i\omega\tau_o}{-\frac{\alpha P}{TG}} I V_\text{dn}(\omega) \tag{3.65}$$

$$\text{NEP}_\text{cn}(\omega) = \frac{1 - \frac{\alpha P}{TG} + i\omega\tau_o}{-\frac{\alpha P}{TG}} I (V_\text{cn}(\omega) - R_\text{L} I_\text{cn}(\omega)) \tag{3.66}$$

The total NEP is the sum in quadrature of these separate terms:

$$\text{NEP}^2(\omega) = P_\text{tn}^2(\omega) + \frac{1 + \omega^2\tau_o^2}{\left(\frac{\alpha P}{TG}\right)^2} I^2 V_\text{dn}^2(\omega)$$
$$+ \frac{(1 - \frac{\alpha P}{TG})^2 + \omega^2\tau_o^2}{\left(\frac{\alpha P}{TG}\right)^2} I^2 (V_\text{cn}^2(\omega) + R_\text{L}^2 I_\text{cn}^2(\omega)) \tag{3.67}$$

This equation can be used to calculate the NEP of a noise source of any spectral shape, and is valid for a voltage-biased calorimeter for all values of the parameters. As noted before, the NEP is not dependent on α_I. Now that we have the NEP, assuming we calculate an estimate of the energy using the optimal filter described above we can define the theoretical resolution from Moseley, Mather, and McCammon (1984) as

$$\Delta E_\text{rms} = \left(\sqrt{\int_0^\infty \frac{4df}{\text{NEP}(f)^2}} \right)^{-1} \tag{3.68}$$

where $f = \omega/2\pi$.

From this equation we can see that the lower the NEP, the better the energy resolution. Since we integrate over all frequencies, the larger the frequency range with small NEP, the better the energy resolution will become. We can solve this algebraically or numerically for any number of noise sources we wish to include in our model. For the ideal calorimeter, we only include phonon noise, detector Johnson noise, and load resistor Johnson noise. Since all these are white noise sources (no frequency dependence), we can solve the resulting integral quite easily. To derive this particular case's theoretical resolution, we will need to

use the following integral:

$$\int_0^\infty \frac{4df}{A + B(2\pi f)^2} = \frac{1}{\sqrt{AB}} \tag{3.69}$$

From Eq. (3.67) we can see that

$$A = P_{tn}^2 + \left(\frac{TG}{\alpha P}\right)^2 I^2 \left(V_{dn}^2 + (V_{cn}^2 + R_L^2 I_{cn}^2) \left(1 - \frac{\alpha P}{TG}\right)^2\right) \tag{3.70}$$

$$B = \left(\frac{TG}{\alpha P}\right)^2 I^2 (V_{dn}^2 + V_{cn}^2 + R_L^2 I_{cn}^2) \tag{3.71}$$

Note that this calculation is only valid if P_{tn}, V_{cn}, I_{cn}, and V_{dn} are constants (white noise sources with no frequency dependence are just constants in frequency space). The answer you get will depend on the magnitude these terms, which is basically their RMS value. The two resistors will just have the classical Johnson noise associated with them. Assuming the thermal link is completely specular the phonon noise becomes (Ashcroft and Mermin, 1976, chap. 25)

$$P_{tn} = \sqrt{2k_B(T^2 + T_b^2)G} \tag{3.72}$$

and the Johnson noise terms are

$$V_{dn} = \sqrt{4k_B T R} \tag{3.73}$$

$$V_{cn} = \sqrt{4k_B T_L R_L} \tag{3.74}$$

where T_L is the temperature of the load resistor. With these values for our noise sources, and including the factor 2.355 to obtain the full width at half maximum (FWHM), some algebraic manipulation leads to

$$\boxed{\Delta E_{\text{FWHM}} = 2.355 \times \sqrt{4k_B T^2 C \frac{1}{\alpha} \sqrt{\frac{1}{P} \frac{TG}{P} (1+r) \left[\frac{1}{2}\left(1 + \frac{T_b^2}{T^2}\right) + \frac{TG}{\alpha^2 P}\left(1 + r\left(1 - \frac{\alpha P}{TG}\right)^2\right)\right]}}} \tag{3.75}$$

where $r = (R_L T_L)/(RT)$. This equation is valid for all feedback and α values, as well as for any value of a bias resistor, and at any bath temperature, assuming a specular thermal link. Again note that the theoretical resolution is not dependent on the parameter α_I.

In the limit where $R_L = 0$, $T_b = 0$, and $\alpha P/TG \gg 1$, we obtain the extreme ETF result

of Irwin (1995b):

$$\Delta E_{\text{FWHM}} = 2.355 \times \sqrt{4 k_{\text{B}} T^2 C \frac{1}{\alpha} \sqrt{\frac{n}{2}}} \tag{3.76}$$

It is customary to express the resolution of a calorimeter as $\Delta E_{\text{rms}} = \xi \sqrt{k_{\text{B}} T^2 C}$. In this derivation we find

$$\xi = 2 \left(\frac{TG}{\alpha^2 P} (1 + r) \left[\frac{1}{2} \left(1 + \frac{T_{\text{b}}^2}{T^2} \right) + \frac{TG}{\alpha^2 P} \left(1 + r \left(1 - \frac{\alpha P}{TG} \right)^2 \right) \right] \right)^{\frac{1}{4}} \tag{3.77}$$

We can also compare our result with the theoretical resolution derived by Moseley, Mather, and McCammon (1984), hereinafter the 3M paper. There the authors used an expression for the phonon noise that included a completely diffusive thermal link. First lets make some relationships between the nomenclature in the 3M paper and this work:

$$\beta + 1 = n \tag{3.78}$$

$$t = T/T_{\text{b}} \tag{3.79}$$

$$T_c = T_{\text{b}} \tag{3.80}$$

$$1 - t^{-(\beta+1)} = \frac{nP}{TG} \tag{3.81}$$

$$T_c t = T \tag{3.82}$$

$$C_o t^\gamma = C \tag{3.83}$$

$$A = \alpha \tag{3.84}$$

The 3M resolution (in their variables) is

$$\Delta E_{\text{rms}} = \sqrt{k_{\text{B}} T_c^2 C_o \frac{4(\beta + 1) t^{2+\gamma}}{A^2 (1 - t^{-(\beta+1)})} \sqrt{1 + \frac{(1 - t^{-(3+2\beta)}) A^2}{3 + 2\beta}}} \tag{3.85}$$

in our nomenclature the same equation becomes

$$\Delta E_{\text{rms}} = \sqrt{4 k_{\text{B}} T^2 C \frac{TG}{\alpha^2 P} \sqrt{1 + \frac{\alpha^2}{2n + 1} \left(1 - \left(\frac{T_{\text{b}}}{T} \right)^{(2n+1)} \right)}} \tag{3.86}$$

The phonon noise for a diffusive thermal link expressed in our variables is

$$P_{\text{3M}} = \frac{4 k_{\text{B}} T^3 G^2}{(2n + 1) P} \left(1 - \left(\frac{T_{\text{b}}}{T} \right)^{(2n+1)} \right) \tag{3.87}$$

(Equation 15 in the 3M paper). Using this equation for phonon noise instead of Eq. (3.72)

leads to

$$
\Delta E_{\mathrm{FWHM}} = 2.355 \times
$$
$$
\sqrt{4k_{\mathrm{B}}T^2 C \frac{TG}{\alpha^2 P} \sqrt{(1+r)\left[1 + r\left(1 - \frac{\alpha P}{TG}\right)^2 + \frac{\alpha^2}{2n+1}\left(1 - \left(\frac{T_{\mathrm{b}}}{T}\right)^{(2n+1)}\right)\right]}} \tag{3.88}
$$

which reduces to the 3M result (Eq. (3.86)) in perfect voltage bias ($r = 0$). This result is valid for a diffusive thermal link, at any value of the bias resistor, for any α, with any base temperature. Note that the 3M derivation was performed for a voltage-readout thermistor under perfect current bias, while we arrived at the same equation (for $r = 0$ or perfect voltage bias) assuming current readout.

3.1.6   Calorimeter example

Table 3.1 shows typical parameters for a single-pixel TES device. The heat capacity has been chosen to satisfy our saturation condition of Section 2.2.6. The critical temperature of the TES, which would normally be 100 mK, has been set to 75 mK to compare it to the PoST results in Chapter 7.

Figure 3.2(a) shows the current noise from Eq. (3.44). Note the load resistor Johnson noise is higher than the detector Johnson noise at low frequencies. Figure 3.2(b) shows the NEP from Eq. (3.67), and the energy resolution from Eq. (3.75). As discussed in Section 3.1.5, the lower the NEP, the better the energy resolution. With this in mind we can see that the lower frequencies are the ones which contribute most to the energy resolution.

The resolution for the values in Table 3.1 is $\Delta E_{\mathrm{FWHM}} = 1.64$ eV. If the extreme ETF limit approximation is used (Eq. (3.76)), one obtains a resolution of 1.35 eV. The discrepancy is due both to the zero base temperature and no load resistor noise assumptions in the extreme ETF limit.

C	1.92	pJ/K
G	200	pW/K
R	10	mΩ
R_{L}	1	mΩ
T	75	mK
T_{b}	50	mK
α	90	
n	3.2	
α_{I}	0	

Table 3.1: Parameters for single-pixel PoST
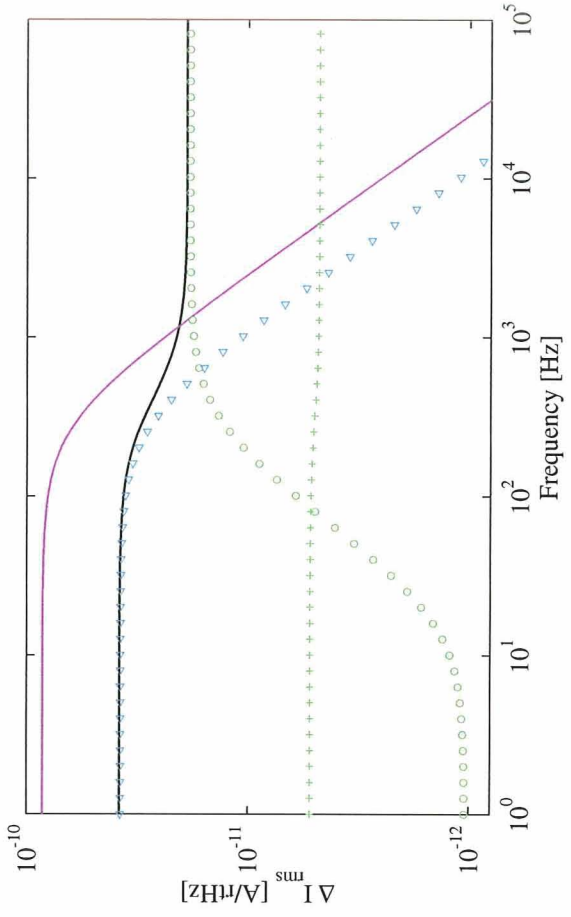
(a) Current noise in a simple calorimeter.
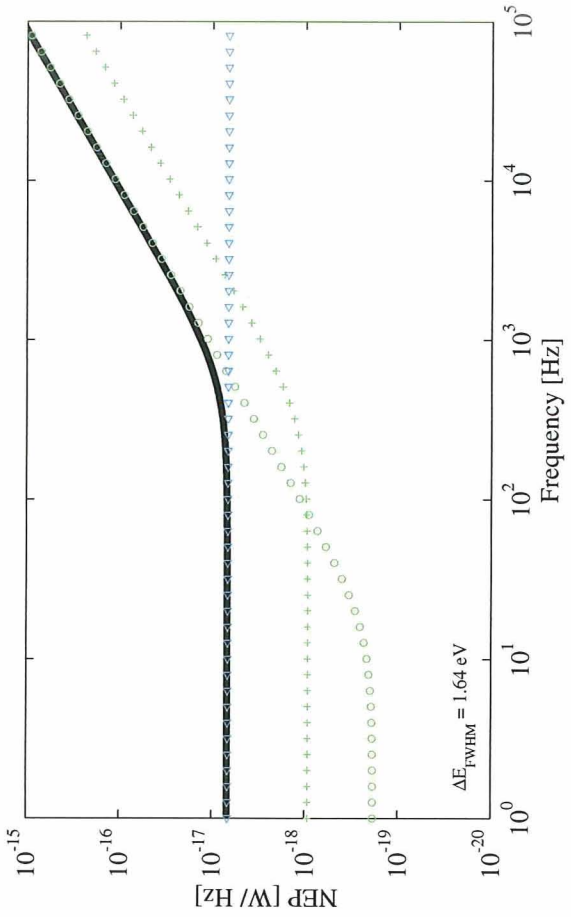
(b) NEP of a simple calorimeter.

Figure 3.2: Example of noise and NEP in a simple calorimeter. The blue triangles ($\triangledown$) are the phonon noise to the bath. The green circles ($\circ$) are the Johnson noise due to the detector resistance. The green crosses ($+$) are the Johnson noise due to the load resistor. The thick black line is the total noise. The magenta line is the signal from a photon.

3.2   Complex calorimeter theory

In the previous section we looked at the noise theory for a simple calorimeter and were able to solve the resulting equations algebraically to obtain our results. In general, however, calorimeters are more complicated than our previous model. The effects of an absorber with non-zero heat capacity connected to the thermometer should be taken into account. In many cases electron-phonon decoupling is important. Furthermore, to realistically model voltage biased and current biased devices, we need to include capacitance and inductance in our electric circuits.

Consider the calorimeter in Figure 3.3. In this model, we have separate heat capacities for the detector phonon system (C_p) and the detector electron system (C_e). We have specified the electron-phonon coupling conductance $G_{ep}(T)$ and the phonon to bath conductance $G_{pb}(T)$.

The absorber (C_a) is attached to both the electron and the phonon system; this simplification assumes that the electron-phonon coupling time constant of the absorber is much faster than the other time constants in the system. If only electron-electron coupling is important, $G_{ap}(T)$ can be set to zero and vice-versa. Adding a separate absorber phonon system only adds one more equation to the system, but for our purposes here this system is already plenty complicated.

The electronic readout circuit has been specified with most of the elements required to accurately portray both voltage readout and current readout systems. The addition of both inductance (L) and capacitance (C_{cap}) splits the circuit into two equations, one for the calorimeter voltage $V(t)$ and another for the current $I(t)$. This apparent complication will come in very handy when we want to compare current and voltage readout systems, since we will have both variables in our matrices and we will be free to switch from one to the other at our leisure without having to change any equations.

Looking at the noise terms, we have, as before, detector noise V_{dn} and circuit noise V_{cn}. We have a thermal noise input for each heat capacity. But, unlike in the previous section, we have separated the phonon noise from other thermal power noise terms. This is because the phonon noise represents power fluctuations flowing from one heat capacity to another. In this exchange of heat power is conserved, and the phonon noise terms will appear with a positive sign in one heat capacity and a negative sign in the other, to indicate that the amount of heat taken from one is equal to that received by the other.

3.2.1   Current noise and responsivity

Solving the equations for this system to arrive at theoretical noise, NEP, and energy resolution algebraically would be a large headache to say the least. Expanding the matrix formulation originally applied by Lindeman (2000) to the calorimeter problem, we can describe these complex calorimeters in matrix notation. The resulting large matrix equations are not any easier to solve algebraically, but now they are in a form where a computer program can take over and numerically compute the noise, NEP, and the energy resolution for very intricate systems. Only time and computer memory restrict how complex your
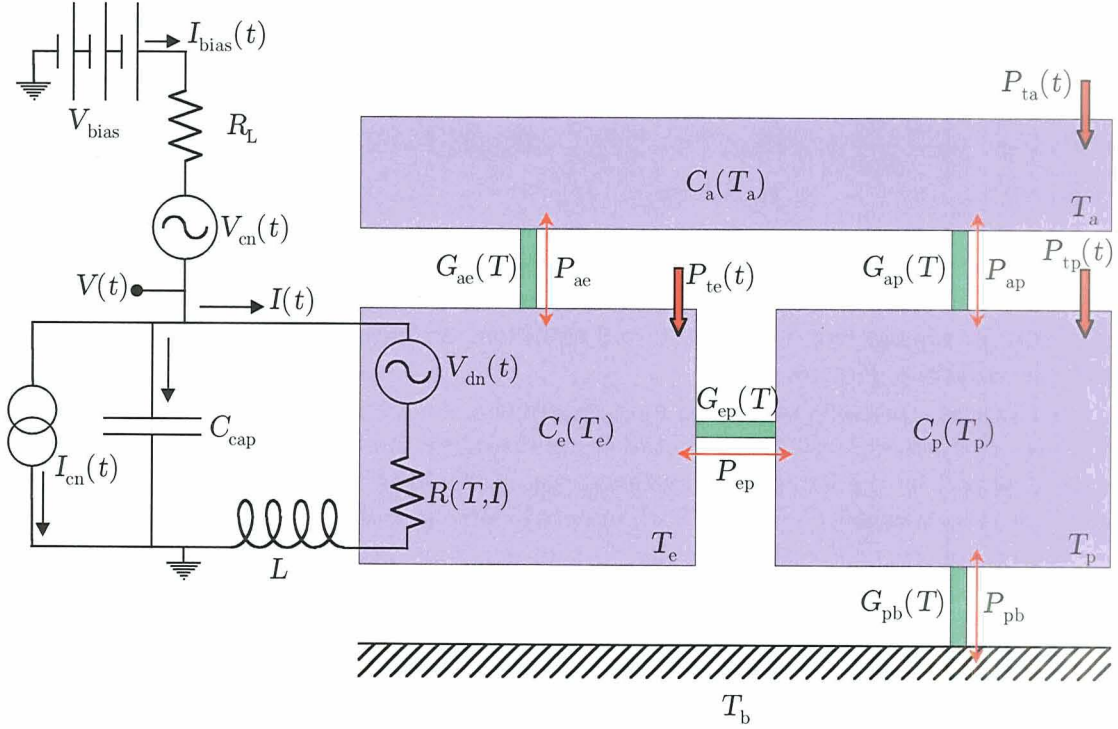
Figure 3.3: Example of a complex calorimeter bias and thermal circuit. V_{bias}, R_L, and I_{bias} are the equivalent bias voltage, load resistance, and bias current. L and C_{cap} are the inductance and capacitance, respectively. V_{cn} and I_{cn} are circuit noise sources. V_{dn} is the detector noise into the circuit. $R(T, I)$ is the resistance of the detector. The filled rectangles represent the different detector elements: the electron system with heat capacity C_e at temperature T_e, the phonon system (C_p) and the absorber (C_a). The thermal link conductance between elements is designated as $G(T)$ with appropriate subscripts. P_{te} is the power input into the thermal circuit via the electron system, etc. The phonon noise between heat capacities is designated as P_{ep} for the electron-phonon phonon noise, etc.

system can be. The equations from this section are a subset of the full PoST equations we will solve in Section 4.3.

Following the steps from Section 3.1.1, we write down this detectors governing equations:

$$L\frac{dI(t)}{dt} = -I(t)R(T, I) + V(t)R(T, I) - V_{dn}(t)R(T, I) \tag{3.89}$$

$$R_L C_{cap}\frac{dV(t)}{dt} = -R_L I(t) - V(t) + V_{bias} + V_{cn}(t) - R_L I_{cn}(t) \tag{3.90}$$

$$C_e\frac{dT_e(t)}{dt} = I(t)^2 R(T, I) - K_{ep}(T_e^{n_{ep}} - T_p^{n_{ep}}) - K_{ae}(T_e^{n_{ae}} - T_a^{n_{ae}}) \tag{3.91}$$
$$+ P_{te}(t) + I(t)V_{dn}(t) + P_{ep} + P_{ae}$$

$$C_{\mathrm{p}}\frac{dT_{\mathrm{p}}(t)}{dt} = -K_{\mathrm{ep}}(T_{\mathrm{p}}^{n_{\mathrm{ep}}} - T_{\mathrm{e}}^{n_{\mathrm{ep}}}) - K_{\mathrm{pb}}(T_{\mathrm{p}}^{n_{\mathrm{pb}}} - T_{\mathrm{b}}^{n_{\mathrm{pb}}})$$
$$\qquad - K_{\mathrm{ap}}(T_{\mathrm{p}}^{n_{\mathrm{ap}}} - T_{\mathrm{a}}^{n_{\mathrm{ap}}}) + P_{\mathrm{tp}}(t) + P_{\mathrm{ap}} - P_{\mathrm{ep}} \tag{3.92}$$

$$C_{\mathrm{a}}\frac{dT_{\mathrm{a}}(t)}{dt} = -K_{\mathrm{ae}}(T_{\mathrm{a}}^{n_{\mathrm{ae}}} - T_{\mathrm{e}}^{n_{\mathrm{ae}}}) - K_{\mathrm{ap}}(T_{\mathrm{a}}^{n_{\mathrm{ap}}} - T_{\mathrm{p}}^{n_{\mathrm{ap}}})$$
$$\qquad + P_{\mathrm{ta}}(t) - P_{\mathrm{ae}} - P_{\mathrm{ap}} \tag{3.93}$$

For generality we have allowed n to be different for each type of coupling. Note that when $L \neq 0$, $V(t)$ is *not* the voltage across the detector, although it is the voltage that we read out. In the electron system thermal equation, we have used $I(t)R(T, I) + V_{\mathrm{dn}}$ as the voltage across the detector.

With these equations numerical modeling of this device could be made. The complexity of a five-equation numerical differential equation solver must be weighed against the information gained by modeling the non-linearities of the detector. The solution of the linear model involves a relatively simple 5×5 matrix inversion problem. In the end, these systems are too complex to solve algebraically, but an amazing amount of information can be deduced and calculated by playing with parameters in a linear model which executes quickly in your computer and gives your the resolution for different values of the parameters.

Now we are again ready to linearize this system. We will skip many of the intermediate steps since they are analogous to the method used in the previous sections. As we progress into more complex models, we will have to rely on these basic methods to lead the way.

We must be careful in our definition of G. G is defined in Eq. (3.14) as $G = dP/dT$ evaluated at T. For the phonon to bath conductance we only need one G_{pb} since T_{b} is a constant and we do not take derivatives with respect to it in our linearization procedure. But for all other conductances, we do end up with two different derivatives in the linearization: one for each temperature. This means we actually need two Gs for each conductance. For example, the electron-phonon conductance will be

$$G_{\mathrm{ep}}^{\mathrm{e}} = \left. \frac{d}{dT_{\mathrm{e}}}K_{\mathrm{ep}}(T_{\mathrm{e}}^{n_{\mathrm{ep}}} - T_{\mathrm{p}}^{n_{\mathrm{ep}}})\right|_{T_{\mathrm{e}}} \tag{3.94}$$
$$= K_{\mathrm{ep}}n_{\mathrm{ep}}T_{\mathrm{e}}^{n_{\mathrm{ep}}-1} \tag{3.95}$$

at the electron system and

$$G_{\mathrm{ep}}^{\mathrm{p}} = \left. \frac{d}{dT_{p}}K_{\mathrm{ep}}(T_{\mathrm{e}}^{n_{\mathrm{ep}}} - T_{\mathrm{p}}^{n_{\mathrm{ep}}})\right|_{T_{\mathrm{p}}} \tag{3.96}$$
$$= K_{\mathrm{ep}}n_{\mathrm{ep}}T_{\mathrm{p}}^{n_{\mathrm{ep}}-1} \tag{3.97}$$

at the phonon system. We will use superscripts to differentiate the two different Gs. For most of these, the values of the two Gs will be equal, since it depends on the quiescent temperature of the elements. For example, in our present calorimeter the absorber and electron system quiescent temperatures will be the same. The electron and phonon temperatures will not, unless K_{ep} is large.

Following the previous section, we Taylor expand around the steady state point, take the Fourier transform and look at one frequency. After a while one arrives at the following linear system of equations:

$$i\omega L \Delta I = -R(1 + \alpha_{\mathrm{I}})\Delta I + \Delta V - \frac{\alpha V}{T_e}\Delta T_e - V_{\mathrm{dn}} \tag{3.98}$$

$$i\omega R_{\mathrm{L}} C_{\mathrm{cap}} \Delta V = -R_{\mathrm{L}}\Delta I - \Delta V + V_{\mathrm{cn}}(\omega) - R_{\mathrm{L}} I_{\mathrm{cn}}(\omega) \tag{3.99}$$

$$i\omega C_e \Delta T_e = (2 + \alpha_{\mathrm{I}})V\Delta I - (G_{\mathrm{ep}}^e + G_{\mathrm{ae}}^e)\Delta T_e + G_{\mathrm{ep}}^p \Delta T_{\mathrm{p}} + G_{\mathrm{ep}}^{\mathrm{a}}\Delta T_{\mathrm{a}}$$
$$+ P_{\mathrm{te}}(\omega) + I V_{\mathrm{dn}}(\omega) + P_{\mathrm{ep}} + P_{\mathrm{ae}} \tag{3.100}$$

$$i\omega C_{\mathrm{p}} \Delta T_{\mathrm{p}} = -(G_{\mathrm{ep}}^p + G_{\mathrm{pb}}^p + G_{\mathrm{ap}}^p)\Delta T_{\mathrm{p}} + G_{\mathrm{ep}}^e \Delta T_e + G_{\mathrm{ap}}^{\mathrm{a}}\Delta T_{\mathrm{a}}$$
$$+ P_{\mathrm{tp}}(\omega) + P_{\mathrm{ap}} - P_{\mathrm{ep}} \tag{3.101}$$

$$i\omega C_{\mathrm{a}} \Delta T_{\mathrm{a}} = -(G_{\mathrm{ae}}^{\mathrm{a}} + G_{\mathrm{ap}}^{\mathrm{a}})\Delta T_{\mathrm{a}} + G_{\mathrm{ae}}^e \Delta T_e + G_{\mathrm{ap}}^p \Delta T_{\mathrm{p}}$$
$$+ P_{\mathrm{ta}}(\omega) - P_{\mathrm{ae}} - P_{\mathrm{ap}} \tag{3.102}$$

We can now write this system of equations in matrix notation:

$$
\begin{pmatrix}
R(1+\alpha_{\mathrm{I}}) + i\omega L & -1 & \frac{\alpha V}{T} & 0 & 0 \\
R_{\mathrm{L}} & 1 + i\omega R_{\mathrm{L}}C_{\mathrm{cap}} & 0 & 0 & 0 \\
-(2+\alpha_{\mathrm{I}})V & 0 & G_{\mathrm{ep}}^{\mathrm{e}} + G_{\mathrm{ae}}^{\mathrm{e}} - \frac{\alpha P}{T} + i\omega C_{\mathrm{e}} & -G_{\mathrm{ep}}^{\mathrm{p}} & -G_{\mathrm{ae}}^{\mathrm{a}} \\
0 & 0 & -G_{\mathrm{ep}}^{\mathrm{e}} & G_{\mathrm{ep}}^{\mathrm{p}} + G_{\mathrm{ap}}^{\mathrm{p}} + G_{\mathrm{pb}} + i\omega C_{\mathrm{p}} & -G_{\mathrm{ap}}^{\mathrm{a}} \\
0 & 0 & -G_{\mathrm{ae}}^{\mathrm{e}} & -G_{\mathrm{ap}}^{\mathrm{p}} & G_{\mathrm{ae}}^{\mathrm{a}} + G_{\mathrm{ap}}^{\mathrm{a}} + i\omega C_a
\end{pmatrix}
\begin{pmatrix}
\Delta I \\ \Delta V \\ \Delta T_{\mathrm{e}} \\ \Delta T_{\mathrm{p}} \\ \Delta T_{\mathrm{a}}
\end{pmatrix}
$$

$$
= \begin{pmatrix}
V_{\mathrm{dn}}(\omega) \\
V_{\mathrm{cn}}(\omega) - R_{\mathrm{L}}I_{\mathrm{cn}}(\omega) \\
P_{\mathrm{te}}(\omega) - IV_{\mathrm{dn}}(\omega) + P_{\mathrm{ep}} + P_{\mathrm{ae}} \\
P_{\mathrm{tp}}(\omega) - P_{\mathrm{ep}} + P_{\mathrm{ap}} \\
P_{\mathrm{ta}}(\omega) - P_{\mathrm{ae}} - P_{\mathrm{ap}}
\end{pmatrix} \qquad (3.103)
$$

We can write this matrix as

$$\mathbf{M}\vec{\Delta} = \vec{N} \tag{3.104}$$

Using the variables $\mathbf{M}$, $\vec{\Delta}$, and $\vec{N}$ for these matrices we can now continue and calculate all parameters of interest for this system. Solving Eq. (3.104) for $\vec{\Delta}$ we have

$$\vec{\Delta} = \mathbf{M}^{-1}\vec{N} \tag{3.105}$$

This matrix inversion is done numerically for each frequency ω. The rows of the matrices represent the following equations:

- Row 1: current

- Row 2: voltage

- Row 3: electrons

- Row 4: phonons

- Row 5: absorber

The first quantity we want to compute is the responsivity $S(\omega)$ of the system. As mentioned in the previous section, the responsivity is defined as the signal measured for a given power input onto the thermal system. Except that now we have two possible output signals (current or voltage) and three input locations in the thermal circuit[11] (electron, phonon, absorber). The derivatives of the system are

$$\frac{d\vec{\Delta}_k}{d\vec{N}_i} = \mathbf{M}_{k,i}^{-1} \tag{3.106}$$

where we will use the following convention for indices: k refers to the readout, i the input location, and j will be a dummy index. So we generalize Eq. (3.37) to obtain the responsivity by adding subscripts to indicate our readout method and power input location:

$$\mathbf{S}_{k,i} \equiv \frac{d\vec{\Delta}_k}{d\vec{N}_i} = \mathbf{M}_{k,i}^{-1} \tag{3.107}$$

For example

$$\mathbf{S}_{v,a} = \mathbf{S}_{2,5} = \frac{d\Delta V}{P_{\text{ta}}} = \frac{d\vec{\Delta}_2}{d\vec{N}_5} = \mathbf{M}_{2,5}^{-1} \tag{3.108}$$

is the responsivity of a power input into the absorber when read out as a voltage.

---

[11]Each heat capacity in the model is a possible absorption location for a photon, whether intended for that purpose or not.

The noise for a particular noise source $\vec{N}$ as seen in the element $\vec{\Delta}_k$ will be

$$\left\langle \left| \vec{\Delta}_k \right|^2 \right\rangle = \left\langle \left| \sum_j \mathbf{S}_{k,j} \vec{N}_j(\omega) \right|^2 \right\rangle \tag{3.109}$$

Each noise source is calculated separately and then summed in quadrature, the same as for NEP in the next section.

3.2.2 NEP and ΔE

Now that we have the responsivity, we can proceed to calculate NEP. The NEP and energy resolution will be different depending on where the photon was absorbed. This is because we need to refer all noise sources back to the place where the signal input occurs to get the noise-equivalent power. The values of the heat capacities and conductances will make the NEP be different on each input location. We have three places for photon absorption (the heat capacities of the phonon, electron, and absorber systems). The energy resolution calculations need to be done separately for each.

We will calculate the NEP for each noise term separately; the total is just the quadrature sum of the individual terms. The matrix $\vec{N}$ contains all of our noise sources. Looking at Eq. (3.103) we see that some noise sources ($V_{\mathrm{dn}}(\omega)$, for example) appear in more that one place in the matrix $\vec{N}$. To calculate the NEP for one noise source, we temporarily disregard all other noise sources so the matrix $\vec{N}$ is only composed of the terms from the noise source of interest. Then extending Eq. (3.63) we find the general form for the NEP of a particular noise source $\vec{N}$ for readout k and assuming a power input at element i:

$$\mathrm{NEP}_{k,i}(\omega) = \left| \frac{1}{\mathbf{S}_{k,i}} \sum_j \frac{d\vec{\Delta}_k}{d\vec{N}_j} \vec{N}_j \right| = \left| \frac{1}{\mathbf{S}_{k,i}} \sum_j \mathbf{S}_{k,j} \vec{N}_j \right| \tag{3.110}$$

where the index j labels the elements of the noise vector $\vec{N}$. For example, the NEP for detector noise referenced to energy input occurring in the absorber, and reading out the current, would be

$$\vec{N}_{\mathrm{dn}} = \begin{pmatrix} V_{\mathrm{dn}}/R \\ 0 \\ -IV_{\mathrm{dn}} \\ 0 \\ 0 \end{pmatrix} \tag{3.111}$$

$$\mathrm{NEP}_{1,5;\mathrm{dn}}(\omega) = \left| \frac{1}{\mathbf{S}_{1,5}} \sum_j \frac{d\vec{\Delta}_1}{d\vec{N}_j} \vec{N}_{j;\mathrm{dn}} \right| = \left| \frac{1}{\mathbf{S}_{1,5}} \left(\frac{d\vec{\Delta}_1}{d\vec{N}_1} \frac{V_{\mathrm{dn}}}{R} - \frac{d\vec{\Delta}_1}{d\vec{N}_3} IV_{\mathrm{dn}} \right) \right| \tag{3.112}$$

$$= \left| \frac{1}{\mathbf{S}_{1,5}} \left(\mathbf{S}_{1,1} \frac{V_{\mathrm{dn}}}{R} - \mathbf{S}_{1,3} IV_{\mathrm{dn}} \right) \right| \tag{3.113}$$

Another example: the electron-phonon noise term would have the following NEP for voltage readout and power input into the electron system:

$$\text{NEP}_{2,3;\text{ep}}(\omega) = \left| \frac{1}{\mathbf{S}_{2,3}} \left(\frac{d\vec{\Delta}_2}{d\vec{N}_3} P_{\text{ep}} - \frac{d\vec{\Delta}_2}{d\vec{N}_4} P_{\text{ep}} \right) \right| = \left| P_{\text{ep}} - \frac{\mathbf{S}_{2,4}}{\mathbf{S}_{2,3}} P_{\text{ep}} \right| \qquad (3.114)$$

The total noise equivalent power NEP_{tot} is the quadrature sum of all the individual noise sources. Once we have the total NEP, it is a simple task to numerically integrate Eq. (3.68) to obtain the ΔE_{FWHM} of the detector.

3.2.3   Complex calorimeter example

In this section we will briefly show one application of the complex calorimeter theory developed in this chapter. We present a fit to the noise of the Goddard-Univ. of Wisconsin X-ray Quantum Calorimeter, or XQC. The XQC is a sounding-rocket payload used to study the diffuse X-ray background. The detector is an array of 36 silicon semiconductor thermistors, and is mounted on a specially designed adiabatic demagnetization refrigerator capable of surviving a rocket launch and being at base temperature 30 seconds after rocket burn-out. This rocket has flown three times (Porter et al., 2000a) and we are currently planning the fourth flight.

Using parameters derived theoretically for the XQC by Galeazzi et al. (2002), we show the excellent agreement between the measured data and the noise spectrum from our model (Figure 3.5). Only at low frequencies was there a discrepancy which was well described by a $1/f^2$ term, which we are still in the process of understanding. Note that since this is a silicon thermistor with a negative α, we are solving the same model described above for the voltage noise. This shows that one model will work equally well with voltage or current readout devices, allowing direct comparisons to be made.

We also show the ability of our model to input frequency-dependent noise sources, such as $1/f$ and $1/f^2$ noise. It is just a matter of setting the function for the detector noise $V_{\mathrm{dn}}(\omega)$ to a $1/f$ term in addition to the usual detector Johnson noise. The same can be done for the circuit noise to model $1/f$ noise in the amplifiers, or a 60 Hz pickup line.

The resolution predicted by integrating the NEP in Figure 3.6 with Eq. (3.110) is in excellent agreement with the baseline noise measured experimentally.

————	Total noise or NEP
$\triangleright$	Det 1/f noise or NEP
$\triangleleft$	Detector Johnson noise or NEP
$\triangle$	RL Johnson noise or NEP
$\bigcirc$	Phonon to Bath noise or NEP
$+$	Electron-Phonon noise or NEP
— — --	Absorber to phonon noise or NEP
$\times$	Electronic noise or NEP
$*$	Mystery 1/f^2 noise or NEP

Figure 3.4: Legend for Figures 3.5 and 3.6.
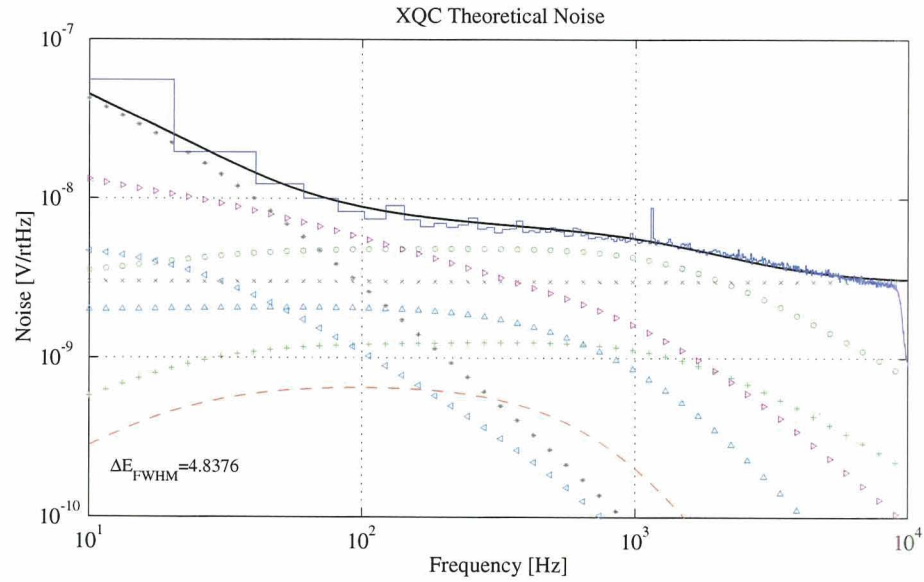
Figure 3.5: Noise for the XQC. The data is shown in blue. The theoretical model is *not* a fit. All parameters were calculated from first principles or measured on the experiment. The agreement between experiment and theory is very good. Only at low frequencies is there disagreement, which was well described by a $1/f^2$ component. The energy resolution is calculated from the NEP in Figure 3.6. The legend is Figure 3.4.
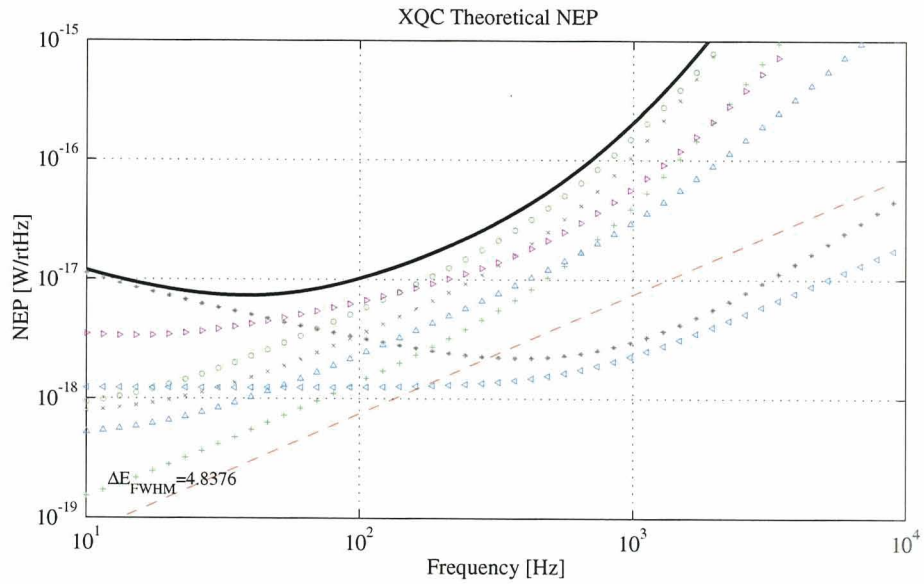
Figure 3.6: Theoretical NEP for the XQC rocket payload detectors. The energy resolution from the integral of these curves (using Eq. (3.110)) is in excellent agreement with the measured values of the detectors.

Chapter 4

PoST Calorimeter Theory

4.1 The simplest PoST theory (just two TES connected together)

Now that we have built up all the mathematical machinery to do multiple pixel calorimeters, we want to start out with the simplest case PoST: two calorimeters connected by a thermal link G_{12} (Figure 4.1). In this simplest case we can get intuition into the features of the system and better understanding of the numerical solutions we will get when studying many-pixel calorimeters. We will take several steps on our way to the full-blown PoST noise theory.

4.1.1 Two-pixel PoST analytic solution: time domain

We begin with the schematic of a two-pixel PoST shown in Figure 4.1. The electron-phonon coupling is taken to be high enough that they both act as a single system with total heat capacity $C = C_{\mathrm{e}} + C_{\mathrm{p}}$. We will look at the current readout case, and our thermometer will be a TES. There is no separate absorber; the photons are absorbed by the TES electron system. We assume the electron-phonon coupling time constant is much larger than other characteristic times in the system and can be neglected.[1] G is the conduction from each TES phonon system into the cold bath, and $G_{12}(T)$ is the conduction between the two TESs.

There is no inductance or capacitance in the circuit; also for now we assume that R_{L} and α_{I} are zero. In this first calculation we will keep only the components needed to show the essential behavior of a PoST. This keeps the analytical solutions to a manageable size. We will solve the time domain equations and plot out the response of the PoST, and then

---

[1]Note that we can equally say the TES phonon to cold bath coupling is much larger that the electron-phonon coupling, in which case the weak link to the cold bath would be via electron-phonon decoupling and we would just substitute our definition of G in the equations and figure to the the electron-phonon conductance. The TES phonon system would form part of the cold bath, and our equations would be unchanged. We will deal with the more complicated system that includes all these couplings in the Section 4.3.
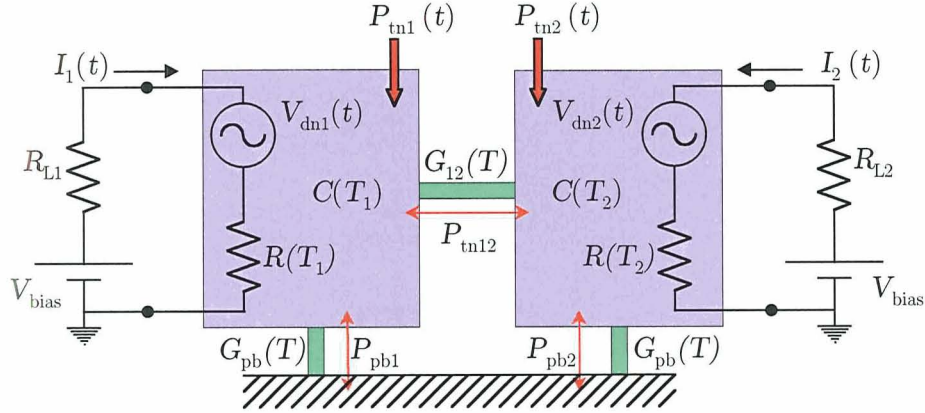
Figure 4.1: Schematic of the simplest PoST (two TES connected together). Two TES calorimeters are connected by a thermal conductance G_{12}. When a photon hits one of the TESs, a signal is sensed on both. The strength and shape of the signal depends on the link conductance G_{12}. The noise sources and circuit elements which will be considered in the following derivations are shown. Some will be neglected in the initial calculations.

calculate the theoretical equations for the phonon noise in the two-pixel device including the link thermal (phonon) noise $P_{tn12}(t)$.

We will disregard circuit and detector noise terms, but keep the thermal noise terms in the equations since we will use them in the noise analysis in the next section. As before, we lump the phonon noise terms between the TES and the bath (P_{pb}) into the general thermal noise terms P_{tn1} and P_{tn2}. We can write the equations for the electrical and thermal circuits as

$$0 = V_{bias} - I_1(t)R(T) \tag{4.1}$$

$$C(T)\frac{dT_1(t)}{dt} = I_1(t)^2 R(T) - K\left(T_1^n(t) - T_b^n\right) - K_{12}\left(T_1^{n_{12}}(t) - T_2^{n_{12}}(t)\right)$$
$$+ P_{tn1}(t) + P_{tn12}(t) + P_\gamma(t) \tag{4.2}$$

$$C(T)\frac{dT_2(t)}{dt} = I_2(t)^2 R(T) - K\left(T_2^n(t) - T_b^n\right) - K_{12}\left(T_2^{n_{12}}(t) - T_1^{n_{12}}(t)\right)$$
$$+ P_{tn2}(t) - P_{tn12}(t) + P_\gamma(t) \tag{4.3}$$

$$0 = V_{bias} - I_2(t)R(T) \tag{4.4}$$

Note that the link phonon noise comes into one equation positive and one equation negative; to conserve energy what goes out one side must come in the other. This will make the link phonon noise have a different spectral shape than the TES-bath phonon noise P_{tn1} and P_{tn2}.

We linearize the system, and as before the current-temperature relation is given by Eq. (2.16), since circuit and detector noise are neglected. We use Eq. (3.14) to define G

and a use a similar definition for G_{12}. We can then write the linear equations as

$$\frac{d}{dt}\Delta I_1(t) = \frac{1}{C}\left(-\frac{\alpha P}{T}\Delta I_1 - (G + G_{12})\Delta I_1 + G_{12}\Delta I_2\right)$$
$$+ \frac{\alpha I}{TC}\left(P_{tn1}(t) + P_{tn12}(t) + P_\gamma(t)\right) \tag{4.5}$$

$$\frac{d}{dt}\Delta I_2(t) = \frac{1}{C}\left(-\frac{\alpha P}{T}\Delta I_2 - (G + G_{12})\Delta I_2 + G_{12}\Delta I_1\right)$$
$$+ \frac{\alpha I}{TC}\left(P_{tn2}(t) - P_{tn12}(t) + P_\gamma(t)\right) \tag{4.6}$$

These equations can be rewritten in matrices as

$$\frac{d}{dt}\begin{pmatrix}\Delta I_1 \\ \Delta I_2\end{pmatrix} = \frac{1}{C}\begin{pmatrix}-\frac{\alpha P}{T} - G - G_{12} & G_{12} \\ G_{12} & -\frac{\alpha P}{T} - G - G_{12}\end{pmatrix}\begin{pmatrix}\Delta I_1 \\ \Delta I_2\end{pmatrix}$$
$$+ \frac{\alpha I}{TC}\begin{pmatrix}P_{tn1}(t) + P_{tn12}(t) + P_\gamma(t) \\ P_{tn2}(t) - P_{tn12}(t) + P_\gamma(t)\end{pmatrix} \tag{4.7}$$

We will disregard the noise terms until we move to the frequency domain. For now we have an equation of the form

$$\frac{d}{dt}\vec{I} = \mathbf{A}\vec{I} \tag{4.8}$$

where $\vec{I}$ is the current vector and $\mathbf{A}$ is the first matrix on the right hand side of Eq. (4.7). The time constants of this system are related to the eigenvalues λ_i of $\mathbf{A}$ by

$$\tau_i = -\frac{1}{\lambda_i} \tag{4.9}$$

Now we need to find the eigenvalues of matrix $\mathbf{A}$. This is where the algebra can quickly become overwhelming in complicated systems. With the aid of *Mathematica*, we can easily find the time constants to be:

$$\tau_{\text{eff}} = \frac{C/G}{1 + \frac{\alpha P}{TG}} \tag{4.10}$$

$$\tau_{\text{link}} = \frac{C/G}{1 + \frac{2G_{12}}{G} + \frac{\alpha P}{TG}} \tag{4.11}$$

where τ_{link} is the time constant of the link between the two TESs. Boyce and DiPrima (1986, sec. 7.8) describe how to create the time propagator matrix $\Phi(t)$ (also called the fundamental matrix), which maps the response of the system to any initial condition vector $\vec{I}(0)$ so that

$$\vec{I}(t) = \Phi(t)\vec{I}(0) \tag{4.12}$$

C	1.92	pJ/K
G	200	pW/K
G_{12}	6.25	nW/K
R	10	mΩ
T	75	mK
T_b	50	mK
α	90	
n	3.2	

Table 4.1: Parameters for analysis of two-pixel PoST

The propagator for our system is

$$\Phi(t) = \frac{1}{2} \begin{pmatrix} e^{-t/\tau_{\text{eff}}} + e^{-t/\tau_{\text{link}}} & e^{-t/\tau_{\text{link}}} \left(e^{2t/\tau_{12}} - 1 \right) \\ e^{-t/\tau_{\text{link}}} \left(e^{2t/\tau_{12}} - 1 \right) & e^{-t/\tau_{\text{eff}}} + e^{-t/\tau_{\text{link}}} \end{pmatrix} \tag{4.13}$$

where $\tau_{12} = C/G_{12}$.

We can now put in values for the parameters and plot the time evolution of the current as a photon hits the two pixel PoST. To keep the saturation condition of a maximum temperature excursion of 0.5 mK (Section 2.2.6), we choose a heat capacity for each TES of 1.92 pJ/K. The PoST has now twice the heat capacity of the single pixel TES, which means its resolution will *at best* be $\sqrt{2}$ worse than the single-pixel result from Section 2.3, but since photons will be hitting each TES, and assuming very rapid thermalization (instantaneous in our models), that is the value of heat capacity we need to use to keep the temperature of each TES from going up more that our fiducial half a milli-Kelvin. We will have more playroom when we do multiple-pixel PoSTs in Section 4.3.

Choosing the representative values shown in Table 4.1 for the constants we can plot the response of a 1 keV photon hitting TES1, shown in Figure 4.2. The signal from TES1 and TES2 converge at about the 0.5 ms mark and then decay exponentially toward zero, as shown in Figure 4.2(b). After 0.5 ms, the two signals are identical. But by looking at the relative pulse heights of the two TESs, one can determine in which of the TESs the photon was absorbed. This seems trivially simple in the two-pixel case, but of course we are just laying the groundwork to move from two to m pixels. The size of the conductance G_{12} determines when the two signals converge. By tuning G_{12} we will to be able to get position resolution in the many-pixel PoST models to come.

4.1.2   Two-pixel PoST analytic solution: phonon noise

Now that we have a time domain model and can plot the response for a particular value of G_{12}, we want to know what the thermodynamic or phonon noise associated with that link
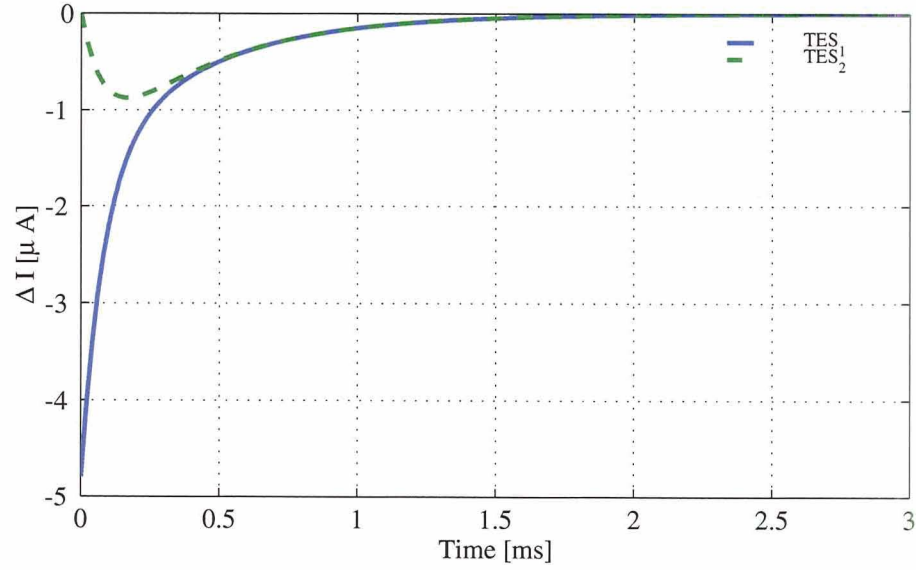
(a) PoST response in linear scale
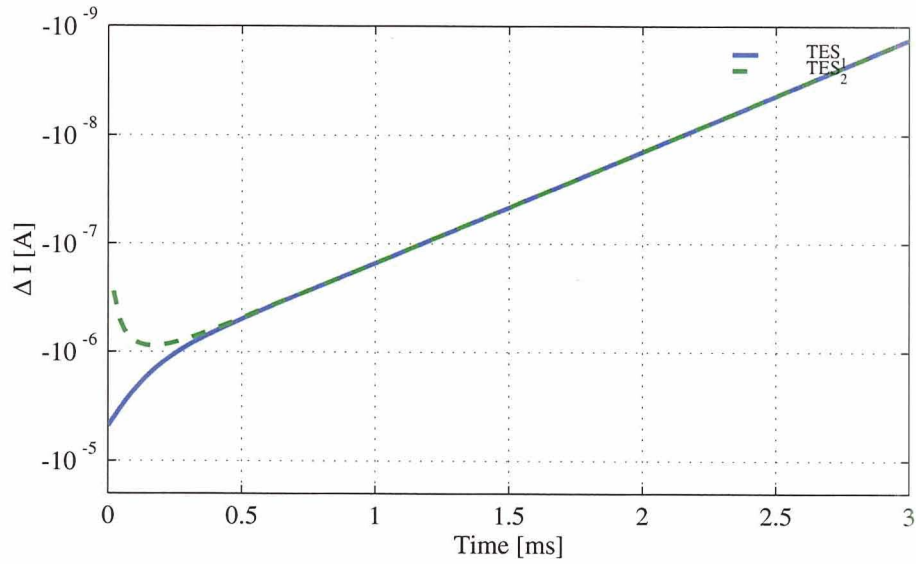
(b) PoST response in semi-log scale

Figure 4.2: Two-pixel PoST current response to a photon hitting TES1. Since there is no inductance, the current drops instantaneously on TES1. The two pixels thermalize and then proceed to cool down as a unit. Which pixel was hit can be easily determined by the respective pulse heights.

is. To do that we take the Fourier transform of Eq. (4.7) to obtain

$$\frac{T}{\alpha I}\begin{pmatrix} \frac{\alpha P}{T} + G + G_{12} + i\omega C & -G_{12} \\ -G_{12} & \frac{\alpha P}{T} + G + G_{12} + i\omega C \end{pmatrix}\begin{pmatrix} \Delta I_1 \\ \Delta I_2 \end{pmatrix} =$$
$$\begin{pmatrix} P_{\text{tn}1}(\omega) + P_{\text{tn}12}(\omega) + P_\gamma(\omega) \\ P_{\text{tn}2}(\omega) - P_{\text{tn}12}(\omega) + P_\gamma(\omega) \end{pmatrix} \quad (4.14)$$

which we can write as

$$\mathbf{M}\vec{\Delta} = \vec{N}_{\text{tot}} \quad (4.15)$$

with

$$\mathbf{M} = \frac{T}{\alpha I}\begin{pmatrix} \frac{\alpha P}{T} + G + G_{12} + i\omega C & -G_{12} \\ -G_{12} & \frac{\alpha P}{T} + G + G_{12} + i\omega C \end{pmatrix} \quad (4.16)$$

or

$$\vec{\Delta} = \mathbf{S}\vec{N}_{\text{tot}} \quad (4.17)$$

with

$$\mathbf{S} = \frac{\alpha I}{T}\begin{pmatrix} \frac{\alpha P}{T} + G + G_{12} + i\omega C & -G_{12} \\ -G_{12} & \frac{\alpha P}{T} + G + G_{12} + i\omega C \end{pmatrix}^{-1} \quad (4.18)$$

As we saw at the end of Section 3.2.1, when we have more than one heat capacity that can absorb the photon, and more than one way to read out the signal, we must define the general responsivity matrix given by Eq. (3.107), which we reproduce here:

$$\mathbf{S}_{k,i}(\omega) \equiv \frac{d\vec{\Delta}_k}{d\vec{N}_i} = \mathbf{M}_{k,i}^{-1} \quad (4.19)$$

In this case, we will want to know what the response is to a photon absorbed in TES1 as measured from TES1 and TES2. The same for absorption in TES2. The elements of this generalized responsivity matrix $\mathbf{S}$ will not only give us the current seen for a thermal input, but will give us the response of any of the variables[2] in $\vec{\Delta}$ to an input (photon or noise) to the system. The noise for a particular noise source $\vec{N}$ as seen in the element $\vec{\Delta}_k$ will be

$$\left\langle \left| \vec{\Delta}_k \right|^2 \right\rangle = \left\langle \left| \sum_j \mathbf{S}_{k,j}\vec{N}_j(\omega) \right|^2 \right\rangle \quad (4.20)$$

Since we assume our noise terms are uncorrelated, we treat them one at a time. The vector $\vec{N}$ will have only the terms for one noise source with all others set to zero. The noise

---

[2]The elements of $\vec{\Delta}$ are just the two currents ΔI_1 and ΔI_2 now, but in the next sections the vector $\vec{\Delta}$ will contain temperatures and voltages as well as currents.

will be computed using Eq. (4.20) for that noise source, and at the end all the terms will be added in quadrature to get the total noise. Considering link phonon noise, for example, $\vec{N} = (P_{\text{tn}12}(\omega), -P_{\text{tn}12}(\omega))$. The noise seen in TES$_1$ from the link phonon noise $P_{\text{tn}12}(\omega)$ will be

$$\left\langle \left|\vec{\Delta}_1\right|^2 \right\rangle = \left\langle |\Delta I_1|^2 \right\rangle = \left\langle \left|\sum_{j=1}^{2} \mathbf{S}_{1,j}\vec{N}_j\right|^2 \right\rangle = \left\langle \left|\mathbf{S}_{1,1}P_{\text{tn}12}(\omega) - \mathbf{S}_{1,2}P_{\text{tn}12}(\omega)\right|^2 \right\rangle \quad (4.21)$$

We use *Mathematica* to determine $\mathbf{S}$ analytically and solve Eq. (4.20) for the current noise due to each phonon term as seen by TES1:

$$\left\langle |\Delta I_{\text{tn}1}(\omega)|^2 \right\rangle = \left(\frac{\alpha P}{TG}\right)^2 \left(\frac{\tau_{\text{eff}}}{\tau_o}\right)^2 \frac{1}{1+\omega^2\tau_{\text{eff}}^2} \left(\frac{P_{\text{tn}1}(\omega)}{V}\right)^2 \left(\frac{\left(\frac{G_{12}}{G} + \frac{\tau_o}{\tau_{\text{eff}}}\right)^2 + \tau_o^2\omega^2}{\left(\frac{2G_{12}}{G} + \frac{\tau_o}{\tau_{\text{eff}}}\right)^2 + \tau_o^2\omega^2}\right)$$

$$(4.22)$$

$$\left\langle |\Delta I_{\text{tn}2}(\omega)|^2 \right\rangle = \left(\frac{\alpha P}{TG}\right)^2 \left(\frac{\tau_{\text{eff}}}{\tau_o}\right)^2 \frac{1}{1+\omega^2\tau_{\text{eff}}^2} \left(\frac{P_{\text{tn}2}(\omega)}{V}\right)^2 \left(\frac{G_{12}^2/G^2}{\left(\frac{2G_{12}}{G} + \frac{\tau_o}{\tau_{\text{eff}}}\right)^2 + \tau_o^2\omega^2}\right)$$

$$(4.23)$$

$$\left\langle |\Delta I_{\text{tn}12}(\omega)|^2 \right\rangle = \left(\frac{\alpha P}{TG}\right)^2 \left(\frac{\tau_{\text{link}}}{\tau_o}\right)^2 \frac{1}{1+\omega^2\tau_{\text{link}}^2} \left(\frac{P_{\text{tn}12}(\omega)}{V}\right)^2 \quad (4.24)$$

These are the theoretical thermal-noise equations for a two-pixel PoST in perfect voltage bias, with $\alpha_I = 0$. Comparing Eq. (4.22) to Eq. (3.41) we see the current noise $\Delta I_{\text{tn}1}$ seen on TES1 due to the thermal noise from itself is the the single pixel result times the terms in the last large parenthesis, which go to 1 as $G_{12} \to 0$ and to $1/4$ as $G_{12} \to \infty$. The same goes from $\Delta I_{\text{tn}2}$, except that the terms in the last parenthesis now go to zero as $G_{12} \to 0$, as expected. The link noise, Eq. (4.24), is structurally identical to Eq. (3.41), except for the change in time constant.

We expect the thermal noise from TES1 to look exactly like the single pixel case as $G_{12} \to 0$, because it *is* a single pixel at that point. $P_{\text{tn}12} = 0$ at $G_{12} = 0$, so we see the total thermal noise is equal to the theoretical single pixel at this limit.

As $G_{12} \to \infty$, the system becomes a single pixel calorimeter of heat capacity $2C$, conductance to the bath $2G$, and instrumented by two TESs in parallel with a total power $2P$, and total resistance $R/2$. The noise from the link goes to zero, since $\tau_{\text{link}} \to 0$ in this limit.

Figure 4.3: Legend for noise and NEP plots for PoSTs. Generally, solid lines imply total response, while non-solid lines are the individual components. Blue triangles are thermal noise. Red dashed lines are link noise. Green markers are detector and circuit voltage noise terms. In this thesis green markers are Johnson noise of some resistor (load or detector). Thin gray lines are the theoretical response at some limit, for example as $G_{12} \to 0$, or at a specific operating point. For NEP plots, substitute 'noise' for 'NEP.'

We define the root-mean-square noise (RMS) for current in $\mathrm{Amps}/\sqrt{\mathrm{Hz}}$:

$$\Delta I_{\mathrm{rms}} = \sqrt{\left\langle |\Delta I|^2 \right\rangle} \tag{4.25}$$

The RMS noise for a two-pixel post thus converges to the single-pixel value as $G_{12} \to 0$ and to $1/\sqrt{2}$ of this value as $G_{12} \to \infty$. This last result comes from the fact that in the $G_{12} \to \infty$ limit, the PoST acts like a single pixel device, and our equations are only reading out half the current in it (just one side).

Now we can use the values in our time-domain example from Table 4.1 and plot the RMS current noise we expect to see on top of the perfect pulses of Figure 4.2. We will be plotting many noise spectra, so in Figure 4.3 we specify what our convention will be. This legend will be valid for all noise plots and NEP plots. The spectrum for the values on Table 4.1 is shown in Figure 4.4. We see three noise sources: the two phonon noise terms from TES1 to bath and TES2 to bath, and the link noise. The link noise dominates the spectrum, and the total noise is essentially due to the link. In Section 4.2 we study the dependence of the noise on the value of G_{12}.

The next question to be answered is what is the theoretical resolution of this device. To answer that question, we need to add all the noise terms to the model. This is what we will do in the following section.
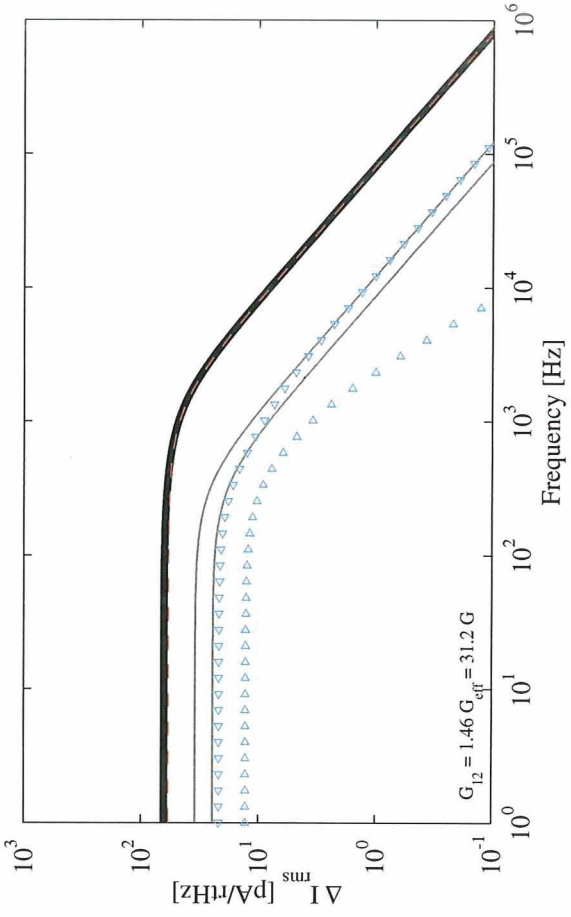
Figure 4.4: RMS current noise for one TES of a two-pixel PoST using values from Table 4.1. The noise is dominated by the link noise. The legend is Figure 4.3. The upper gray line is the theoretical noise for the $G_{12} \to 0$ limit, and the lower gray line is the $G_{12} \to \infty$ limit.

4.1.3 Two-pixel PoST with all noise terms

To get energy resolution, we need to include all the sources of noise. This at minimum includes phonon noise from all three sources (two TESs-bath links and the TES-TES link) plus Johnson noise from the TESs and Johnson noise from the load resistors (if present). To solve this problem we will set up the equations, and then solve them numerically. This will allow us to calculate quantities of interest for much more complicated PoSTs than is practical with analytic solutions. We begin with the equations for the system:

$$L\frac{dI_1(t)}{dt} = V_{\text{bias}} - I_1(t)\big(R_{\text{L1}} + R(T_1, I_1)\big) - V_{\text{dn1}}(t) + V_{\text{cn1}}(t) \tag{4.26}$$

$$C(T)\frac{dT_1(t)}{dt} = I_1(t)^2 R(T_1, I_1) - K\big(T_1(t)^n - T_{\text{b}}^n\big) - K_{12}\big(T_1^{n_{12}}(t) - T_2^{n_{12}}(t)\big) \\ + P_{\text{tn1}}(t) + P_{\text{tn12}}(t) + I_1(t)V_{\text{dn1}}(t) \tag{4.27}$$

$$C(T)\frac{dT_2(t)}{dt} = I_2(t)^2 R(T_2, I_2) - K\big(T_2(t)^n - T_{\text{b}}^n\big) - K_{12}\big(T_2^{n_{12}}(t) - T_1^{n_{12}}(t)\big) \\ + P_{\text{tn2}}(t) - P_{\text{tn12}}(t) + I_2(t)V_{\text{dn2}}(t) \tag{4.28}$$

$$L\frac{dI_2(t)}{dt} = V_{\text{bias}} - I_2(t)\big(R_{\text{L2}} + R(T_2, I_2)\big) - V_{\text{dn2}}(t) + V_{\text{cn2}}(t) \tag{4.29}$$

These are the same as Eq. (4.5) and Eq. (4.6), with the addition of the detector noise and circuit noise terms and inductance in the circuits, which decouple temperature and current so we now need four equations instead of two.

C	1.92	pJ/K
G	200	pW/K
G_{12}	6.25	nW/K
R	10	mΩ
R_{L}	1	mΩ
L	100	nH
T	75	mK
T_{b}	50	mK
α	90	
α_{I}	~ 0	
n	3.2	

Table **4.2**: Representative parameters for analysis of two-pixel PoST numerical model.

We follow our linearization procedure, take the Fourier transform, and put in matrix notation:

$$
\begin{pmatrix}
R(1+\alpha_{\mathrm{I}})+R_{\mathrm{L}1}+i\omega L & \frac{\alpha V}{T} & 0 & 0 \\
-(2+\alpha_{\mathrm{I}})V & G+G_{12}+i\omega C & -G_{12} & 0 \\
0 & -G_{12} & G+G_{12}+i\omega C & -(2+\alpha_{\mathrm{I}})V \\
0 & 0 & \frac{\alpha V}{T} & R(1+\alpha_{\mathrm{I}})+R_{\mathrm{L}2}+i\omega L
\end{pmatrix}
$$

$$
\times
\begin{pmatrix}
\Delta I_1 \\
\Delta T_1 \\
\Delta T_2 \\
\Delta I_2
\end{pmatrix}
=
\begin{pmatrix}
V_{\mathrm{dn}1}(\omega)+V_{\mathrm{cn}1}(\omega) \\
IV_{\mathrm{dn}1}(\omega)+P_{\mathrm{tn}1}(\omega)+P_{\mathrm{tn}12}(\omega) \\
IV_{\mathrm{dn}2}(\omega)+P_{\mathrm{tn}2}(\omega)+-P_{\mathrm{tn}12}(\omega) \\
V_{\mathrm{dn}2}(\omega)+V_{\mathrm{cn}2}(\omega)
\end{pmatrix}
\quad (4.30)
$$

Now, we can define the constants for this second model, which includes inductances, load resistors, and $\alpha_{\mathrm{I}} \neq 0$. We show the parameters we will be working with in Table 4.2.

To solve this matrix, we apply Eq. (4.15) and Eq. (4.20), and numerically calculate **S** and ΔI_{rms} for each frequency to generate the plot on Figure 4.5. For this figure we have set the load resistor to zero, which puts the device in perfect voltage bias, and sets the circuit noise to zero (since we are considering load resistor Johnson noise as the only circuit noise component for this example). The inductor has also been set to zero, to see the intrinsic high frequency behavior. The noise is still dominated by the link noise at lower frequencies, and by Johnson noise from TES1 at higher frequencies. The Johnson noise from TES2 couples only through the thermal system, so it has the same shape as the thermal noise. The upper gray line is the theoretical noise for the $G_{12} \to 0$ limit, and the lower gray line is the $G_{12} \to \infty$ limit. Comparing to Figure 4.4, we see the low frequency noise has not been affected too much by the addition of the Johnson noise from the detector.

In Figure 4.6 we plot the noise for all the numbers on Table 4.2. Now we have the noise from the load resistors. The noise is still dominated by the link noise at lower frequencies, and by Johnson noise from TES1 at higher frequencies. The noise from $R_{\mathrm{L}2}$ couples to TES1 only through the thermal system, and so has the same shape as the thermal noise
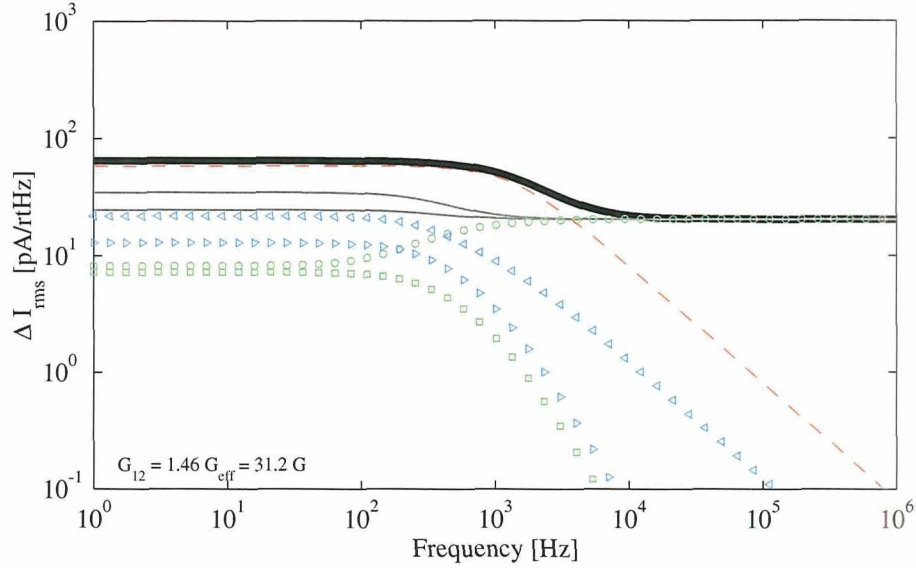
Figure 4.5: RMS current noise for one TES of a two-pixel PoST using values from Table 4.2, but with $R_L = 0$ and $L = 0$. The noise is still dominated by the link noise at lower frequencies, and by Johnson noise from TES1 at higher frequencies. The Johnson noise from TES2 couples only through the thermal system, so it has the same shape as the thermal noise. The upper gray line is the theoretical noise for the $G_{12} \to 0$ limit, and the lower gray line is the $G_{12} \to \infty$ limit. The legend is Figure 4.3.

terms.

Figure 4.6(b) shows two important effects of the fact that R_L is similar in size to R. Including the load resistors and α_I means the time constant of the device is given by Eq. (3.19). This means $\tau_{\text{eff}} \to \tau_o$ as $R_L \to R$. Comparing Figure 4.6(a) to Figure 4.6(b) we see the roll-off of the phonon noise occurs at a much lower frequency for the larger R_L case. The gain[3] in Eq. (4.22) depends on τ_{eff}/τ_o, so we expect the gain to increase as $R_L \to R$. Note the low-frequency level of the phonon noise on Figure 4.6(a) and compare it to the level in Figure 4.6(b).

From Eq. (4.24), we see the link phonon noise gain is a function of $\tau_{\text{link}}/\tau_o$. Doing the same analysis we did in Section 4.1.1, we can find the time constant for the link when $R_L \neq 0$ and $\alpha_I \neq 0$ to be

$$\tau_{\text{link}} = \frac{\tau_o}{1 + \frac{2G_{12}}{G} + \frac{\alpha P}{TG}\frac{1-\frac{R_L}{R}}{1+\alpha_I+\frac{R_L}{R}}} \tag{4.31}$$

We note that

$$\lim_{G_{12}\to\infty} \tau_{\text{link}} = \frac{C}{2G_{12}} \tag{4.32}$$

---

[3]By gain we mean the overall RMS level of the noise. We can also think of it as the level the noise goes to in the low frequency limit.
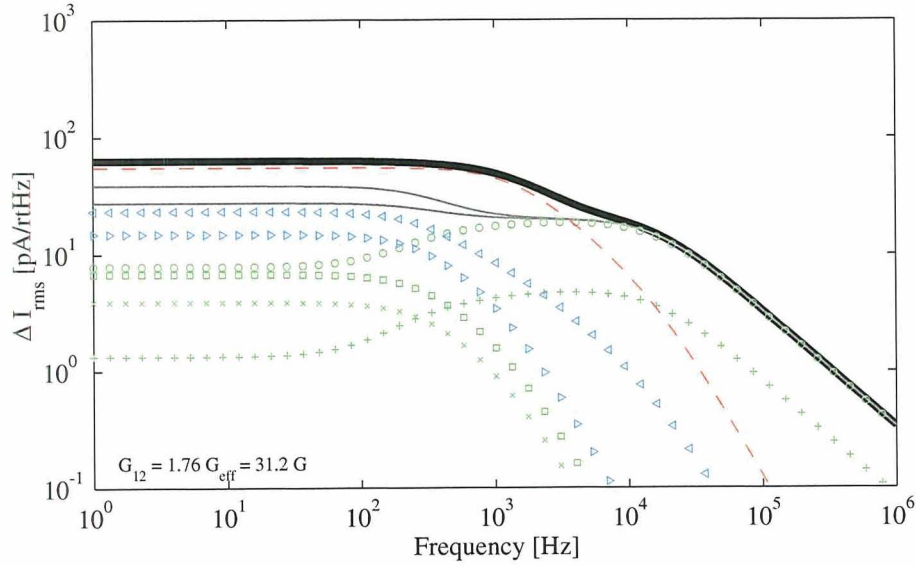
(a) Noise with $R_L = 1$ mΩ, $L = 0$
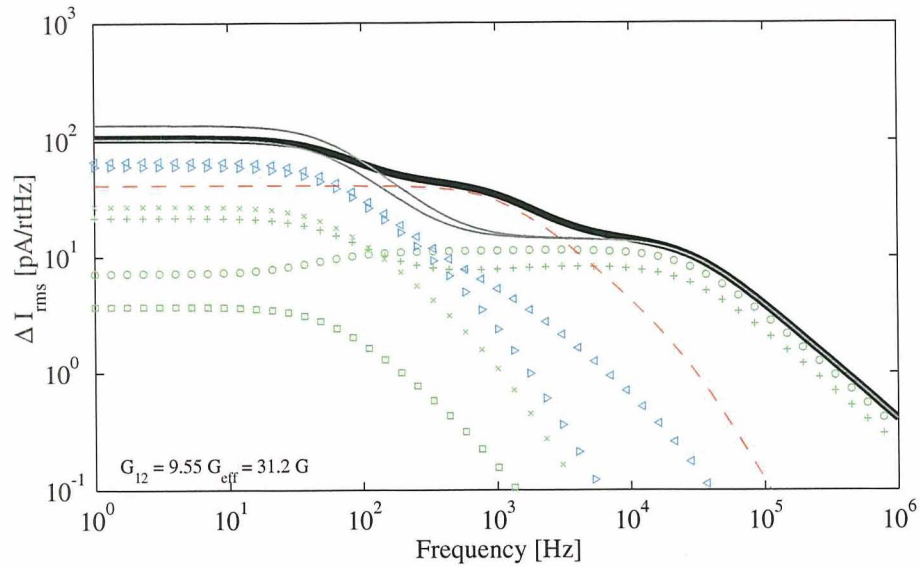
(b) Noise with $R_L = 8$ mΩ, $L = 100$ nH. The larger R_L lowers the amount of negative ETF, and thus there is less suppression at lower frequencies.

Figure 4.6: RMS current noise for one TES of a two-pixel PoST using values from Table 4.2. The roll off at high frequencies is due to the non-zero inductance. The upper gray line is the theoretical noise for the $G_{12} \to 0$ limit, and the lower gray line is the $G_{12} \to \infty$ limit. The legend is Figure 4.3.

which is independent of α or R_L or τ_{eff}. This implies that for $G_{12} \gg \frac{\alpha P(R-R_L)}{2T(R+\alpha_I R + R_L)} = G_{\text{ETF}}/2$, the link time constant and noise gain do not change with R_L or α. Comparing Figure 4.6(a) and Figure 4.6(b) we see the link noise changes by a much smaller amount both in gain and in roll-off frequency than the phonon noise.

With some more help from *Mathematica*, we can prove that Eq. (4.24) is valid for the system with $R_L \neq 0$ and $\alpha_I \neq 0$ when τ_{link} is defined by Eq. (4.31).

What if the load resistors are different? In this case neither Eq. (4.24) or Eq. (4.31) hold. We can at least look at the zero frequency case, with $\alpha_I = 0$, and after some hard work arrive at

$$\left\langle |\Delta I_{\text{tn}12}(0)|^2 \right\rangle = \left(\frac{P_{12}(\omega)}{V} \right)^2 \left(\frac{\alpha P}{TG} \right)^2$$

$$\times \frac{\left(1 + \frac{\alpha P}{TG} \frac{R - R_{L2}}{R + R_{L2}} \right)^2}{\left(1 + \frac{2G_{12}}{G} + 2\frac{\alpha P}{TG} \frac{R^2 - R_{L1}R_{L2}}{(R+R_{L1})(R+R_{L2})} + \left(\frac{\alpha P}{TG} \right)^2 \frac{(R-R_{L1})(R-R_{L2})}{(R+R_{L1})(R+R_{L2})} \right)^2} \quad (4.33)$$

This equation is fairly complicated; a graphical analysis will prove much more insightful. We will look at this and the general behavior of link phonon noise more detail in Section 4.2.2.

4.1.4 Two-pixel PoST NEP and ΔE

We are now in a position to calculate the NEP and energy resolution for this detector. We will calculate the NEP for each term separately; the total is just the quadrature sum of the individual terms. The vector $\vec{N}_{\text{tot}}$ contains all of our noise sources. Looking at Eq. (4.30) we see that some noise sources ($V_{\text{dn}}(\omega)$, for example) appear in more that one place in the vector $\vec{N}_{\text{tot}}$. To calculate the NEP for one noise source, we temporarily disregard all other noise sources; the vector $\vec{N}$ is only composed of the terms from the noise source of interest, just like we did when calculating the RMS current noise. Then extending Eq. (3.63) we find the general form for the NEP of a particular noise source $\vec{N}$ for readout k and assuming a power[4] input at element i:

$$\text{NEP}_{k,i}(\omega) = \left| \frac{1}{\mathbf{S}_{k,i}} \sum_j \frac{d\vec{\Delta}_k}{d\vec{N}_j} \vec{N}_j \right| = \left| \frac{1}{\mathbf{S}_{k,i}} \sum_j \mathbf{S}_{k,j} \vec{N}_j \right| \quad (4.34)$$

---

[4]Remember from Section 3.1.5 that the NEP is referred to some input; in our case we have two heat capacities where thermal power can be deposited. These are rows 2 and 3 in our matrix equation (Eq. (4.30)), so i can have the value of 2 (for power into TES1) or 3 (for power into TES2).

For example, the NEP for detector noise in TES2, read out by TES1, assuming power input to TES1 would be

$$
\vec{N} = \begin{pmatrix} 0 \\ 0 \\ IV_{\text{dn2}} \\ V_{\text{dn2}} \end{pmatrix}
\tag{4.35}
$$

$$
\text{NEP}_{1,2}(\omega) = \left| \frac{1}{\mathbf{S}_{1,2}} \sum_{j=1}^{4} \frac{d\vec{\Delta}_1}{d\vec{N}_j} \vec{N}_j \right| = \left| \frac{1}{\mathbf{S}_{1,2}} \left(\frac{d\vec{\Delta}_1}{d\vec{N}_3} IV_{\text{dn2}} + \frac{d\vec{\Delta}_1}{d\vec{N}_4} V_{\text{dn2}} \right) \right|
\tag{4.36}
$$

$$
= \left| \frac{1}{\mathbf{S}_{1,2}} \left(\mathbf{S}_{1,3} V_{\text{dn2}} + \mathbf{S}_{1,4} IV_{\text{dn2}} \right) \right|
\tag{4.37}
$$

The subscripts in $\text{NEP}_{1,2}$ indicate current readout in TES1 (which is row 1 in Eq. (4.30)), referenced to a power input in the electron system of TES1 (row 2 in Eq. (4.30)). Another example: the link noise term would have the following NEP for TES1 readout and power input into the electron system of TES2:

$$
\text{NEP}_{1,3}(\omega) = \left| \frac{1}{\mathbf{S}_{1,3}} \left(\frac{d\vec{\Delta}_1}{d\vec{N}_2} P_{12} - \frac{d\vec{\Delta}_1}{d\vec{N}_3} P_{12} \right) \right| = \left| \frac{\mathbf{S}_{1,2}}{\mathbf{S}_{1,3}} P_{12} - P_{12} \right|
\tag{4.38}
$$

The total NEP is the quadrature sum of all the individual noise sources.

Once we have the total NEP, it is a simple task to numerically integrate Eq. (3.68) to obtain the ΔE_{FWHM} of the detector when reading just one TES. The NEP for a two-pixel PoST using the values on Table 4.2 is shown in Figure 4.7. The quoted resolution is from integrating the NEP numerically. For comparison, at $G_{12} = 0$ we get the single pixel resolution of 1.64 eV, which is the resolution for a 1.92 pJ/K single TES with other parameters per Table 4.2 (see Section 3.1.6). The resolution of a single-pixel TES with a heat capacity of 3.84 pJ/K (the total heat capacity of this PoST) is 2.32 eV. This is the energy resolution of our PoST as $G_{12} \to \infty$, and is the best resolution a calorimeter with these parameters could obtain. We are 57% higher than the theoretical limit for this device. We will look at the effects of different parameters on the resolution in Section 4.2. Remember at this point we are still ignoring the other TES, which we will consider in Section 4.5.

One word of caution: the integral in Eq. (3.68) is from 0 to ∞, yet we integrate over a discrete bandpass. This actually means that the theoretical energy resolution will be better than what we calculate, since the integral in Eq. (3.68) is smaller for larger integration ranges. Since when we take data, we are limited to a specific bandpass, as long as we do our numerical integrals over a larger bandpass than our data we will have an accurate number. We also must be careful with the low frequencies, since we must assume the lowest frequency we use for the integral is representative of the NEP for frequencies from there down to zero. In the case of 1/f noise, for example, this is not the case, and we must go to
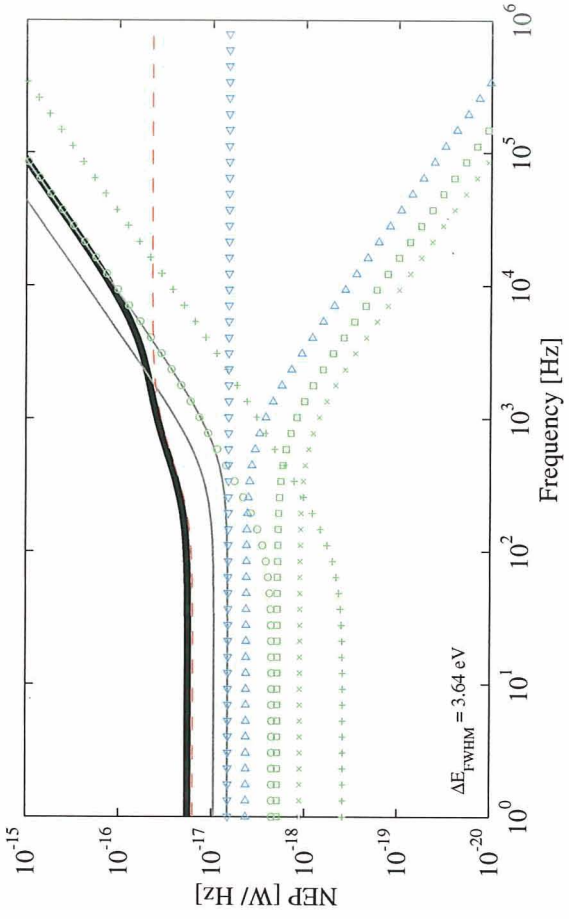
Figure 4.7: NEP for two-pixel PoST using values from Table 4.2.   The resolution is calculated by integrating Eq. (3.68). The upper gray line is the theoretical NEP for the $G_{12} \rightarrow \infty$ limit, and the lower gray line is the $G_{12} \rightarrow 0$ limit.   The legend is Figure 4.3 on page 74.

low enough frequencies where the NEP is large so those frequencies have a negligible impact on the energy resolution.

4.2   Turning the knobs: a detailed look at PoST noise theory

This section delves into some details of PoST behavior. Feel free to skip to Section 4.3.

Before we move on the full PoST theory with many pixels, we want to take a closer look at the two-pixel PoST theory to get some intuition into the behavior of a PoST as a function of various parameters. We will look at models where we vary one parameter and study the effects of variations on the noise and resolution of the device.

For all the following figures we have set the inductance of the devices to zero. The inductance just rolls off the signal at high frequency and does not change the resolution (since it equally rolls the signal and noise). Zero inductance plots show the inherent PoST behavior, which is what we are interested in right now. When fitting data, we will fit with the appropriate inductor value.

4.2.1   Turning the knob on G_{12}

The first parameter we will study is, of course, the link conductance G_{12}, keeping other parameters per Table 4.2. We want to know how does the total noise scale with the value of G_{12}. Figure 4.8 shows the RMS noise for eight different values of G_{12}. We have only shown the three phonon noise terms: TES1 to bath phonon noise ($\lhd$), TES2 to bath phonon noise ($\rhd$), and link phonon noise (--). The legend for this and the following figures is in Figure 4.3 on page 74. The thin gray lines are the theoretical PoST noise limits as $G_{12} \rightarrow 0$ (upper line, same as single-pixel TES), and as $G_{12} \rightarrow \infty$ (lower line). In the first panel, $G_{12} = 0.001G$, and the total noise is close to the theoretical single-pixel value. The link noise is small, but smaller still is the phonon noise from TES2, which is below the axis shown on the figure. This is the expected behavior; as $G_{12} \rightarrow 0$, we expect no noise from TES2 or the link to be seen by TES1. As we increase the value of G_{12}, we see the noise from the link become the dominant term, and the phonon noise from TES2 becomes comparable and then equal to the phonon noise from TES1.

An obvious question to ask is at what value of G_{12} the link noise component is maximum (where we define noise levels with their zero frequency values). In Section 2.2.4 we introduced the quantity $G_{\text{eff}} = G + G_{\text{ETF}}$, where G_{ETF} for our device includes the load resistor and α_I effects as defined by Eq. (3.22). Looking at the expression for link noise in the two-pixel PoST (Eq. (4.24)), we note that the zero-frequency value depends on G_{12} by the expression $P_{12}^2 \tau_{\text{link}}^2 / \tau_o^2$. Assuming $P_{12}^2 \propto G_{12}$, and using the definition of τ_{link} from Eq. (4.31), we can find the maximum noise to occur when

$$G_{12} = \frac{G}{2}\frac{\tau_o}{\tau_{\text{eff}}} = \frac{G_{\text{eff}}}{2} \quad \text{(Condition for maximum link phonon noise)} \quad (4.39)$$

As the value of G_{12} becomes much greater than G_{eff}, the noise from the link gets spread over a larger and larger frequency, becoming a negligible term as $G_{12} \rightarrow \infty$.

For large values of G_{12}, the two TES phonon noise terms are almost identical at low frequencies (the two triangles form a star when on top of each other). From the last four panes we can see the separation point of the two TES phonon noise terms related to the
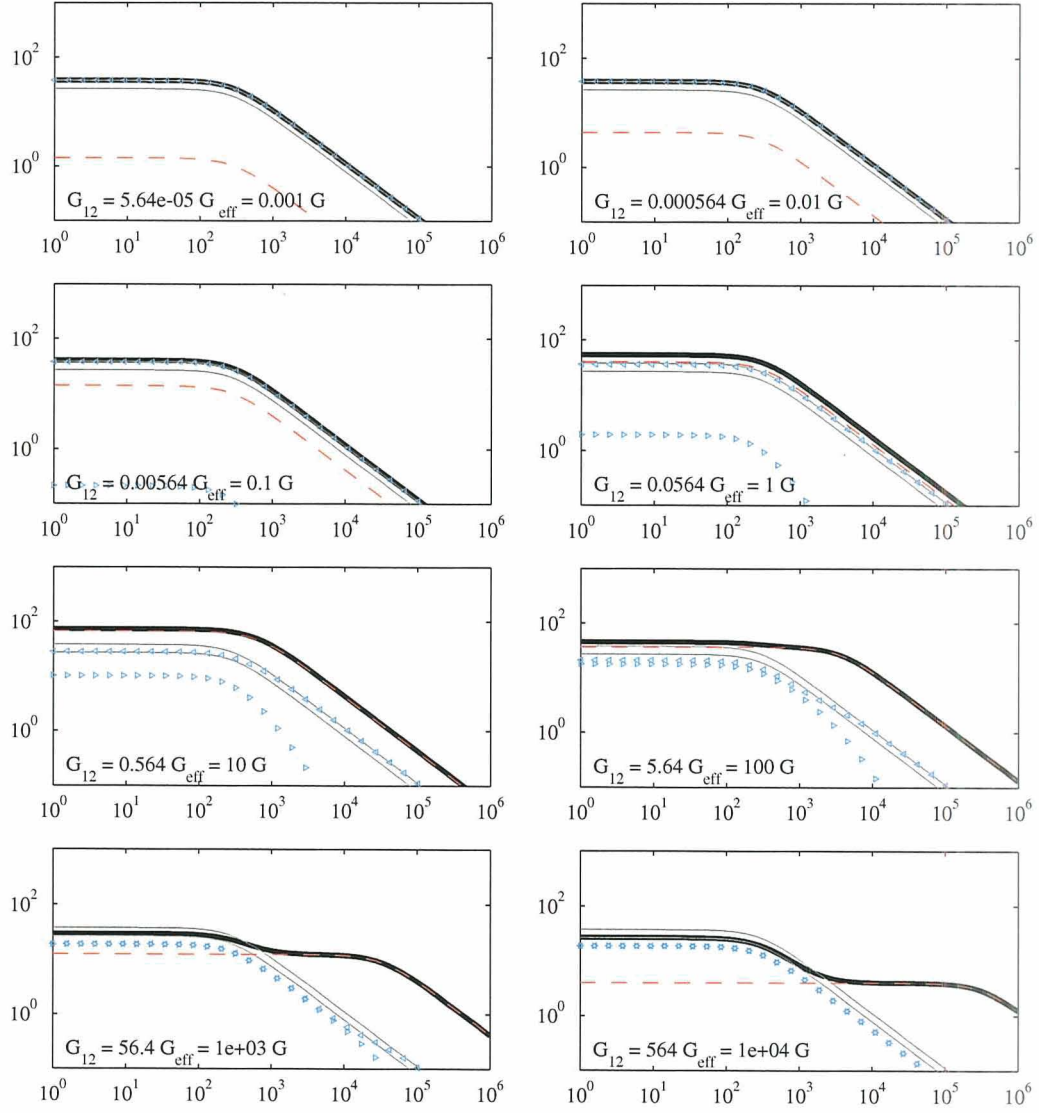
Figure 4.8: Theoretical phonon noise for a 2-pixel PoST vs. the link conductance G_{12}. The two thin gray lines are the theoretical limits of the 2-pixel PoST. The top gray line is the single pixel result, which should be the limit as $G_{12} \rightarrow 0$. The lower gray line is $1/\sqrt{2}$ lower than the top line, and should be the limit as $G_{12} \rightarrow \infty$. The legend is in Figure 4.3 on page 74. The X-axis is frequency in Hz, and the Y-axis is RMS current noise in pA/$\sqrt{\text{Hz}}$.

roll-off frequency of the link noise, $1/\tau_{link}$. As this roll-off frequency is approached, the signal from TES2 gets filtered, since at these frequencies heat can no longer freely move from one side to the other. One gets this characteristic "zipper" effect between the two TES noise terms. Note that for large G_{12}, at frequencies higher than $\sim 1/\tau_{link}$ the noise from TES1 goes back up to the single pixel level (notably in the $G_{12} = 10$ and $100G$ panes). At these high frequencies, above the link roll-off, the two TESs stop communicating to each other, and each TES acts as a single-pixel TES.

In Figure 4.9 we plot the same detector model, but now throw in all our noise terms: three phonon noise terms, Johnson noise from both detectors, and Johnson noise from both load resistors. The general behavior is the same, but now we have many more lines to play with.

Let us begin by looking at the detector Johnson noise in the $G_{12} \to 0$ single pixel limit for TES1 (○) and TES2 (□). Johnson noise is assumed to be a white voltage noise on the detector. We see the characteristic drop in Johnson noise at frequencies below $\sim 1/\tau_{eff}$ due to ETF suppression. The noise from TES2's Johnson noise is highly suppressed by the low value of G_{12}, so low it does not appear on the first plots. As we increase the link conductance, the Johnson noise term from TES2 increases, and we see it has the shape of a thermal noise, which we expect since it only couples to TES1 through the thermal system.

The circuit noise for TES1 (+) is slightly suppressed by ETF in-band. We see that in band the load resistor noise is higher than the detector noise. As G_{12} gets bigger, the Johnson noise from the load resistor of TES2 (×) comes into view, again with a thermal spectrum.

By studying Figure 4.9 we can begin to get a feeling for how different noise sources react to a change in G_{12}. What we want to know is what the resolution of the device is as a function of G_{12}. Calculating the NEP as we did in Section 4.1.4, we then numerically integrate to get the resolutions shown in Figures 4.10 and 4.11.

The NEP is defined for a specific input in the system; we have two. We must specify which TES we are assuming absorbs the photon, to then calculate the resolution we would get by analyzing the signal from TES1. Note that at this point we are *not* trying to combine the signals from TES1 and TES2 to try to get a better signal-to-noise ratio. We will do this in Section 4.5.

On Figure 4.10 the photon is assumed to be absorbed in TES1. The theoretical energy resolution goes to the single-pixel level when $G_{12} \sim 0$, and starts approaching the $2C$ single-pixel resolution of 2.32 eV as G_{12} becomes large. The worst the resolution gets is a factor of around 2 worse than the single pixel limit. One very interesting thing to note is that although the largest low frequency noise on G_{12} per Eq. (4.39) between $G_{12} = 1G$ and $G_{12} = 10G$, the worst resolution occurs near $G_{12} = 100G$. This is an important point: the resolution is not dictated by the low frequency noise level, but by the overall signal to noise.

Now we look at the energy resolution and NEP for photons hitting TES2 while still only reading out TES1. Figure 4.11 tells the very interesting story. We immediately see why we want large G_{12}: at low link conductance, very little information comes through the link, and our resolution suffers accordingly. In the first two plots the total NEP is above the range shown. The resolution increases very rapidly as G_{12} becomes comparable to G_{eff},
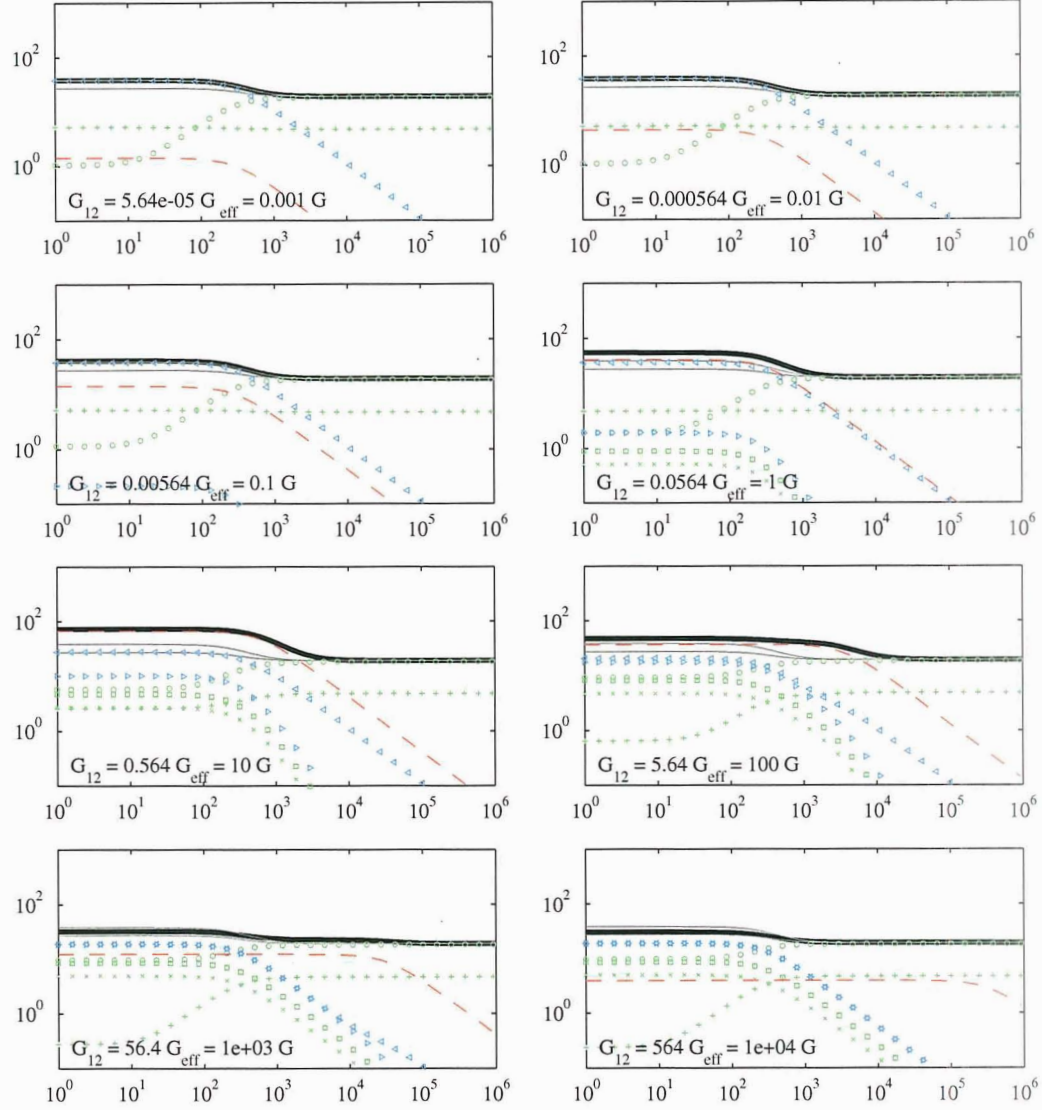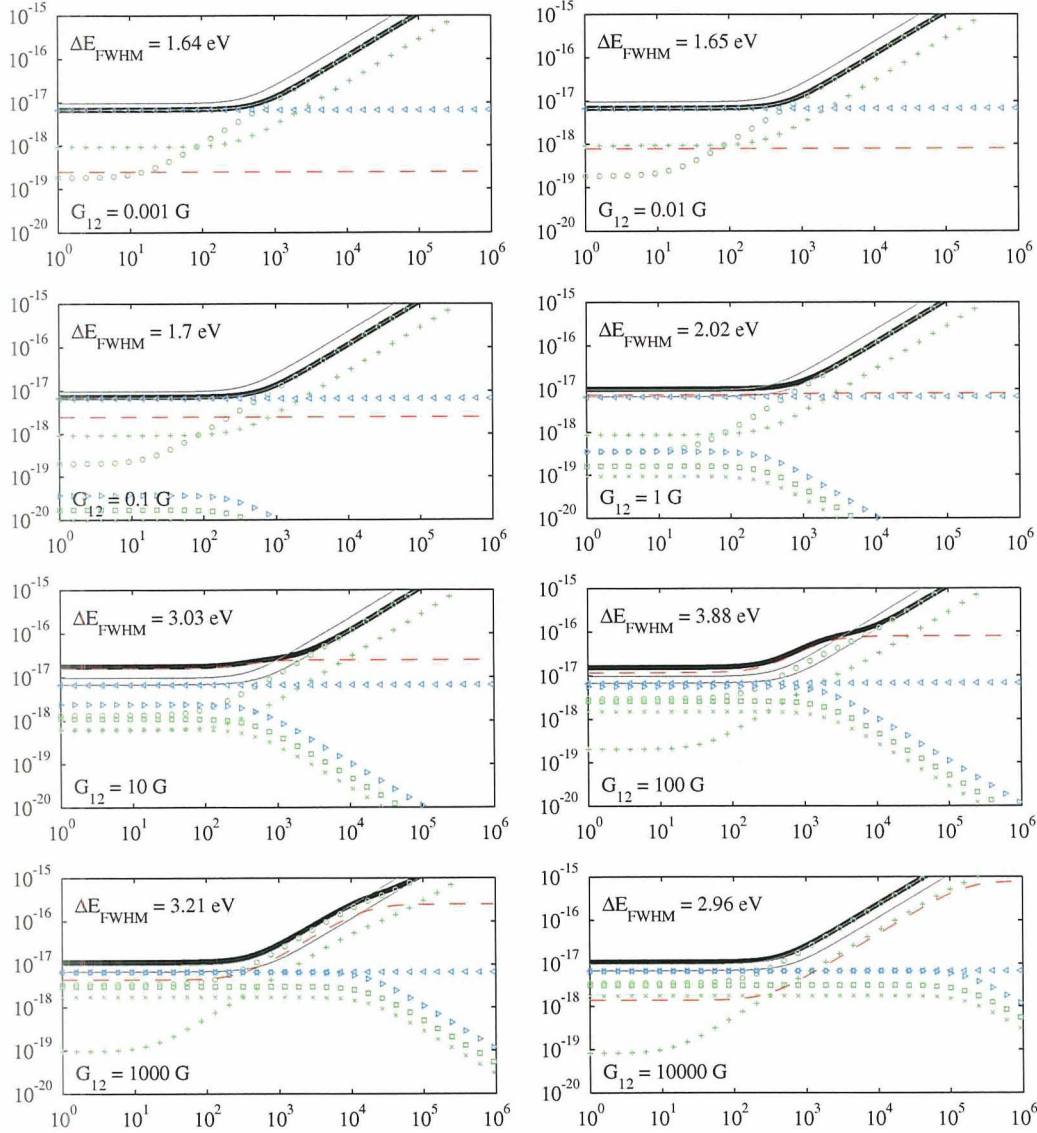
Figure 4.9: Theoretical noise for a 2-pixel PoST vs. the link conductance G_{12} (all noise terms present). The two thin gray lines are the theoretical limits of the 2-pixel PoST. The top gray line is the single pixel result, which should be the limit as $G_{12} \to 0$. The lower gray line is $1/\sqrt{2}$ lower than the top line, and should be the limit as $G_{12} \to \infty$. The legend is in Figure 4.3 on page 74. The X-axis is frequency in Hz, and the Y-axis is RMS current noise in pA/$\sqrt{\text{Hz}}$. Parameters are in Table 4.2.

Figure 4.10: Theoretical NEP for a 2-pixel PoST vs. the link conductance G_{12}. The signal is coming into TES1. The two thin gray lines are the theoretical limits of the 2-pixel PoST. The lower gray line is the single pixel result, which is the limit as $G_{12} \to 0$. The upper gray line is the limit as $G_{12} \to \infty$. The legend is in Figure 4.3 on page 74. The X-axis is frequency in Hz, and the Y-axis is NEP in $W/\sqrt{Hz}$. Parameters are in Table 4.2.
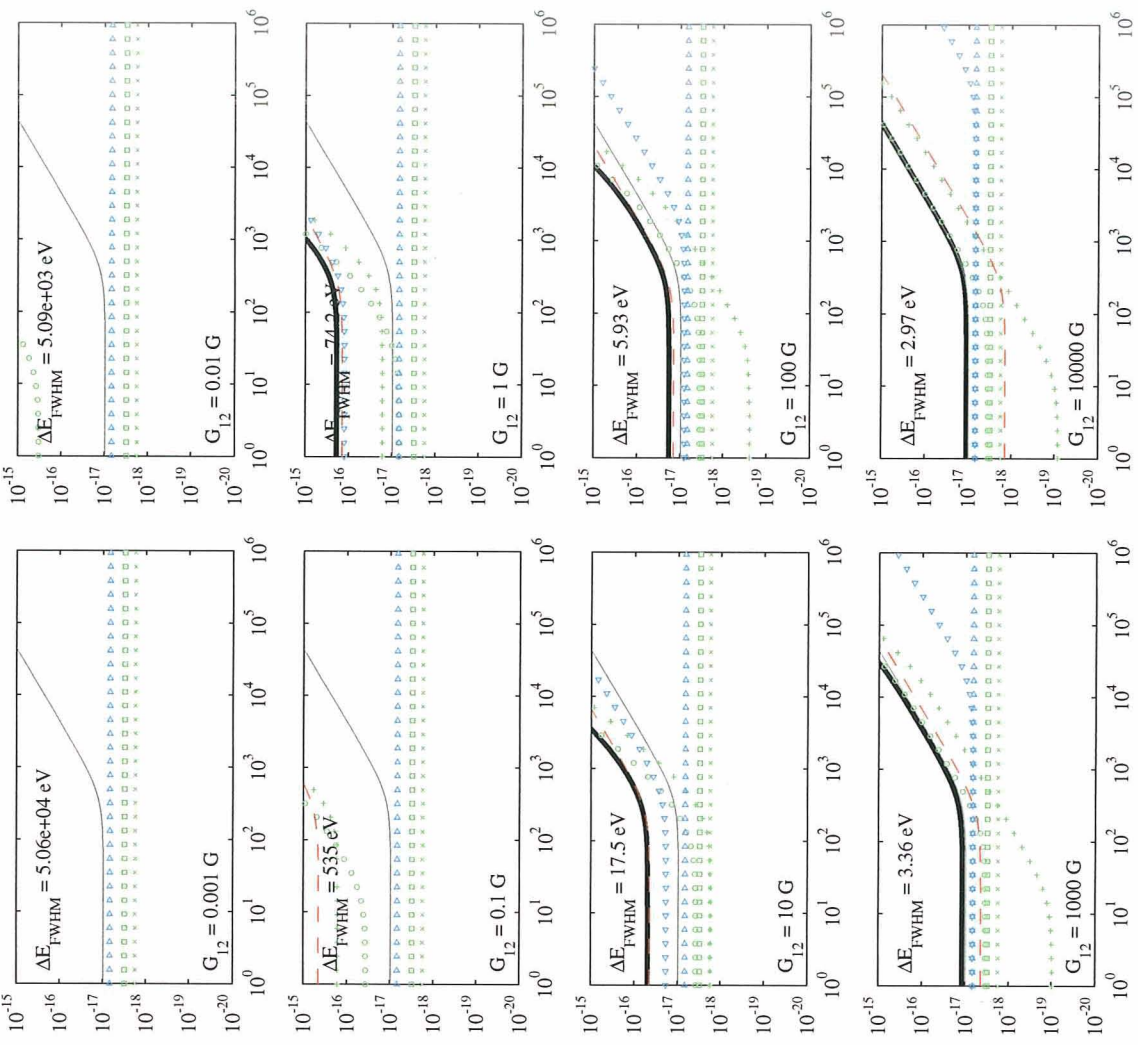
Figure 4.11: Theoretical NEP for a 2-pixel PoST vs. the link conductance G_{12} when the signal is coming into TES2. The thin gray line is the theoretical limit as $G_{12} \rightarrow \infty$. At $G_{12} = 0$, the NEP $= \infty$ since we are looking at TES2 from TES1. The legend is in Figure 4.3 on page 74. The X-axis is frequency in Hz, and the Y-axis is NEP in $W/\sqrt{Hz}$.

and at high G_{12} the resolution for photons hitting TES2 is the same as for photons hitting TES1 while reading out only TES1. This means the link conductance is so big that the PoST is starting to act as a single pixel, and it does not matter where the photon hits, the signal is the same. Of course at this limit one loses the position resolution; one has to play the game between position resolution and energy resolution to come up with the right answer for the specific application.

Flan de queso (cheese flan). One 8 oz. bar of cream cheese. One can of condensed milk (Carnation is what I always get). One can of evaporated milk. Three eggs lightly beaten. One capful of vanilla extract. Sugar for the caramel. Directions: First make the caramel. In a pan, put a small amount of water, medium heat, and pour sugar in while beating. Melt sugar to dark brown (I like my caramel dark, its up to you). Pour into the mold for the flan, turning the mold to cover up the wall with caramel. Cake molds with a hole in the middle work quite well. Keep turning the mold until the caramel hardens and you get a fair coat around the mold. Now for the flan. Put all ingredients in a blender, whip up good and pour in mold. Place mold in a double boiler (a pot with boiling water will do, I have a pot that fits great around my mold, and the mold handles keep it from falling in. Watch the water level, don't let the thing dry up. After about 45 minutes start checking the consistency with a knife. Take mold out of boiler when knife comes out clean (about an hour). (There is some experimenting to do here, also personal taste. I like my flan soft, so I usually under do it. If you leave the flan a little longer, it will have the consistency of cheese cake.) Let it cool at room temperature (it will continue to harden) for at least 45 minutes (better if you wait longer) and then chill in the refrigerator. Enjoy!

4.2.2 Turning the knob on R_L: ETF and signal-to-noise in a PoST

Now we focus our attention on the load resistors. By changing the value of the load resistors, we can change the ETF time constant τ_{ETF} and ETF conductance G_{ETF} (Eq.(3.22)) on each TES separately and see the interesting implications of this. We therefore change the matrix in Eq. (4.30) to include separate load resistors R_{L1} and R_{L2}. Here's where the power of numerical solutions really comes into its own. Numerically there is no penalty for making this change in the matrix, but the algebraic solution when the load resistors are not equal is much, much more complicated.

We plot out various cases in Figure 4.12. As before, the values for other parameters are in Table 4.2, and inductance is zero. We will disregard the load resistor noise, since we want to see the effect of ETF on signal to noise, and therefore we want constant noise input at each setting. The load resistor Johnson noise obviously depends on the value of the resistor, and will muddy the water we are trying to look through. We show the ratio of G_{12} to G_{eff} to G. We are showing the $G_{eff} = G + G_{ETF}$ for TES1. Since we are changing load resistor values each TES will have a different G_{eff}.

The first pane in Figure 4.12 shows the noise when in perfect voltage bias, with both load resistors equal to zero. The link phonon noise (--) dominates the total noise up its knee at about 20 kHz. On the next three panes we change the load resistor on TES2 from zero to R. The effect on the link noise can at first seem disconcerting. The link phonon
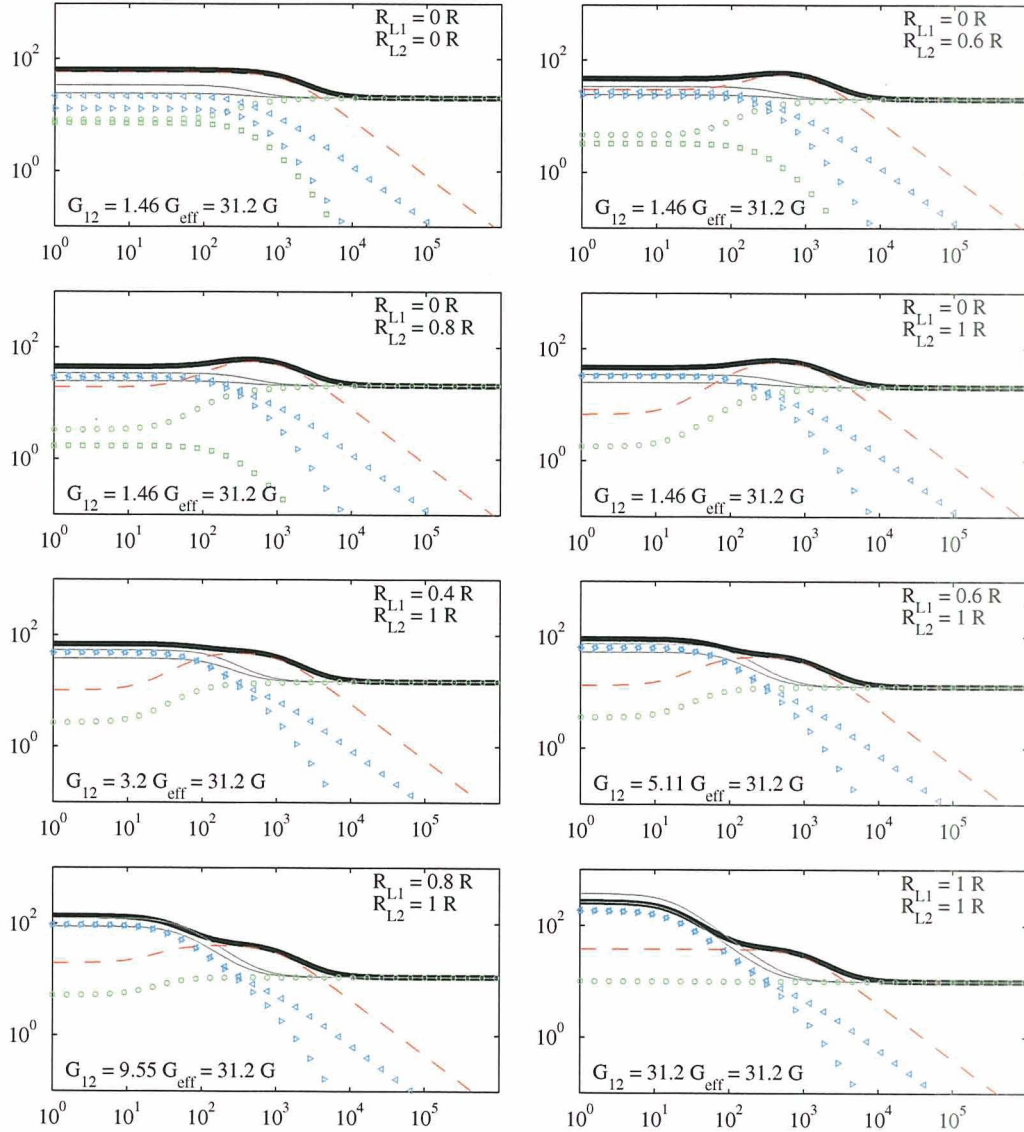
Figure 4.12: Theoretical noise for a 2-pixel PoST vs. the load resistors R_{L1} and R_{L2}. The two thin gray lines are the theoretical limits of the 2-pixel PoST. The top gray line is the single pixel result, which should be the limit as $G_{12} \to 0$. The lower gray line is $1/\sqrt{2}$ lower than the top line, and should be the limit as $G_{12} \to \infty$. The legend is in Figure 4.3 on page 74. The X-axis is frequency in Hz, and the Y-axis is RMS current noise in pA/$\sqrt{\text{Hz}}$.
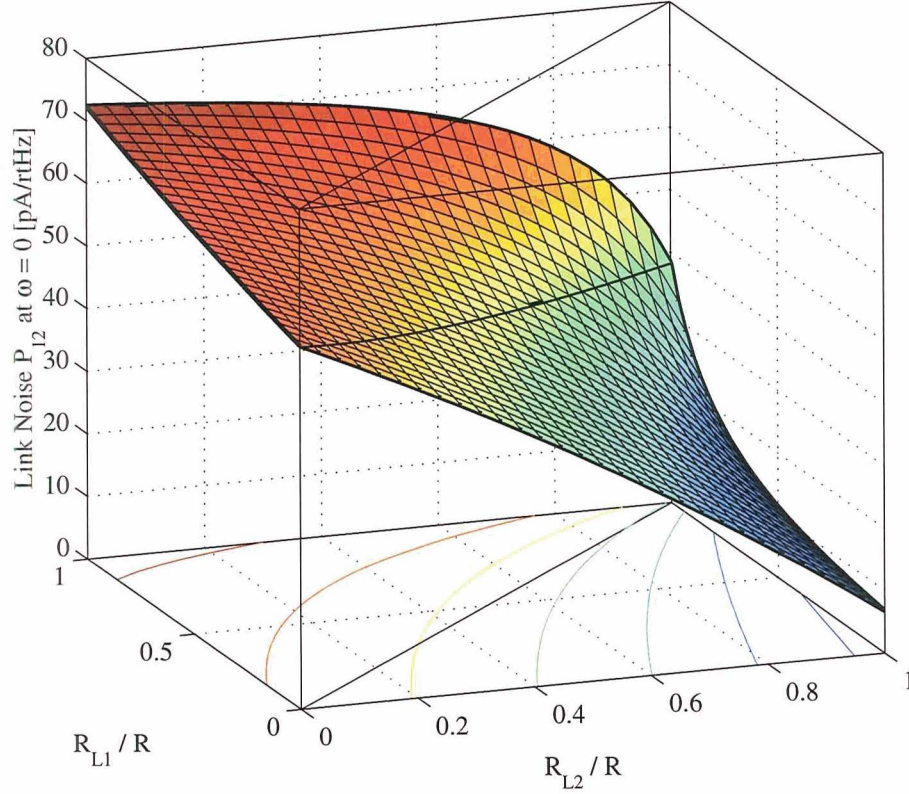
Figure 4.13: Two-pixel PoST link phonon noise at zero frequency as a function of R_{L1} and R_{L2}. The lines on the $P_{12} = 0$ plane are contours. The plane bisecting the figure is the $R_{L1} = R_{L2}$ plane.

noise gets suppressed at low frequencies. Note that when $R_{L2} = R$, the link noise parallels TES1s detector Johnson noise at low frequencies, and then rolls off at frequencies above $1/\tau_{\text{link}}$.

This is a very interesting feature of PoSTs. It is due to the same phenomenon we saw back in Figure 4.6. Comparing Figure 4.6(a) and Figure 4.6(b) we see that the model with lower ETF (due to a value of the load resistor of $0.8R$, which lowers the value of G_{ETF}) has a lower roll frequency and a higher level of noise than the same model in perfect voltage bias (which has a larger G_{ETF} and is thus in stronger ETF). This is just the ETF suppression of the noise: electrothermal feedback lowers the noise level at low frequencies and pushes the roll-off point (the "knee") out to higher frequencies. In Section 3.1.3 we argued that the signal to noise ratio on a single-pixel TES is not changed by the amount of ETF present in the device. All noise terms and signal get suppressed by the same amount, so no change in the *SNR* or resolution is expected.

But now we look at Figures 4.5 and 4.6, and the first four panes of Figure 4.12, and we clearly see the ratio of the link noise to the other terms does *not* remain constant as we change the ETF. This effect is due to the nature of the link noise in our system.
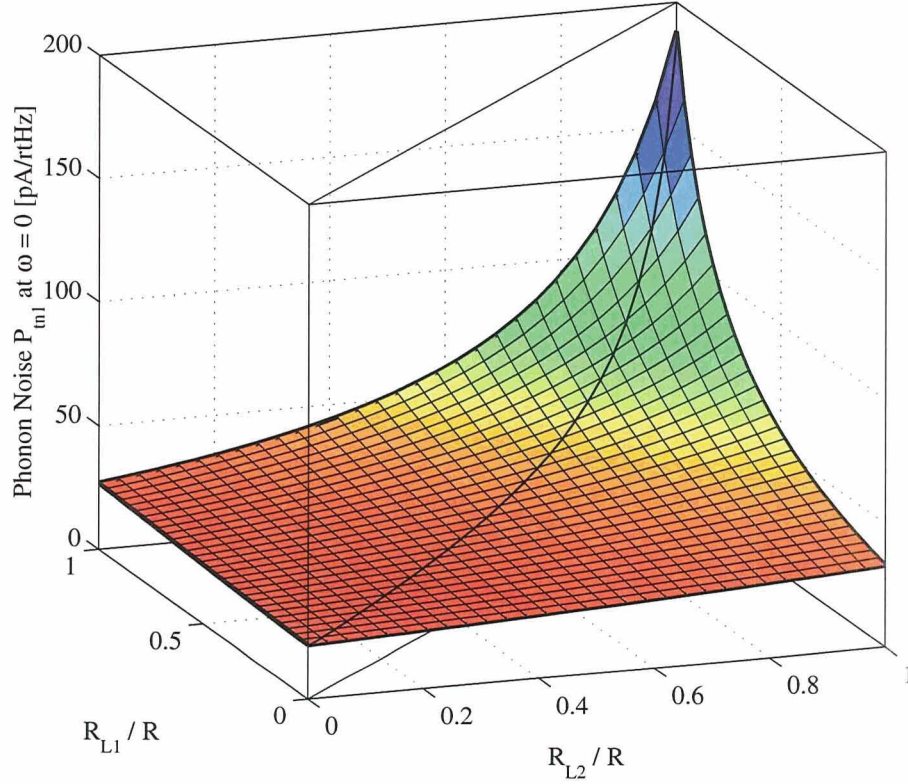
Figure 4.14: Two-pixel PoST TES1 phonon noise at zero frequency as a function of R_{L1} and R_{L2}. The plane bisecting the figure is the $R_{L1} = R_{L2}$ plane.

The link noise is a movement of heat from one TES to the other through the link. Since energy must be conserved, the amount of heat leaving one TES must be the same amount of heat received by the other. This means if TES1 sees and increase in temperature due to a thermal fluctuation from the link, TES2 will see a *decrease* in temperature of the same size. On TES1, ETF will sense this increase in temperature and lower the power (lower power for higher temperature, Figure 2.2(b)). TES2 will increase the power. In the linear model, the power increase by TES2 is exactly equal to the power decrease by TES1. So although TES1 is decreasing the power to lower the temperature of the TES back to T, TES2 is at the same time *increasing* the power on its side, and ends up cancelling TES1s efforts to suppress the noise. As long as $G_{ETF1} = G_{ETF2}$, they will cancel each other out, and you will see the un-suppressed level of noise from the link on both TESs.

But this cancellation only happens when the ETF terms are equal. As we change R_L, we change G_{ETF}. In the first four panes of Figure 4.12, we see the link phonon noise decrease as we increase R_{L2}, decreasing G_{ETF2} to zero when $R_{L2} = R$. Note the displayed $G_{eff} = G + G_{ETF}$ does not change, because we are showing the effective conductance for TES1 and R_{L1} has up to now been held constant.
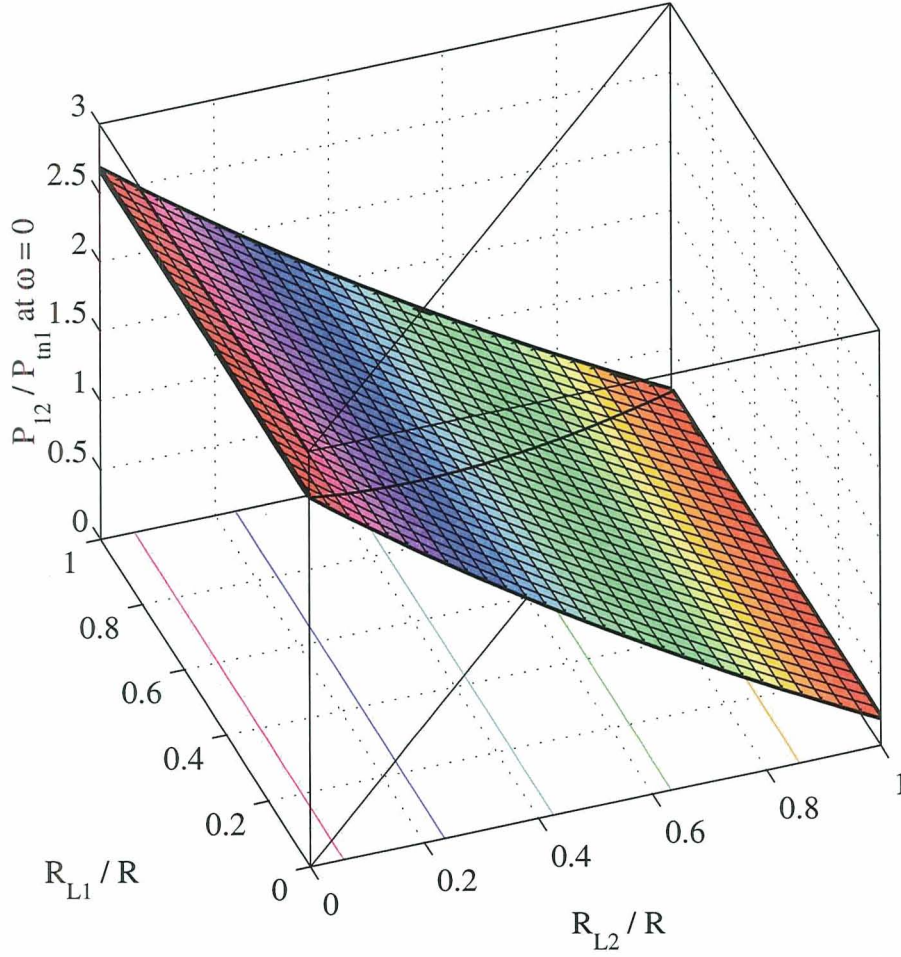
Figure 4.15: Two-pixel PoST link to phonon noise ratio at zero frequency as a function of R_{L1} and R_{L2}. Note this ratio is independent of R_{L1}. The lines on the $P_{12}/P_{tn1} = 0$ plane are contours. The plane bisecting the figure is the $R_{L1} = R_{L2}$ plane.

Since we are decreasing G_{ETF2}, there is less ETF power coming from TES2 to cancel TES1's efforts to suppress the noise. Thus as G_{ETF2} decreases, TES1 can suppress the link noise. When $G_{ETF2} = 0$, there is maximum suppression for the given parameters of the system, and we see the suppression of the link and the detector Johnson noise parallel each other in-band.

Now that we have set $R_{L2} = R$ and thus $G_{ETF2} = 0$, we can start changing R_{L1}. Since there is no ETF on TES2, we expect to see the normal behavior for a TES as the ETF is decreased over the next four panes in the figure. We see all noise sources moving upward as the suppression diminishes, by the same amount, keeping the signal-to-noise ratio constant. In the last pane, both ETF conductances are zero, and $G_{eff} = G$. There is no suppression of any of the noise terms. The the link noise has just one "knee" only in pane 1 and pane

8, when $G_{\text{ETF1}} = G_{\text{ETF2}}$.

The low-frequency link noise level on pane 1 is higher than on pane eight. The noise level depends on the value of both load resistors. We can look at the zero-frequency level to get an overall picture of how noise scales with changing R_Ls. Figure 4.13 shows the zero-frequency link noise as a function of R_{L1} and R_{L2}. The lines in the $P_{12} = 0$ plane are contours of the surface. The plane bisecting the plot is the $R_{L1} = R_{L2}$ plane. The curve on this plane is Eq. (4.24) evaluated at $\omega = 0$. Outside this plane we must use Eq. (4.33).

Looking at the $R_{L1} = R_{L2}$ line, we see that the noise at $R_L = 0$ is larger than when $R_L = R$, as we saw by comparing panes 1 and 8 of Figure 4.12. Notice the large gradient of the surface at the $R_{L1} = R_{L2}$ line, especially as $R_L \rightarrow R$. This means that a small difference between the two load resistors can make a big difference in the link noise level. The curve we traces out in Figure 4.12 start in the $R_{L1} = 0$ plane, and goes from $R_{L2} = 0$ to $R_{L2} = R$. Then it makes a 90 degree turn onto the $R_{L1} = 1$ plane and follows the curve to $R_{L2} = 1$.

What we really want to know is not the level of the link noise, but the level of the link noise compared to the TES phonon noise. This ratio is proportional to the *SNR* of the device, since the signal has the same shape as the TES phonon noise, and we already know other sources of noise scale with the phonon noise. Figure 4.14 shows the TES phonon noise vs. the load resistors. This figure is easy to understand; we know the phonon noise gets suppressed with strong ETF which happens at small load resistor values. As the load resistors approach the TES resistance, ETF goes away and we see the intrinsic noise level.

The quantity of interest is shown in Figure 4.15. The immediate realization is that the ratio of link to TES1 phonon noise (as seen by TES1) does not depend on the value of R_{L1}. This was noted when looking at Figure 4.12; in the last 5 panes, where R_{L2} was held constant, the TES phonon noise and the link noise moved in unison as R_{L1} changed.

We can compare this analysis now to the assertion made in Section 3.1.3 when we said the signal-to-noise ratio is constant under a change in ETF strength. Now we can say that is true for each *individual* TES in the PoST, when the other TES's parameters are held constant. But the interaction between the two TESs acts to cancel ETF for the link phonon noise, and the lack of ETF suppression makes this noise larger than one would have hoped.

To prove ourselves right, we just need to look at the NEP for these conditions. Figure 4.16 shows the NEP and energy resolution for photons hitting TES1 as seen by TES1 for the same parameters in Figure 4.12. We can see that while R_{L2} changes, the total NEP and energy resolution changes. As soon as R_{L2} is held constant, the NEP and energy resolution are frozen in place, as they must be if the *SNR* remains constant under changes in R_{L1}. Figure 4.17 shows the NEP and energy resolution for photons hitting TES2 as seen by TES1. Notice the same effect takes place, even though we are looking at photons on the *other* TES. The *SNR* does not care where the signal is coming from, as long as the ETF in TES2 is not changed, changes in the ETF of TES1 have no impact on the resolution seen by TES1.

We will see all these strange behaviors go away in Section 4.5, when we sum both TESs together and the resulting signal behaves in a more traditional manner.
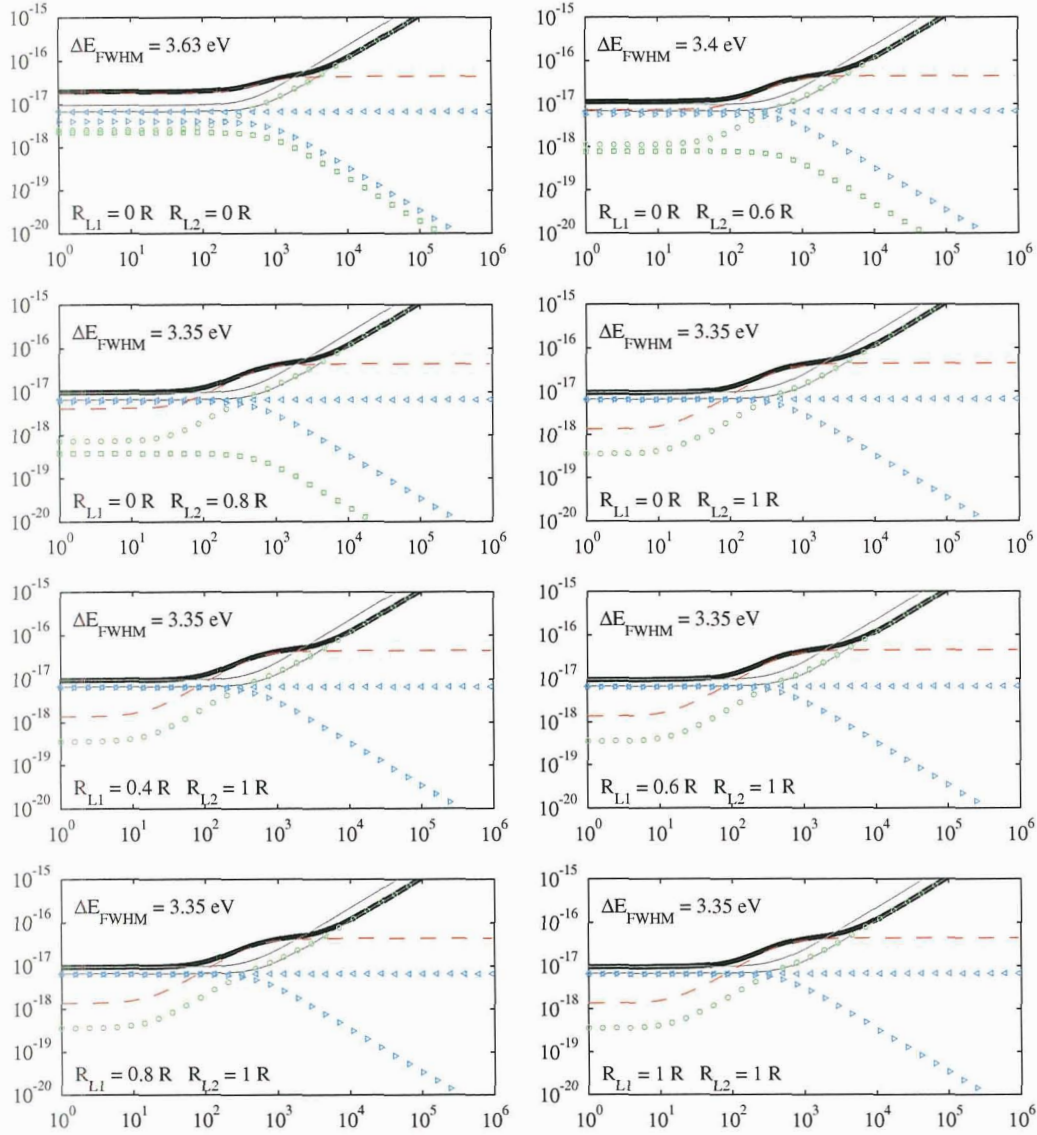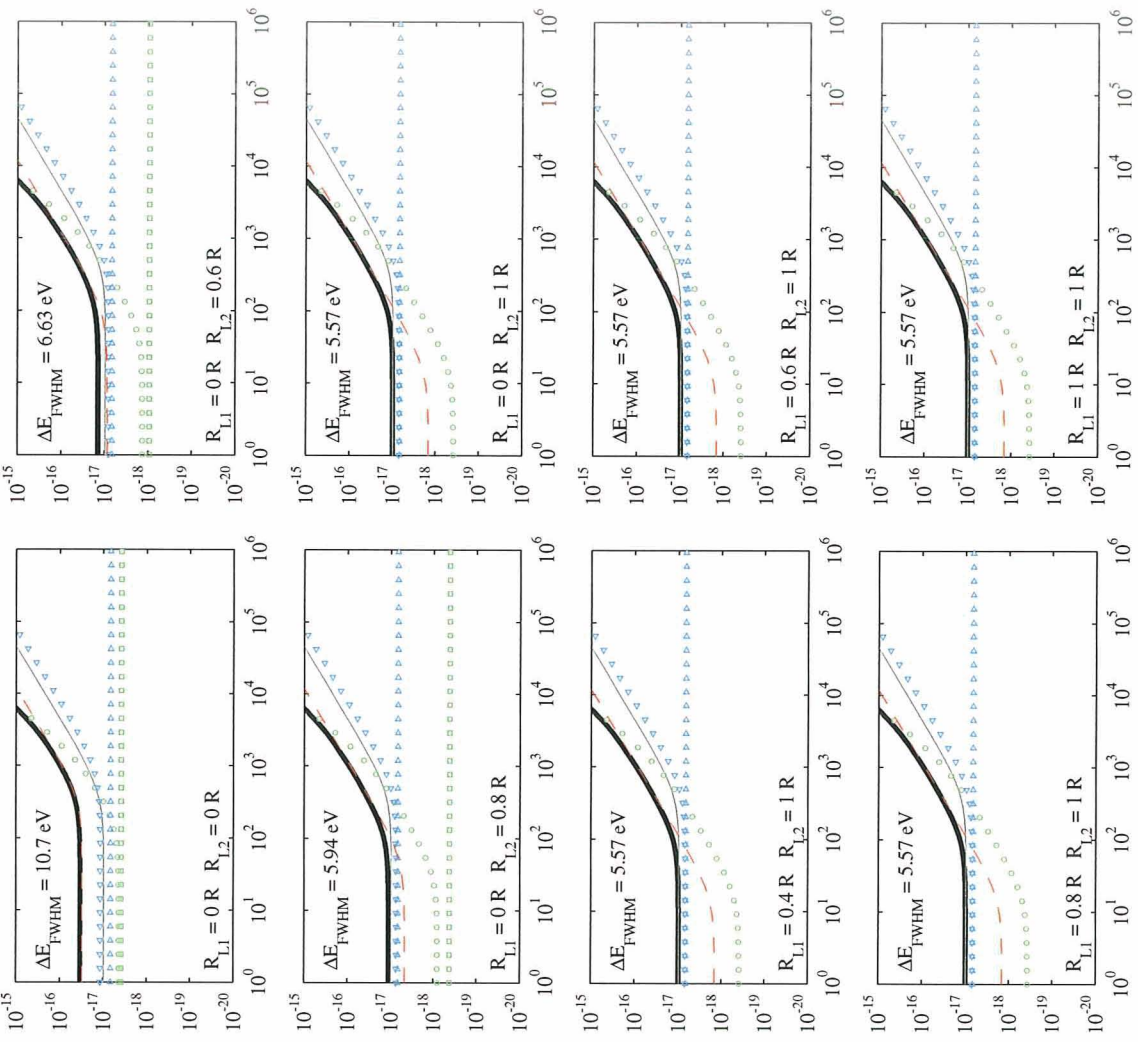
Figure 4.16: Theoretical NEP for a 2-pixel PoST vs. the load resistors R_{L1} and R_{L2}. The signal is coming into TES1. The two thin gray lines are the theoretical limits of the 2-pixel PoST. The lower gray line is the single pixel result, which is the limit as $G_{12} \to 0$. The upper gray line is the limit as $G_{12} \to \infty$. The legend is in Figure 4.3 on page 74. The X-axis is frequency in Hz, and the Y-axis is NEP in W/$\sqrt{\text{Hz}}$.

Figure 4.17: Theoretical NEP for a 2-pixel PoST vs. the load resistors R_{L1} and R_{L2}. The signal is coming into TES2. The two thin gray lines are the theoretical limits of the 2-pixel PoST. The lower gray line is the single pixel result, which is the limit as $G_{12} \rightarrow 0$. The upper gray line is the limit as $G_{12} \rightarrow \infty$. The legend is in Figure 4.3 on page 74. The X-axis is frequency in Hz, and the Y-axis is NEP in $W/\sqrt{Hz}$.

4.3 Formulation of m-pixel PoST theory

We are finally ready to put elements worked out in the previous sections together into the full multi-pixel PoST theory. Figure 4.18 shows the layout of a multi-pixel PoST calorimeter. A number m of absorbers link two TESs that are read out by different circuits. Both TESs are modeled by a phonon system C_p connected to the cold bath by a phonon-bath thermal conductance $G_{pb}(T)$, and an electron system connected to the phonons by $G_{ep}(T)$ and to the first absorber by $G_{ae}(T)$. The electrical circuit is the same as Section 3.2, except that we have two TES, and thus we have $I_1(t)$, $V_1(t)$, $I_m(t)$, and $V_m(t)$ (I'll use the subscript "m" for the second calorimeter so it matches the absorber number). For simplicity we have made the two TESs identical, as well as all absorbers, although computationally there is no penalty for having each be a different value. Between all thermally connected elements there is an associated phonon noise term, for example between two absorbers we have P_{aa} (it should be $P_{tn,aa}(t)$, but we will drop the "tn" thermal noise designator to save some space). Since all absorbers are the same, the phonon noise between them has the same magnitude. But since they are uncorrelated to each other, the noise terms do *not* cancel. To avoid confusion we have labeled them separately, as P_{a1a2}, P_{a2a3}, etc. As before each thermal element has a thermal power noise term associated with it; $P_{a1}(t)$ is the thermal noise for absorber 1. We could also include the photon input terms $P_{\gamma a1}$ but at this point we know they are exactly the same as the thermal noise terms so we will not explicitly include them). The equations for the system depicted in Figure 4.18 are just an extension of the complex calorimeter of Section 3.2. The voltage equations are included (by not assuming $C_{cap} = 0$) for generality; with these equations one can calculate the resolution of a PoST instrumented with silicon thermistors as easily as one with TESs.

The general system of equations for a PoST detector with m pixels is:

$$L\frac{dI_1(t)}{dt} = -I_1(t)R(T_1, I_1) + V_1(t) - V_{dn1}(t) \tag{4.40}$$

$$R_L C_{cap}\frac{dV_1(t)}{dt} = -R_L I_1(t) - V_1(t) + V_{bias} + V_{cn1}(t) - R_L I_{cn1}(t) \tag{4.41}$$

$$C_e\frac{dT_{e1}(t)}{dt} = I_1(t)^2 R(T, I) - K_{ep}(T_{e1}^{n_{ep}} - T_{p1}^{n_{ep}}) - K_{ae}(T_{e1}^{n_{ae}} - T_{a1}^{n_{ae}})$$
$$+ P_{e1}(t) + P_{ep} + P_{ae} + I_1(t)V_{dn1}(t) \tag{4.42}$$

$$C_p\frac{dT_{p1}(t)}{dt} = -K_{ep}(T_{p1}^{n_{ep}} - T_{e1}^{n_{ep}}) - K_{pb}(T_{p1}^{n_{pb}} - T_b^{n_{pb}}) + P_{p1}(t) - P_{ep} + P_{pb} \tag{4.43}$$

$$C_a\frac{dT_{a1}(t)}{dt} = -K_{ae}(T_{a1}^{n_{ae}} - T_{e1}^{n_{ae}}) - K_{aa}(T_{a1}^{n_{aa}} - T_{a2}^{n_{aa}}) + P_{a1}(t) - P_{ae} + P_{a1a2} \tag{4.44}$$

$$C_a\frac{dT_{a2}(t)}{dt} = -K_{aa}(T_{a2}^{n_{aa}} - T_{a1}^{n_{aa}}) - K_{aa}(T_{a2}^{n_{aa}} - T_{a3}^{n_{aa}}) + P_{a2}(t) - P_{a1a2} + P_{a2a3} \tag{4.45}$$
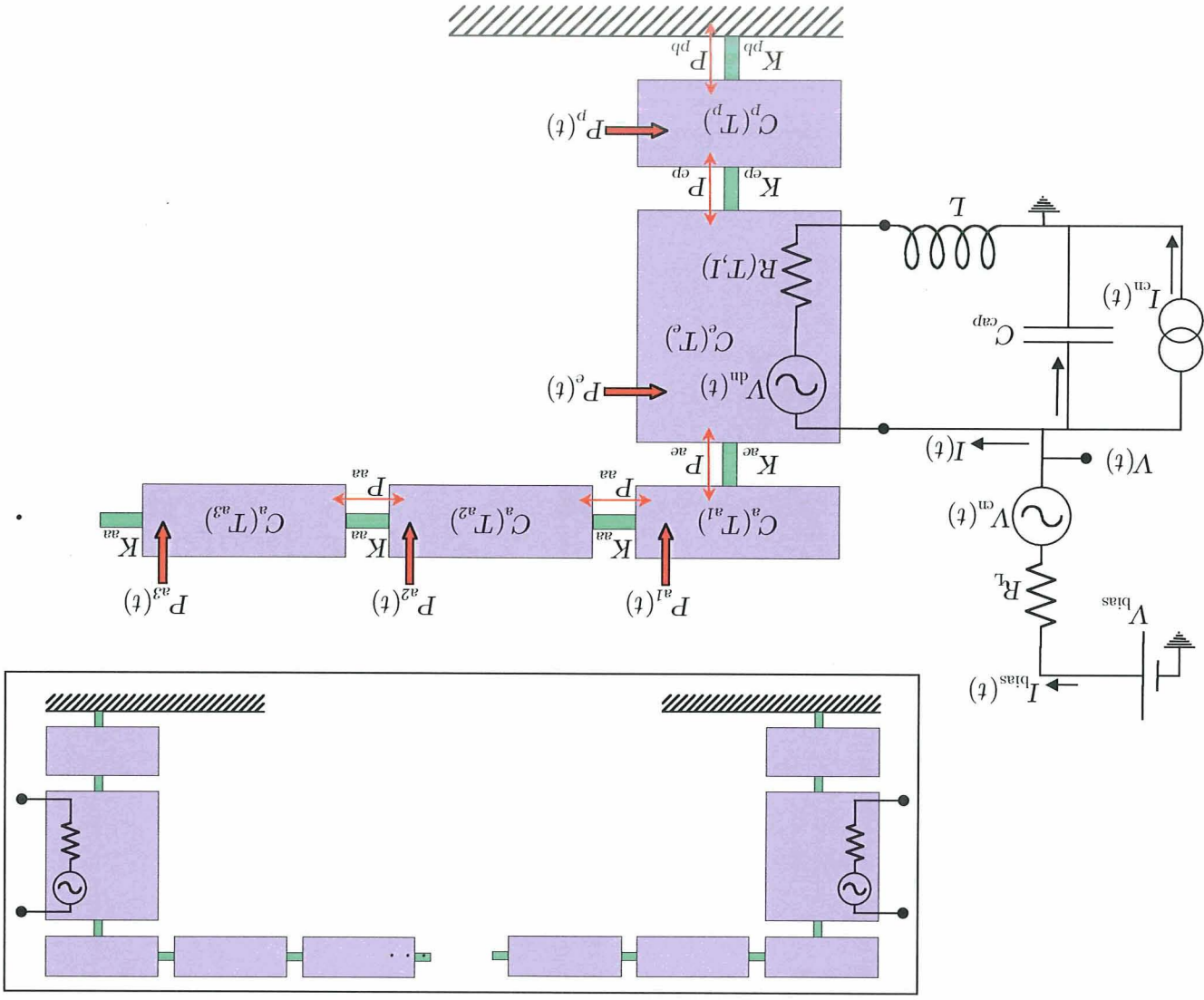
$$\vdots$$

Figure 4.18: Position-sensitive transition-edge calorimeter bias and thermal circuit. The boxed insert shows the general layout. The electrical circuit is the similar to the complex calorimeter in Figure 3.3. The thermal circuit consists of two transition-edge sensors connected by a row of absorbers. The variables are defined in the text.

$$C_{\mathrm{a}}\frac{dT_{\mathrm{a}(m-1)}(t)}{dt} = -K_{\mathrm{aa}}(T_{\mathrm{a}(m-1)}^{n_{\mathrm{aa}}} - T_{\mathrm{a}(m-2)}^{n_{\mathrm{aa}}}) - K_{\mathrm{aa}}(T_{\mathrm{a}(m-1)}^{n_{\mathrm{aa}}} - T_{\mathrm{a}\,m}^{n_{\mathrm{aa}}})$$
$$+ P_{\mathrm{a}(m-1)}(t) - P_{\mathrm{a}(m-2)\mathrm{a}(m-1)} + P_{\mathrm{a}(m-1)\mathrm{a}\,m} \tag{4.46}$$

$$C_{\mathrm{a}}\frac{dT_{\mathrm{a}\,m}(t)}{dt} = -K_{\mathrm{aa}}(T_{\mathrm{a}\,m}^{n_{\mathrm{aa}}} - T_{\mathrm{a}(m-1)}^{n_{\mathrm{aa}}}) - K_{\mathrm{ae}}(T_{\mathrm{a}\,m}^{n_{\mathrm{ae}}} - T_{\mathrm{e}\,m}^{n_{\mathrm{ae}}})$$
$$+ P_{\mathrm{a}\,m}(t) - P_{\mathrm{a}(m-1)\mathrm{a}\,m} + P_{\mathrm{a}\,m\,\mathrm{e}\,m} \tag{4.47}$$

$$C_{\mathrm{p}}\frac{dT_{\mathrm{p}\,m}(t)}{dt} = -K_{\mathrm{ep}}(T_{\mathrm{p}\,m}^{n_{\mathrm{ep}}} - T_{\mathrm{e}\,m}^{n_{\mathrm{ep}}}) - K_{\mathrm{pb}}(T_{\mathrm{p}\,m}^{n_{\mathrm{pb}}} - T_{\mathrm{b}}^{n_{\mathrm{pb}}}) + P_{\mathrm{p}\,m}(t) - P_{\mathrm{ep}} + P_{\mathrm{pb}} \tag{4.48}$$

$$C_{\mathrm{e}}\frac{dT_{\mathrm{e}\,m}(t)}{dt} = I_m(t)^2 R(T,I) - K_{\mathrm{ep}}(T_{\mathrm{e}\,m}^{n_{\mathrm{ep}}} - T_{\mathrm{p}\,m}^{n_{\mathrm{ep}}}) - K_{\mathrm{ae}}(T_{\mathrm{e}\,m}^{n_{\mathrm{ae}}} - T_{\mathrm{a}\,m}^{n_{\mathrm{ae}}})$$
$$+ P_{\mathrm{e}\,m}(t) + P_{\mathrm{ep}} + P_{\mathrm{ae}} + I_m(t)V_{\mathrm{dn}\,m}(t) \tag{4.49}$$

$$R_{\mathrm{L}}C_{\mathrm{cap}}\frac{dV_m(t)}{dt} = -R_{\mathrm{L}}I_m(t) - V_m(t) + V_{\mathrm{bias}} + V_{\mathrm{cn}\,m}(t) - R_{\mathrm{L}}I_{\mathrm{cn}\,m}(t) \tag{4.50}$$

$$L\frac{dI_m(t)}{dt} = -I_m(t)R(T_m, I_m) + V_m(t) - V_{\mathrm{dn}\,m}(t) \tag{4.51}$$

Now that we have the general system of equations, following our previous procedure, we linearize the system. As in Section 3.2 we will be using superscripts to denote the evaluation point of $G(T)$.

We again write

$$\mathbf{M}\vec{\Delta} = \vec{N}_{\mathrm{tot}} \tag{4.52}$$

$$\vec{\Delta} = \mathbf{M}^{-1}\vec{N}_{\mathrm{tot}} = \mathbf{S}\vec{N}_{\mathrm{tot}} \tag{4.53}$$

The matrices are now much larger, but apart from size, there is nothing new. The signal vector is

$$\vec{\Delta} = \begin{pmatrix} \Delta I_1 \\ \Delta V_1 \\ \Delta T_{\mathrm{e}1} \\ \Delta T_{\mathrm{p}1} \\ \Delta T_{\mathrm{a}1} \\ \Delta T_{\mathrm{a}2} \\ \vdots \\ \Delta T_{\mathrm{a}(m-1)} \\ \Delta T_{\mathrm{a}\,m} \\ \Delta T_{\mathrm{p}\,m} \\ \Delta T_{\mathrm{e}\,m} \\ \Delta V_m \\ \Delta I_m \end{pmatrix} \tag{4.54}$$

and the noise vector becomes

$$
\vec{N}_{\text{tot}} =
\begin{Bmatrix}
-V_{\text{dn}1}(\omega) \\
V_{\text{cn}1}(\omega) - R_{\text{L}} I_{\text{cn}1}(\omega) \\
P_{\text{e}1}(\omega) + P_{\text{ep}} + P_{\text{ae}} + I V_{\text{dn}1}(\omega) \\
P_{\text{p}1}(\omega) - P_{\text{ep}} \\
P_{\text{a}1}(\omega) - P_{\text{ae}} + P_{\text{a2a1}} \\
P_{\text{a}2}(\omega) - P_{\text{a1a2}} + P_{\text{a2a3}} \\
\cdots \\
P_{\text{a}(m-1)}(\omega) - P_{\text{a}(m-2)\text{a}(m-1)} + P_{\text{a}(m-1)\text{a}\,m} \\
P_{\text{a}\,m}(\omega) - P_{\text{a}(m-1)\text{a}\,m} + P_{\text{ae}} \\
P_{\text{p}\,m}(\omega) - P_{\text{ep}} \\
P_{\text{e}\,m}(\omega) + P_{\text{ep}} - P_{\text{ae}} + I V_{\text{dn}\,m}(\omega) \\
V_{\text{cn}\,m}(\omega) - R_{\text{L}} I_{\text{cn}\,m}(\omega) \\
-V_{\text{dn}\,m}(\omega)
\end{Bmatrix}
\tag{4.55}
$$

Because of shortage of display real estate, we define a vector $\vec{D}$ composed of the diagonal elements of $\mathbf{M}$:

$$
\vec{D} =
\begin{Bmatrix}
R(1+\alpha_{\text{I}}) + i\omega L \\
1 + i\omega R_{\text{L}} C_{\text{cap}} \\
G_{\text{ep}}^{\text{e}} + G_{ae} - \frac{\alpha P}{T} + i\omega C_{\text{e}} \\
G_{\text{ep}}^{\text{p}} + G_{\text{pb}} + i\omega C_{\text{p}} \\
G_{ae} + G_{aa} + i\omega C_{\text{a}} \\
2G_{aa} + i\omega C_{\text{a}} \\
\cdots \\
2G_{aa} + i\omega C_{\text{a}} \\
G_{ae} + G_{aa} + i\omega C_{\text{a}} \\
G_{\text{ep}}^{\text{p}} + G_{\text{pb}} + i\omega C_{\text{p}} \\
G_{\text{ep}}^{\text{e}} + G_{ae} - \frac{\alpha P}{T} + i\omega C_{\text{e}} \\
1 + i\omega R_{\text{L}} C_{\text{cap}} \\
R(1+\alpha_{\text{I}}) + i\omega L
\end{Bmatrix}
\tag{4.56}
$$

and then we can write the sparse matrix $\mathbf{M}$ (empty spaces imply zeros):

$$
\mathbf{M} =
\begin{pmatrix}
\vec{D}_1 & -1 & \frac{\alpha V}{T} \\
R_{\mathrm{L}} & \vec{D}_2 & 0 & 0 \\
-(2+\alpha_{\mathrm{I}})V & 0 & \vec{D}_3 & -G_{\mathrm{ep}}^{\mathrm{p}} & -G_{\mathrm{ae}}^{\mathrm{a}} \\
& 0 & -G_{\mathrm{ep}}^{\mathrm{e}} & \vec{D}_4 & 0 & 0 \\
& & -G_{\mathrm{ae}}^{\mathrm{e}} & 0 & \vec{D}_5 & -G_{\mathrm{aa}} & 0 \\
& & & 0 & -G_{\mathrm{aa}} & \vec{D}_6 & -G_{\mathrm{aa}} & 0 \\
& & & & \ddots & \ddots & \ddots & \ddots & \ddots \\
& & & & & 0 & -G_{\mathrm{aa}} & \vec{D}_8 & -G_{\mathrm{aa}} & 0 \\
& & & & & & 0 & -G_{\mathrm{aa}} & \vec{D}_9 & 0 & -G_{\mathrm{ae}}^{\mathrm{e}} \\
& & & & & & & 0 & 0 & \vec{D}_{10} & -G_{\mathrm{ep}}^{\mathrm{e}} & 0 \\
& & & & & & & & -G_{\mathrm{ae}}^{\mathrm{a}} & -G_{\mathrm{ep}}^{\mathrm{p}} & \vec{D}_{11} & 0 & -(2+\alpha_{\mathrm{I}})V \\
& & & & & & & & & 0 & 0 & \vec{D}_{12} & R_{\mathrm{L}} \\
& & & & & & & & & & \frac{\alpha V}{T} & -1 & \vec{D}_{13}
\end{pmatrix}
\tag{4.57}
$$

We numerically invert $\mathbf{M}$ to find the responsivity matrix $\mathbf{S}$ and with it calculate the noise and energy resolution. We can see the power of the numerical linear theory, as very complex systems are reduced to big matrices that are in principle no more difficult for a computer to solve than a simple one-pixel TES.

4.4   Analysis of a 7-pixel PoST calorimeter

We will concentrate on the seven-pixel PoST case, since that's the size of some of the devices we have made, but this analysis will be valid for any number of pixels.

We have to determine the values of the heat capacities and conductances for the seven-pixel PoST. To be able to compare different calorimeter designs with each other, in Section 2.2.6 we established a fiducial maximum temperature excursion for any TES in the calorimeter of 0.5 mK. We assumed this value represented the linear part of the R vs. T curve. This meant that a single pixel TES would have a heat capacity of 1.92 pJ/K. A two-pixel PoST, with two TESs acting as absorbers, had to have a heat capacity of 1.92 pJ/K on each TES. In our seven-pixel PoST design, we have seven absorbers, and can specify that the TESs will not be placed in the path of the incoming X-rays, i.e., they will never absorb a photon directly into the electron or phonon system. The PoST will then have seven different absorption locations, and we have to decide how to apply our saturation condition.

The more conservative approach is to look at the temperature of TES1 when the photon is absorbed in pixel 1. The maximum temperature of TES1 will depend on the heat capacity of the absorbers, the heat capacity of TES1 and the link conductance. If we size the TES so a 6 keV photon increased TES1's temperature by half a milli-Kelvin, then the TES's ΔT for a 6 keV in pixel 2, 3 or 4 will be lower than 0.5 mK. In other words, if we constrain the PoST so that the linear energy range of pixel one ends at 6 keV, the linear range for pixels 2 through 6 (71% of the pixels) will have higher linear ranges than our specification.

We could also apply the saturation condition to pixel 2. Then we would have three pixels that exceeded the condition, and two that did not. In reality the R-T curve is not a straight line as depicted in Figure 2.3, but a curved line with a non-linear region before reaching full saturation (Figure 2.2(a)). The exact definition of saturation energy is actually quite fluid, and defining where the response is too non-linear depends on the algorithms used to analyze the data. We will calculate parameters based on both saturation condition standards.

Since we have the matrix set up, we can use the values in Table 4.2 as a starting point, solve the time-domain problem as in Section 4.1.1, but looking at the temperature instead of the current, and look for heat capacities and link conductances that satisfy our restrictions.

Using the values in Table 4.3 we obtain the noise for TES1 in a 7-pixel PoST. The absorber pixels heat capacities are taken from calculated values from our designs, which we will talk about in Chapter 6. The link conductances are higher, since there are now eight of them in the system. For simplicity we assume the phonon heat capacity and electron-phonon decoupling are such that we can treat the electrons and phonons as one system (C_e).
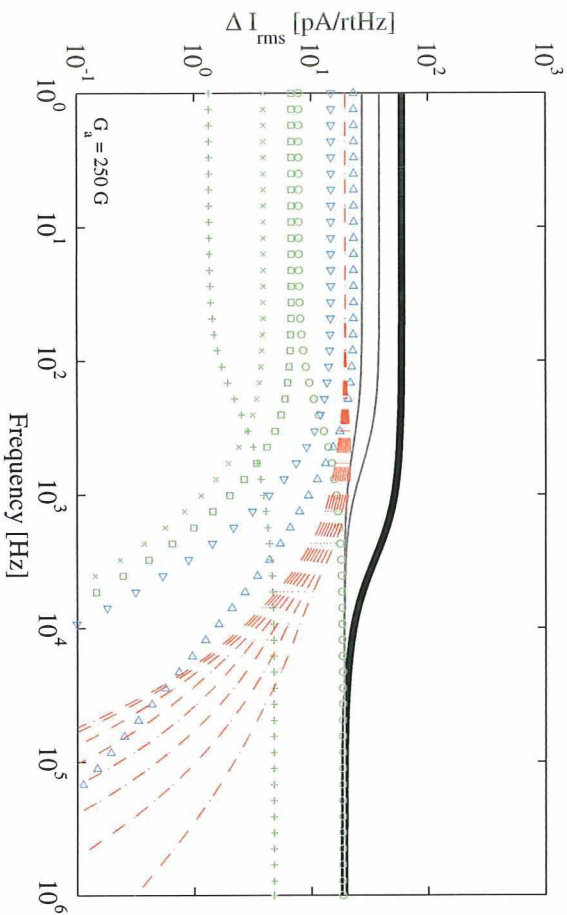
Figure 4.19: Noise for 7-pixel PoST using parameters from Table 4.3. Notice the link noise terms are now eight separate lines that converge at low frequencies. The other noise sources are as before. The link nearest TES1 is the highest link noise line.

C_{tot}	3.12	pJ/K
C_e	1.27	pJ/K
C_p	$\ll C_e$	
C_a	83.2	fJ/K
G_{pb}	200	pW/K
G_{ep}	$\gg G_{pb}$	
G_{ae}	50	nW/K
R	10	mΩ
R_L	1	mΩ
T_b	50	mK
T	75	mK
T_L	50	mK
L	1	nH
α	90	
α_I	~ 0	
n	3.2	

Table 4.3: Parameters for noise analysis of a 7-pixel PoST. The total heat capacity $C_{tot} = 2C_e + 7C_a$.
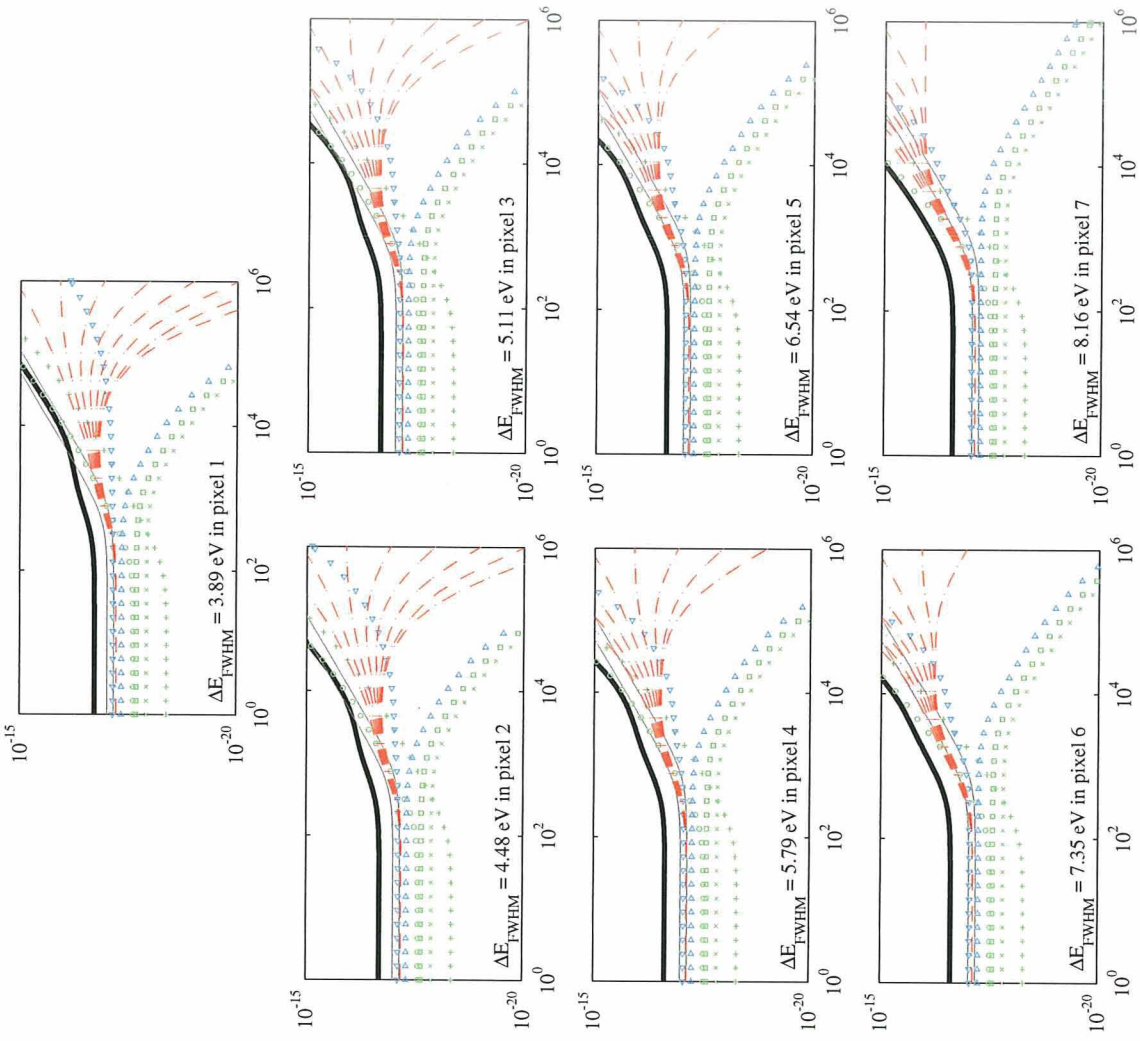
Figure 4.20: Theoretical NEP for a 7-pixel PoST with values from Table 4.3 on page 102. The signal is coming into TES1. The thin gray line is the theoretical limit as $G_a \rightarrow \infty$. The legend is in Figure 4.3 on page 74. The X-axis is frequency in Hz, and the Y-axis is NEP in $W/\sqrt{Hz}$.

Resolution on Pixel	eV FWHM
1	3.90
2	4.48
3	5.11
4	5.79
5	6.54
6	7.35
7	8.16

Table 4.4: Comparison of theoretical resolution of signal from just one channel on a 7-pixel PoST. The saturation condition of a 0.5 mK maximum temperature excursion for any TES has been applied for 6 keV photons on pixel 1. Model parameters are in Table 4.3 on page 102. For comparison, a 1.92 pJ/K single-pixel TES (which satisfies the saturation condition) with similar parameters has a 1.76 eV resolution.

We also set the capacitance C_{cap} to a negligible value, and concentrate on the current. As before, at this point we are just looking at one of the two TESs in the calorimeter.

Figure 4.19 shows the noise for the 7-pixel PoST. There is only one new feature in this plot from the previous ones: the link phonon noise line is now eight separate lines, six between absorbers and two from absorber to electron system. At low frequencies, heat can propagate without problems through the links, and the absorber looks monolithic; all phonon noise terms look the same at low frequencies (note there are eight link noise lines on top of each other in this low frequency region). This means there is no position dependence at low frequencies, as per our design. At high frequencies, the finite conductance between each link starts affect the signal, and the noise profile for the links splits into individual lines. The highest link noise line in the figure is the noise from the nearest absorber pixel to TES1's electron system, and the lowest noise line corresponds to the to the seventh absorber to the other TES. The separate link noise lines remain semi-parallel to each other until after the roll-off frequency of the links. Then they split apart as they rapidly go down in magnitude at higher frequencies.

We calculate the NEP and energy resolution for each pixel, which are shown in Figure 4.20 and Table 4.4. The resolution goes from 3.90 eV in the nearest pixel to 8.16 eV in the farthest pixel. This looks rather discouraging, compared to the 1.64 eV single-pixel TES result we calculated in Section 3.1.6. Part of the problem is that in order to comply with our 0.5 mK temperature excursion limit (Section 2.2.6) on a TES the total heat capacity of the PoST is larger than a single pixel TES, as discussed before.

There is a second point to make on the resolution shown on Table 4.4. These resolution numbers have been computed by integrating the NEP for the signal seen on TES1. This is very easy to do, but we are ignoring half of or our signal! We will solve this problem in the next section.

4.5 Generalized formulation of theoretical noise and resolution for multiple-absorber, multiple-thermistor distributed-readout imaging calorimeters

The original idea for a PoST was to measure position by staging two thermistors at the ends of an absorber and comparing their signals. When we described the concept in Chapter 2, we said the energy could be determined by adding the signals, but up to now we have been looking at one TES at a time. Now we will describe the correct way of joining the signals in the linear model to arrive at the real PoST energy resolution for each pixel.

The two TESs are reading temperatures at different locations on the same calorimeter. We know the time constant of the calorimeter to the bath is much lower than any of the internal time constants (absorber-absorber, absorber-TES). For low-frequency bath thermal noise, the calorimeter can thermalize to one temperature across itself and both TESs will read the same temperature. The TESs *will be in phase.*

And so it is for most other noise sources. Any noise source that generates a thermal fluctuation will be sensed by both TESs. It will be in phase at very low frequencies and will add.

Link phonon noise between TESs in PoST is heat moving from one heat capacity to an adjacent one through the link. Let us say we take some heat from absorber 2 and move it to absorber 3. The temperature in absorber 2 drops, and the temperature in absorber 3 increases. If this is done slowly, the rest of the PoST on either side thermalizes, so from absorber 2 back to TES1 every temperature will drop, and from absorber 3 onward every temperature will rise. TES1 will record a drop in temperature, while TES2 will record a rise in temperature. When these two signals are added, they will tend to cancel. At low frequencies, *link thermal noise is in phase but with opposite signs* .

For any calorimeter, we have a $\vec{\Delta}$ matrix of outputs, a number of noise sources $\vec{N}_{\text{tot}}$ and a generalized responsivity matrix $\mathbf{S}$ that connects the two (Eq. (4.53)). In the specific case of the PoST, Eq. (4.54) tells us that the rows 1 and m are the current signals that we seek.[5] We want to add these signals together, to see what the total signal is when a noise source $\vec{N}$ acts on the system:

$$\Delta I_{\text{added}} = \vec{\Delta}_1 + \vec{\Delta}_m$$
$$= \sum_{j=1}^{m} \mathbf{S}_{1,j} \vec{N}_j + \sum_{j=1}^{m} \mathbf{S}_{m,j} \vec{N}_j$$
$$= \sum_{j=1}^{m} \left(\mathbf{S}_{1,j} + \mathbf{S}_{m,j} \right) \vec{N}_j \tag{4.58}$$

We take each noise term separately as done before, to account for the fact that noise sources are uncorrelated from one another. We do this addition *before* taking the absolute

---

[5]We will assume we have a current readout from now on, but the equations will allow the conversion to voltage readout by just changing an index. See Section 3.2.

magnitude squared. The beauty is that we have already done all the hard work by setting up the equations. The phase lags at high frequencies between ΔI_1 and ΔI_m are already in the generalized responsivity matrix $\mathbf{S}$. The correlations between phonon noise seen on both TESs is there. The cancellation of link noise is there. All we have to do is evaluate this equation. The added noise for one noise source $\vec{N}$ is then

$$\left\langle |\Delta I_{\text{added}}(\omega)|^2 \right\rangle = \left\langle \left| \sum_{j=1}^{m} \left(\mathbf{S}_{1,j} + \mathbf{S}_{m,j} \right) \vec{N}_j(\omega) \right|^2 \right\rangle \qquad (4.59)$$

The total noise is the sum of Eq. (4.59) evaluated for each noise source $\vec{N}$.

From Eq. (4.58) and the definition of NEP (Eq. (4.34)) we can determine the NEP and resolution for our PoST when adding both signals together. The NEP for a particular noise source $\vec{N}$ as seen from a particular pixel is just the thermal power into that pixel required to produce the same signal ΔI_{added} as $\vec{N}$ produces. If i is the row in Eq. (4.55) corresponding to the temperature of the pixel of interest,

$$\Delta I_{\text{added}} = \sum_{j=1}^{m} \left(\mathbf{S}_{1,j} + \mathbf{S}_{m,j} \right) \vec{N}_j = \left(\mathbf{S}_{1,i} + \mathbf{S}_{m,i} \right) \text{NEP}_i \qquad (4.60)$$

and the NEP for pixel i becomes

$$\left\langle |\text{NEP}_{i,\text{added}}(\omega)|^2 \right\rangle = \left\langle \left| \frac{\sum_{j=1}^{m} \left(\mathbf{S}_{1,j} + \mathbf{S}_{m,j} \right) \vec{N}_j(\omega)}{\mathbf{S}_{1,i} + \mathbf{S}_{m,i}} \right|^2 \right\rangle \qquad (4.61)$$

As an example, the NEP for pixel 2 (row 6 in Eq. (4.55)) of TES1's detector noise is

$$\left\langle |\text{NEP}_{6,\text{added}}(\omega)|^2 \right\rangle = \left\langle \left| \frac{-\left(\mathbf{S}_{1,1} + \mathbf{S}_{7,1} \right) V_{\text{dn1}}(\omega) + \left(\mathbf{S}_{1,3} + \mathbf{S}_{7,3} \right) IV_{\text{dn1}}(\omega)}{\mathbf{S}_{1,6} + \mathbf{S}_{7,6}} \right|^2 \right\rangle \qquad (4.62)$$

4.5.1   Theoretical resolution for our 7-pixel PoST model

Now we can come back to our seven-pixel PoST model and calculate the true noise and resolution for this device. Figure 4.21 shows the noise for a 7-pixel PoST with values from Table 4.3 on page 102. Since the device is symmetric, it is not surprising that the addition of the two TES signals makes the noise seen from Johnson noise at TES1 identical to that seen from Johnson noise at TES7. Note that the there are now two separate noise terms on each line: two phonon noise terms ($\lhd$ and $\rhd$ overlapping each other), two detector noise terms ($\bigcirc$ and $\square$ overlapping each other), two circuit noise terms ($+$ and $\times$ overlapping each other), and finally the link phonon noise terms. The link noise for pixels 1 and 7 are over each other (the largest link noise line), 2 and 6 form the second line, 3 and 5 the third, and pixel 4 the fourth. The link noise is now suppressed in-band, something that we always expect from a hanging heat capacity but had not seen in the PoSTs when looking
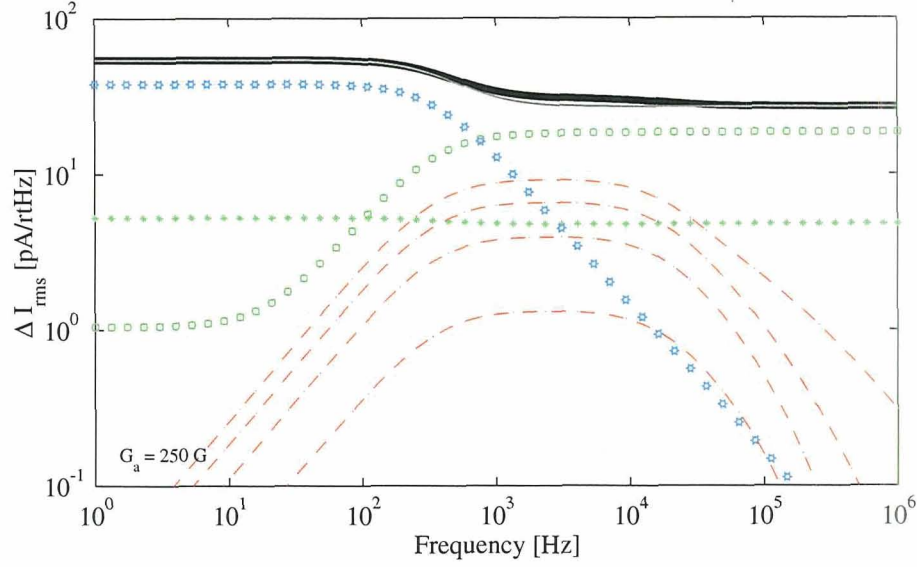
Figure 4.21: Theoretical noise for a 7-pixel PoST with values from Table 4.3 on page 102. Both TES signals are added together. Because of the symmetry imposed by adding the signals together, many terms are overlapping each other. The inductor is set to zero to show the intrinsic behavior of the noise. The thin gray line is the theoretical limit as $G_a \to \infty$. The legend is in Figure 4.3 on page 74.
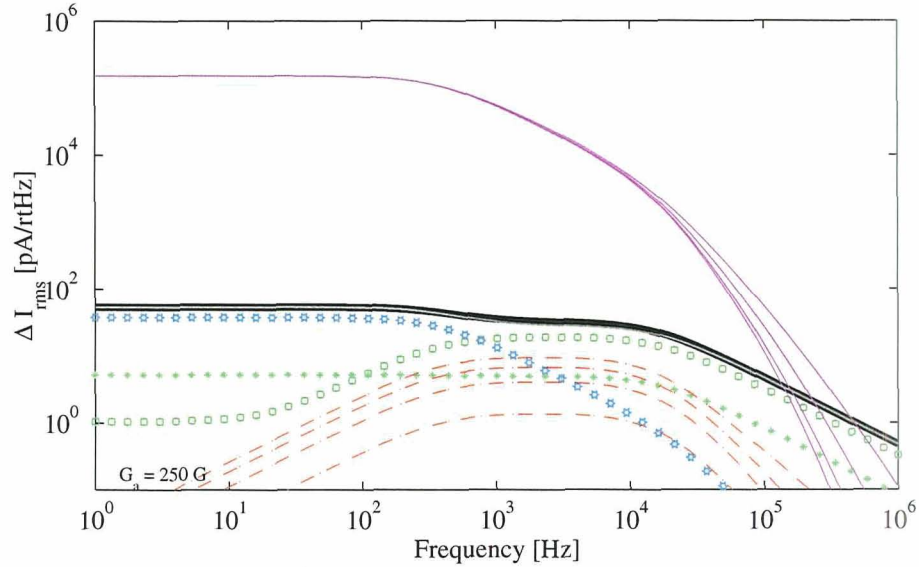
Figure 4.22: Theoretical noise and 6 keV signal for a 7-pixel PoST when both TES signals are added. Because of the symmetry imposed by adding the signals together, many terms are overlapping each other. The inductor has been included, following the model parameters in Table 4.3 on page 102. The thin gray line is the theoretical limit as $G_a \to \infty$. The legend is in Figure 4.3 on page 74.
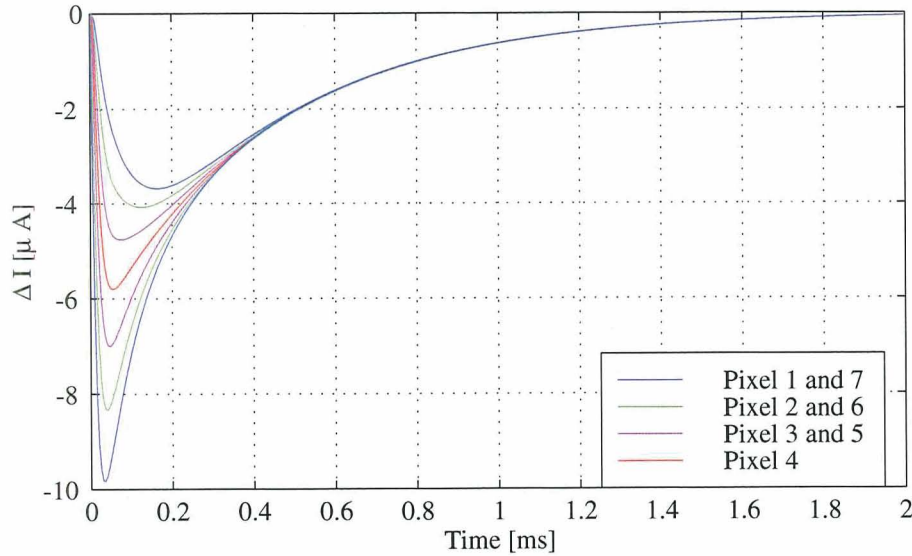
Figure 4.23: Time domain plot of 7-pixel plot response to 6 keV X-rays. The inductor has been included, following the model parameters in Table 4.3 on page 102. For an X-ray on pixel 1, TES1 would output the largest curve, and TES7 would output the smallest curve. For an X-ray on pixel 4, both TESs would output the middle curve. Note the large difference in shapes, which will allow very good position resolution.

at just one channel. Please see Appendix A for a discussion of the expected spectrum from a hanging heat capacity. The thin gray line is the theoretical noise for a single-pixel TES of heat capacity C_{tot} with conductance $2G$, power $2P$, and resistance $R/2$ (to account for the two TESs). We see we are almost at that limit, except for a bump in the noise around 2 kHz due to the link noise. This is what we wanted to see. The higher we make the link conductances, the closer we will be to the theoretical single-pixel limit, and the better resolution we will have. There is a limit on how strong we can make the link conductance: how well we can differentiate pulses from different pixels.

Figure 4.22 shows the same PoST, but with the inductance added, and the signals from a 6 keV X-ray into each pixel. We can see how the signals overlap and only diverge from each other at high frequencies. In the time domain the signals from each TES look like Figure 4.23. For an X-ray hitting pixel 1, TES1 will have a response like the largest pulse on the figure, while TES7 will have the smallest pulse on the figure. For an X-ray on pixel 2, TES1 will have the second largest signal and TES7 will have the second smallest, and so on. In this figure we can see that the difference from pixel to pixel is substantial, making the determination of the pixel hit a simple matter.

To get the energy resolution, we add the signals from the two TESs together, and obtain Figure 4.24. It is amazing how similar each of the added signals is to the others. It would be almost impossible to tell which pixel was hit by looking at this plot. This is the great advantage of the 1-D PoST: we have two TESs measuring each event, and there are two
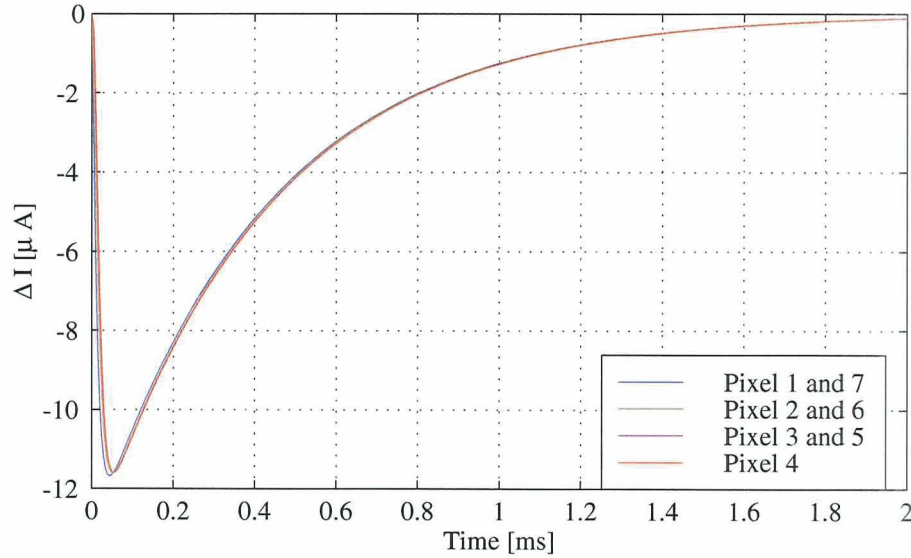
Figure 4.24: Time domain plot of 7-pixel plot response to 6 keV X-rays, both TESs added. The inductor has been included, following the model parameters in Table 4.3 on page 102. Note that the pulses look almost identical no matter where the X-ray hits. This is a great feature of the 1-D PoST: we have separated position and energy resolution into two orthogonal measurements. One measurement is TES1 - TES7 (position) and the other is TES1 + TES7 (energy). We therefore expect the resolution of the pixels to be fairly flat across the PoST. This is what we see in Table 4.5.

orthogonal measurements we are making. The first measurement is TES1 - TES7. This will give us the position resolution. Of course to obtain the position of the X-ray more complicated algorithms that include all points in the pulse can be used to allow the best differentiation of the pixels. This will be necessary for low energy photons (the lowest we expect to see for Constellation-X is around 200 eV) since these will have very small pulses and the noise will make it harder to determine their position on the PoST.

The second measurement is TES1 + TES7. This will give us the energy resolution. Figure 4.24 shows how little the shape of this measurement depends on which pixel was hit. This implies that the energy resolution of the PoST will be fairly constant across the pixels. We will soon see that this is indeed the case.

The total NEP for each pixel are calculated and theoretical resolution are shown in Figure 4.25. We see the dramatic improvement of resolution mainly from the cancellation at low frequencies of the link noise terms. By symmetry pixels 5-7 are the same as pixels 3-1. The thin gray line is the theoretical NEP for a single-pixel TES of the same heat capacity as the PoST, or the limit as $G_a \to \infty$. Note that as we move from pixel 1 to pixel 4, the PoST NEP deviates more and more at the high frequencies from the single-pixel case. This is because we are looking at the noise-equivalent power in each pixel, and the further toward the middle of the PoST we get, the more we see the effects of the several G_a's that separate the pixel from the readout TESs. The great thing is that looking at the resolution,
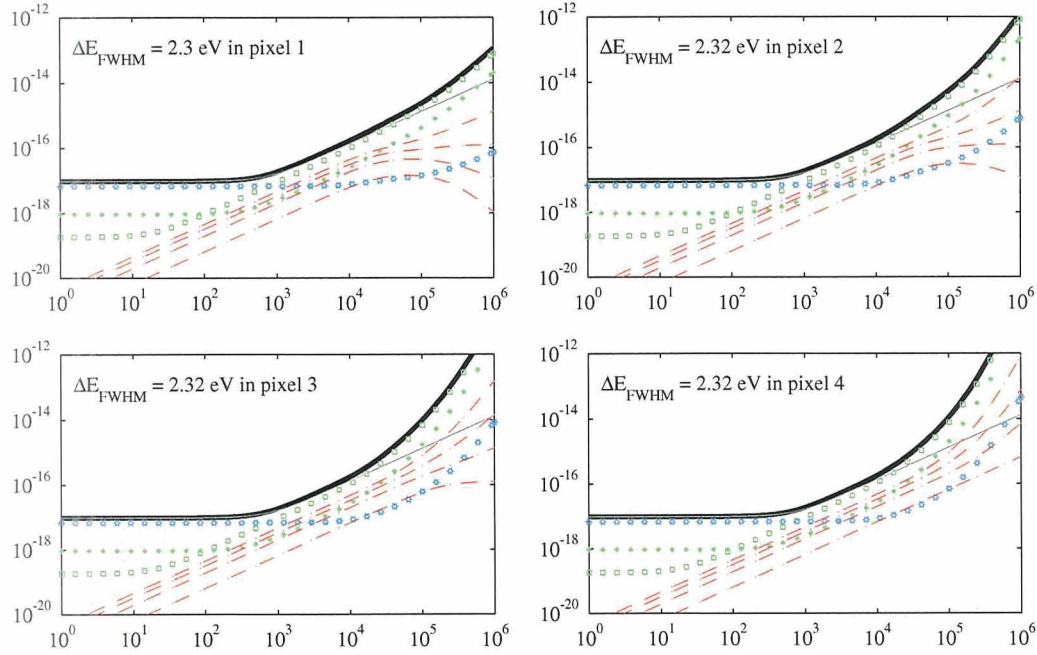
Figure 4.25: Theoretical NEP for a 7-pixel PoST with values from Table 4.3 on page 102. Both TES signals are added. The thin gray line is the theoretical limit as $G_a \to \infty$. The legend is in Figure 4.3 on page 74. Note that many terms are now overlapping each other. The X-axis is frequency in Hz, and the Y-axis is NEP in $W/\sqrt{Hz}$.

it does not change much from one pixel to the next. This is because the deviation from the theoretical NEP occurs at high frequencies, where the signal-to-noise ratio is small. As discussed in Section 3.1.5, the energy resolution comes mostly from the low NEP at low frequencies, which all pixels share. This is a graphical proof that we have succeeded in our original intent for the design: to have the signals be as similar as possible at low frequencies, where the SNR is large, and use the high frequencies for position resolution, where the SNR is small. The differences in pulse shapes will not affect the energy resolution very much because the NEP is so large at those high frequencies that its contribution to the energy resolution via Eq. (3.68) is very small.

In Table 4.5 we show the resolution obtained in each pixel for four cases: two with the saturation condition applied to pixel 1, and two with it applied to pixel two. In each case we tried two link conductances. ΔE $(G_a \to \infty)$ is the energy resolution of a single-pixel TES with the total heat capacity of the PoST. This is the best resolution attainable by that particular set of parameters, if one increased G_a. E_{sat} (pixel 4) is the photon energy that is needed to raise the TES temperature in the PoST to 0.5 mK (our saturation condition) when the photon hits pixel 4. This quantity gives an idea of the extra dynamic range the PoST has in the inner pixels due to the fact that they are further away from the TESs and thus can't deposit all the photon energy instantaneously into them.

Saturation on:	Pixel 1		Pixel 2		units
G_a	50	100	50	100	nW/K
C_e	1.27	1.3	0.97	1.02	pJ/K
C_{tot}	3.1224	3.1824	2.5224	2.6224	pJ/K
ΔE $(G_a \to \infty)$	2.0	2.02	1.8	1.83	eV
E_{sat} (pixel 4)	9.76	9.95	7.88	8.2	keV
Pixel	PoST resolution per pixel				
1	2.2635	2.1842	2.1085	2.0217	eV
2	2.2792	2.1917	2.1272	2.0304	
3	2.2829	2.1935	2.1315	2.0325	
4	2.2832	2.1937	2.1319	2.0327	
5	2.2829	2.1935	2.1315	2.0325	
6	2.2792	2.1917	2.1272	2.0304	
7	2.2635	2.1842	2.1085	2.0217	

Table 4.5: Comparison of theoretical resolution of 7-pixel PoST with both signals added together. The saturation condition of a 0.5 mK maximum temperature excursion for any TES has been applied for 6 keV photons on pixel 1 and 2. Two link conductances have been used. Other model parameters are in Table 4.3 on page 102. For comparison, a 1.92 pJ/K single-pixel TES (which satisfies the saturation condition) with similar parameters has a 1.64 eV resolution.

Because these are theoretical limits on the resolution for devices with these parameters, we have calculated them under perfect voltage bias conditions ($R_L = 0$), which mean $V_{cn} = 0$. A load resistor would add Johnson noise and would degrade the resolution. Compare the resolutions for the first column (which is the case we have been using corresponding to the parameters in Table 4.3 on page 102) to the resolutions shown in Figure 4.25, which include the load resistor. We see that a small load resistor cooled to base temperature is a less than a 2% effect in the energy resolution. If the load resistor was a at a higher temperature, the resolution would be affected accordingly.

We can conclude that a 7-pixel PoST has a theoretical resolution only $\sim$ 10% worse than the resolution of a single-pixel TES with its same heat capacity and other parameters. Compared to a lower heat capacity TES with the same saturation energy, the PoST has a 15-30% degradation depending on how the saturation condition is implemented in the PoST. The resolution is competitive for high-energy-resolution calorimeter designs.

To study the resolution of longer PoSTs, only a larger matrix and more computing power is needed, since we developed the theory for an m-pixel PoST. Future projects will include 15- and 30-pixel PoSTs. We may need to vary G_a as a function of pixel position along the PoST to ensure proper differentiation in these very long PoSTs. The energy resolution in these devices must be calculated, to understand at what length PoST the energy resolution degradation becomes unacceptable.

4.5.2   Beyond the PoST

In the previous derivation we have obtained the noise and energy resolution for a two-TES calorimeter. This formulation can be easily extended to more thermometers, as in the case of a 2-D PoST with four TESs, one on each side of a grid of pixels. The equations for this two dimensional system would be set up in the same way as the linear PoST, except that now we would have four current equations. If a, b, c, and d are the indices in the vector $\vec{\Delta}$ that correspond to the currents of the four TESs, then the total signal when a noise source $\vec{N}$ acts on the system is

$$\Delta I_{\text{added}} = \sum_j \left(\mathbf{S}_{a,j} + \mathbf{S}_{b,j} + \mathbf{S}_{c,j} + \mathbf{S}_{d,j} \right) \vec{N}_j \tag{4.63}$$

The NEP for pixel i is then

$$\left\langle \left| \text{NEP}_{i,\text{added}}(\omega) \right|^2 \right\rangle = \left\langle \left| \frac{\sum_j \left(\mathbf{S}_{a,j} + \mathbf{S}_{b,j} + \mathbf{S}_{c,j} + \mathbf{S}_{d,j} \right) \vec{N}_j(\omega)}{\mathbf{S}_{a,i} + \mathbf{S}_{b,i} + \mathbf{S}_{c,i} + \mathbf{S}_{d,i}} \right|^2 \right\rangle \tag{4.64}$$

The procedure developed in this thesis is easily extended or modified to other interesting systems, as long as a valid linearization is possible. The energy resolution for very complex devices can be determined using this general formalism.

Part II

Experiment

Chapter 5

Experimental Apparatus

We begin Part II of this thesis with a short overview of the hardware and software required to run and analyze PoST calorimeters.

5.1 Getting cold

To run our 100 mK devices we use a dilution refrigerator (DR) provided to Goddard by the SHE corporation around 1985. The refrigerator cold plate can reach 30 mK, and has 4 K, 1.2 K, 700 mK, and 200 mK stages. Figure 5.1 shows the setup. The detector assembly (on the table to the right of the refrigerator) mounts on the bottom to the copper part that resembles a spool.

The detector assembly was originally designed for a Kelvinox 25, where our first single-pixel TES results were obtained. The available space in the Kelvinox was very restricted, which shows in the design. Figure 5.2 shows a rendered CAD drawing of the detector assembly. To fit in the tight cylindrical space the bias circuit, the detectors and the X-ray sources[1] we implemented a "T" configuration which allowed the detectors to lie perpendicular to the centerline. The bias circuit is placed in the beam of the "T", along with a GRT thermometer and a heater, to regulate the temperature as close to the detector as possible (Figure 5.3).

A 6 mCi ^{55}Fe annular source radiates 5.9 keV Mg K_α and 6.4 keV Mg K_β X-rays onto an aluminum target that fluoresces 1.5 keV Al K_α X-rays. About one in six of the Mn X-rays backscatters, so the output of the source is 83% Al, 17% Mn X-rays. We also have a separate ^{44}Ca source that emits 3.3 keV K K_α X-rays.

For magnetic shielding, the entire helium dewar is surrounded by a sheet of Mu-metal. Since the dilution refrigerator has no magnets, we are only trying to cut down on the Earth's magnetic field. The detector assembly itself is enclosed in an aluminum cylinder which is heat sunk through copper straps, and the copper "T" is heat sunk via a 1 mm thick 99.999%

---

[1]Neither the Kelvinox nor the SHE have window ports, so X-ray sources have to be placed in the refrigerator with the calorimeters.
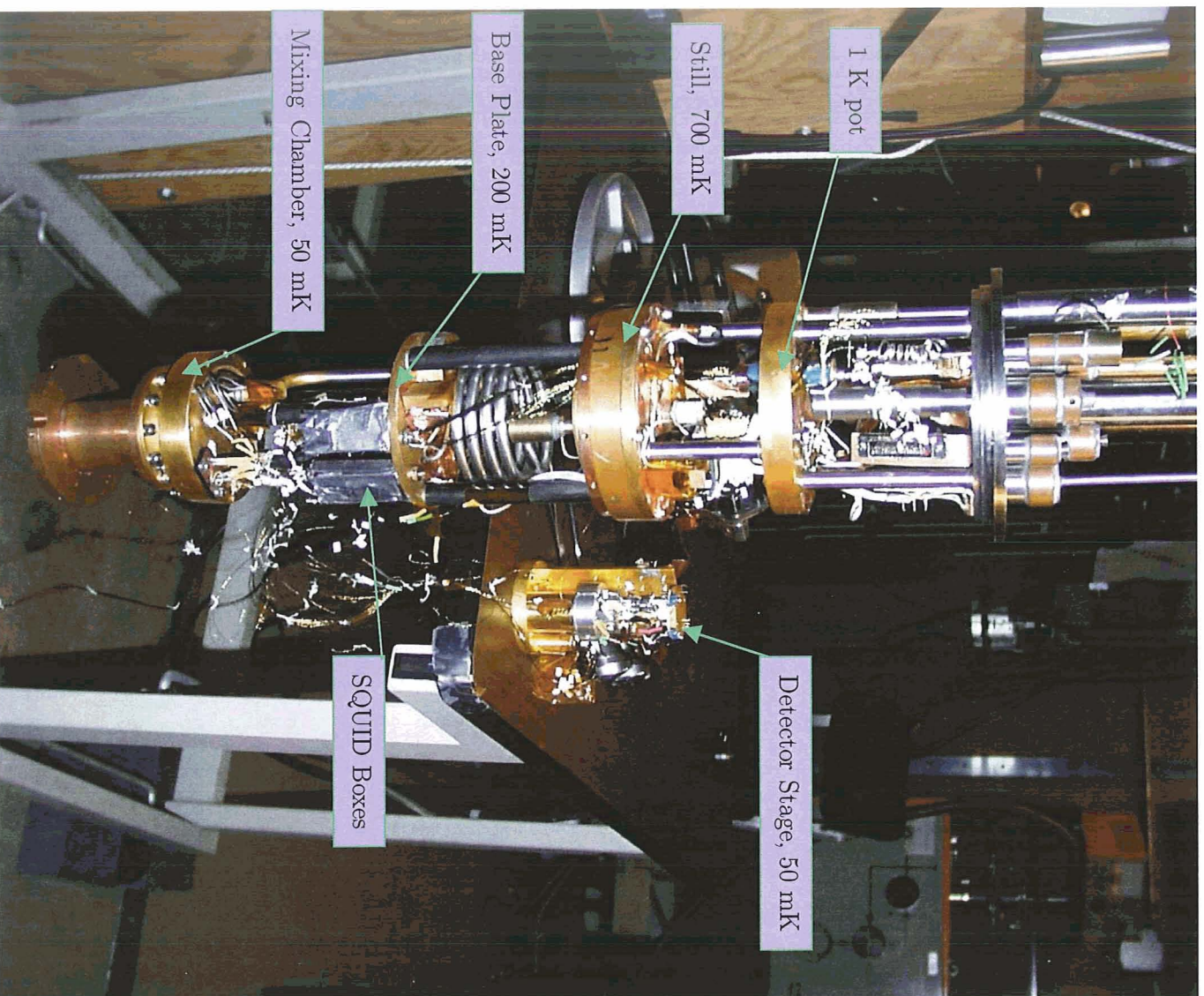
Figure 5.1: Picture of the dilution refrigerator.
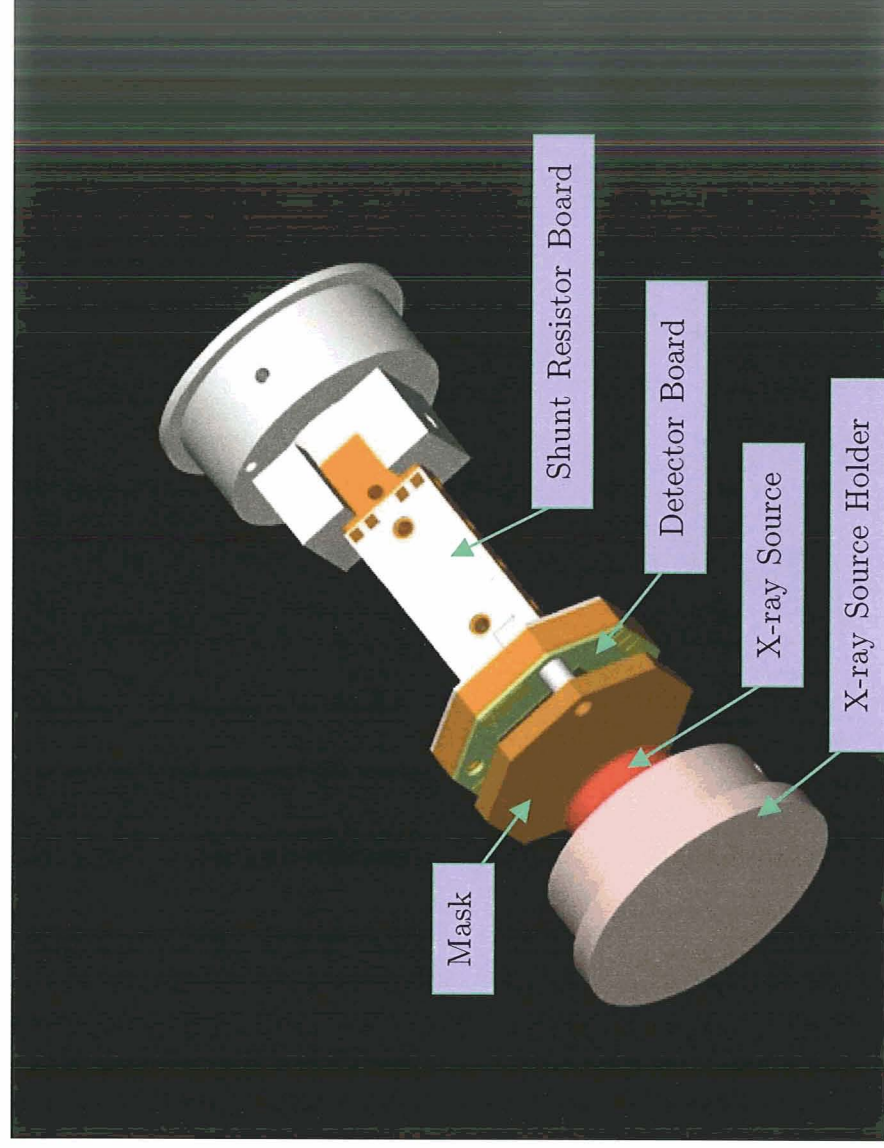
Figure 5.2: Rendering of the detector mount design.
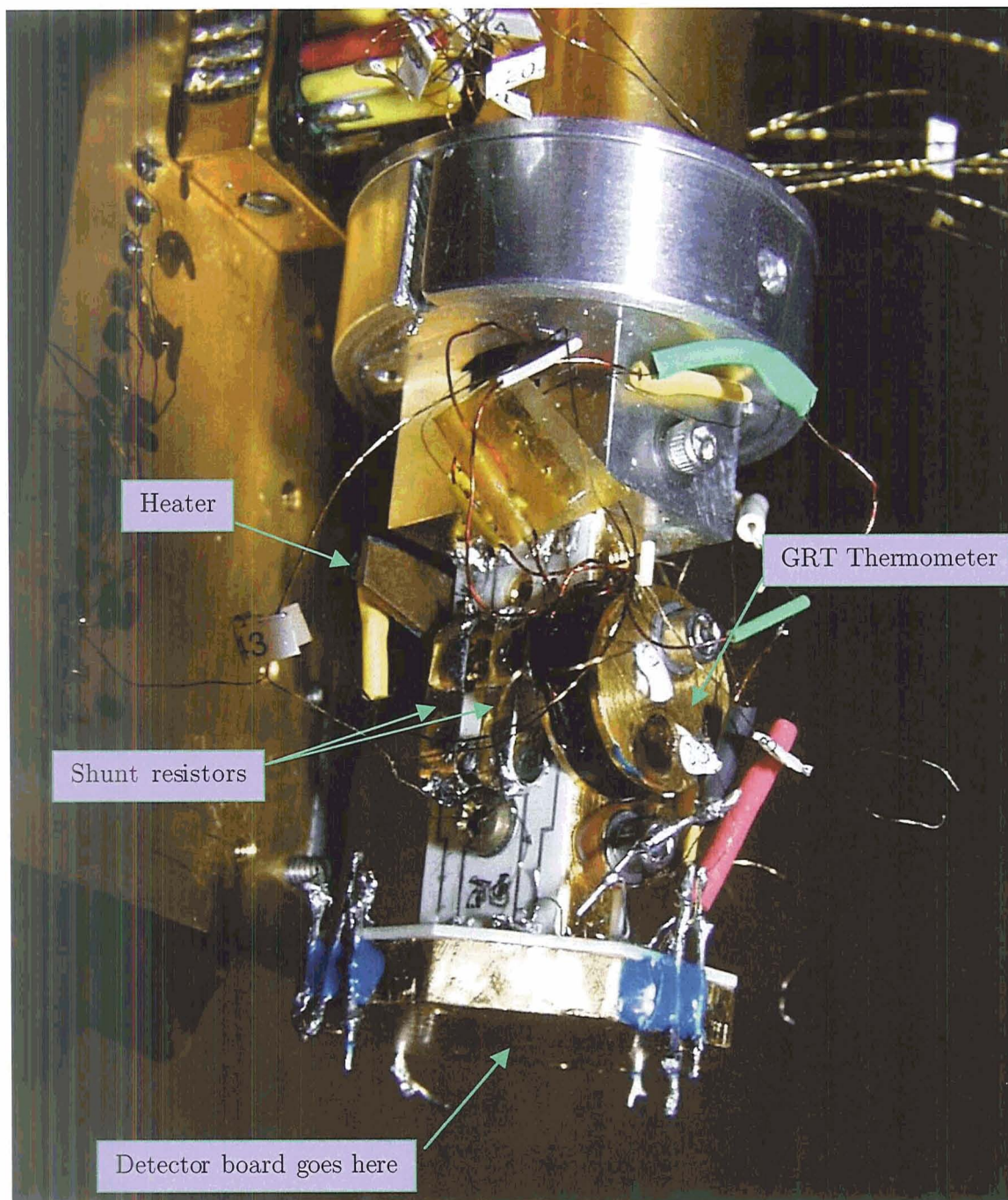
Figure 5.3: Close-up of detector mount.
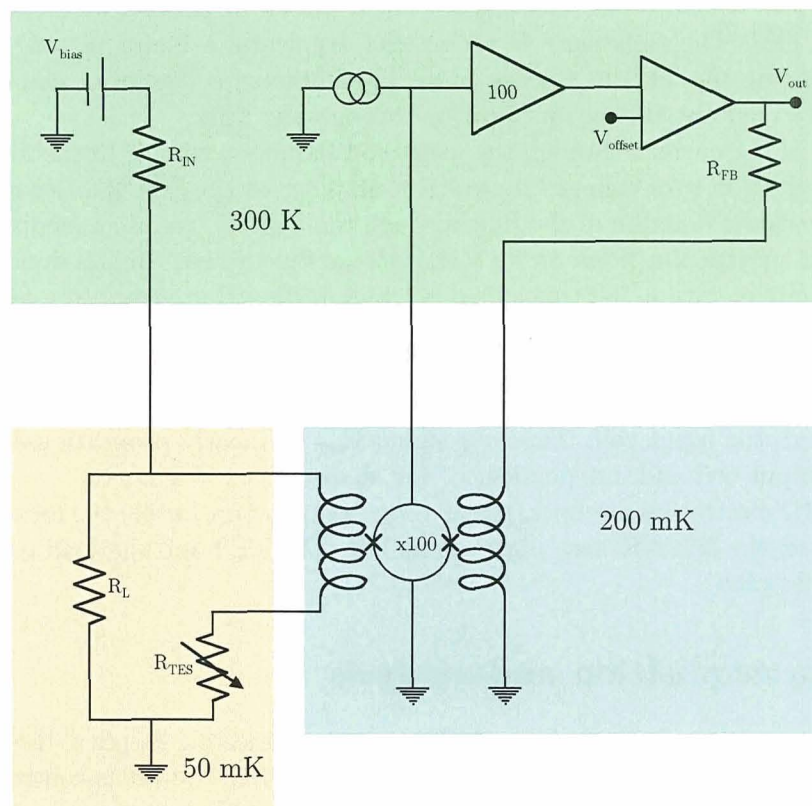
Figure 5.4: TES bias and SQUID readout circuit.

pure silver wire. The entire DR is enclosed in an shielded room to keep out radio-frequency (RF) signals.

5.2   SQUID electronics

Because TESs have a low resistance, they are not well matched to the JFET amplifiers used with doped silicon and germanium thermistors. To read out our 5-20 mΩ resistance, we use Superconducting Quantum Interference Devices, or SQUIDs. A good reference for SQUID fundamentals is Vanduzer and Turner (1999, chap. 5). SQUIDs are well matched to low impedance sources, and act as very sensitive ammeters. To get the high bandwidth and slew rate that we need for our signals, we use SQUID arrays provided by the National Institute of Standards and Technology (NIST) in Boulder, CO (Huber et al., 1997). These SQUID arrays can consist of about 100 SQUIDS in series, which act coherently to provide a much larger signal than a single SQUID. A schematic of the circuit is shown in Figure 5.4.

The TES is biased by a voltage source with an large resistor R_{in} (~ 1 kΩ), approximating a current source. A load (or shunt) resistor R_L is placed in parallel with the SQUID input coil and the TES. The resistance R_L is smaller (typically a factor of ten) than the TES resistance, placing the TES in voltage bias. The inductor is the input coil of the SQUID, and with it we read out the current flowing through the TES.

A change in the current through the input coil induces a change in the flux (Φ) through the SQUID, which in turn changes the voltage drop across the SQUID. Because the SQUID voltage is a periodic function of the flux through the SQUID, we use a feedback coil to lock the SQUID at a particular point on its V-Φ (voltage-flux) curve. This is done by amplifying the SQUID voltage with a 100 times preamp, and feeding that signal to a feedback circuit, which is connected to the feedback coil through a resistor R_{FB} (~ 1 kΩ). The lock point of the V-Φ curve is chosen by setting V_{offset}. Since the feedback circuit keeps a constant flux through the SQUID, the current flowing through the feedback coil is proportional to the current through the input coil. Thus our signal V_{out} is linearly proportional to the current through the input coil and independent of the shape of the V-Φ curve.

The SQUID electronics are operated at room temperature, while the four SQUID arrays are mounted on the 200 mK base plate of the DR. The TES and the load resistor reside at the 50 mK cold plate.

5.3 Data acquisition and analysis

The output signal V_{out} is feed differentially into a Princeton Applied Research Systems preamplifier and then to a Nicolet digital oscilloscope. The Nicolet is controlled through a GPIB interface by a computer. The computer software triggers on pulses and saves them to disk in our own binary format. The usual digitization frequency is around 100 kHz, and the saved pules are 8192 points long.

To analyze the data, an array of about 200 noise traces is obtained from the data and an average noise power spectrum is computed. A rise-time pulse-height plot is made to pick out a particular line for the creation of the optimal filter (usually the Al K$_\alpha$ line). About 100 pulses are summed to obtain the average pulse, taking care to reject double pulse hits, and its frequency spectrum is computed, keeping the phase information. The optimal filter is computed by dividing the average pulse spectrum by the average noise squared, as per Section 3.1.4. This optimal filter is inverse-transformed back to the time domain. The optimal filter is now operated on each trace, again rejecting double pulses. This involves multiplying point for point the optimal filter with the trace and summing the result. This is done for several phase shifts of the optimal filter (3 to 10 around zero phase) to determine trigger jitter. A quadratic function is fitted to the top four values, and its maximum is taken as the optimally filtered estimate of the energy of the X-ray.

Once this has been done, we gain correct the data and histogram it. Lines are identified and used to calibrate the energy scale, and finally the histogram is fit to the natural line shapes taken from Fischer and Baun (1965); Nordfors (1955) to obtain the energy resolution of the device.

Chapter 6

Position-Sensitive Transition-Edge Sensor Design

Chapters 2 and 4 explained the concept and theory of a PoST calorimeter. This chapter presents the implementation of this idea into a working detector. This PoST design is based on the knowledge gained from our single-pixel TES development using molybdenum/gold bilayer TESs (Figueroa-Feliciano et al., 2000b; Lindeman et al., 2002; Stahle et al., 2000, 2002). We have successfully designed a device that is completely compatible with our single-pixel process, to allow seamless integration of both technologies into a single detector.

6.1 Single-Pixel TES design and results

The energy resolution of a PoST will only be as good as the TESs we instrument it with. We will briefly describe the progress made in the past two years on our ongoing single-pixel TES development for Constellation-X.

We operate our devices at very cold temperatures ($\sim$ 100 mK) to obtain good energy resolution. The operating temperature is chosen by an optimization of all parameters. Generally, the lower the temperature, the better the energy resolution (Eq. (3.75)). The refrigerators we use have base temperatures of $\sim$ 50 mK (Section 5.1). The operating temperature of the TES has to be higher to be able to put in bias power into the thermistor (Eq. (2.7)). The optimization of signal strength, decay time and energy resolution gives optimum results for 50 mK base temperatures around $\sim$ 100 mK.

To obtain good control of the transition temperature, our TES are made of molybdenum/gold bilayers. These thin superconducting films can be designed to have a specific superconducting-transition temperature by taking advantage of the proximity effect. The proximity effect makes two thin films in contact with each other have a superconducting transition at a temperature between the bulk critical temperature T_c of the two materials. See Guerron (1997, chap. 5) and references therein for a thorough derivation of proximity-effect theory. The T_c of Mo is 920 mK, and that of gold is 0 K (theoretical). We tune the T_c of the bilayer film to 100 mK by the appropriate choice of thickness of molybdenum and
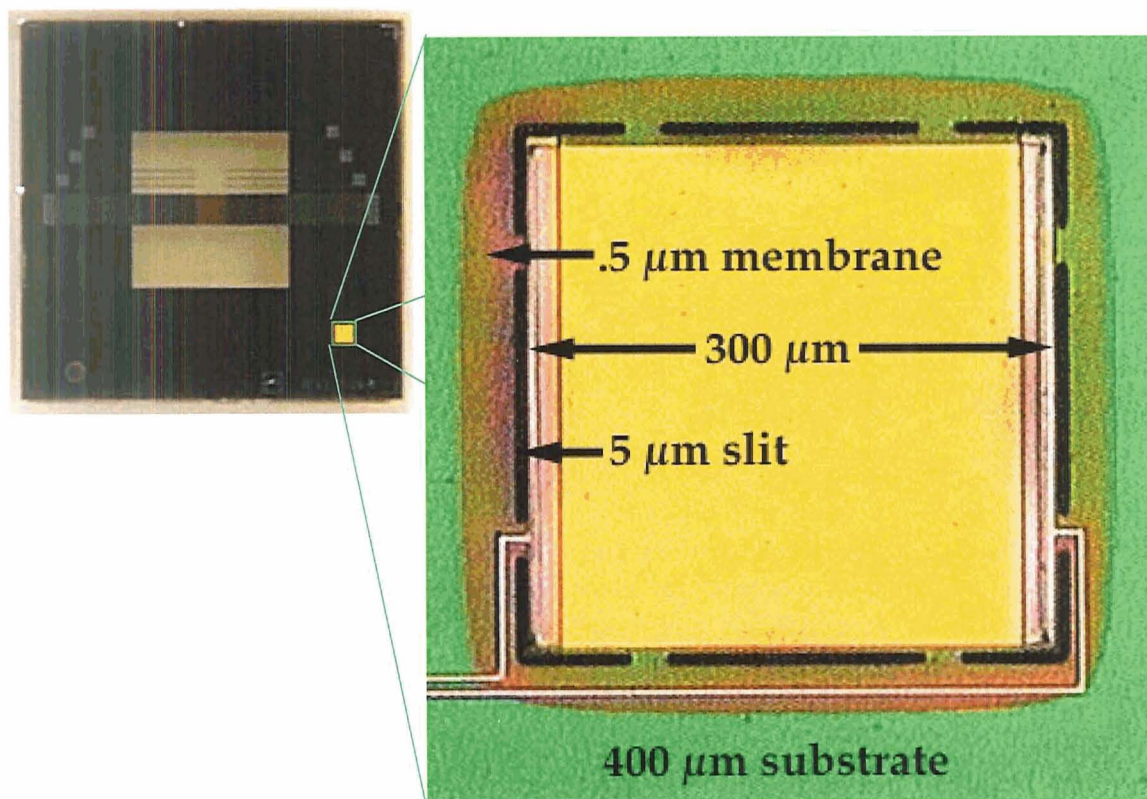
Figure 6.1: Picture of a NASA-Goddard-designed single-pixel TES calorimeters. The new devices (on the right) have a very small footprint compared to the old Goddard TES devices (on the left) and have demonstrated high energy resolution.

gold.

Figure 6.1 shows our state-of-the-art calorimeters. 5×5 arrays of these calorimeters have been successfully fabricated. The upper right chip is our old detector design, to show the progress we have made in shrinking the devices to the necessary size for Constellation-X. In the old design, a large (mm size) membrane served as the weak thermal link between the TES and the substrate. The new devices establish a 20 mK thermal gradient[1] across a 5 μm slitted membrane with low thermal conductances. We found that the thermal conductance of our nitride membrane is specular, and the thermal conduction behaves more like ballistic propagation of admissible phonon modes through the nitride between the TES and the cold silicon than like diffusion through a link (Stahle et al., 2002). Thus the conductivity depends very weakly on the length of the nitride bridge, and strongly on the radiative perimeter of the TES. This breakthrough allows us to make much smaller devices which

---

[1]The devices we did this test on had 70 mK transitions, thus the 20 mK gradient. We do not foresee any problem with establishing a 50 mK gradient when we test the 100 mK transition devices.
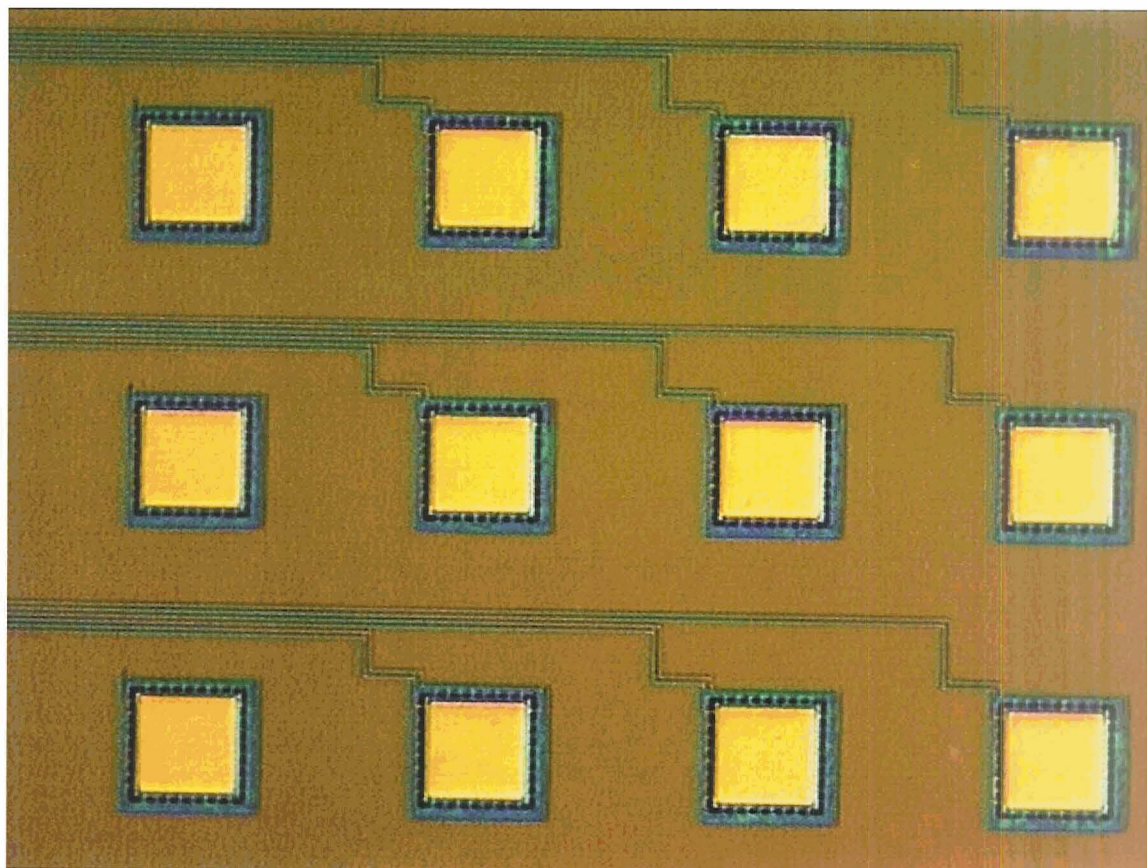
Figure 6.2: Picture of a NASA-Goddard-designed single-pixel TES array of calorimeters.

will fit in the Constellation-X design envelope. Figure 6.2 shows one of our arrays. The devices are 150 μm squares set at a 400 μm pitch. The pitch was originally set to 400 μm to accommodate a wet etching process, but we have since acquired a deep RIE (reactive ion etcher) that will allow us to make arrays in the required 250 μm pitch.

In order to have high filling fractions, we have developed a technique for depositing bismuth absorbers larger than the TES they are connected to. A schematic is shown in Figure 6.3(a). The bismuth absorber has an overhang that spans out over the nitride film and covers the cell area without touching the nitride or substrate. Only the central "stem" area of the absorber is in contact with the TES. We call these structures "mushrooms." Figure 6.3(b) shows a validation test of a 32 × 32 array of bismuth absorbers (no TES underneath) showing the excellent packing fraction achievable with this design. One can see the stem area, which is the only area of the mushroom actually touching the substrate.

Figure 6.4 shows our current resolution at Al Kα of 2.4 eV FWHM. The energy resolution of our PoSTs will be compared to this single-pixel result, which is limited by an excess voltage noise across the TES that gets worse for lower bias position in the transition (Lindeman et al., 2002). Since the same processing is done on the TESs used on our PoSTs,
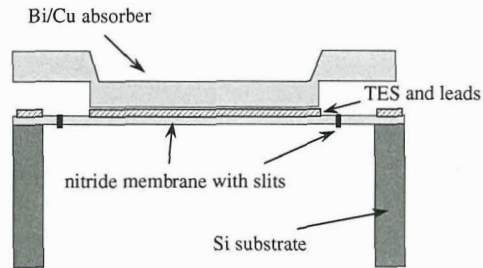
(a)
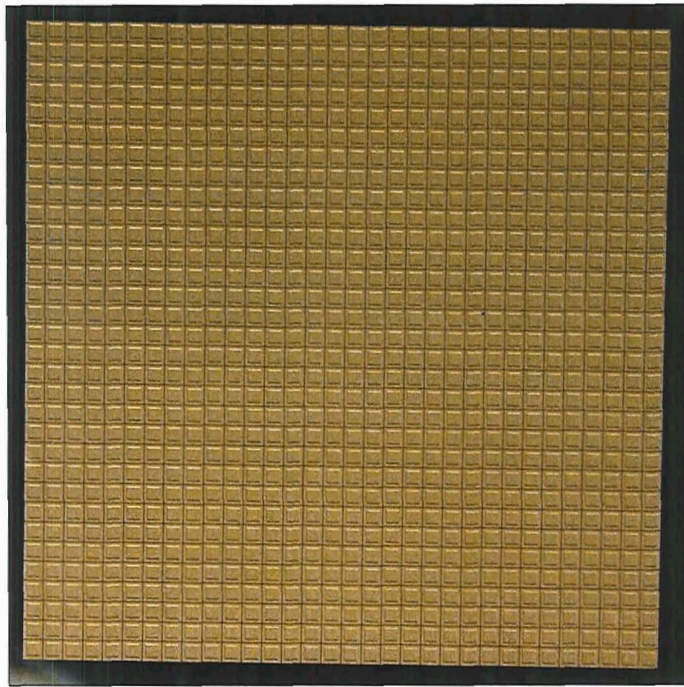
(b)

Figure 6.3: (a) Absorber mushroom schematic. Overhangs give the absorber its "mushroom" shape, and allow the entire pixel cell area to be used, creating excellent packing fractions in our arrays. (b) A 32×32 array of bismuth mushroom absorbers on nitride membranes. This demonstration shows the packing fraction possible with this scheme. There are no TESs under these absorbers, this was a feasibility test.
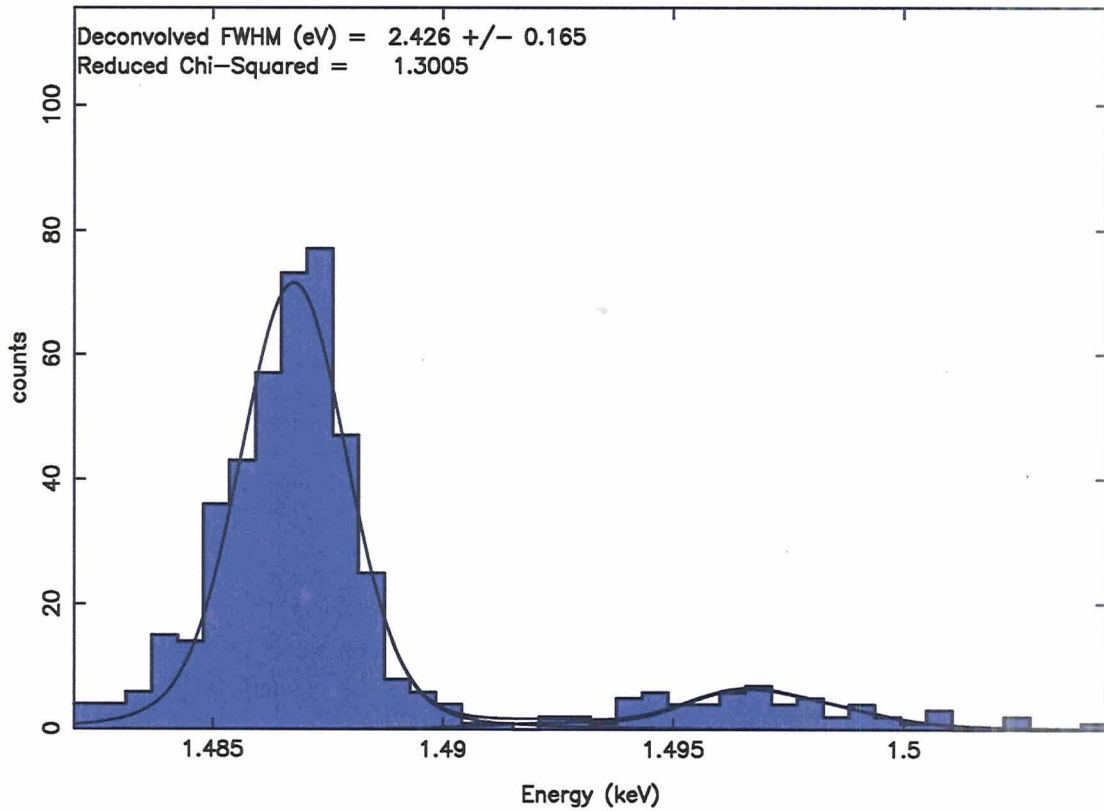
Figure 6.4: Al Kα line at 1.5 keV. The 2.4 eV FWHM resolution is limited by an excess voltage noise seen in our TESs.

we expect to have the same excess noise present in our devices.

6.2 Absorber selection

There are several options for the absorber to be used: metals, semiconductors, or superconductors. This critical element of the calorimeter will drive the physics of the device, so we will look at all three options.

6.2.1 Position dependence in absorbers

On a single pixel device, position dependence is an adversary. When designing a single pixel calorimeter, one needs the signal from a 1.5 keV X-ray, for example, to look identical no matter if it hits the absorber dead center or near one of the corners. If there is a difference in the shape or size of the signal then the pixel has "position dependence." Since energy is determined by the shape and size of the signal, any change in these parameters implies a

degradation in energy resolution for the device.

In our imaging calorimeter, position dependence is exactly what we want. In a single pixel no attempt is being made to determine where in the pixel the photon hit, so all photons are binned together to create the spectrum seen by the pixel. In an imaging calorimeter, one intends to determine the position of the absorption event in the absorber, and for that one needs position dependence. Once the position of the event has been determined, photons can be grouped according to location, in other words, one can "pixellate" the absorber, and thus bin like signals together to retain the high energy resolution while simultaneously gaining position resolution.

This binning is normally done in software. As discussed in Section 2.4.3, we have taken another route by physically pixellating the long absorber. This produces discrete pulse shapes in the detector, from which the pixel can be determined. A drawback of this approach is that it fixes the pixel size, but one gains intrinsic pixellation and allows for easier data analysis.

6.2.2 Semiconductor absorbers

When X-ray calorimetry was proposed, using silicon as the absorber was one of the first things looked at. The problem with silicon (and semiconductors in general) is that the initial photoelectron breaks apart many electron-hole pairs. If the thermometer used only measures the phonon temperature, then the electron-hole pairs have to recombine before the energy that went into breaking them can be measured. Electrons and holes that make it to the surfaces of the sample, where there are numerous dangling bonds, crystal deformities, and impurities (gunk stuck to the surface), will easily find a counterpart to annihilate with (because of the many states available). When they annihilate, they release their energy as phonons. But if they hit an impurity site or a dislocation in the bulk, they will get trapped and will not be able to recombine. The statistics of a few electron-hole pairs that do not recombine for each X-ray are enough to be the dominant noise term in your energy resolution. Thus, you really want 100% recombination, which is very hard to guarantee. Ultra-pure germanium is a possibility which we are investigating. See Cabrera et al. (1993); Tamura (1993) for a detailed discussion on phonon thermalization in semiconductors.

6.2.3 Superconducting absorbers

Superconductors have the great advantage that their heat capacity is dominated by the phonon term in the material, which is proportional to $(T/\Theta_D)^3$, where Θ_D is the Debye temperature (Ashcroft and Mermin, 1976). To obtain the lowest heat capacity, one would want a superconducting material with high Debye temperature. When an X-ray is absorbed, the resulting photoelectron creates phonons and also breaks Cooper pairs into quasiparticles. Phonons with energy above the gap (2Δ) of the superconductor can be absorbed by Cooper pairs and create more quasiparticles. The number of quasiparticles produced is proportional to $2\Delta/E$ (where E is the X-ray energy). Because the gap in superconductors is much smaller than the gap in semiconductors, the number of quasiparticles created for an energy E is

much higher than the number of electron-hole pairs in a semiconductor for the same energy. The size of the signal seen in the calorimeter depends on the number of these quasiparticles that recombine into Cooper pairs within the decay time constant of the pulse, releasing the excess energy as phonons that the calorimeter can sense. Fluctuations in this number from X-ray to X-ray will degrade the resolution, just as fluctuations in the number of electron-hole pair recombination affects the resolution of semiconductors. Because the energy of each particle is much smaller in superconductors ($\sim$ meV) than in semiconductors ($\sim$ eV), superconductors have an advantage since they are less sensitive to statistical variations associated with incomplete thermalization (Vitale et al., 1992).

The problem with superconductors is thermalization. In order to obtain a signal in the calorimeter, the quasiparticles must recombine to create phonons. The problem is that the phonons created by the quasiparticle recombination are of energy 2Δ or higher, enough to break another Cooper pair. The time constant for a phonon to break a Cooper pair is often much less than the time constant for the phonon to escape the superconductor and enter the TES. Thus a bottleneck can form, where phonons created by quasiparticle recombination are absorbed by Cooper pairs before they can escape into the TES. This effect has been studied by Rothwarf and Taylor (1967) and Kozorezov (2000). Its application to calorimeters has been studied by Cosulich et al. (1993); Stahle (1991); and Vitale et al. (1992).

To aid in thermalization, it has been realized (see Booth, 1987; Zehnder, 1995) that one needs superconductors with low Debye temperatures (which imply a lower-energy phonon distribution, i.e. less phonons with energies over 2Δ) and higher gaps (so the energy 2Δ is higher and thus less phonons break Cooper pairs). A low Debye temperature is in direct opposition to the heat capacity considerations. For this reason elements such as rhenium, which is a prime candidate as an absorber, is being compared with tin, which has a good compromise between Debye temperature, gap and heat capacity (van den Berg et al., 2000). Bandler et al. (2000) has achieved excellent results with tin.

6.2.4 Metal absorbers

Metals have no gap, and no long lived states like the semiconductors and superconductors. They thermalize very quickly (Fann et al., 1993) and have good X-ray stopping power. The problem, of course, is heat capacity.

In low α devices, the heat capacity budget makes metal absorbers impractical for most applications. In high α devices, the heat capacity can be much bigger, per Eq. (2.26). Because the high α gives a larger heat capacity budget to obtain the same saturation energy as a low α device, TESs, with their high α, can consider metals as candidates for absorbers.

For a $\Delta T_{sat} = 0.5$ mK saturation at 6 keV, the desired total heat capacity for a single-pixel calorimeter is 1.92 pJ/K, or 12 keV/mK. To stop 6 keV X-rays, the thickness required still poses a heat capacity problem for most metals. If we use gold, with an attenuation length of 1 μm at 6 keV, we would need 5 μm for 95% absorption (see Center for X-ray optics; NIST physical reference data). For Constellation-X, with a pixel unit cell size of 250 μm, that would be 2.2 pJ/K, or 14 keV/mK, already above the desired heat capacity,

without taking into account the heat capacity of the TES itself.

We are studying a composite absorber made from bismuth and gold. Bismuth is a semimetal with low heat capacity and good X-ray stopping power. At 100 mK, the electron system heat capacity of bismuth is about the same as the phonon heat capacity. Bismuth has an attenuation length for 6 keV photons of about 2 μm. For 95% absorption, one needs 10 μm of bismuth. The heat capacity per unit volume of bismuth is roughly 100 times less than that of gold. A 10 μm thick 250 μm wide bismuth absorber would have a heat capacity of 57 fJ/K, or 0.356 keV/mK.

The low number of conduction band electrons in bismuth means the thermalization time is much slower (Kopylov and Mezhov-Deglin, 1974; Mezhov-Deglin et al., 1975). If we use our mushroom design for the absorbers to get a high packing fraction, position dependence becomes an issue. An X-ray hitting the wing of the mushroom might have a different pulse shape than the same X-ray hitting over the stem (Figure 6.3). Since bismuth has such a low heat capacity, a layered absorber made of bismuth and gold layers might provide the right combination of X-ray stopping power, low heat capacity, and rapid thermalization. This concept has yet to be demonstrated on a TES with mushroom absorbers, but it is one of the high-priority items to be investigated by our group.

6.3   PoST design

When engineering a never-before-tested detector design, coverage of parameter phase space is very important. No matter how much modeling one does, there is always the possibility of overlooking something, and ending up with devices that behave very differently from the computer models. It is therefore prudent to be conservative in the design and have various versions of the device that range from the "this has to work" devices to the "these would run great!" devices. In this spirit we designed 7-, 15-, and 31-pixel PoSTs, each with several versions of different time constants and in different places in the security vs. aggressiveness phase space.

It is also prudent to use as much proven technology as possible. Many fabrication techniques were borrowed from our single-pixel TESs. The PoST design leveraged heavily on the great work already done by the Goddard calorimeter group, and using our existing techniques as building blocks, we came up with the initial PoST design. Figure 6.5 shows the general features of our first iteration of PoSTs. A large silicon nitride membrane has been slit into strips. On each strip there are two moly/gold TESs flanking a linear array of bismuth absorber pixels. Beneath the bismuth we have deposited a layer of gold that acts as the thermal link between each pixel. This gold film also connects to each TES at either end. This figure shows an array of seven 15-pixel PoSTs, for a total of 105 pixels read out by 14 TESs.

Once the initial design was done, the task of calculating hard numbers for each parameter and dimension was tackled.
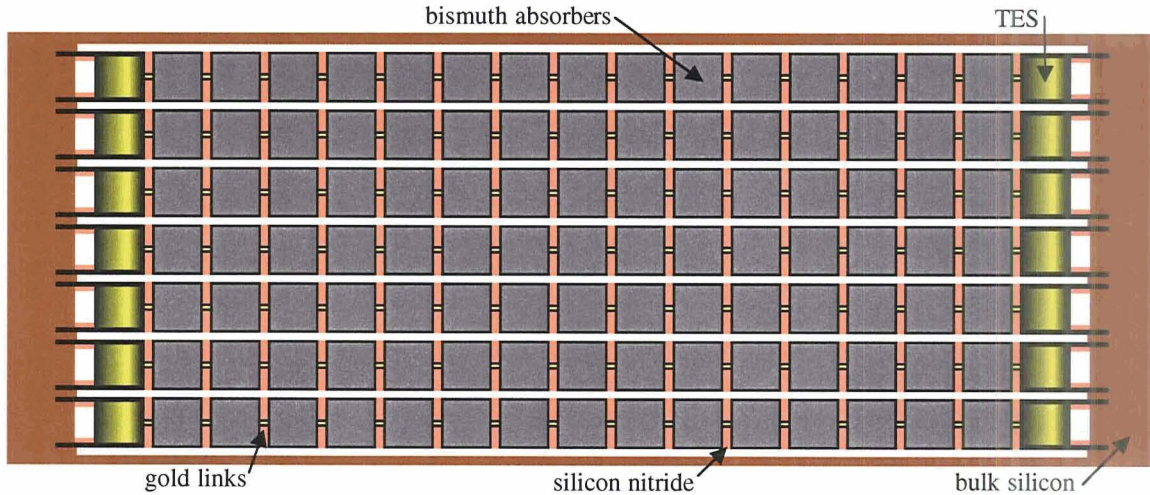
Figure 6.5: Goddard PoST design. Using the elements from our single pixel TES development, we suspend the PoST in silicon nitride and use it as the weak thermal link to the bath. We use moly/gold TESs, bismuth absorbers, and connect the absorber pixels with gold links.

6.3.1 Time constants and heat capacity

In the previous chapter we calculated the theoretical resolution for a 7-pixel PoST calorimeter. We used "typical" values for heat capacities and conductances. In those calculations no assumptions were made as to the actual dimensions of these devices, nor to the materials to be used. Our current development of PoSTs is geared toward eventual adaptation of this technology to the Constellation-X mission. Therefore we wanted to design devices that would work under the Constellation-X requirements. For a first cut at making PoSTs, however, much more conservative numbers were used.

Constellation-X count rate specifications place a limit on how long the decay time constant (also called effective time constant) of the pulses can be. This turns out to be ~ 100 μs. For a new detector design, this is a very aggressive number. We opted for much more conservative values ranging from ~ 300 μs to 1.5 ms.

The τ_{eff} depends on α, the conductance to the bath, and the heat capacity, among other parameters.[2] If we assume $\alpha \sim 90$, and given a total heat capacity of the PoST C_{tot} (2 TESs plus absorbers), we can use Eq. (4.10) to engineer τ_{eff} by the appropriate selection of G.[3]

---

[2]The τ_{eff} for a multi-pixel PoST in a full bias circuit has not been calculated analytically, but we can determine it numerically. Eq. (4.10) gives us an approximately correct form in the low-inductance, high link conductance limit (with $\alpha_{\text{I}} = R_{\text{L}} = 0$). This equation was derived for a 2-pixel PoST, which has no absorbers, so he total heat capacity is 2C, the conductance is 2G, and the power is 2P; all the factors of two cancel.

[3]G is the weak link from the PoST to the substrate. Here we assume the electron phonon coupling of the

In the initial PoST design, we wanted the to count as "pixels" only the absorbers in the link, not the TESs themselves. The main reason is heat capacity and saturation. Heat deposited by X-rays in the absorber pixels diffuses into the TES through the gold links. The heat capacities of the absorbers and the conductance of the link act as a low pass filter preventing thermal spikes (like that due to a photon absorption) to go through to the TES instantaneously. Since the signal is thermalized in the absorbers before it arrives at the TES, the total temperature rise of the TES is smaller than if the X-ray had been absorbed in the TES and *all* of the energy of the X-ray had been deposited in the TES at once. In other words, for a given heat capacity the saturation energy of the PoST is larger if one does not count the TESs as pixels.

So when we talk about a 7-pixel PoST, we are talking about a device with 7 absorbers connected to two TESs. But there is an area coverage problem. If we look at Figure 6.5, we see the TESs and the weak thermal link stick out on either side of the absorbers. This is all dead area of the detector. One solution is to make the TES very small and cover it by the mushroom overhang from the edge pixels. But this is a complicated geometry and we wanted to keep things as simple as possible. We chose to make the TES the same size as the bismuth absorbers, making the TES the size of an extra pixel. So the 7-pixel PoSTs actually have 9 pixels, but as we will see the signal from the TESs is very different than from the absorbers, and for now we just disregard TES hits in our prototype PoST design. In future designs we will study the trade-offs between just using the TES as a pixel (in which case it will be a 250 μm square) or not (in which case it will have to "hide" under a bismuth mushroom overhang from an adjacent pixel).

In Section 4.4 we determined the values of the heat capacities needed on the TESs to not exceed the saturation condition of Section 2.2.6. Those heat capacities ended up in the 1.3 pJ/K range. Because we wanted to keep the PoST size to the Constellation-X specifications and we decide to make the TESs the same size as the pixels, 250 μm square TESs were baselined. A 250 μm square of our Mo/Au TES bilayer has a heat capacity at 100 mK of ~ 0.15 pJ/K, almost an order of magnitude smaller. In order to maximize the chances of the PoST working; no change to the TES thickness was desired, and no extra heat capacity was added. The saturation energy of the PoST would therefore be smaller than 6 keV.

The absorber heat capacity depends on the material used for the absorber. In Section 6.2 we presented several different options for PoST absorbers. Bismuth is a very good candidate for the absorber material, and our single-pixel devices use bismuth as their absorber, so bismuth was the obvious route to take in the first PoST devices. As we will see shortly, we needed gold to aid in the thermalization of the pixels. Using 10 μm of Bismuth for good X-ray stopping power and accounting for the gold we need to place on the absorbers we obtained an estimate of the heat capacity of each 250 μm pixel in the absorber of ~ 83 fJ/K (total, gold plus bismuth). Once the heat capacity of the PoST is fixed, then the thermal conductance to the bath can be determined using the models developed in Section 4.4. We selected conductances for the nitride conductance from the PoST to the

---

TES is strong, and the weak link occurs between the phonon system of the TES and the substrate phonon system. In this case $G = G_{pb}$.

bath of G_{pb} = 11 to 68 pW/K. From Dorozhkin et al. (1986) we determined that the electron-phonon conductance G_{ep} was orders of magnitude larger than these numbers, so we could disregard the phonon system of the TES for the model.

At the time, we had not yet obtained the result that our nitride membranes were specular (see page 122) and thus the conductance did not depend strongly on the length of the nitride, but on TES perimeter (Stahle et al., 2002). Using values from Holmes et al. (1998) and Levio and Pekola (1998), which assume a diffusive nitride membrane, we calculated the length of nitride needed to provide the decay times desired ($\sim$ 300 to 1.5 μs) with the heat capacities determined above. We calculated numbers from 140 to 875 μm. Since the conductance turned out to be specular, the length did not really matter that much, and for our tests we used the shortest PoSTs with good results.

6.3.2   Thermal conductances and position resolution

The final quantity in the design was the link conductance. We know that the energy resolution gets better for higher link conductances. We want the conductance to be as big as we can make it as still resolve the pixels. But how big is that?

To answer this question, we calculated the theoretical noise for the parameter numbers determined above. We modeled the noise as white with a RMS value equal to the zero frequency RMS value of the calculated noise spectrum from Figure 6.7(a) (this is a conservative estimate, since the theoretical noise drops to the Johnson noise level at higher frequencies). We created noise traces in the time domain by adding random phases to the white noise spectrum and taking the inverse Fourier transform. The noiseless pulse shape from the PoST model for a 1.5 keV X-ray hitting pixel 1 was added to these noise traces, to create some fake data. This was repeated for the other 6 pixels. This data set was analyzed for position resolution as a function of conductance. The same analysis was done for the 15- and 31-pixel PoSTs. In each case, conductances were picked ranging from 1 to 50 nW/K.

Once the conductance numbers were picked, the link could be designed. The absorber pixels and links are deposited on a nitride membrane. To get a high filling fraction along the PoST, the absorbers should be as close to each other as possible. The minimum gap we could leave between to adjacent bismuth absorbers is 6 μm (this is determined by the photoresist used in the liftoff process).

We considered the Kapitza boundary resistance from the absorber to the nitride but quickly realized that this conductance was orders of magnitude higher than our design goals (Swartz and Pohl, 1989).

One possibility was that the nitride could act as the thermal link between pixels. Using the same published nitride conductance numbers from Holmes et al. (1998); Levio and Pekola (1998), we concluded the nitride would not be thermally conductive enough. Because of fabrication, we could not make that gap smaller than 6 μm. We now know that our nitride is specular. Using the current TES conductance measurements we can get an estimate of the conductance of the nitride in the specular limit, which still comes out too small. More testing in this area must be done to get an accurate number for the inter-pixel nitride conductance in our PoSTs.

Even if the nitride conductance turned out to be the number we wanted, there is another reason for not wanting the nitride to be the thermal link between pixels. If the nitride is the thermal link between each pixel, we would have to rely on electron-phonon coupling to thermally equilibrate each pixel as the heat deposited from an X-ray diffused across the PoST. There might be longer-than-acceptable time constants associated with these processes, especially for bismuth films, whose electrical properties are dependent on deposition parameters (Ashcroft and Mermin, 1976; Dorozhkin et al., 1986; Jezequel and Thomas, 1997; Mezhov-Deglin et al., 1975). Tests to determine the heat conductance of electrons and phonons in our deposited bismuth have to be carried out, as we as a determination of the bismuth electron-phonon coupling. Worst of all, there might be loss terms associated with phonons in the nitride escaping out of the PoST through the nitride without interacting in the TESs. There is some evidence to suggest that our 0.5 μm membrane has a phonon population resembling a 2-dimensional gas, a behavior that has been seen in thinner nitride membranes by Schwab et al. (2001). This implies that most phonon modes propagating through the membrane are parallel to the membrane plane, and do not interact (or interact very little) with the surfaces. Once a phonon went into the nitride, there would be a very small probability for the phonon to tunnel back into one of the pixels or the TESs. The effect would be seen as an energy loss term. To minimize these possible problems, we can use a metal as the thermal link between each pixel. Then the electrons will dominate the thermal conduction and phonons will just be "going along for the ride." We looked at copper and gold, but since we are already using gold in our TESs that seemed like the obvious candidate. The gold electrons will easily couple to the TESs on each side, and the energy exchange between electrons and phonons is not as important. There can still be losses in the nitride, but now we are not forcing *all* of the heat to flow down the TES by coupling to the nitride phonon system. In fact, most of the energy will diffuse through the gold electron system and the nitride phonon system will just equilibrate locally with the electrons, with negligible contribution to the diffusion time constant.[4]

If we made the absorber gaps 6 μm, then the link would be 6 μm long. The conductance could be tuned by the cross sectional area of the gold. For processing reasons, the link width should not be less than 5 μm wide. The thermal conductivity of the link is given by Ashcroft and Mermin (1976)

$$G_{\text{link}} = \frac{1}{3}v_F \lambda c_v \frac{A}{L} = \frac{1}{3}\lambda^2 c_v \frac{w}{L} \tag{6.1}$$

where v_F is the Fermi velocity of the electrons in the gold, c_v is the specific heat, A is the cross-sectional area and L is the length of the link. We take λ, the mean free path, to equal roughly the thickness of the film, so $A = \lambda w$ where w is the width. We realized the thickness of gold needed to get the right conductance for $w = 5$ μm and $L = 6$ μm was very thin (~ 24 nm). The conductance is proportional to the square of the thickness, so errors in thickness can make large fluctuations in conductance. A film thickness of several hundred

---

[4]Even that is not known for sure; since the nitride is a specular medium, ballistic phonons see the nitride as a wave guide. If the interactions of the ballistic phonons with the nitride membrane are few, it is possible the nitride stays at the cold bath temperature T_b all the time.
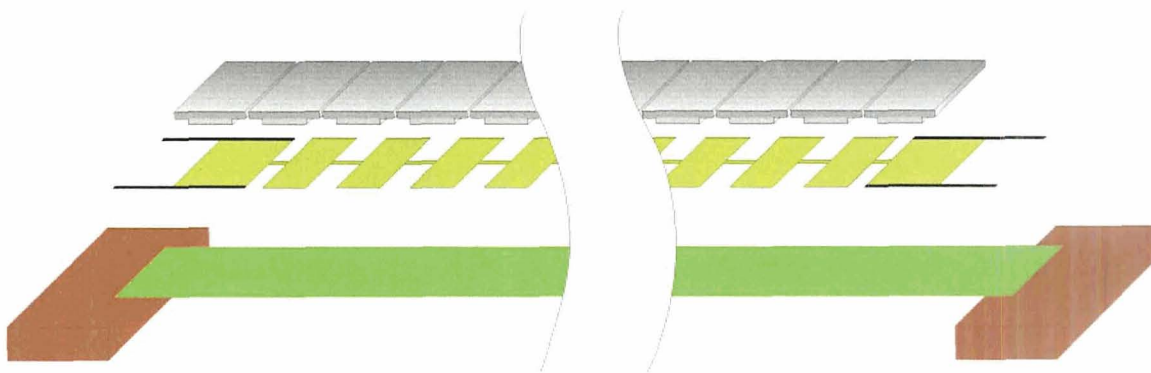
Figure 6.6: Goddard PoST design in an exploded view. The bottom film is the nitride membrane that acts as the support structure for the PoST. The second layer is the dominant thermal conductance across the PoST, and consists of gold links connecting gold pads that aid the thermalization of the absorber pixels. At each end we have a Mo/Au bilayer TES. The top layer is our Bismuth mushrooms, which serve as our X-ray stopping layer. The stems of the mushrooms lie over a gold film that makes the thermalization in each pixel much faster than the diffusion time to the adjacent pixel, thus preventing position dependence inside each individual pixel.

nanometers would be less dependent on the fluctuations in thickness from deposition to deposition. There is also a step coverage problem with having the links be too thin. A 25 nm film will not be able to maintain continuity over a 250 nm thick TES film.

To solve this problem, we invoked the proven bismuth mushroom technology described in Section 6.1. Figure 6.6 shows and exploded view of the final design. The absorber unit cell is a 250 μm square. Using an absorber with lateral wings (a 1-dimensional mushroom) the length of the gold link can be substantially increased. We opted for 150 μm wide stems (the area of the mushroom that is not raised), leaving 100 μm long links between adjacent pixels. Now with this link length gold thicknesses in the hundreds of nanometers were possible. This long link also reduces the conductance of the nitride, ensuring the nitride conductance is a negligible term compared to the gold conductance. This gives us full control of the link conductance by varying gold link thickness and width.

Bismuth has poor thermal conductivity at 100 mK. The whole concept of a pixellated absorber rests upon the notion that each pixel will have a different signal, and will be easy to separate in the data analysis. But to get good energy resolution, we need the pulses from a particular pixel and a particular energy to be the same. Position dependence in a pixel will lead to energy resolution degradation, just as it will in a single pixel calorimeter. To insure proper thermalization of the pixel, no matter where the X-ray hit (in the middle of the pixel, in the corner, etc.), we covered the stem area with gold, so the mushroom would be laying on a gold film which would help it thermalize quickly. This has the added bonus that a PoST without bismuth will still have a gold target for X-ray absorption, although

C_e	0.154	pJ/K
C_p	$\ll C_e$	
C_a	26.36	fJ/K
C_{tot}	0.492	pJ/K
G_{pb}	32	pW/K
G_a	1.63	nW/K
G_{ae}	1.63	nW/K
G_{ep}	$\gg G_{pb}$	
R	3.4	mΩ
R_L	2.4	mΩ
T_b	50	mK
T	75	mK
T_L	50	mK
L	250	nH
α	90	
α_I	~ 0	
n	3.2	
ΔE $(G_a \to \infty)$	0.927	eV
E_{sat} (pixel 4)	1.54	keV

	PoST resolution, as seen by	
Pixel	TES1	both TESs added
1	1.544 eV	1.444 eV
2	1.959	1.527
3	2.351	1.547
4	2.739	1.548
5	3.131	1.547
6	3.530	1.527
7	3.929	1.444

Table **6.1**: Parameters and resolution for prototype 7-pixel PoST. The TES heat capacity C_e is much lower than in the device described in Section 4.5 because our current Mo/Au bilayer has a low heat capacity per square micron.

the X-ray stopping power of this gold film is poor (but not zero).

6.4   Final parameters and energy resolution

In Chapter 4 a 7-pixel PoST model was designed that obtained better than 2.3 eV resolution at 6 keV without saturating the detector. For our first prototype detector, the parameters that were chosen (shown in Table 6.1) are significantly different from the detector in Chapter 4. We wanted the prototype detector to be a very conservative design, so we chose much lower conductances than those on Table 4.5. The heat capacity of our TESs is much lower than that of the devices in Table 4.5 because we wanted to use our proven Mo/Au bilayer
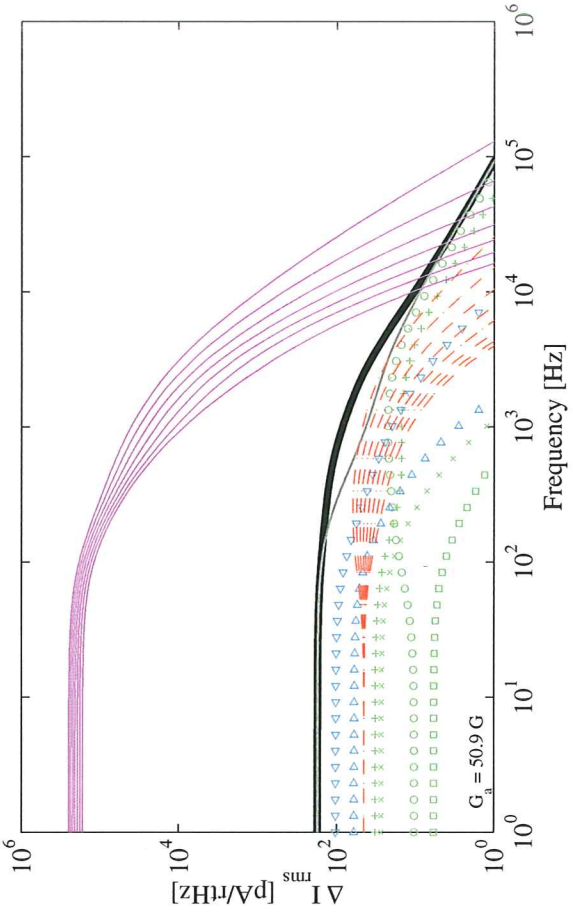
(a) 7-pixel PoST expected noise as seen from TES1
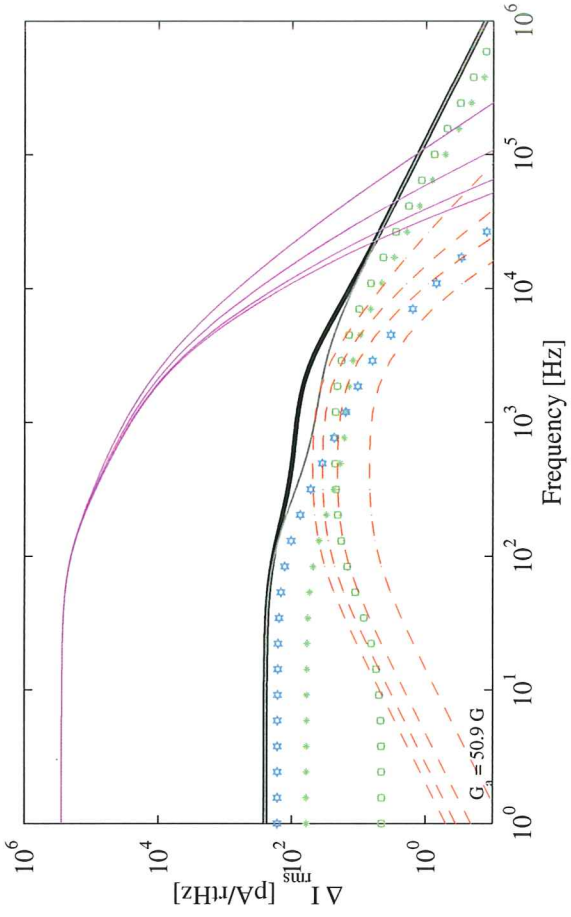
(b) 7-pixel PoST expected noise, both TESs added

Figure 6.7: 7-pixel PoST expected noise. (a) shows the noise and signal (magenta solid lines) expected when looking at just one TES. (b) shows the noise and signal expected when adding both TES signals together. The legend is Figure 4.3 on page 74. The gray lines depict the theoretical single pixel behavior.
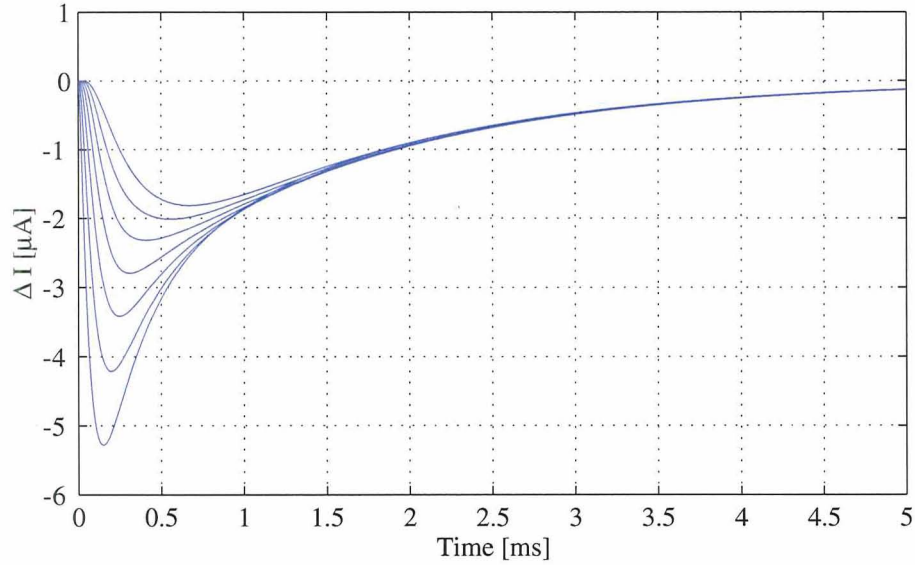
(a) 7-pixel PoST expected response in linear scale
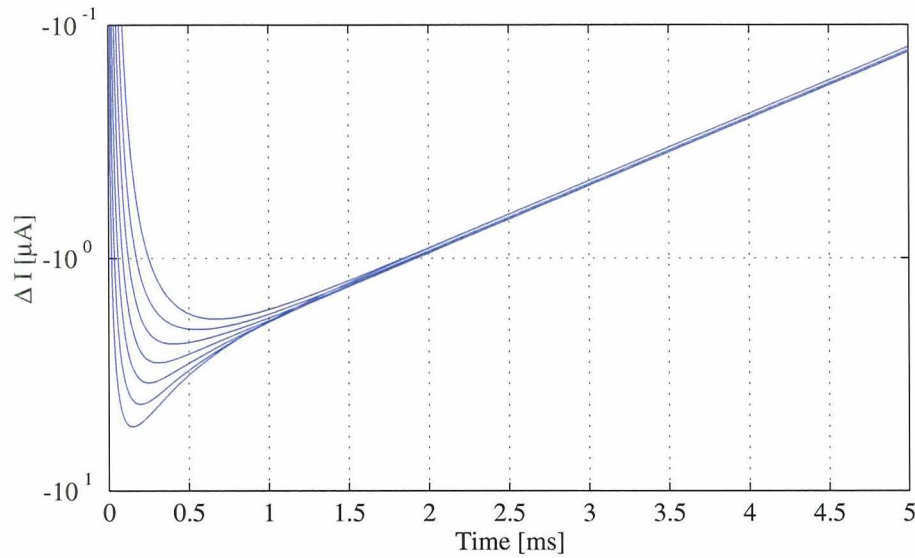
(b) 7-pixel PoST expected response in semi-log scale

Figure 6.8: 7-pixel PoST expected response for prototype design. The low conductances in Table 6.1 make the decay times for the PoST long, but make determining the position easier. All 7 pixels in the PoST come in thermal equilibrium around the 1.5 ms mark, and decay exponentially from there.

TESs and the heat capacity of our 250 μm TESs is much less than the values required on Table 4.5. This has the effect of lowering the saturation energy of the PoST. We have 1.5, 3.3, and 5.9 keV X-ray sources, so we felt that we would be able to see the 1.5 keV line without saturating and that would be enough for a demonstration device. Although the heat capacity is much lower, the conductance is also lower; the result is that the time constants of the prototype device are fairly slow. We have used the operating points of data taken on the actual devices (which will be the subject of the next chapter) to specify R, to be able to compare these predictions with the fit we obtained. The operating resistance of the TES is 3.4 mΩ, which is very close to the 2.4 mΩ resistance of our load resistor. We therefore expect some increase in the time constants (longer decay times) due to this bias point.

The predicted energy resolution in Table 6.1 is very good, but the 0.5 mK TES temperature rise (our fiducial saturation condition) occurs for X-rays of about 1.5 keV. We therefore expect to have some non-linearity at 1.5 keV and saturation for higher energies. Figueroa-Feliciano et al. (2000a); Fixsen and Moseley (2002) discuss methods to analyze non-linear data, but for now we assume there will be an energy resolution degradation associated with operating in the non-linear range.

Figure 6.7 shows the predicted noise and signal from our design values (assuming 1.5 keV photons for the signal). Figure 6.7(a) is the signal and noise when looking at one TES only. The seven blue solid lines correspond to the response of 1.5 keV pulses on the seven pixels. Notice how differentiated the pulses are from each other all the way to low frequencies. Figure 6.7(b) shows the noise and signal on the same device, but adding the two TES signals together. As discussed before, the low-frequency link noise is cancelled, and the response per pixel becomes much more uniform. The signals only deviate at high frequency, and we see four lines since the symmetry of the device makes pixels 5, 6 and 7 the same as 3, 2, and 1.

Figure 6.8 shows the response of the PoST in the time domain. These should be our average 1.5 keV pulses. The differentiation of each pulse should be easy to determine. The pulses are still very exponential after the pixels thermalize, demonstrating that once the initial thermalization phase is over, the PoST indeed acts as one heat capacity C_{tot} cooling down through the weak link to the substrate.

6.5   Other considerations

Many things beside the thermalization properties of the device can affect its final performance. A major one is whether one can make a nitride strip that long be structurally and mechanically stable. What are the vibrational modes of a PoST? To answer all these questions, we had a mechanical finite element analysis (FEA) done of a PoST. The first pane in Figure 6.9 shows the stress concentration around the corners of the membrane. The second pane shows the elements of the FEA model. The last two panes show the first two vibrational modes of the PoST. Although the first vibrational mode was around two kiloHertz, the model parameter were not known very well at the time of the analysis, and
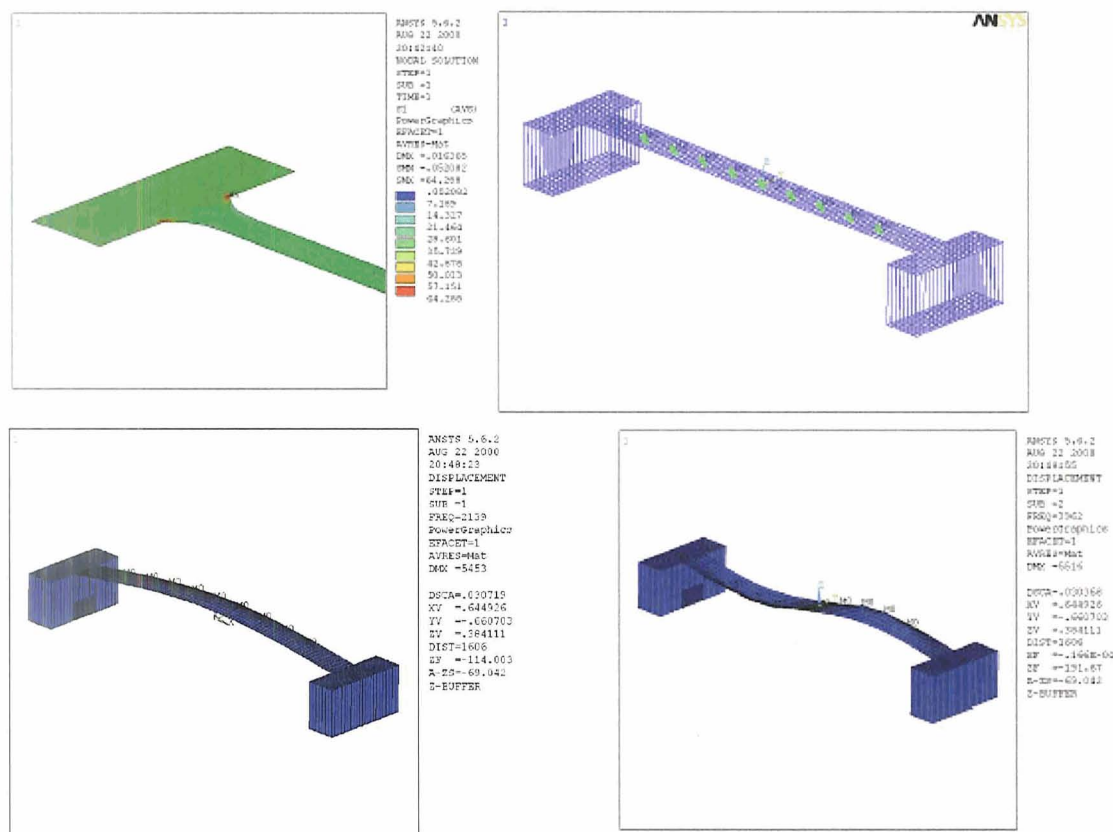
Figure 6.9: We studied the resonant frequencies of PoST, and calculated the stress in the nitride to parametrize the robustness of PoSTs as the absorber number becomes large. Image by Jonathan Kuhn.

we decided that this study would be best done experimentally: we would see whether the PoSTs survived in the fabrication lab, and we would determine whether microphonics would be an issue when looking at data.

A second issue arising from the design was grounding. Because we used a gold thermal conductance bridge between the two TESs on the PoST, they are electrically connected. If the potential across the two TESs is not zero, current will flow through the gold conductance bridge. This current would be a source of heat into the PoST, and could cause the TESs to go normal, or prevent much power from being dissipated in the TESs. To prevent this, the conductance bridge was connected on the ground side of the TESs, to try to ensure the voltage on both sides of the conductance bridge was the same (zero). Unfortunately, as we will see in the next chapter, this was not enough to prevent currents from flowing through the conductance bridge. This is because the return of each bias line has a resistance of about 300 Ω, thus the ground side of the PoST is not really ground. This give rise to the possibility of creating a potential across the PoST and driving current through the gold links.
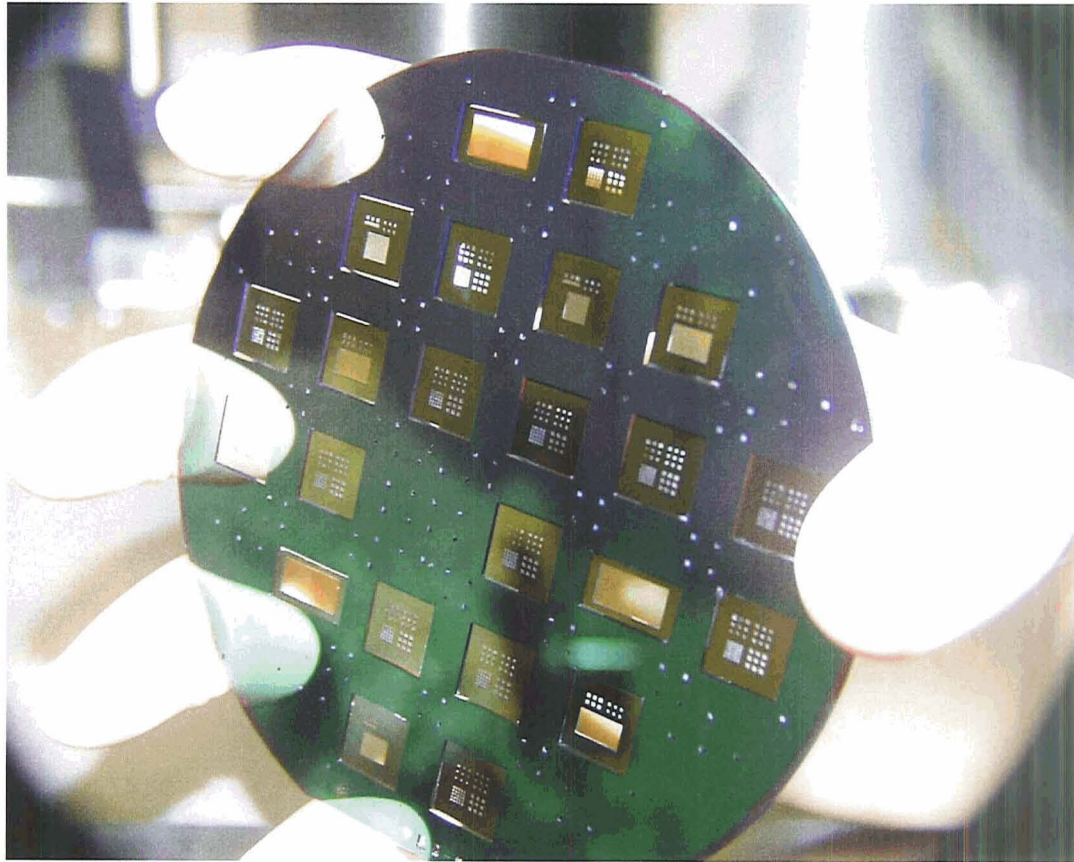
Figure 6.10: Picture of single-pixel TES and PoST calorimeters on a single wafer, demonstrating the ability to fabricate both single-pixels and PoST with the same process.

6.6   Fabrication

One thing we wanted to prove in our design was the flexibility to fabricate PoSTs and single-pixel TESs at the same time, on the same wafer. That would demonstrate the ability to create hybrid detectors that had single-pixel TESs in the center (a 6×6 array, for example) and a cadre of PoSTs around this central core. As explained in Chapter 1, this will provide a very versatile detector capable of satisfying Constellation-X requirements while gaining a large factor in field of view. Figure 6.10 shows one of our wafers during fabrication. The large windows are were PoSTs will go, and the small holes are the single-pixel nitride membranes. On this mask we designed 7-, 15-, and 31-pixel PoSTs.

Figure 6.11 shows the first 7-pixel PoSTs. This chip contains an array of 7 PoSTs, each with 7 pixels, for a total of 49 pixels read out by 14 channels. Even here the number of pixels per channel makes this an interesting device. For these initial tests, no bismuth mushroom absorbers were placed, and we relied on the gold absorbers (100 nm thick) for X-ray absorption. The TESs are the squares on either side.
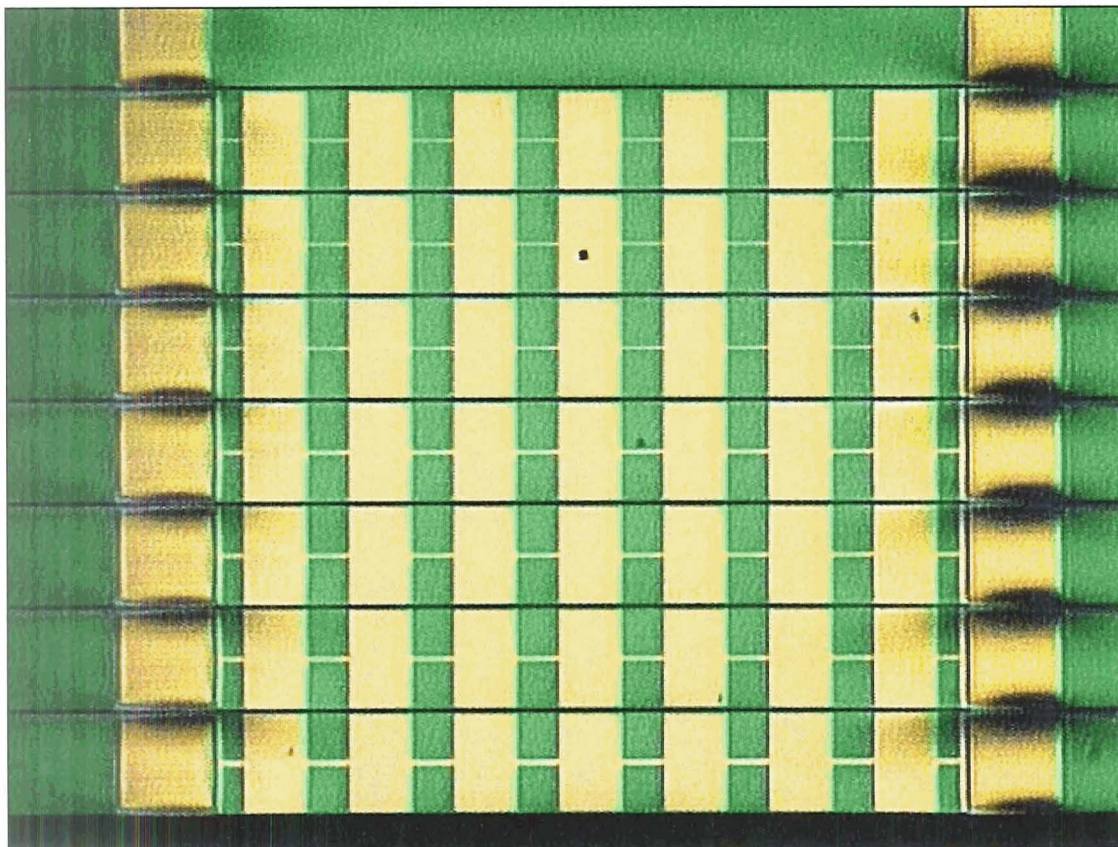
Figure 6.11: Picture of the first 7-pixel PoST array. There are 7 PoST (one per row) each with 7 gold absorbers and 2 Mo/Au TESs. These prototype devices have slow link conductances and no bismuth absorbers. The gold conductance links vary in thickness from PoST to PoST to test different conductance performance. Each PoST is 2.25 mm long. This array has 49 pixels read out by 14 channels.

Figure 6.12 shows the first 15-pixel PoST chip. The single-pixel devices seen on the top above the array of PoSTs are for testing and demonstration of single-pixel devices and PoSTs on the same chip. The first three PoSTs have only nitride bars, which will be used in the future to calculate the nitride thermal conductance, and when covered with bismuth, the bismuth thermal conductance. Notice the three pads per device. The third pad is to connect the shunt resistor, which is located just above the pads. In this run, no shunt resistor was deposited, as we were using the shunt resistors in our detector mount (see Figure 5.3).

Figure 6.13 shows a close-up of the array. Here we have 120 pixels read out through 16 channels. The shadows on the TESs are due to slight warping of the nitride due to stress in the TES, and the lighting angle which enhances this effect. The actual deflection is very small.

For more details on the fabrication procedures, please see Finkbeiner et al. (2002).
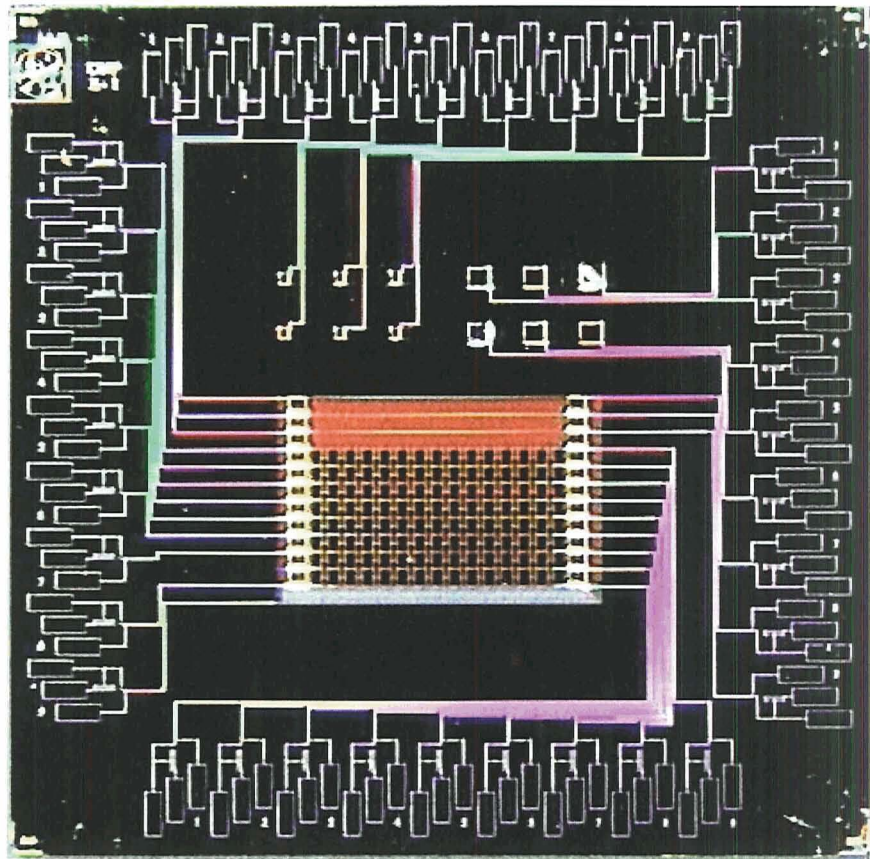
Figure 6.12: Picture of a 15-pixel PoST array chip. The devices on the top half of the chip are test devices and single-pixel TESs, demonstrating the capability of fabricating both types of devices on the same chip. This is an important capability for future implementations of PoST calorimeters, since hybrid detectors with both single-pixel and PoST calorimeters are possible.
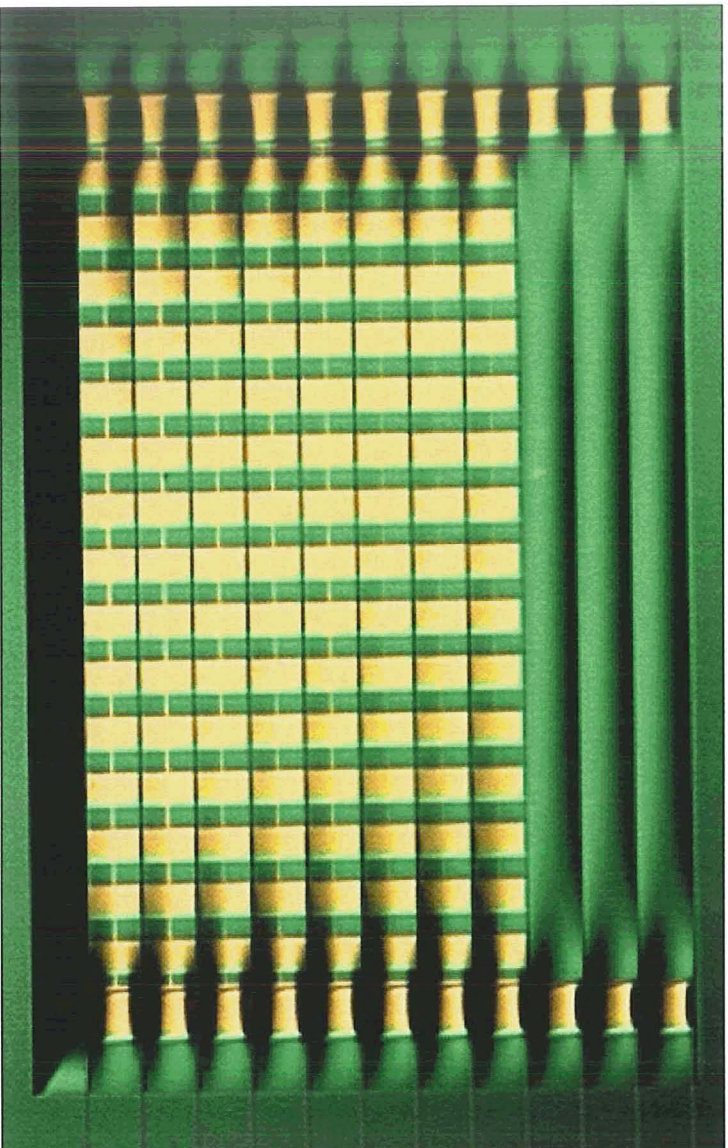
Figure 6.13: Picture of the first 15-pixel PoST array. These prototype devices have slow link conductances and no bismuth absorbers. Each PoST is 4.25 mm long, and the array covers 8.5 mm². This array has 120 pixels read out by 16 channels.

Chapter 7

Results

No matter how much careful analysis and modeling is done on a detector, or how beautifully it performs in the computer, until real data is obtained, no champagne can flow.

7.1   Model fit to the data

We have described the concept, derived the theory, explained the design, and shown the fabrication of PoSTs. The moment of truth had arrived. By the time the PoSTs had been successfully fabricated, the results from our single-pixel research had shown that the nitride membrane was mostly specular. This meant that the different weak link conductances we had designed by varying the length of the nitride between the TES and the substrate were not going to be that different at all. Although we had successfully fabricated the PoSTs, still a critical test lay ahead: cooling. There still was no assurance the PoST nitride membrane would not break under the stress imposed by the cooling process. So the logical first PoST to test was the shortest PoST we had. We used the slowest link conductance we had to maximize the chances of the PoST working.

Upon cooling down, we saw the PoST was still there, so the nitride test was successful. Trying to do I-V curves, we noticed the TESs had a very small superconducting region. After much trial, we traced the problem to the bias circuit and the way the TESs were grounded. Unfortunately, the TESs were on channels that had different shunt resistors on them. This meant that if both TESs were biased with the same input voltage, each would have a different bias voltage across them. In this run the two TESs were not grounded together. The result was that there was a voltage across the PoST link. The resistance of the link conductances is estimated to be $\sim$ 2 Ω. A current was flowing across the link, from one TES to another, and the power dissipated was $\delta V^2/2\Omega$, where δV is the voltage across the link. This power was heating the PoST when I-V curves were taken, and the TESs were going normal because of their increased temperature. The only way to prevent this from happening was to have exactly the same voltage on each side of the link. To do this, we set up a variable resistor in series with the input voltage of one TES. Doing voltage sweeps to see the PoST I-V curve, we tuned the variable resistor to maximize the input voltage
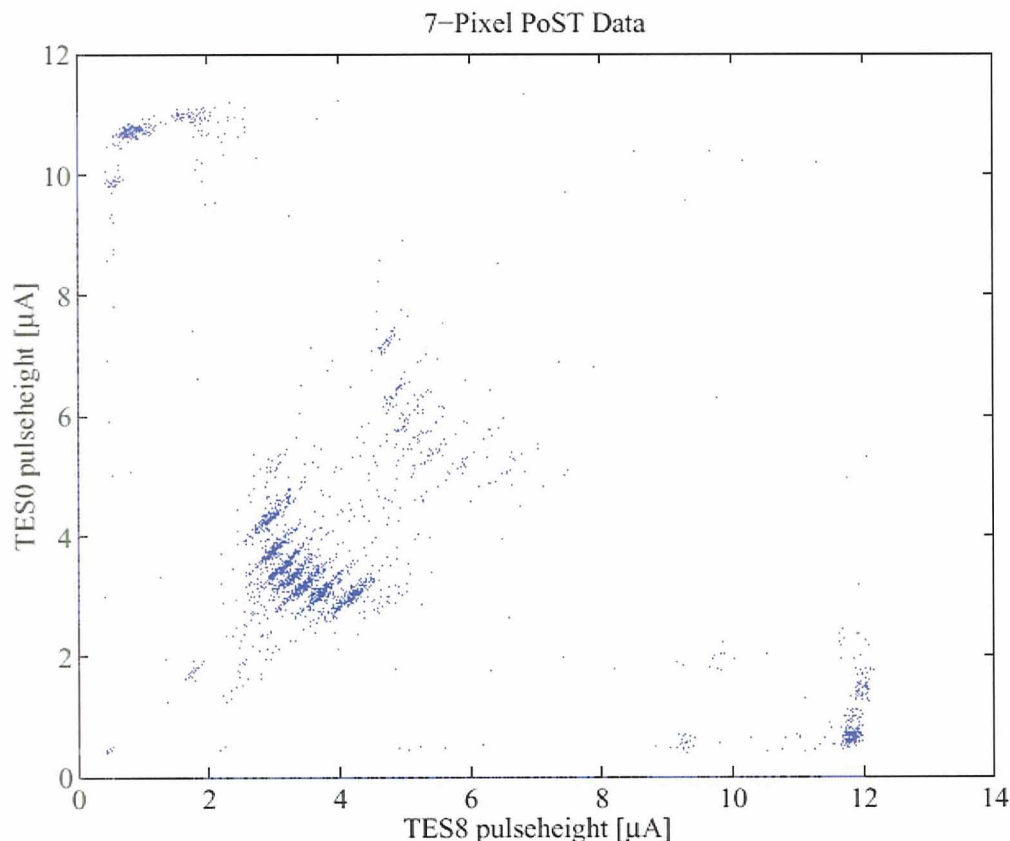
Figure 7.1: Initial data from first run of the 7-pixel PoST array in Figure 6.11. Only two PoSTs were instrumented since we only have 4 channels in our current system. Doing a simple box-car filter and picking out the pulse heights, the 7-pixels are clearly differentiated.

required to drive the TESs from their superconducting state to their normal state.

Once the bias circuits were balanced this way, we proceeded to take our first pulse data. The data was very noisy, we had lots of 60 Hz pickup. We also saw a very strange phenomenon: thermal coupling of the 120 Hz and its harmonics into the PoST. When superconducting or normal, the signal would look reasonably clean. As soon as the bias was set so the TESs entered their transition, huge 120 Hz pick up lines would appear. Repeated tests seemed to indicate the signals was coupling in thermally, since it only appeared when the TESs were biased in the transition (which is when the output signal is sensitive to the temperature of the PoST), and the 120 Hz and its harmonics were much stronger than the 60 Hz line, which is consistent with V^2/R heating.

As we had never seen this before, we were worried this was an intrinsic problem with the PoSTs, but recently we saw the same effect on our single-pixel devices. We are still looking for the cause of this heating, but we presume it is a grounding issue, not an inherent problem of the detectors.

Fit Parameters		
C_e	0.154	pJ/K
C_p	$\ll C_e$	
C_a	26.36	fJ/K
C_{tot}	0.492	pJ/K
G_{pb}	23	pW/K
G_a	3	nW/K
G_{ae}	0.38	nW/K
G_{ep}	$\gg G_{pb}$	
R	3.4	mΩ
R_L	2.4	mΩ
T_b	50	mK
T	75	mK
T_L	50	mK
L	250	nH
α	90	
α_I	~ 0	
n	3.2	
2-pole anti-alias filter	30	kHz
ΔE ($G_a \to \infty$)	0.927	eV
E_{sat} (pixel 4)	1.75	keV

Table 7.1: Parameters for fit to 7-pixel PoST data. The main difference from the predicted values (Table 6.1) is in the conductance between the edge absorbers and the TESs (G_{ae}). This was about 10 times lower than expected.

Finally we took some data, and did a simple boxcar smoothing and recorded the maximum pulse height of each pulse. The result is Figure 7.1. This was the first data we looked at, and the plot it is pretty much raw data. We were both surprised and extremely happy to see the 7 blobs in the center just pop out at you with hardly no work done in the analysis. The strong line is assumed to be Al K$_\alpha$, and the other line is either K, Mn, or both. The blobs at the upper-left- and lower-right-hand corners are the direct hits on the TESs. After the initial euphoria subsided, we started taking a harder look at this plot. We noticed there was something unexpected going on: the X-rays directly hitting the TES were saturating it, as we expected, but the pulse height of X-rays hitting the TES were much bigger than those hitting the adjacent gold absorber pixel.

The hypothesis was that the conductance between the last pixel and the TES was much lower than the inter-pixel link conductance (in the variables of our model, $G_{ae} < G_{aa}$). An X-ray hitting any of the pixels would thermalize across the pixels before the heat leaked to the TESs, so the temperature rise of the TESs would be lower than if the link conductances were the same across the PoST. When an X-ray hit the TES, the low link conductance keeps the heat deposited by the X-ray in the TES longer, allowing the TES temperature to rise more than it would if the link conductance G_{ae} were larger.
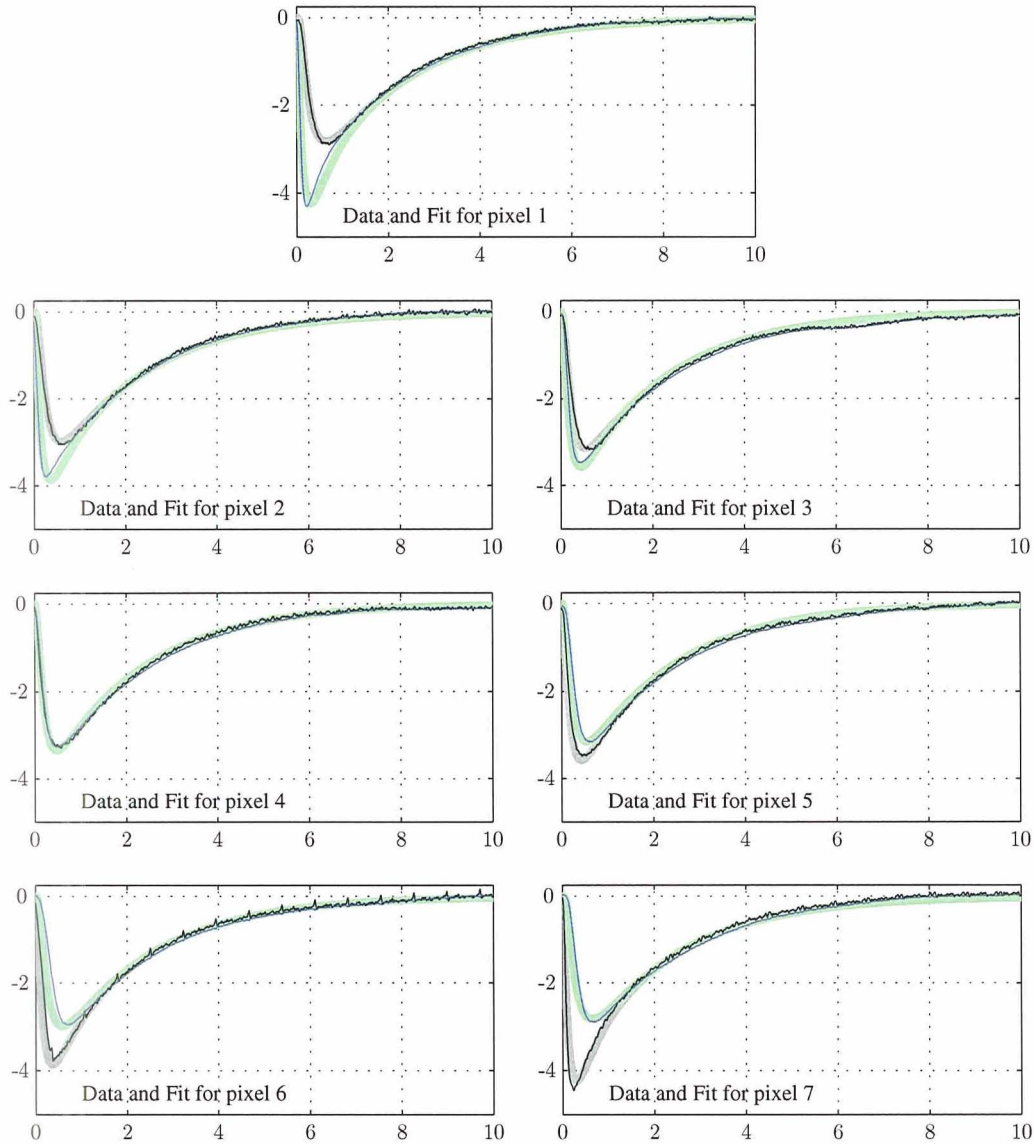
Figure 7.2: Al K_α average pulses as seen from TES1 and TES7 are shown for each pixel. The model pulses, whose parameters where selected by trial and error (not a χ^2 fit), fit the data reasonably well.
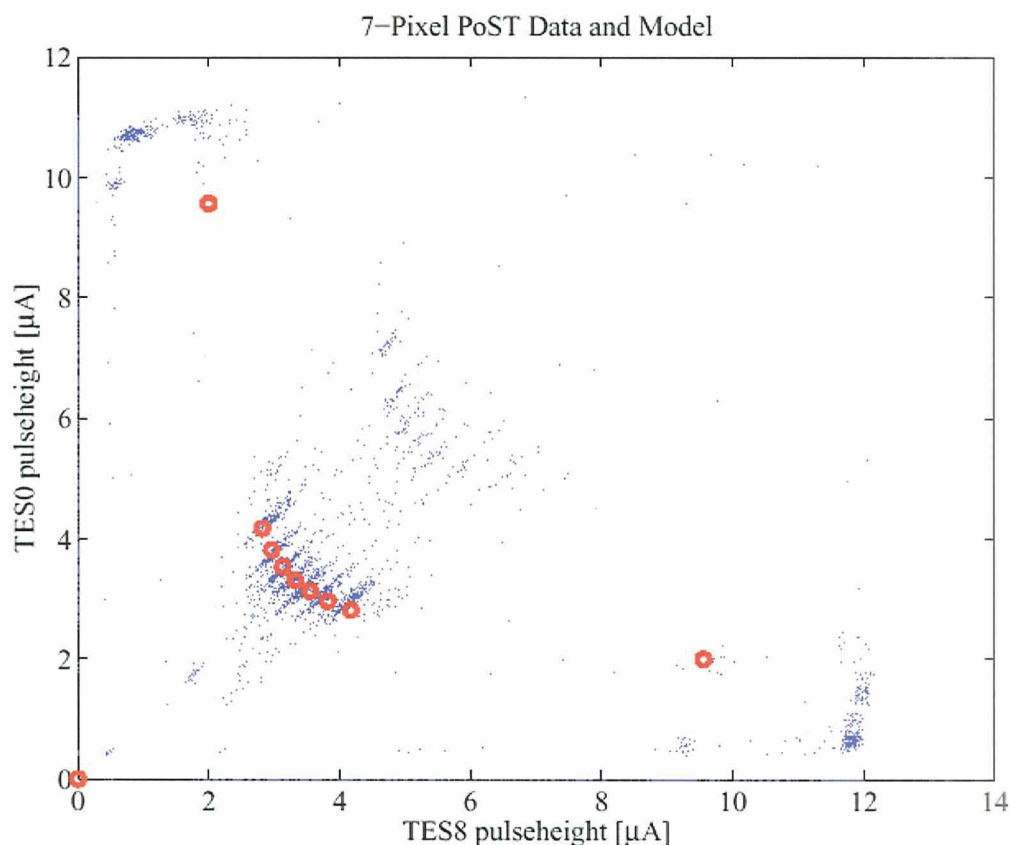
Figure 7.3: Using the parameters in Table 7.1, we can calculate the theoretical response of the device. The model (red circles) is superposed over the data. Note the good agreement with the absorber hits but not with the TES hits.

To test this hypothesis, we fit the average 1.5 keV pulses from each pixel to our model, starting with the model parameters on Table 6.1. In this first pass at this analysis a "χ by eye" fit was done, manually tweaking the parameters between the values we expected to get a good fit. A more detailed and careful fit of the model needs to be done. Our fit results are shown in Figure 7.2. The decay time fits very well, but there is some discrepancy in the initial drop after the maximum is reached (although the pulses are really current drops, we will refer to the signals as is customary in terms of pulses, with the pulse height maximum being the minimum current of the trace).

To do this fit, we took the channel that had the worst noise and scaled it to match the other channel, so that the average pulses on pixel 4 (the middle pixel) were the same height. The shunt (or load) resistor value of the good channel was 2.4 mΩ, so we fitted both signals assuming that load resistor value. The integral of the sum of the pulses gives 1.4 keV for the 1.5 keV X-ray energy. The fit parameters are shown in Table 7.1.

Having obtained a reasonable fit, we passed our model pulses through the same pulse
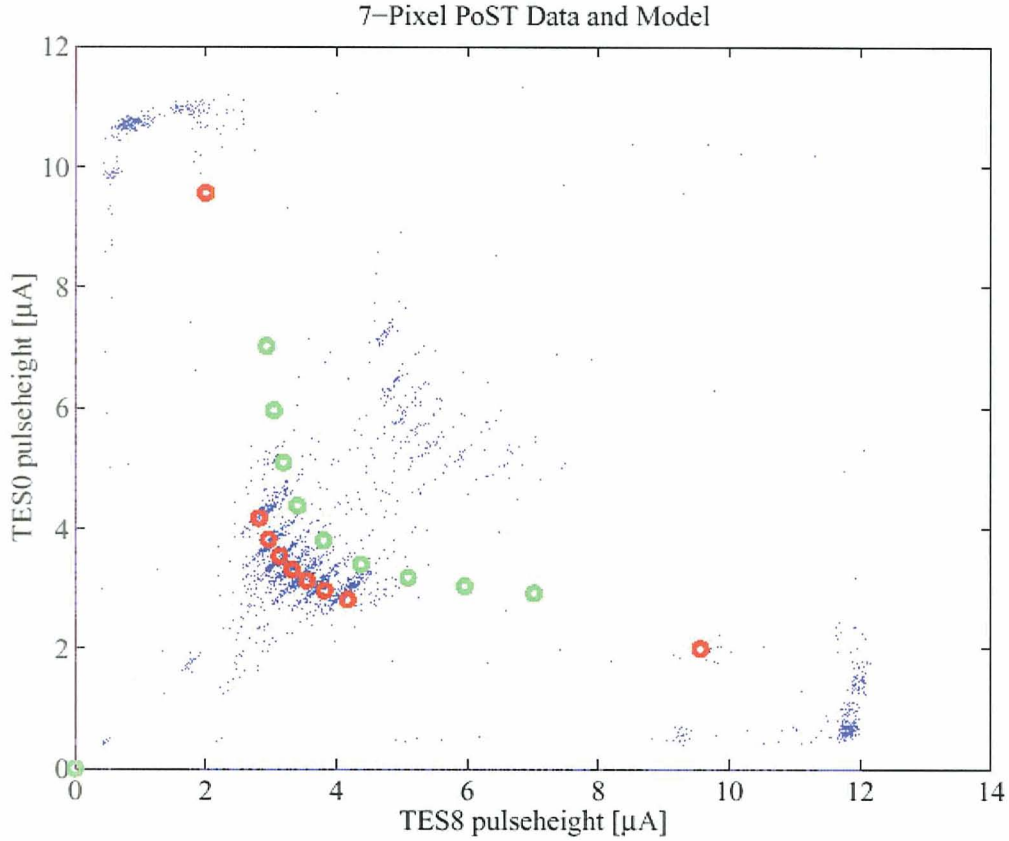
Figure 7.4: If $G_{ae} = G_a$, and all other parameters remained the same, our linear model predicts the response shown by the green circles. Note that the peak heights are bigger (larger signal) and that the spacing between pixels is greater (more differentiation). Also note the TES hits are now very similar to the absorber hits.

height algorithm used to produce Figure 7.1, and plotted the model results on top of the data, as shown in Figure 7.3. The pixel points match up very nicely on top of the data (which is no surprise since that is just a reflection of our good fit). But notice where the model predicts the TESs should be. Even with the lowered G_{ae} used in the model, the predicted signal is less than the signal seen. Saturation effects should make the signal seen be smaller than the signal predicted, opposite of what is seen (think of a 1 GeV photon on our PoST and on the PoST model. Since the model is linear, it will just give you a very large signal, while in real life the TESs would be very saturated). We still need to understand this discrepancy.

Since we have this fit model, we can ask what we *would* have seen if the $G_{ae} = G_{aa}$, as we had intended. The result is shown in Figure 7.4. The green circles are the predicted signal. There are three consequences (two good, one bad). The first good one is that the spacing between each pixel signal is larger, which implies better differentiation of the pixels.
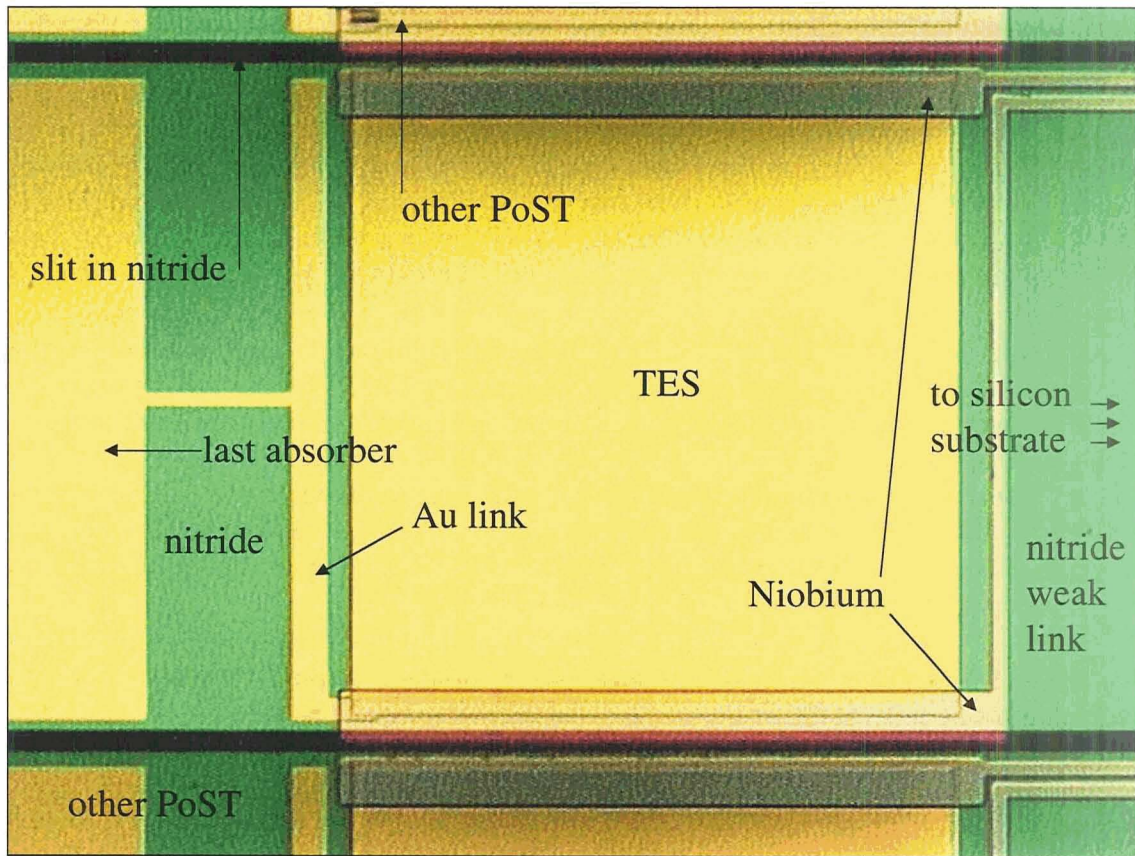
Figure 7.5: Close-up of PoST TES. One possible explanation for the low G_{ae} is that there is a super-conducting barrier between the electron system of the link and the TES. Here we see the gold link goes into the niobium lead and then touches the TES. We are currently investigating this possibility.

The second effect is that we get a larger signal, which means we get better resolution. The bad consequence is related to the second good consequence. Since the signal is bigger, the TES temperature rises higher. Then it follows that the saturation energy will be lower.

This is a design space that needs to be explored: having a lower G_{ae} than G_{aa} provides higher saturation energy for the same heat capacity PoST. Another way to approach this is that for the same saturation energy, the heat capacity of the PoST can be lower for lower G_{ae}. Preliminary studies with the computer models seem to suggest one does not get better energy resolution for the same saturation energy by lowering both the G_{ae} and the heat capacity of the TESs. More studies of this possibility must be done.

Now that we have some supporting evidence to point to a lower G_{ae}, we looked at our design to try to explain how that was happening. Figure 7.5 is a close-up of one of the TESs in a PoST. Because of the grounding concerns (Section 6.5), the link to the TESs was done on the ground side of each TES. As can be seen in the figure, the niobium ground rail covers the place where the gold link and the TES overlap, on a small part of the link

itself. If any of these regions are being proximitized by the niobium, so their transition temperature is higher than the 70 mK of this particular PoST, then hot electrons coming from the pixels through the gold link would encounter a barrier. The electrons would hit Cooper pairs in the superconductor and create quasi-particles. These quasi-particles would have to diffuse to the edge of the niobium and make their way into the TES, or combine with other quasi-particles to shed their energy into phonons. In either case, the path for heat to couple from the pixel to the TES has become much more complex. These processes could explain the G_{ae} conductance being a factor of 10 less than expected, if our model is correct.

One way to see if this is correct, is to shift the the gold links to the right, so the whole bar at the end of the link is on top of the edge of the TES. The bar on the other side would be farther away from its TES, and the protrusion at the bottom would not touch the niobium. In other words, we would have a solid gold-gold connection along the full edge of one TES, and no connection at all on the other end. This would yield two results: it would tell us if indeed there is a superconducting barrier in the current design, and it would give us the nitride conductance between the link and the TES on the other side, since the nitride would be the only way for heat to go from the link to the TES.

Of course we cannot do this shift on the PoSTs we have fabricated, but we *can* do it on a new PoST by shifting the gold link mask to get the desired result. We have fabricated PoSTs with this link configuration and are getting ready to test them.

7.2   Energy resolution

In the initial run the amount of noise in our data was large. Our grounding scheme was not particularly good and we had a lot of pickup. An analysis of one of the pixels gave a resolution of $\sim$ 100 eV at 1.5 keV. This was not too bad considering it was the first run ever for the devices, but we felt we were nowhere near the actual resolution of the detector. In the following run, we grounded both TESs together on the chip holder, as discussed in Section 6.5.

Another problem we were having was pickup from one of the analog SQUID feedback boxes to the other in the form of a large repeating glitch at about 2 kHz. We need to run both TESs at the same time, so this was a real problem. A test of the offending feedback box pointed to a capacitor which we replaced. The feedback boxed then looked clean in the test room. Upon cooling down we realized the glitch was still present when the feedback box was operated in the lab. As we were unsuccessful in making the glitch go away, we opted to run the SQUID in open loop mode. This allowed us to dispense with both feedback boxes, so the signal was much cleaner. But now the SQUID were not running in feedback mode, so the current going through the TESs was now unknown. Since the voltage output vs. current into the input coil of a SQUID is a periodic function, a large current input sweep will produce an output at the SQUID which folds back on itself. Our signals are small enough that they do not reach the fold-back point, so our pulses still looked like pulses.
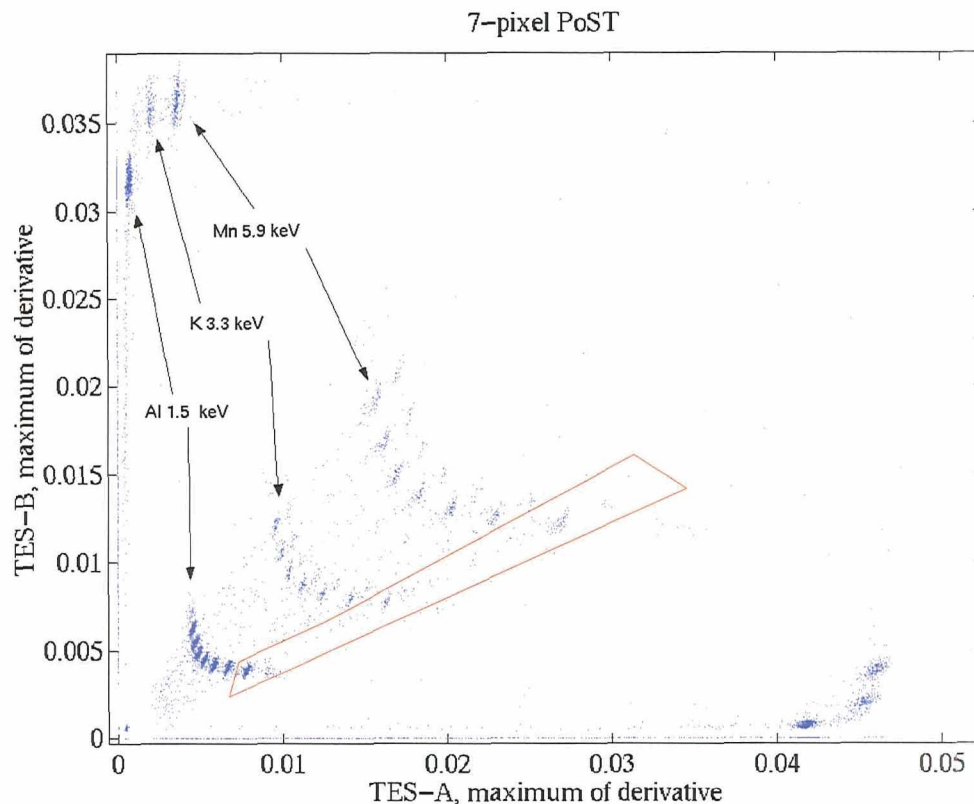
Figure 7.6: Second PoST run data. The maximum of the derivative (a measure of the rise time) is plotted. The boxed data is plotted in Figure 7.8.

We took data and experimented with other ways of determining position from the data. Figure 7.6 shows data from the second PoST run. Here the maximum of the derivative of each pulse on TES1 vs. its counterpart in TES7 is plotted. This is basically a measure of how fast the rise of the pulse was. The seven pixels can again be easily differentiated. Furthermore, the three X-ray lines that were illuminating the detector can be clearly picked out. Even some of the K_β lines are visible. Again this is slightly processed raw data, not the optimally filtered result.

If we take the data in the polygon in Figure 7.6 and make a histogram, we get Figure 7.7. This nice spectrum clearly shows the three main lines and some of the secondary lines.

The software for efficiently analyzing PoST data has not been completed yet. Using the single-pixel software we can optimally filter one of the pixels at a time. Looking at pixel 1 and making a fit to the aluminum line, we get 32 eV FWHM at 1.5 keV (Figure 7.8). This is a great result considering this is the second run of a new calorimeter concept. This result is just looking at one TES, not the added signal from both. Because the devices were operating in open loop, the pulse shapes of from the two TESs were slightly different. We
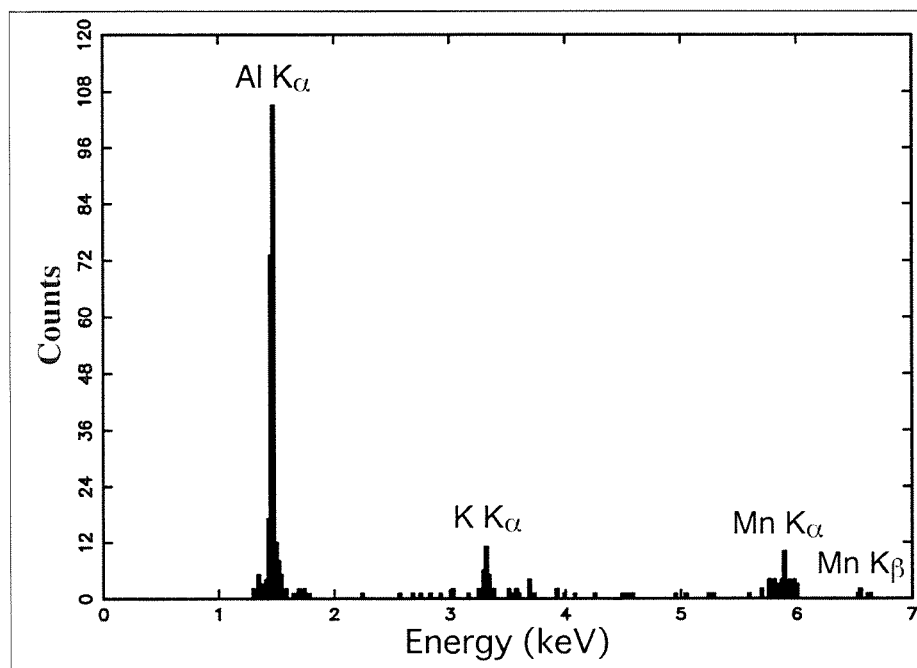
Figure 7.7: Spectrum from pixel 1 (the boxed part of the data in Figure 7.6). We can see the Al, K, and Mn K_α lines.

have not yet done the analysis of this data adding the two signals together. A fix to the feedback box glitch problem must be found in order to run the PoSTs in SQUID-locked mode and have any hope of getting detector limited noise performance in our PoSTs.

Table 7.2 summarizes the analysis done so far on this device. From the fit done from the first run, we plot the theoretical resolution of each pixel when looking at one TES and when adding the signals together. The last two columns are the results of analysis on the data. The baseline resolution was calculated by taking the average noise and the average pulse and calculating the NEP of the data. Using Eq. (3.68), we can integrate the NEP to get the predicted energy resolution for this particular data's noise spectrum. In this way we can calculate the energy resolution an optimal filter would get in a perfect world. In the real world, there is time drift, position dependence, gain drift, non-stationary noise, and non-linearities that degrade the energy resolution from this calculated value. The last column is the optimally filtered result.

Figure 7.9 shows the theoretical noise for a PoST with the parameters from the fit (Table 7.1). The actual noise from the first run is overlaid. Note we are nowhere near the intrinsic detector noise.

Figure 7.10 shows the NEP for pixel one, with the calculated NEP from the data overlaid. Figure 7.11 shows the theoretical NEP for each pixel for our fit parameters. Note these are for analyzing the data from one TES only. This data is far from the theoretical NEP for this device. Work must be done on reducing other sources or noise and pickup to be able
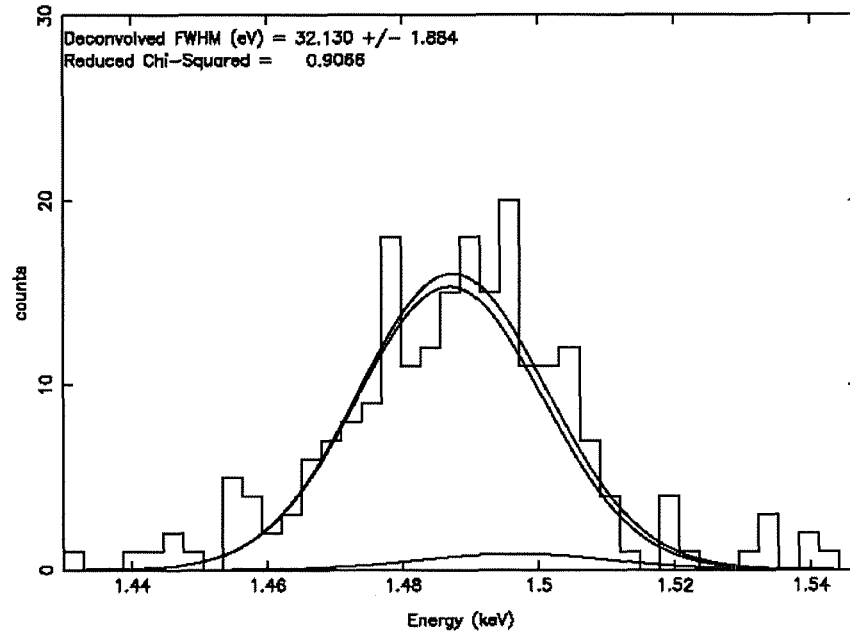
Figure 7.8: Fitting the Al K$_\alpha$ line in Figure 7.7, we obtain 32 eV FWHM at 1.5 keV.

Pixel	PoST resolution			
	both TESs	TES1	NEP Integral	1.5 keV line
1	2.821	5.287 eV	22 eV	32 eV
2	2.836	5.815		
3	2.839	6.235		
4	2.839	6.586	36	
5	2.839	6.896		
6	2.836	7.187		
7	2.821	7.477	43	

Table 7.2: Resolution for fit to 7-pixel PoST data. The first column is the theoretical resolution adding both TESs together, using parameter from Table 7.1. The second column is the resolution obtained for the same device but looking at just TES1. The third column is the calculated baseline resolution from the data. The fourth column is the fitted Al line.

to see true detector-limited performance from PoSTs.
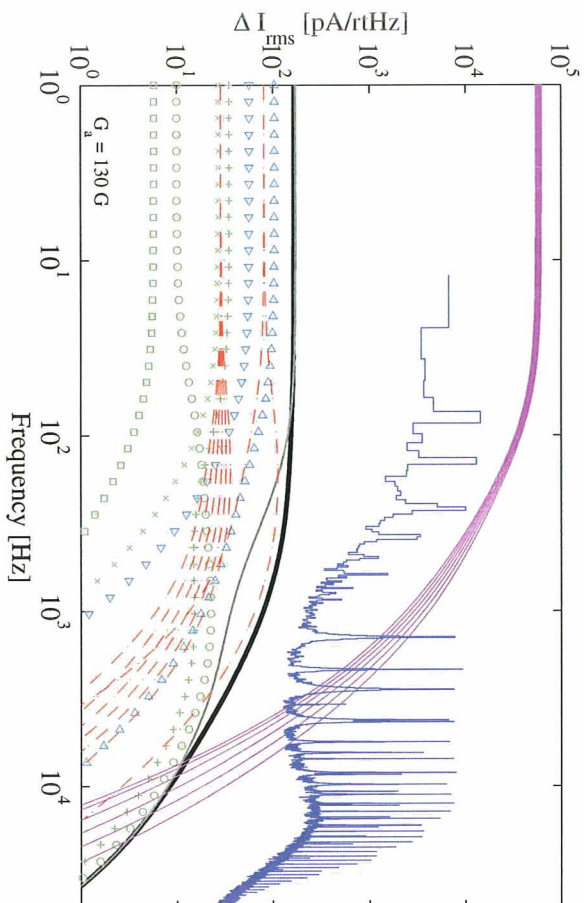
Figure 7.9: This is the noise from the fit to the data, and the noise data from the 7-pixel PoST. Although the pulses are fit reasonably well, the actual noise is much larger than the theoretical noise predicted by the model. The legend is Figure 4.3 on page 74
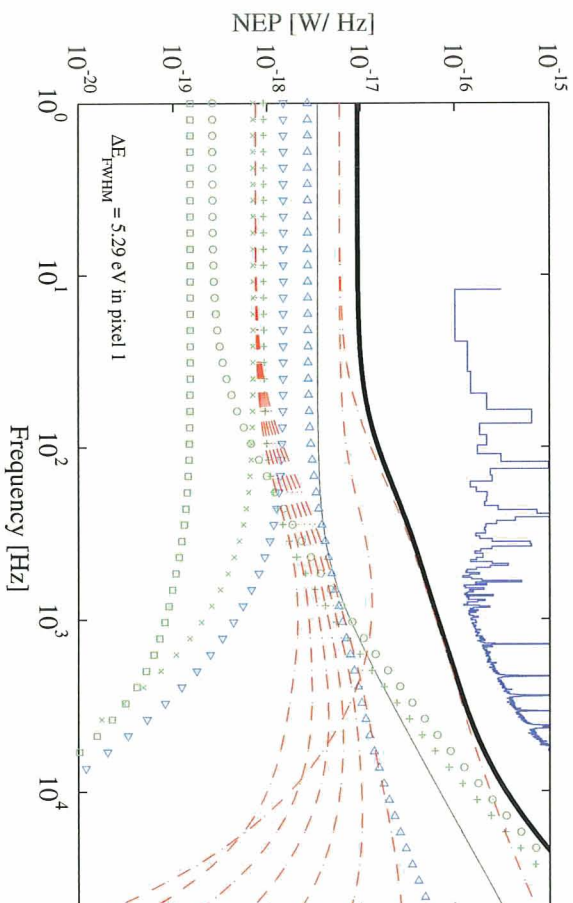
Figure 7.10: Theoretical and measured NEP for pixel 1 of 7-pixel PoST, signal on TES1. The NEP calculated from the data is far greater than the theoretical NEP, which is expected since the noise in this run was much worse than the theoretical noise. The legend is Figure 4.3 on page 74
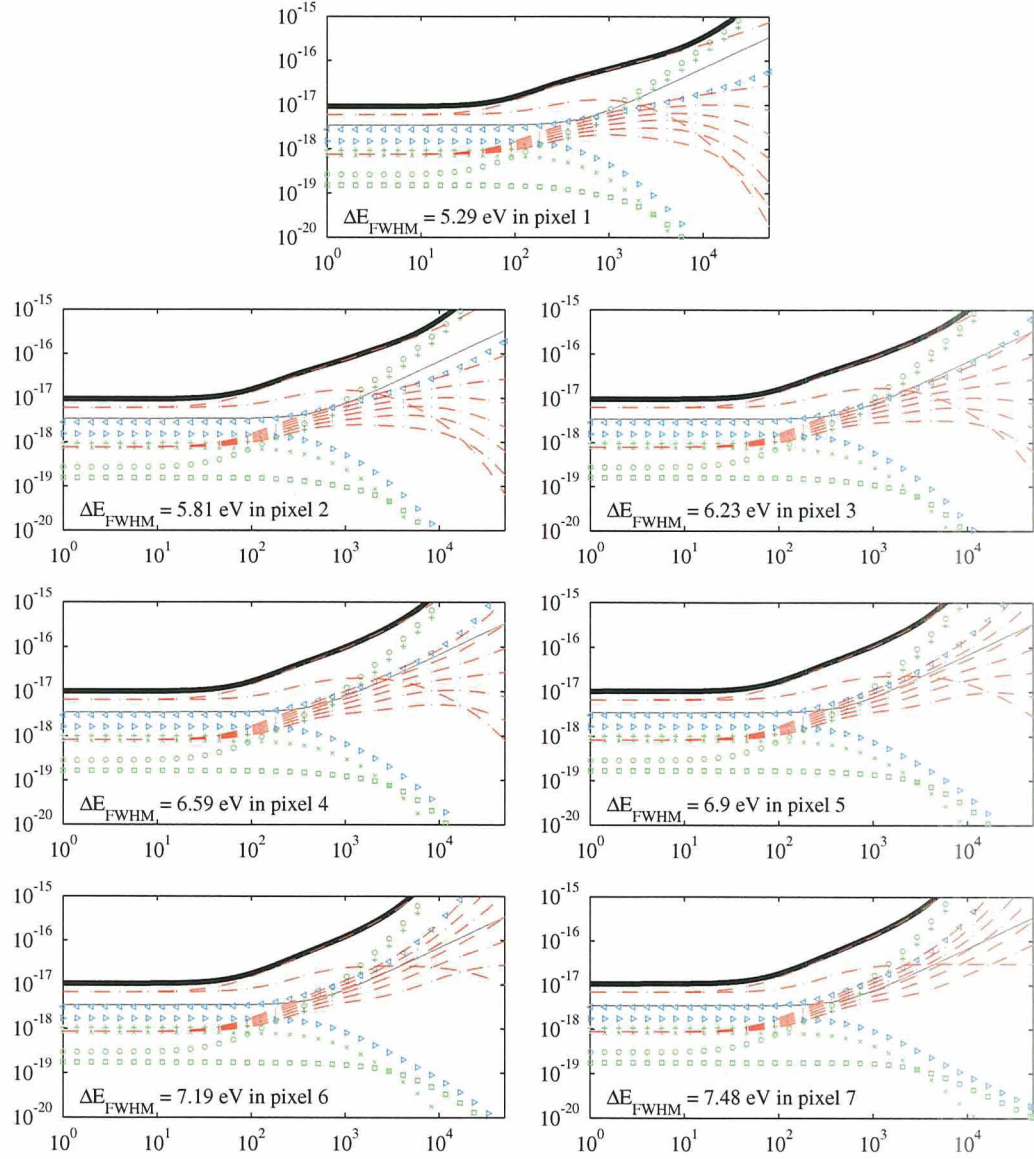
Figure 7.11: Theoretical NEP and resolution for 7-pixel PoST for data fit, signal on TES1. The link noise from the two absorber next to the TESs (G_{ae}) is the largest contributor to the NEP, and thus the limiting term in the resolution. Making $G_{ae} = G_a$ would result in a better theoretical resolution.

Chapter 8

Conclusion

8.1 Assessment

I started posing a simple question: how do we get to large pixel numbers in high-energy-resolution calorimeters?

Since the number of readout channels available is the current limiting quantity for going to large number of pixels, I investigated the idea of having multiple absorbers for every thermometer (and thus for every readout channel). To understand the operating parameters of this concept I had to expand the noise theory of Moseley, Mather, and McCammon (1984) to include not only multiple absorbers, but multiple thermometers in a single calorimeter. I expanded the matrix formulation first applied to calorimeters by Lindeman (2000) to describe our PoSTs. From these, I proceeded to derive a generalized method for calculating the noise spectrum and energy resolution of any complex calorimeter with multiple heat capacities and thermometers. This method relies on numerical matrix manipulation, so the complexity of the system is only limited by the processing power and memory of the computer.

One of the limitations of the theory is that it is still a linear theory. Non-linear effects stemming from saturation, hot phonon and electron processes, particle or photon escapes or losses, etc. are not yet accounted for.

Other effects that degrade resolution, such as time and gain drifts, position dependence, double pulses, etc., are not part of the noise theory.

This method can be easily adapted to other calorimeter systems as long as their behavior can be modeled by a linearized system of equations and the noise terms can be described by known frequency spectra. This includes superconducting absorbers, other thermometry schemes, etc.

I have also designed and tested a prototype of a PoST calorimeter. Many fabrication issues have been hashed out by our group, and through the optimization of the single-pixel and PoST processes we have arrived at a fairly robust and proven fabrication process. First light was achieved, and we have demonstrated 32 eV FWHM resolution at 1.5 keV. The tests done are preliminary and I expect we will have improved energy resolution results

shortly. The design is still in the prototype stage and there is much analysis to be done to understand the best operating conditions of the calorimeter and its trade-offs. However, the excellent results obtained with a small amount of data analysis show the great potential of this technology.

I believe that a detector design based on this work will be a strong contender for the main detector of the Constellation-X mission.

8.2 The future

One of the main drawbacks of the current PoST design is its excessive heat capacity. I have several ideas of how to achieve comparable absorbers-per-TES ratios in devices which don't suffer from this problem. I'll be trying these new ideas out soon. Stay tuned.

The electronics must be improved. We are almost ready to move to a two stage SQUID system which will have better wiring, better grounding, better heat sinking, etc. The readout system will get redone in the next year. We need a robust analog system that will give us no cross talk and be the workhorse in our single-pixel optimizations and high energy resolution runs.

We are also designing a two-stage ADR which will someday house an 8×8 SQUID multiplexer. With 64 channels, PoST arrays from 256 to 1024 pixels (depending on the absorbers-per-TES ratio) will be possible.

Different absorbers should be investigated. Superconductors might give better results for very large absorbers-to-TES ratios. The low heat capacity of superconductors must be weighted against quasi-particle recombination losses and associated time constants.

Other energies should be explored. My design was for an X-ray detector, but the theory will work for detectors from the sub-mm or lower to gamma rays. I have put together numbers for a UV version of this detector, and obtained $\sim$ 0.1 eV resolution estimates, comparable with the current optical TES results by Miller (2001). Gamma ray detectors, where large heat capacities are needed, might also be good candidates for this technology.

The obvious extension to 2-dimensional detectors will be made. I have several different designs in the works for 2-D PoSTs. In a 2-D detector, the number of pixels per detector goes as m^2, where m is the number of pixels on one side of the PoST. For large numbers of pixels, a 2-D PoST might be a better solution. The problem is that the PSF of your optics will now all fall within *one* detector, whereas in the linear PoST the PSF covers *three* different detectors (on average). These trade-offs must be studied.

There are many other applications for PoSTs apart from Constellation-X. Any application that wants X-ray imaging spectroscopy will benefit from this design. PoSTs are perfect for photon-starved situations where the rate is very low, and more area is needed. In some applications there is no need to image, but a larger detector area is needed. Materials analysis and laboratory astrophysics will benefit from larger detectors. The problem with large absorbers is position dependence. A PoST can be designed as a large absorber calorimeter where the position dependence is engineered and controlled so as to not be a problem. The real problem here is the count rate. For some materials analysis the excitation voltage used

is low so that only the surface of the sample is probed. In these applications the flux of X-rays is low and the experiment is photon-starved. For recombination line measurements in the Electron Beam Ion Trap (see Porter et al., 2000b, and references therein for a description of EBIT) the lines of interest are thousands of times weaker than the lines produced by direct excitation, which are at lower energy. If a good filter is used to prevent the direct excitation line from saturating the detector, then a PoST with a large area will allow the weak recombination lines to be studied. The X-ray background is another photon-starved system where one desires the biggest detector one can get.

The future looks bright for PoSTs. PoST development will continue here at Goddard, and I hope other researchers get excited about this technology and take it out for a spin ...

Appendix A

Hanging heat capacity study

In this appendix, we look at the very simple system in Figure A.1(a). This will show us how hanging heat capacities behave, and why their noise spectrum goes toward zero at low frequencies. It also demonstrates the versatility of the analysis method developed in this thesis.

We start with a simple thermal system: three equal heat capacities connected together, floating adiabatically in space: no heat in, no heat out. They are all at a temperature T. We place an ideal thermometer on C_1, and look at the noise spectrum from the thermodynamic temperature fluctuations of that heat capacity. These fluctuations arise from phonon noise. The phonon noise acts like a white-spectrum power noise source with RMS fluctuations of $P_{12} = \sqrt{4k_B T^2 G_{12}}$ between C_1 and C_2 and likewise between C_1 and C_b. Following the formulation derived in this thesis, we can write the theoretical model for this system:

$$\begin{pmatrix} \Delta T_b \\ \Delta T_1 \\ \Delta T_2 \end{pmatrix} = \begin{pmatrix} i\omega C_b + G_{1b} & -G_{1b} & 0 \\ -G_{1b} & i\omega C_1 + G_{1b} + G_{12} & -G_{12} \\ 0 & -G_{12} & i\omega C_2 + G_{12} \end{pmatrix}^{-1} \begin{pmatrix} P_{1b} \\ P_{12} - P_{1b} \\ -P_{12} \end{pmatrix} \quad (A.1)$$

To make things simple, at first we will assume all three heat capacities are the same value C. Following the time domain analysis in Section 4.1.1 we find the time constants of the system:

$$\tau_{12} = \frac{C}{G_{1b} + G_{12} + \sqrt{G_{12}^2 - G_{12}G_{1b} + G_{1b}^2}} \quad (A.2)$$

$$\tau_{1b} = \frac{C}{G_{1b} + G_{12} - \sqrt{G_{12}^2 - G_{12}G_{1b} + G_{1b}^2}} \quad (A.3)$$

The time constants are named this way since the values of the time constants tend toward $C/2G_{12}$ and C/G_{1b} as $G_{12} \gg G_{1b}$.

We can now use this model to understand the spectrum from a decoupled absorber in

161
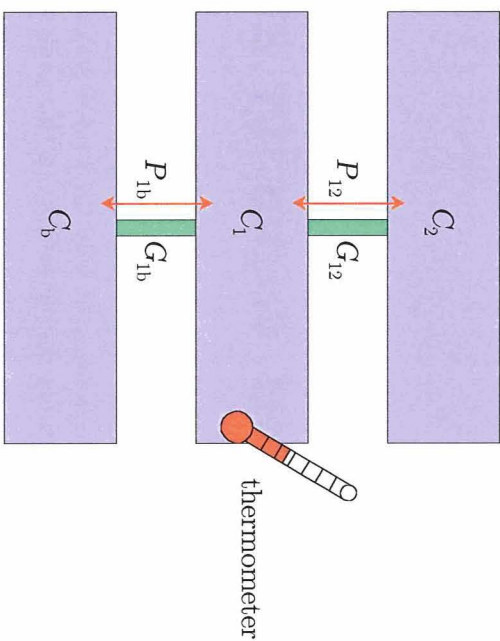
(a) A simple system of three heat capacities connected together. No electronics, just an ideal thermometer on C_1. Adiabatically isolated from the rest of the universe.
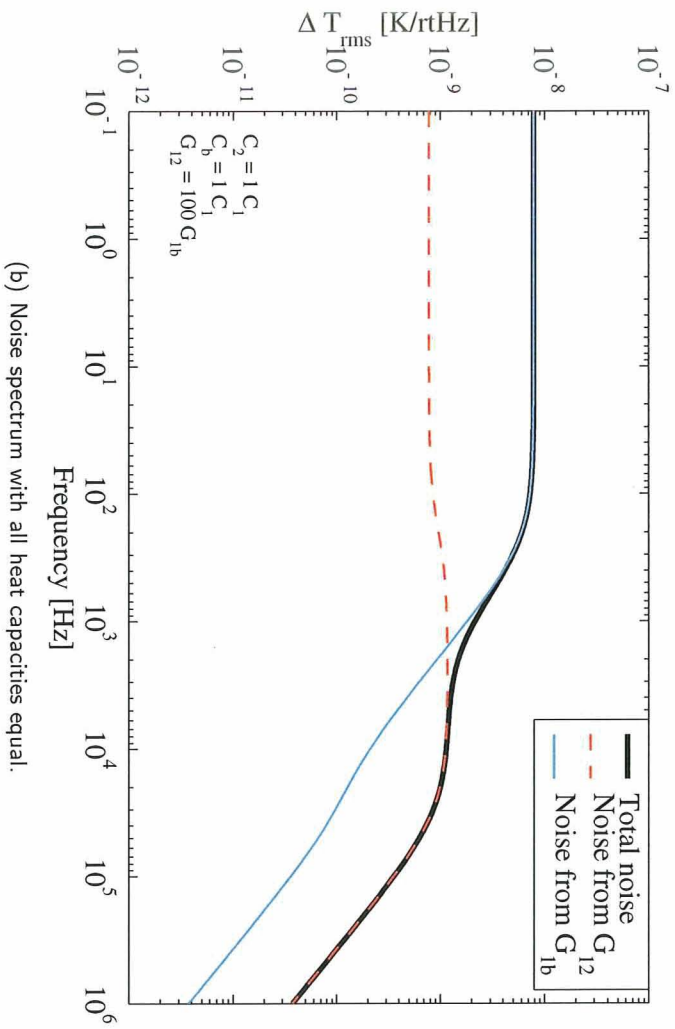
(b) Noise spectrum with all heat capacities equal.

Figure A.1: Hanging heat capacity schematic and noise.

a calorimeter. Figure A.1(b) shows the spectrum we get when we set $G_{12} = 100G_{1b}$ and all heat capacities the same. For this model, the heat capacity value used was 1 pJ/K, the conductance $G_{1b} = 1$ nW/K, and the temperature was set to 100 mK. Since all heat capacities are the same, the differences in the two noise terms are due solely to the different conductances to each heat capacity.

Let's consider the noise from conductance G_{12} and assume the other noise is zero. We would then have only the dashed red line. At frequencies much higher than $1/2\pi\tau_{12}$, the white noise source P_{12} is not able to push heat through the link G_{12} and the temperature fluctuations in C_1 are small. At frequencies lower than $1/2\pi\tau_{12}$ but higher than $1/2\pi\tau_{1b}$, P_{12} is able to move heat between C_1 and C_2, causing temperature fluctuations in C_1 that are sensed by our ideal thermometer. Since we are still above $1/2\pi\tau_{1b}$, heat cannot flow freely at these frequencies between C_1 and C_b. C_b is still decoupled from the other two heat capacities at these frequencies. The temperature fluctuations in C_1 are

$$\Delta T_{1rms} \sim \frac{P_{12}}{C_1\sqrt{\delta B}} \qquad (A.4)$$

where δB is the bandwidth of the signal. At frequencies lower than $1/2\pi\tau_{1b}$, heat starts flowing into C_b. The power being pumped in by P_{12}, which always has the same RMS value (white noise), now goes into both C_1 *and* C_b. The result is that the temperature fluctuations in C_1 becomes

$$\Delta T_{1rms} \sim \frac{P_{12}}{(C_1 + C_b)\sqrt{\delta B}} \qquad (A.5)$$

If the heat capacities are the same, the temperature fluctuations at low frequencies are about half of their maximum value at the middle frequencies. We see that as $G_{1b} \to 0$, the dip in the G_{12} noise spectrum moves to lower and lower frequencies, and if G_{1b} is zero, the noise from G_{12} looks flat at low frequencies just like we always expect phonon noise to look. Conclusion: the dip in the noise from G_{12} at low frequencies is due to the third heat capacity C_b.

Well, what happens if we increase C_b? The time constants are not given by the equations above, but we will not reproduce the messy formulae here. Figure A.2 tells the story. The high frequency part of the noise from G_{12} remains unchanged, but we clearly see that as C_b increases, the dip in the noise gets bigger and bigger due to the difference between Eq. (A.4) and Eq. (A.5). It is now clear that as the heat capacity $C_b \to \infty$, i.e., it becomes a heat sink, the noise of $G_{12} \to 0$ at zero frequency.

Now we can look at the noise from G_{1b}. In Figure A.1(b) it looks just like phonon noise should, except for a little kink around $1/2\pi\tau_{12}$. In Figure A.3 we vary the value C_2 to expose the "kink" into a shelf between the two time constants of the system. Since C_2 is increasing, the overall time constant $(C_1 + C_2)/G_{1b}$ increases, lowering the roll frequency of the phonon noise G_{1b}.

Let's look at Figure A.3(b). At very high frequencies, very little heat flows through G_{1b}, and the signal in C_1 is small. Moreover, C_2 is "disconnected" from C_1 at these frequencies.

APPENDIX A. HANGING HEAT CAPACITY STUDY

$C_2 = 1 C_1$
$C_b = 10 C_1$
$G_{12} = 100 G_{1b}$

Total noise
Noise from G_{12}
Noise from G_{1b}

(a)

$C_2 = 1 C_1$
$C_b = 1e+03 C_1$
$G_{12} = 100 G_{1b}$

Total noise
Noise from G_{12}
Noise from G_{1b}

(b)
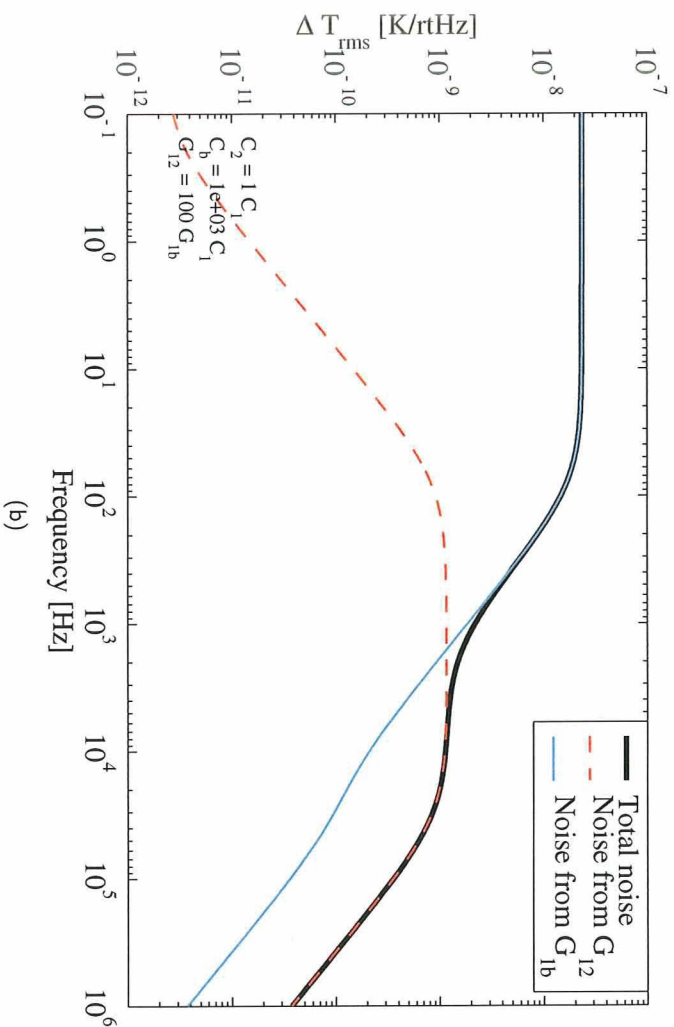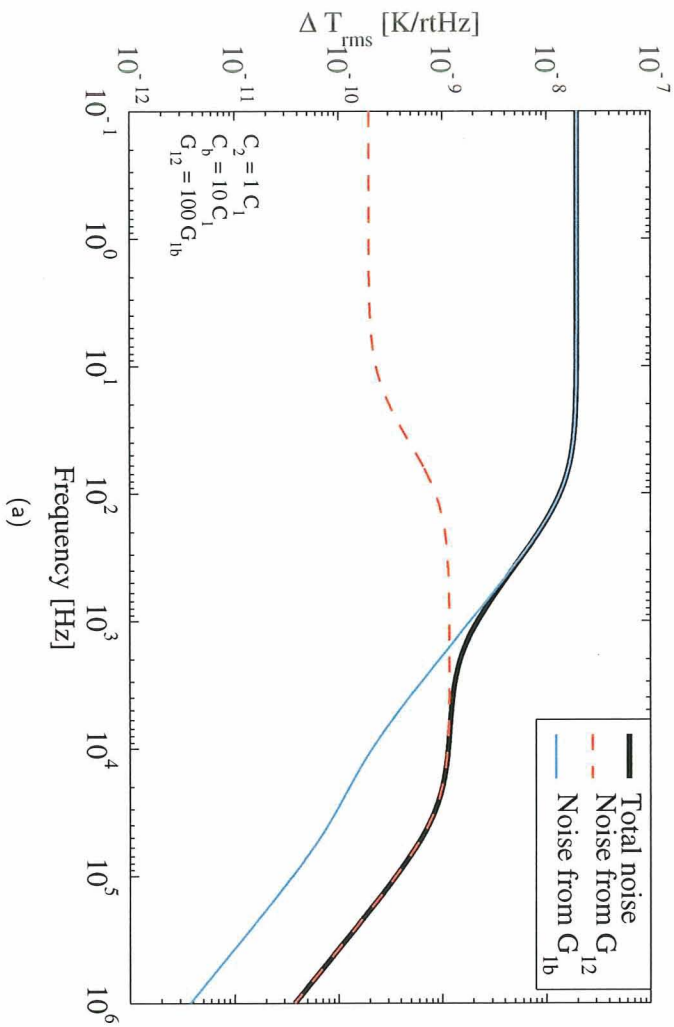
Figure A.2: Now we start increasing the heat capacity of the "bath"
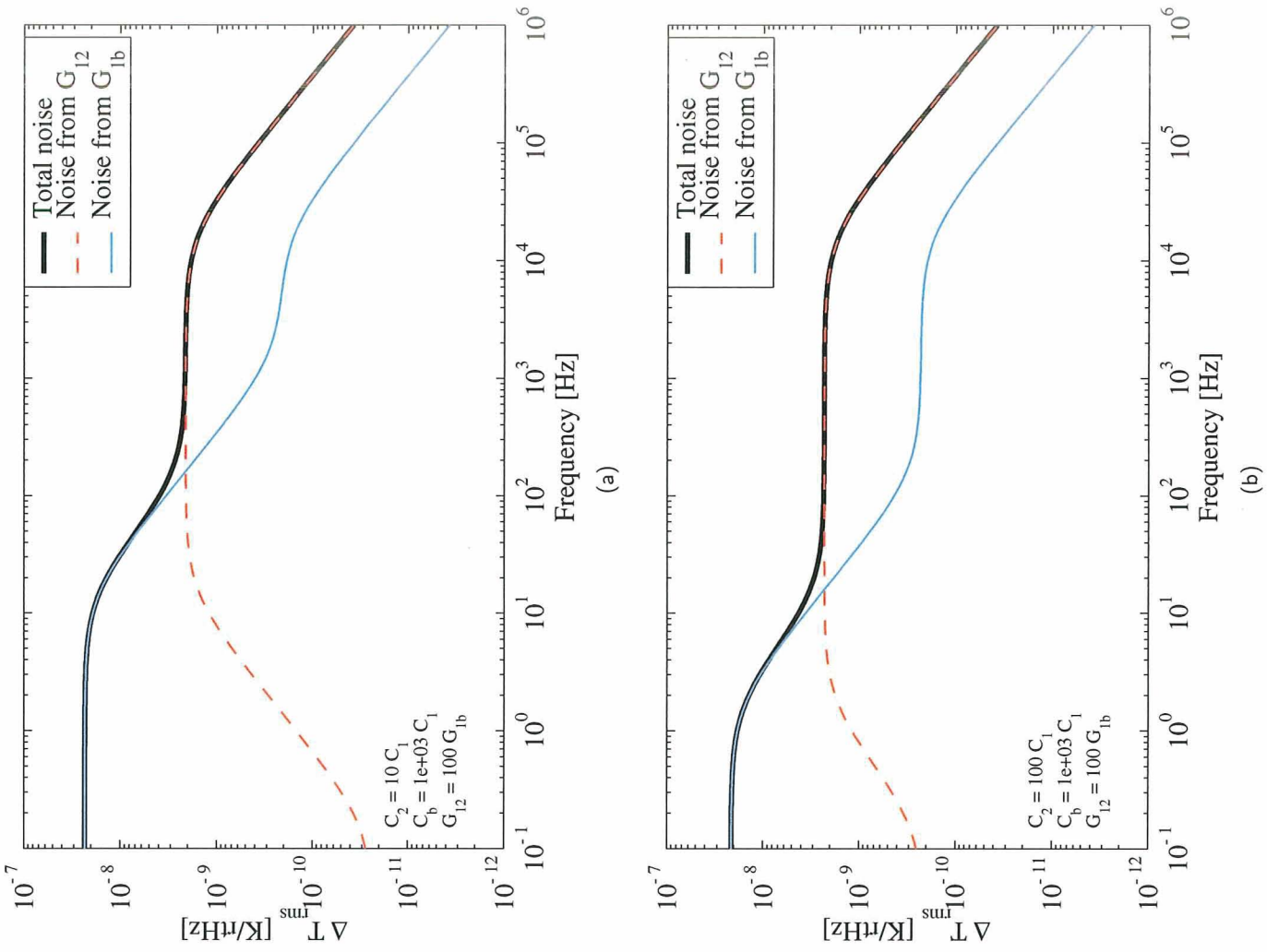
Figure A.3: Here we increase the heat capacity of the absorber C_2.

The small amount of heat that gets through G_{1b} goes to heating C_1, as in Eq. (A.4). As we lower the frequency, but still above 50 kHz, the amount of heat making it through the link increases, and the RMS value of the temperature fluctuations increases. Now as we approach 50 kHz, C_1 starts being able to communicate with C_2. This means that as we lower the frequency, more heat makes it through G_{1b}, but more heat also makes it through G_{12}, increasing the "effective" heat capacity that P_{1b} sees. As we lower the frequency, these two effects, the increase in heat through G_{1b} and the increase in "effective" heat capacity due to more heat leaking into C_2, cancel each other out, creating the flat part we see in Figure A.3(b). In this flat part, the frequency is low enough that heat freely moves into C_2 though G_{12}, and we are in the regime of Eq. (A.5). But we are still above the rolloff frequency $\sim G_{1b}/(C_1 + C_2)2\pi$, which means not all the power P_{1b} is making it though G_{1b}. So as we lower the frequency and cross 100 Hz, we start rising again, until G_{1b} is fully "open". At that point we flatten out and remain that way down to zero frequency. The noise from G_{1b} in the previous figures behaves the same way.

Appendix B

Two TESs on one calorimeter

In this appendix we study the limits of the response of a PoST when looking at just one channel, to understand the values of Eq. (4.22) as $G_{12} \to \infty$. Since we want to model the effect of a high link conductance on a PoST we will analyze the system in Figure B.1. We assign a heat capacity of $2C$ and a conductance to the bath of $2G$ since that will be the total values for the PoST in this limit. Since the quantity of interest is the phonon noise, we will disregard detector and circuit noise and assume for simplicity perfect voltage bias. We will also assume $\alpha_I = 0$. With these simplifications we have the two current equations and one thermal equation:

$$V = I_1(t)R_1(T) \tag{B.1}$$
$$V = I_2(t)R_2(T) \tag{B.2}$$
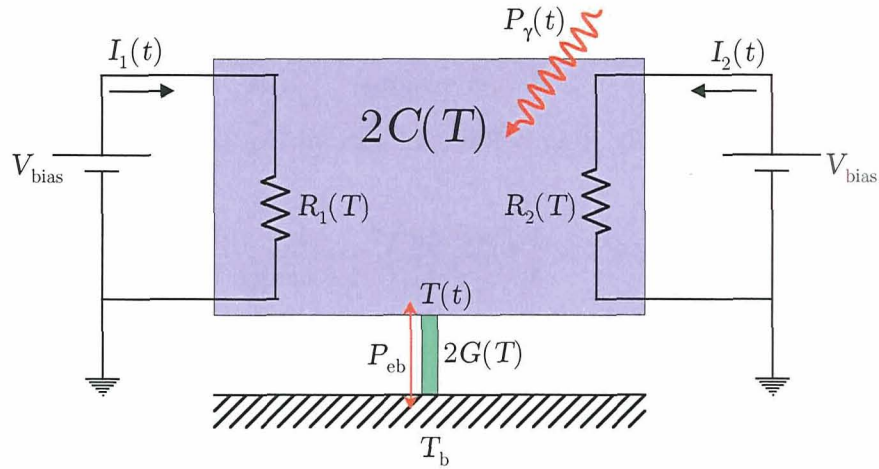
Figure B.1: Two TESs on one calorimeter. This is the limit as $G_{12} \to \infty$ for our PoST design. For the analytic solution we disregard detector and circuit noise and assume perfect voltage bias.

$$2C'\frac{dT}{dt} = VI_1(t) + VI_2(t) - 2K(T^n(t) - T_b^n(t)) + P_{tn}(t) + P_\gamma(t) \qquad (B.3)$$

We linearize the system to obtain

$$0 = \frac{\alpha I R}{T}\Delta T + R\Delta I_1 \qquad (B.4)$$

$$0 = \frac{\alpha I R}{T}\Delta T + R\Delta I_2 \qquad (B.5)$$

$$2C\frac{d}{dt}\Delta T = V(\Delta I_1 + \Delta I_2) - 2KnT^{n-1}\Delta T + P_{tn}(t) + P_\gamma(t) \qquad (B.6)$$

where we have assumed both TES are biased at the same steady-state resistance R with a voltage V. From these equations it is clear that $\Delta I_1 = \Delta I_2$. Since we have two TESs on one calorimeter this is expected. The temperature vs. current relationship is

$$\Delta T = -\frac{T}{\alpha I}\Delta I_1$$

Which is the same result obtained in Eq. (2.16). Note that Eq. (B.7) is valid only when detector and circuit noise are neglected. Using the definition of G (Eq. (3.14)) we can now solve for ΔI_1 and obtain

$$\frac{d}{dt}\Delta I_1 = -\left(\frac{\alpha P}{TC} + \frac{G}{C}\right)\Delta I_1 - \frac{\alpha I}{2TC}(P_{tn}(t) + P_\gamma(t)) \qquad (B.7)$$

Now taking the Fourier transform and looking at one frequency we can rearrange to arrive at

$$\Delta I_1 = \frac{-\frac{\alpha I}{2TG}(P_{tn}(\omega) + P_\gamma(\omega))}{1 + \frac{\alpha P}{TG} + i\omega\tau_o}$$

$$= -\frac{\alpha P}{TG}\frac{\tau_{eff}}{\tau_o}\frac{1}{1+i\omega\tau_{eff}}\frac{P_{tn}(\omega) + P_\gamma(\omega)}{2V} \qquad (B.9)$$

where τ_{eff} is defined in the $R_L = \alpha_I = 0$ limit (same as Eq. (2.19)). The magnitude of the noise will then be

$$\langle|\Delta I_1|^2\rangle = \frac{1}{4}\frac{1}{\left(\frac{\alpha P}{TG}\frac{\tau_{eff}}{\tau_o}\right)^2}\frac{1}{1+\omega^2\tau_{eff}^2}\frac{P_{tn}^2(\omega)}{V^2} \qquad (B.11)$$

Comparing with Eq. (3.41) with $R_L = \alpha_I = 0$ we can see that this current noise is smaller by a factor of $1/4$, which is the limit as $G_{12} \to \infty$ of Eq. (4.22). But now we need to put in the noise $P_{tn}(\omega)$. If we only look at phonon noise, the phonon noise for the system in Figure B.1 will be $P_{tn}^2 = 2k_B T^2(2G)$. The phonon noise for a single pixel calorimeter of conductance G will be $P_{tn}^2 = 2k_B T^2 G$, a factor of 2 less.

The ratio of the noise seen in a 1G, 1C calorimeter with one TES compared to a 2G,

$2C$ calorimeter with two TESs is

$$\frac{\Delta I_{\text{rms}}^{2G,2TES}}{\Delta I_{\text{rms}}^{1G,1TES}} = \frac{1}{\sqrt{2}} \tag{B.12}$$

We expect a one-dimensional PoST to behave as two individual TESs when $G_{12} \rightarrow 0$, so the signal from TES_1 will be the nominal single pixel RMS noise, while as $G_{12} \rightarrow \infty$, the RMS current noise on TES_1 will drop to $1/\sqrt{2}$ its single-pixel value. We can see these two limits in the theoretical gray lines in figures like Figure 4.19.

There is an interesting corollary to this exercise. In the system on Figure B.1, if we add both currents to get the total current, we get

$$\Delta I_{\text{rms}}^{2G,2C} = \sqrt{\Delta I_{1\text{rms}}^2 + \Delta I_{2\text{rms}}^2} = \sqrt{\left(\frac{\Delta I_{\text{rms}}^{1G,1C}}{\sqrt{2}}\right)^2 + \left(\frac{\Delta I_{\text{rms}}^{1G,1C}}{\sqrt{2}}\right)^2} = \Delta I_{\text{rms}}^{1G,1C} \tag{B.13}$$

The total RMS current noise and spectral shape do not change if one scales C, G, and P proportionately, while keeping R, α, α_I and the temperatures constant.

APPENDIX B. TWO TESS ON ONE CALORIMETER

Appendix C

Theoretical noise when reading voltage

It is trivial ;-) to show that Eq. (3.33) in the voltage readout case becomes

$$\left(1 + \frac{\alpha P}{TG}\frac{R - R_\mathrm{L}}{R + R_\mathrm{L}}\right)\left(1 + i\omega\tau_\mathrm{eff}\right)\Delta V =$$

$$\left(1 + \frac{\alpha P}{TG} + i\omega\tau_o\right)\frac{(V_\mathrm{cn}(\omega) - R_\mathrm{L}I_\mathrm{cn}(\omega))R}{R + R_\mathrm{L}} -$$

$$(1 + i\omega\tau_o)\frac{V_\mathrm{dn}(\omega)R_\mathrm{L}}{R + R_\mathrm{L}} + \frac{\alpha P}{TG}\frac{P_\mathrm{tn}(\omega)R_\mathrm{L}}{I(R + R_\mathrm{L})} \qquad \text{(C.1)}$$

and the voltage noise terms are

$$\left\langle|\Delta V_\mathrm{tn}(\omega)|^2\right\rangle = \left(\frac{P_\mathrm{tn}(\omega)R_\mathrm{L}}{I(R + R_\mathrm{L})}\right)^2 \frac{\left(\frac{\alpha P}{TG}\right)^2}{\left(1 + \frac{\alpha P}{TG}\frac{R - R_\mathrm{L}}{R + R_\mathrm{L}}\right)^2}\frac{1}{\left(1 + \omega^2\tau_\mathrm{eff}^2\right)} \qquad \text{(C.2)}$$

$$\left\langle|\Delta V_\mathrm{dn}(\omega)|^2\right\rangle = \left(\frac{V_\mathrm{dn}(\omega)R_\mathrm{L}}{R + R_\mathrm{L}}\right)^2 \frac{1}{\left(1 + \frac{\alpha P}{TG}\frac{R - R_\mathrm{L}}{R + R_\mathrm{L}}\right)^2}\frac{1 + \omega^2\tau_o^2}{\left(1 + \omega^2\tau_\mathrm{eff}^2\right)} \qquad \text{(C.3)}$$

$$\left\langle|\Delta V_\mathrm{cn}(\omega)|^2\right\rangle = \frac{V_\mathrm{cn}(\omega)^2 + R_L^2 I_\mathrm{cn}(\omega)^2}{(R + R_\mathrm{L})^2}\frac{R}{\left(1 + \frac{\alpha P}{TG}\frac{R - R_\mathrm{L}}{R + R_\mathrm{L}}\right)^2}\frac{\left(1 + \frac{\alpha P}{TG}\right)^2 + \omega^2\tau_o^2}{\left(1 + \omega^2\tau_\mathrm{eff}^2\right)} \qquad \text{(C.4)}$$

$$\left\langle|\Delta V_\mathrm{tot}(\omega)|^2\right\rangle = \left\langle|\Delta V_\mathrm{tn}(\omega)|^2\right\rangle + \left\langle|\Delta V_\mathrm{dn}(\omega)|^2\right\rangle + \left\langle|\Delta V_\mathrm{cn}(\omega)|^2\right\rangle \qquad \text{(C.5)}$$

Comparing with Eq. (3.41) and Eq. (3.42) we can show that the thermal and detector current noise equations are related to the thermal and detector voltage noise equations by

$$\left\langle|V_\mathrm{tn}(\omega)|^2\right\rangle = \left\langle|-I_\mathrm{tn}(\omega)R_L|^2\right\rangle \qquad \text{(C.6)}$$

$$\left\langle |V_{\mathrm{dn}}(\omega)|^2 \right\rangle \;\; = \;\; \left\langle |-I_{\mathrm{dn}}(\omega)R_L|^2 \right\rangle \tag{C.7}$$

Now in the circuit noise case, it is a little more complicated. Compare Eq. (3.43) to Eq. (C.4). First off, the multiplying resistance is R_o instead of R_L. There are sign differences inside the equations also. The difference in the current vs. voltage equations comes not only from the fact that we are changing from current to voltage as the means of reading out the signal, but also because to get negative feedback with a detector under current bias the detector must have a negative α, whereas to get the same negative feedback on a detector under voltage bias you need a positive α. In other words, to get the same behavior with all other things being equal, a current biased device must have an α of the opposite sign as a voltage biased device. In the perfect bias case ($R_{\mathrm{L}} = 0$), voltage bias requires current readout and current bias requires voltage readout. So there is an inherent association between current readout and voltage bias, and of voltage readout and current bias. Note that this does not mean that you cannot read out the voltage of a partially voltage biased device, this just means that when setting up the equations we end up with these differences in the results so that analogous systems show the same behavior. The term $1 + \frac{\alpha P}{TG}$ in Eq. (C.4) has a plus sign, but since α must have the opposite sign as in the current readout case, we see that it is equivalent to the term $1 - \frac{\alpha P}{TG}$ in Eq. (3.43). The other terms work out the same in both equations because they contain both α and $R - R_{\mathrm{L}}$. $R - R_{\mathrm{L}}$ is another term that needs to have opposite signs in the current bias and voltage bias cases, so the signs from the $R - R_{\mathrm{L}}$ term and the α term cancel out and you get the same equations in both cases.

Following the procedure outlined in Section 3.1.5 we can derive the NEP for negative α calorimeters to be

$$\mathrm{NEP}(\omega)^2 = P_{\mathrm{tn}}(\omega)^2 + \frac{1 + \omega^2 \tau_o^2}{\left(\frac{\alpha P}{TG}\right)^2} I^2 V_{\mathrm{dn}}(\omega)^2 + \frac{R}{R_{\mathrm{L}}} \frac{(1 + \frac{\alpha P}{TG})^2 + \omega^2 \tau_o^2}{\left(\frac{\alpha P}{TG}\right)^2} I^2 V_{\mathrm{cn}}(\omega)^2 \tag{C.8}$$

Note the similarities between this equation and the equations in Section 3.1.5. The factor R_o/R_L insures circuit voltage noise sources go to zero under perfect current bias. There is also a sign change in the term $1 + \frac{\alpha P}{TG}$. $1/f$ noise can be added by inserting another term into the NEP with the same form as the $V_{\mathrm{dn}}(\omega)$ term. The theoretical resolution can be found by using Eq. (3.68).

The final word is that one must be *very* careful when changing from current to voltage noise formulations. Assuming the answer can quickly lead to the wrong result. These results are correct for the case where $\alpha_{\mathrm{I}} = 0$. We are still not sure if the voltage equations are correct when $\alpha_{\mathrm{I}} \neq 0$. The problem stems from the fact that one should really define α_{V}, and we are not sure yet how to do that.

Appendix D

Alternative formulation when $L = C_{\text{cap}} = 0$

In this section we show an equivalent formulation for the calorimeter equations derived in Section 3.1 that will allow us to simplify the algebra in the limit when $L = 0$.

If there is no inductance or capacitance in the circuit, then current and temperature are related by constants and only one equation is needed to characterize the system. But keeping the two equations makes it easier to see how the ETF goes to work, and for complex calorimeters this really involves no extra effort since one is already committed to use matrices. Referring back to Figure 3.1, we write down the two equations

$$0 = V_{\text{bias}} - I(t)\Big(R_{\text{L}} + R(T, I)\Big) + V_{\text{cn}}(t) - R_{\text{L}}I_{\text{cn}}(t) + V_{\text{dn}}(t) \tag{D.1}$$

$$C(T)\frac{dT(t)}{dt} = I(t)V(t) - P_{\text{link}}(T(t), T_{\text{b}}) + P_{\text{tn}}(t) \tag{D.2}$$

in the previous derivation, we used Eq. (3.3) to solve for $V(t)$ in the thermal equation. Since we have set $L = 0$, the variables $I(t)$, $V(t)$ and $T(t)$ are all related by constants. In this special case, we can solve for $V(t)$ and its partials when we do the linearization:

$$V(t) = V_{\text{bias}} + V_{\text{cn}}(t) - IR_{\text{L}} \tag{D.3}$$

$$\left.\frac{\partial V}{\partial I}\right|_{\frac{I}{T}} = -R_{\text{L}} \tag{D.4}$$

$$\left.\frac{\partial V}{\partial T}\right|_{\frac{I}{T}} = 0 \tag{D.5}$$

Substituting for $V(t)$ and following the same linearization procedure as before, we arrive at

$$(R + R_{\text{L}})\Delta I + \alpha\frac{V}{T}\Delta T = V_{\text{cn}}(t) - R_{\text{L}}I_{\text{cn}}(t) + V_{\text{dn}}(t) \tag{D.6}$$

$$-I(R - R_{\text{L}})\Delta I + (iC\frac{d}{dt} + G)\Delta T = P_{\text{tn}}(t) - I(V_{\text{cn}}(t) - R_{\text{L}}I_{\text{cn}}(t)) \tag{D.7}$$

173

Compare to Eq. (3.11) and Eq. (3.15). The current equation is the same, but the thermal equation is quite different. In the thermal equation the ETF term $I(R_{\mathrm{L}} - R)$ is clear. As $R_{\mathrm{L}} \to R$ the ETF term vanishes. This happens because when $R = R_{\mathrm{L}}$ the circuit is in the saddle point between voltage and current bias. The circuit and detector current noise terms have switched places, so now only the circuit sources appear in the thermal equation. For more complicated systems with various heat capacities linked, this formulation is simpler, especially if one is only interested in the device Johnson noise and disregards the other electrical noise sources. Instead of combining the two equations as we did in Eq. (3.33) we will convert these equations to matrix notation. Taking the Fourier transform and looking at one frequency component we have:

$$
\begin{pmatrix} R_o + R_{\mathrm{L}} & \alpha \frac{V_o}{T_o} \\ -I_o(R_o - R_{\mathrm{L}}) & i\omega C + g \end{pmatrix} \begin{pmatrix} \Delta I \\ \Delta T \end{pmatrix} = \begin{pmatrix} V_{\mathrm{dn}}(\omega) + V_{\mathrm{cn}}(\omega) \\ P_{\mathrm{tn}}(\omega) + I_o V_{\mathrm{cn}}(\omega) \end{pmatrix} \tag{D.8}
$$

Solving this matrix for ΔI and ΔT gives the same results we obtained in Section 3.1. We want to restate that this formulation is only valid in the case where $L = 0$ and $C_{\mathrm{cap}} = 0$. All we have done is manipulate the equations into a form where V_{dn} only appears in the current equation, to make the algebra simpler and the ETF term clear. This formulation is advantageous when one is working with only Johnson and phonon noise and one wants to solve the equations algebraically.

Bibliography

D. V. Anghel, J. P. Pekola, M. M. Leivo, J. K. Suoknuuti, and M. Manninen. Properties of the Phonon Gas in Ultrathin Membranes at Low Temperature. *Physical Review Letters*, 81:2958–2961, October 1998.

N. Ashcroft and N. Mermin. *Solid State Physics*. Saunders College, 1976.

S. Bandler, E. Silver, H. Schnopper, S. Murray, M. Barbera, N. Madden, D. Landis, J. Beeman, E. Haller, and G. Tucker. Ntd-ge-based microcalorimeter performance. In *Proceedings of the 8th International Workshop on Low Temperature Detectors (LTD-8)*, volume 444, pages 273–277. Nucl. Inst. & Meth. A, 2000.

N. E. Booth. Quasiparticle trapping and the quasiparticle multiplier. *Applied Physics Letters*, 50:293–295, February 1987.

N. E. Booth, B. Cabrera, and E. Fiorini. Low-temperature particle detectors. *Annual Reviews of Nuclear and Particle Science*, 46:471–532, 1996.

W. E. Boyce and R. C. DiPrima. *Elementary Differential Equations and Boundary Value Problems*. Wiley & Sons, 1986.

B. Cabrera, B. L. Dougherty, A. T. Lee, M. J. Penn, J. G. Pronko, and B. A. Young. Prompt phonon signals from particle interactions in Si crystals. In *Fifth International Workshop on Low Temperature Detectors (LTD-5)*, volume 93, pages 365–375. Journal of Low Temperature Physics, 1993.

Center for X-ray optics. http://www-cxro.lbl.gov/. A good place for X-ray data. Their X-ray data booklet is excellent.

J. A. Chervenak, K. D. Irwin, E. N. Grossman, J. M. Martinins, C. D. Reintsema, and M. E. Huber. Superconducting multiplexer for arrays of transition edge sensors. *Applied Physics Letters*, 74(26):4043–5, 1999.

E. Cosulich, F. Gatti, and S. Vitale. Further results on μ-calorimeters with superconducting absorbers. *Journal of Low Temperature Physics*, 93:263–268, November 1993.

S. I. Dorozhkin, F. Lell, and W. Schoepe. Energy relaxation of hot electrons and inelastic collision time in thin metal films at low temperatures. *Solid State Communications*, 60 (3):245–248, 1986.

R. D. Evans. *The Atomic Nucleus*. McGraw-Hill, 1955.

A. E. Evrard, C. A. Metzler, and J. F. Navarro. Mass Estimates of X-Ray Clusters. *Astrophysical Journal*, 469:494–507, October 1996.

W. S. Fann, H. W. K. Tom, and J. Bokor. Observation of the thermalization of electrons in a metal excited by femtosecond optical pulses. In *Proceedings of the 8th International Conference on Ultrafast Phenomena*, volume 55, pages 331–334. Springer Ser. Chem. Phys., 1993.

E. Figueroa-Feliciano, B. Cabrera, A. J. Miller, S. F. Powell, T. Saab, and A. B. C. Walker. Optimal filter analysis of energy-dependent pulse shapes and its application to TES detectors. In *Proceedings of the 8th International Workshop on Low Temperature Detectors (LTD-8)*, volume 444, pages 453–456. Nucl. Inst. & Meth. A, 2000a.

E. Figueroa-Feliciano, C. K. Stahle, F. M. Finkbeiner, R. Kelley, M. A. Lindeman, F. S Porter, N. Tralshawala, M. Li, and C. M. Stahle. Mo/Au TES X-ray calorimeter with 2.8 eV resolution at 1.5 keV. In *From X-rays to X-band: Space Astrophysics Detectors and Detector Technologies Conference*, STScI, Baltimore, MD, 2000b. in print, see http://www.stsci.edu/stsci/meetings/space_detectors/.

F. M. Finkbeiner, R. P. Brekosky, J. A. Chervenak, E. Figueroa-Feliciano, M. J. Li, M. A. Lindeman, N. Tralshawala, C. K. Stahle, and C. M. Stahle. Fabrication of close-packed TES microcalorimeter arrays using superconducting molybdenum/gold transition-edge sensors. In *9th International Workshop on Low Temperature Detectors (LTD-9)*. AIP Conference Proceedings, in print, 2002.

D. W. Fischer and W. L. Baun. Diagram and nondiagram lines in K spectra of aluminum and oxygen from metallic and anodized aluminum. *Journal of Applied Physics*, 36:534–537, 1965.

D. J. Fixsen and S. H. Moseley. Optimal fitting of nonlinear detector responses. In *9th International Workshop on Low Temperature Detectors (LTD-9)*. AIP Conference Proceedings, in print, 2002.

M. Galeazzi. An external electronic feedback system applied to a cryogenic microcalorimeter. *Review of Scientific Instruments*, 69:2017–2023, May 1998.

M. Galeazzi, D. Liu, D. McCammon, W. T. Sanders, P. Tan, E. Figueroa-Feliciano, and C. K. Stahle. Performance modeling of micro-calorimeter detectors. In *9th International Workshop on Low Temperature Detectors (LTD-9)*. AIP Conference Proceedings, in print, 2002.

S. Guerron. *Quasiparticles in a diffusive conductor: Interaction and paring*. PhD thesis, L'Université Paris 6, 1997.

H. F. C. Hoevers. Superconducting transition edge sensors for X-ray microcalorimetry. In *9th International Workshop on Low Temperature Detectors (LTD-9)*. AIP Conference Proceedings, in print, 2002.

D. W. Hogg. Distance measures in cosmology. *astro-ph/9905116*, December 2000.

W. Holmes, J. M. Gildemeister, and P. L. Richards. Measurements of thermal transport in low stress silicon nitride films. *Applied Physics Letters*, 72(18):2250–2252, may 1998.

D. J. Horner. *X-ray scaling laws for galaxy clusters and groups*. PhD thesis, University of Maryland, College Park, 2001.

M. E. Huber, A. M. Corey, K. L. Lumpkins, F. N. Nafe, J. O. Rantschler, G. C Hilton, J. M Martinis, and A. H. Steinbach. DC SQUID series arrays with intracoil damping to reduce resonance distortions. *Journal of Applied Superconductivity*, 5:425–429, July 1997.

K. D. Irwin. An application of electrothermal feedback for high resolution cryogenic particle detection. *Applied Physics Letters*, 66:1998–2000, April 1995a.

K. D. Irwin. *Phonon-Mediated Particle Detection using Superconducting Transition-Edge Sensors*. PhD thesis, Stanford University, 1995b.

G. Jezequel and J. Thomas. Experimental band structure of semimetal bismuth. *Physical Review B*, 56(11):6620–6626, sep 1997.

R. L. Kelley, M.D. Audley, K.R. Boyce, S.R. Breon, R. Fujimoto, Gendreau K.C., S.S. Holt, Y. Ishisaki, Dan McCammon, Tatehiro Mihara, Kazushita Mitsuda, Samuel H. Moseley, David B. Mott, F. Scott Porter, Caroline K. Stahle, and Andrew E. Szymkowiak. The ASTRO-E High-Resolution X-Ray Spectrometer. In *EUV, X-Ray, and Gamma-Ray Instrumentation for Astronomy X*, volume 3765, page 114. SPIE, 1999.

G. R. Knoll. *Radiation Detection and Measurement*. Wiley and Sons, 1979.

V. N. Kopylov and L. P. Mezhov-Deglin. Investigation of the kinetic coefficients of bismuth at helium temperatures. *Sov. Phys.-JETP*, 38(2):357–364, feb 1974.

A. G. Kozorezov. Kinetics of interacting quasiparticles and phonons in non-equilibrium superconductors. In *Proceedings of the 8th International Workshop on Low Temperature Detectors (LTD-8)*, volume 444, pages 3–7. Nucl. Inst. & Meth. A, 2000.

M. M. Levio and J. P. Pekola. Thermal characteristics of silicon nitride membranes at sub-Kelvin temperatures. *Applied Physics Letters*, 72(11):1305–1307, 1998.

M. A. Lindeman. *Microcalorimetry and the Transition-Edge Sensor*. PhD thesis, University of California at Davis, 2000.

M. A. Lindeman, R. P. Brekosky, E. Figueroa-Feliciano, F. M. Finkbeiner, M. J. Li, C. K. Stahle, C. M. Stahle, and N. Tralshawala. Performance of Mo/Au TES microcalorimeters. In *9th International Workshop on Low Temperature Detectors (LTD-9)*. AIP Conference Proceedings, in print, 2002.

H. J. Maris. Phonon physics and low temperature detectors of dark matter. In *Fifth International Workshop on Low Temperature Detectors (LTD-5)*, volume 93, pages 355–364. Journal of Low Temperature Physics, 1993.

J. C. Mather. Bolometer noise: nonequilibrium thoery. *Journal of Applied Optics*, 21: 1125–1129, March 1982.

J. C. Mather. Bolometers: ultimate sensitivity, optimization, and amplifier coupling. *Journal of Applied Optics*, 23:584–588, February 1984.

O. Meier, M. Bravin, M. Bruckmayer, P. Di Stefano, T. Frank, M. Loidl, P. Meunier, F. Probst, G. Safran, W. Seidel, I. Sergeyev, M. Sisti, L. Stodolsky, S. Uchaikin, and L. Zerle. Active thermal feedback for massive cryogenic detectors. In *Proceedings of the 8th International Workshop on Low Temperature Detectors (LTD-8)*, volume 444, pages 350–352. Nucl. Inst. & Meth. A, 2000.

L. P. Mezhov-Deglin, V. N. Kopylov, and É. S. Medvedev. Contributions of various phonon relaxation mechanisms to the thermal resistance of the crystal lattice of bismuth at temparatures below 2 K. *Sov. Phys.-JETP*, 40(3):557–563, 1975.

A. J. Miller. *Development of a broadband optical spectrophotometer using superconducting transition-edge sensors*. PhD thesis, Stanford University, 2001.

S. H. Moseley, J. C. Mather, and D. McCammon. Thermal detectors as x-ray spectrometers. *Journal of Applied Physics*, 56:1257–1262, September 1984.

S. W. Nam, B. Cabrera, P. Colling, R. M. Clarke, E. Figueroa-Feliciano, A. J. Miller, and R. W. Romani. A new biasing technique for transition edge sensors with electrothermal feedback. In *IEEE Transactions of Applied Superconductivity*, volume 9, pages 4209–4212, June 1999.

NIST physical reference data. http://physics.nist.gov/PhysRefData/. Form this website one can get photon crossections for different materials, among many other things.

B. Nordfors. A note on the Al $K\alpha_3\alpha_4$ lines in metal oxide. *Proc. Phys. Soc. A*, 68:654–656, 1955.

P. J. E. Peebles. *Principles of Physical Cosmology*. Princeton University Press, 1993.

F. S. Porter, E. Apodaca, E. Figueroa-Feliciano, M. Galeazzi, R. Kelly, D. McCammon, C. K. Stahle, A. E. Szymkowiak, and W. T. Sanders. The XQC microcalorimeter sounding rocket: a stable ltd platform 30 seconds after rocket motor burnout. In *Proceedings of the*

8th International Workshop on Low Temperature Detectors (LTD-8), volume 444, pages 220–223. Nucl. Inst. & Meth. A, 2000a.

S. F. Porter, M. D. Audley, P. Beiersdorfer, K. R. Boyce, R. P. Brekosky, G. V. Brown, K. C. Gendreau, J. Gygax, S. Kahn, R. L. Kelley, C. K. Stahle, and A. e. Szymkowiak. Laboratory astrophysics using a spare XRS microcalorimeter. In *X-Ray and Gamma-Ray Instrumentation for Astronomy XI*, volume 4140, pages 407–418. SPIE, 2000b.

A. Rothwarf and B. N. Taylor. Measurement of recombination lifetimes in superconductors. *Physics Review Letters*, 19:27–30, jul 1967.

M. L. Roukes, M. R. Freeman, R. S. Germain, R. C. Richardson, and M. B. Ketchen. Hot electrons and energy transport in metals at millikelvin temperatures. *Physical Review Letters*, 55:422–425, July 1985.

K. Schwab, J. L. Arlett, J. M. Worlock, and M. L. Roukes. Thermal conductance through discrete quantum channels. *Physica E Low-Dimensional Systems and Nanostructures*, 9: 60–68, January 2001.

C. K. Stahle. *The Development of High Resolution Calorimetric X-ray Detectors for Compton Scattering Experiments*. PhD thesis, Stanford University, 1991.

C. K. Stahle. X-ray calorimeters. In *X-ray to X-band: Space Astrophysics Detectors and Detector Technologies Conference*, STScI, Baltimore, MD, 2000. in print, see http://www.stsci.edu/stsci/meetings/space_detectors/.

C. K. Stahle, R. P. Brekosky, E. Figueroa-Feliciano, F. M. Finkbeiner, J. D. Gygax, M. Li, M. A. Lindeman, F. S. Porter, and N. Tralshawala. Progress in the development of Mo/Au transition-edge sensors for X-ray spectroscopy. In *X-Ray and Gamma-Ray Instrumentation for Astronomy XI*, volume 4140, pages 367–375. SPIE, 2000.

C. K. Stahle, M. A. Lindeman, E. Figueroa-Feliciano, M. J. Li, N. Tralshawala, F. M. Finkbeiner, R. P. Brekosky, and J. A. Chervenak. Arraying compact pixels of transition-edge microcalorimeters for imaging x-ray spectroscopy. In *9th International Workshop on Low Temperature Detectors (LTD-9)*. AIP Conference Proceedings, in print, 2002.

C. K. Stahle, D. McCammon, and K. D. Irwin. Quantum calorimetry. *Physics Today*, 52 (8):32–37, August 1999.

E. T. Swartz and R. O. Pohl. Thermal boundary resistance. *Reviews of Modern Physics*, 61(3):605–668, jul 1989.

A. E. Szymkowiak, R. L. Kelley, S. H. Moseley, and C. K. Stahle. Signal processing for microcalorimeters. *Journal of Low Temperature Physics*, 93:281–285, March 1993.

S. Tamura. Monte carlo simulations of quasidiffusion in silicon. In *Fifth International Workshop on Low Temperature Detectors (LTD-5)*, volume 93, pages 433–438. Journal of Low Temperature Physics, 1993.

M. L. van den Berg, D. T Chow, A. Loshak, M. F. Cunningham, T. W. Barbee Jr., M. Frank, and S. E. Labov. High-resolution hard X-ray and gamma-ray spectrometers based on superconducting absorbers coupled to superconducting transition-edge sensors. In *X-Ray and Gamma-Ray Instrumentation for Astronomy XI*, volume 4140, pages 436–444. SPIE, 2000.

T. Vanduzer and C. Turner. *Superconductive Devices and Circuits*. Prentice Hall, 1999.

S. Vitale, G. Gallainaro, and F. Gatti. Alpha- beta- and gamma-ray detection with microcalorimeters made with superconducting absorbers. In *EUV. X-Ray, and Gamma-Ray Instrumentation for Astronomy III*, volume 1743, pages 368–379. SPIE, 1992.

A. Zehnder. Response of superconductive films to localized energy deposition. *Physical Review B*, 52:12858–12866, November 1995.

Index

181

REPORT DOCUMENTATION PAGE

1. AGENCY USE ONLY *(Leave blank)*	2. REPORT DATE	3. REPORT TYPE AND DATES COVERED
	October 2001	Technical Memorandum

4. TITLE AND SUBTITLE
Theory and Development of Position-Sensitive Quantum Calorimeters

5. FUNDING NUMBERS
662

6. AUTHOR(S)
Enectalí Figueroa-Feliciano

7. PERFORMING ORGANIZATION NAME(S) AND ADDRESS (ES)

Goddard Space Flight Center
Greenbelt, Maryland 20771

8. PEFORMING ORGANIZATION REPORT NUMBER

2002-00289-0

9. SPONSORING / MONITORING AGENCY NAME(S) AND ADDRESS (ES)

National Aeronautics and Space Administration
Washington, DC 20546-0001

10. SPONSORING / MONITORING AGENCY REPORT NUMBER

TM—2001–209994

11. SUPPLEMENTARY NOTES

12a. DISTRIBUTION / AVAILABILITY STATEMENT
Unclassified–Unlimited
Subject Category: 76
Report available from the NASA Center for AeroSpace Information,
7121 Standard Drive, Hanover, MD 21076-1320. (301) 621-0390.

12b. DISTRIBUTION CODE

13. ABSTRACT *(Maximum 200 words)*

Quantum calorimeters are being developed as imaging spectrometers for future X-ray astrophysics observatories. Much of the science to be done by these instruments could benefit greatly from larger focal-plane coverage of the detector (without increasing pixel size). An order of magnitude more area will greatly increase the science throughput of these future instruments. One of the main deterrents to achieving this goal is the complexity of the readout schemes involved. We have devised a way to increase the number of pixels from the current baseline designs by an order of magnitude without increasing the number of channels required for readout. The instrument is a high energy resolution, distributed-readout imaging spectrometer called a Position-Sensitive Transition-Edge Sensor (PoST). A PoST is a quantum calorimeter consisting of two Transition-Edge Sensors (TESs) on the ends of a long absorber capable of one-dimensional imaging spectroscopy. Comparing rise time and energy information from the two TESs, the position of the event in the PoST is determined. The energy of the event is inferred from the sum of the two pulses. We have developed a generalized theoretical formalism for distributed-readout calorimeters and apply it to our devices. We derive the noise theory and calculate the theoretical energy resolution of a PoST. Our calculations show that a 7-pixel PoST with 6 keV saturation energy can achieve 2.3 eV resolution, making this a competitive design for future quantum calorimeter instruments. For this thesis we fabricated 7- and 15-pixel PoSTs usingMo/Au TESs and gold absorbers, and moved from concept drawings on scraps of napkins to a 32 eV energy resolution at 1.5 keV, 7-pixel PoST calorimeter.

14. SUBJECT TERMS
Calorimeters, X-ray detectors, spectrometers, astrophysics.

15. NUMBER OF PAGES
184

16. PRICE CODE

17. SECURITY CLASSIFICATION OF REPORT	18. SECURITY CLASSIFICATION OF THIS PAGE	19. SECURITY CLASSIFICATION OF ABSTRACT	20. LIMITATION OF ABSTRACT
Unclassified	Unclassified	Unclassified	UL